Title
Surface Nanostructured Reverse Osmosis Membranes

Permalink
https://escholarship.org/uc/item/9wq976p4

Author
Moses, Kari J.

Publication Date
2016

Peer reviewed|Thesis/dissertation

UNIVERSITY OF CALIFORNIA

Los Angeles

Surface Nanostructured Reverse Osmosis Membranes

A dissertation submitted in partial satisfaction of the

Requirements for the degree Doctor of Philosophy

in Chemical Engineering

by

Kari Jane Moses

2016

ABSTRACT OF THE DISSERTATION

Surface Nanostructured Reverse Osmosis Membranes

by

Kari Jane Moses

Doctor of Philosophy in Chemical Engineering

University of California, Los Angeles, 2016

Professor Yoram Cohen, Chair

Surface wettability (or surface hydrophilicity) is of considerable importance in a variety of applications, including membrane separations, lubrication, fibers (e.g., textiles), and biomedical applications. Alteration of surface wettability to the desired level can be of significant benefit in the above applications. Accordingly, the present study focused on a systematic investigation of the modification of surface hydrophilicity via the synthesis of hydrophilic surface tethered polymers. This approach to surface nanostructuring (SNS) was achieved by a two-step process, whereby surface activation is achieved using atmospheric pressure plasma (APP) followed by graft polymerization with a suitable vinyl monomer. The resulting polymer layer consists of chains that are terminally and covalently attached to the underlying surface, being polyamide in the present study. Polyamide (PA) was the selected substrate given the importance of this

polymer in various applications (e.g., reverse osmosis (RO) membranes, clothing, body armor, etc.). The degree of surface hydrophilicity imparted to the PA surface was evaluated with respect to the conditions of APP surface activation (i.e., hydrogen, oxygen, and helium as plasma source gases, and exposure time) and graft polymerization (i.e., reaction time, 2-hydroxyethyl methacrylate, acrylamide, acrylic acid, n-vinylpyrrolidone, methacrylic acid, and vinylsulfonic acid monomers, and initial monomer concentration). Helium APP was found to be most effective for the synthesis of tethered polymers on the PA surface leading to an increase in hydrophilicity as quantified by a 15 – 51% reduction in the free energy of hydration (ΔG_{iw}) of the underlying PA substrate. In particular, polymer-water affinity of the nanostructured PA surfaces, as quantified by the polar component of the surface energy, was a factor of 2.2 – 6.5 higher than for the native PA surface. Overall, surface hydrophilicity increased with increasing tethered polymer layer surface roughness, volume, and thickness; the above trend is consistent with the expected corresponding increased water sorption capacity by the grafted water soluble polymers.

The hydrophilic polymer brush layer effectiveness in reducing biofouling propensity and improving surface cleaning post-biofouling (i.e., decreasing surface-solute affinity) was demonstrated for SNS-PA thin-film composite (TFC) RO membranes. SNS-PA RO membranes with polyacrylamide (PAAm), poly(acrylic acid) (PAA), poly(methacrylic acid) (PMAA), and poly(vinylsulfonic acid) (PVSA) brush layers were synthesized, yielding permeability and salt (NaCl) rejection ranges of 4.8 – 6.7 L/m^2·h·bar and 95.2 – 96.6%, respectively. Performance testing of the SNS-PA-TFC membranes was carried out using secondary wastewater from a municipal wastewater treatment (MWT) plant. Performance tests with the PMAA-SNS-PA and PAAm-SNS-PA membranes (highest and lowest ranking with regard to hydrophilicity, respectively) demonstrated measurable resistance to biofouling. Biofilm layer thickness was up

to 4.7 times lower for the above SNS-PA membranes relative to a commercial TFC membrane of similar salt rejection. Moreover, up to 89% of the SNS-PA membrane permeability was recovered after water cleaning, and complete restoration of membrane permeability was attained after chemical (Na$_2$·EDTA) cleaning. In summary, the present approach for tailor-designing surfaces is effective for wettability control through adjustment of the brush layer topography and chemistry which affect the polymer-water affinity. Such hydrophilic tethered polymer surface layers can reduce the biofouling propensity of surfaces, and in particular, increase the biofouling resistance and improve cleaning efficiency of RO membranes.

The dissertation of Kari Jane Moses is approved.

Panagiotis D. Christofides

Shaily Mahendra

Yoram Cohen, Committee Chair

University of California, Los Angeles

2016

For my family.

Table of Contents

List of Tables

List of Figures

Acknowledgements

My journey to advance science and achieve my dreams would not have been possible without several people who have supported me and contributed to both the breadth and depth of my technical education. I would like to extend my deepest gratitude to my advisor, Professor Yoram, for his insightful and analytical guidance. I would also like to acknowledge all of my colleagues in Professor Cohen's research group for their stimulating discussions, research collaborations, and critical feedback. Notably, I would like to express special thanks to Dr. Nancy Lin, Dr. Sirikarn Surawanvijit, Soomin Kim, Dr. Alex Bartman, Dr. Muhammad Bilal, and Diana Chien for their friendship, advice, and encouragement. I am also very grateful for research funding provided by fellowships from the National Science Foundation (NSF), UCLA Graduate Division, and the National Water Research Institute Southern California Salinity Coalition (NWRI-SCSC).

I am forever grateful to my family, who has shaped me to become the person I am today. Thank you to my parents for your love, sacrifices, and for teaching me the value of being a strong, self-motivated, independent person. I would also like to thank all of my siblings and friends for their inspiration and optimism, as well as for the happiness that they bring to my life. Finally, I would like to thank my husband, Dan, for his infinite love, support, and encouragement.

Vita

2009   Honors Bachelor of Science, Chemical Engineering

                Oregon State University

                Corvallis, Oregon

2009-2015   Graduate Student Researcher

                Department of Chemical and Biomolecular Engineering

                University of California, Los Angeles

<div align="center">

Publications

</div>

Kari J. Moses (Varin), Muhammad Bilal, and Yoram Cohen. "Hydrophilicity of Tethered Polymers Synthesized by Atmospheric Pressure Plasma Induced Graft Polymerization onto a Polyamide Surface." *Submitted to Langmuir*.

Kari J. Moses (Varin) and Yoram Cohen. "Wettability of terminally anchored polymer brush layers on a polyamide surface." Journal of Colloid and Interface Science. 436 (2014) 286-295.

Kari J. Varin, Nancy Lin, and Yoram Cohen. "Biofouling and Cleaning Effectiveness of Surface Nanostructured Reverse Osmosis Membranes." Journal of Membrane Science. 446 (2013) 472-481.

Yoram Cohen, Nancy Lin, **Kari J. Varin**, Diana Chien, and R. F. Hicks (2013). Membrane Surface Nano-Structuring with Terminally Anchored Polymers Chains. In M. Duke, D. Zhao, and R. Semiat, Functional Nanostructured Materials and Membranes for Water Treatment (1 Ed., p. 85-124). Wiley-VCH Verlag GmbH & Co. KGaA.

Selected Conference Presentations

Kari J. Moses (Varin) and Yoram Cohen. "Synthesis, Characterization, and Performance of Polyamide Membranes Structured with Hydrophilic Polymeric Brush Layers." American Institute of Chemical Engineers (AIChE) National Conference, Salt Lake City, Utah, 11 Nov 2015.

Kari J. Moses and Yoram Cohen. "Biofouling Resistant Surface Nanostructured Reverse Osmosis Membranes." 248th American Chemical Society (ACS) National Meeting, San Francisco, California. 12 Aug 2014.

Kari J. Varin, N. Lin, and Y. Cohen. "Fouling Resistance and Ease of Cleaning Post Biofouling of Atmospheric Pressure Plasma Induced, Surface Nanostructured, Reverse Osmosis Membrane." North American Membrane Society (NAMS) Annual Meeting. New Orleans, Louisiana. 11 Jun 2012.

Kari J. Varin, N. Lin, and Y. Cohen. "High performance nano-structured NF/RO membranes - synthesis, surface characterization and performance." International Congress on Membranes (ICOM). Amsterdam, The Netherlands. 26 July 2011.

Kari J. Varin, N. Lin, and Y. Cohen. "Characterizations of Surface Nano-Structured RO/NF Membranes: Surface Properties and Membrane Performance." American Institute of Chemical Engineers (AIChE) Annual Conference. Salt Lake City, Utah. 10 Nov 2010.

Selected Honors

National Science Foundation (NSF) Graduate Research Fellowship, 2010-2015

University of California, Los Angeles Dissertation Year Fellowship, 2014

National Water Research Institute (NWRI) Fellowship, 2011

Chapter 1.   Introduction and Objectives

1.1   Introduction

Access to sustainable fresh water resources has been of increasing concern across the globe due to population growth and increases in agricultural, commercial, and industrial activities. Most of our planet's water is saline (97.5%), while 0.8% of our water is considered to be fresh water, and 1.7% of water is located in ice caps [1]. Saline water (seawater, inland brackish water, and water reuse) could represent a significant sustainable water resource if upgraded to potable water quality at a reasonable cost. Reverse osmosis (RO) membrane desalination, a technology developed nearly 50 years ago, is capable of removing ~99% of dissolved solids from saline water to produce water of potable quality (< 500 mg/L total dissolved solids (TDS)) [1]. In RO desalination, pressure (higher than the osmotic pressure) is applied to the feed side of a semipermeable RO membrane, which drives a solute lean (i.e., permeate) product water through the membrane leaving behind a solute rich (i.e., retentate) solution. Current RO membranes used for water desalination are thin film composite (TFC) membranes based on a selective polyamide (PA) layer, which is the active layer responsible for solute (e.g., salt) rejection.

Despite progress in RO technology, membrane surface biofouling remains a critical impediment [2]. During RO desalination, biofilm can form on the membrane surface due to deposition and proliferation of bacteria and production (i.e., metabolism) of extracellular polymeric substances (EPS) [3-4]. Biofouling can cause significant permeate flux (i.e., fresh water production) decline, thus shortening of the membrane useful life (Figure 1-1) [5]. Furthermore, biofouling can result in decreased salt rejection and elevated hydraulic resistance and trans-membrane osmotic pressure [2]. Once biofilms form, they can be difficult to remove and require aggressive membrane cleaning, which leads to additional maintenance costs and can

quicken the need for membrane replacement [6]. There are mechanical (e.g., microfiltration (MF), ultrafiltration (UF)) and chemical (e.g., UV, ozone, chlorination, chloramination) pretreatment methods that are used to mitigate biofouling [7] which may remove 99.99% of bacteria cells; however, biofouling still occurs due to the self-replicating nature of the small number of microorganisms that elude the pretreatment process [4, 8]. Given that biofouling is an impediment to RO technology, a variety of methods to combat biofouling have been proposed, of which various membrane surface modification methods have been touted as the most promising for developing high performance fouling resistant membranes [9-12].
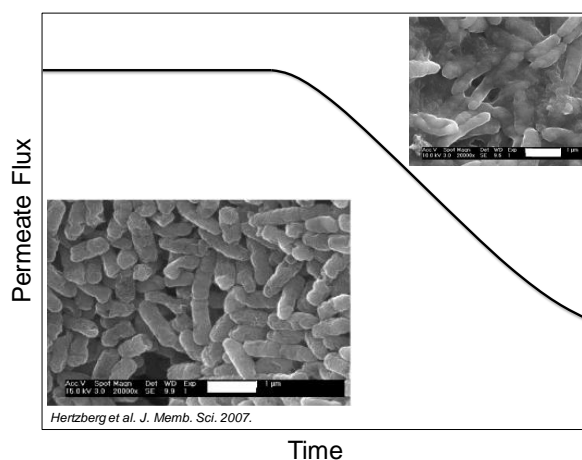
Figure 1-1. Over time, biofouling results in decreased permeate flux. Inset scanning electron microscopy (SEM) images show biofouling layers on RO membrane surfaces (1 μm scale bar) [2].

Several methods have been reported for membrane surface modification to impart biofouling resistance including physical (e.g., surface coating) [10] and chemical (e.g., attaching polymer chains to the PA surface via chemical [13], UV [14-17], gamma [18-19], or plasma [20-21]

exposure) surface modifications. Physical modifications (e.g., surface coating) are often succumbed to mere temporary improvements in repelling biofoulants due to leeching or desorption of the coating [10]. In contrast, attaching polymer chains or a polymer "brush" layer directly to the PA surface is particularly advantageous because the resulting polymeric chains are terminally anchored to the membrane support at one end of the chain. Furthermore, the hydrophilic brush layer swells away from the surface when exposed to water (a good solvent for the hydrophilic polymers) [9, 11, 22]. The tethered hydrophilic polymer chains on the PA surface enhance membrane surface hydrophilicity as well as induces some degree of surface chain mobility (caused by thermal and physical fluctuation of liquid surrounding the unbound end of the polymer chain [23]), which increases repulsion of hydrophobic biofoulants. There are various methods to nanostructure surfaces with tethered polymer chains, of which atmospheric pressure plasma (APP) surface activation followed by graft polymerization is regarded as the most promising approach [9-12]. In particular, APP surface activation followed by subsequent graft polymerization is an effective approach for surface modification due to its ability to create a dense, surface nanostructured (SNS) polymer brush layer without the use of chemical initiators or possible exposure to harmful radiation [10]. Additionally, the APP approach is low-cost and potentially a commercially viable approach as it can be adapted for continuous large-scale manufacturing at atmospheric pressure [10].

Current approaches on creating biofouling resistant membranes focus on altering the surface properties (e.g., topography, hydrophilicity, surface charge) of PA-based RO membranes with functional polymers to promote biofouling resistance [24]. In nature, most biofoulants are typically hydrophobic and negatively charged [5]. Hence, it is known that surface modification to impart increased hydrophilicity and negative charge on RO membranes is preferred in order to

induce hydrophilic-hydrophobic interactions and electrostatic repulsion between the membrane surface and biofoulants [5, 10, 13, 25-26]. Additionally, low surface roughness is ideal [5] in order to decrease the amount of valleys of the rough surface for foulants to accumulate in. It is clear that surface chemistry and topography can affect solute-membrane surface interactions [27], which suggest that fouling could depend on membrane surface chemistry, hydrophilicity, and topography. Although it is known that smooth, negatively-charged, hydrophilic surfaces promote biofouling resistance, there is a major knowledge gap regarding how to synthesize SNS grafted polymer brush layers on PA surfaces with a specific degree of hydrophilicity in order to impart biofouling resistance. A major research challenge is to identify and quantify the relevant contributions of SNS polymer layer thickness and surface topography (e.g., surface roughness, polymer volume, number density of major end-grafted polymer features, etc.) on surface wettability/hydrophilicity, and how the surface properties are affected by surface activation and graft polymerization conditions (e.g., plasma type and exposure time, monomer type and concentration, graft polymerization time).

In order to elucidate the impact of SNS polymer layers on surface hydrophilicity, the present research focuses on investigating the relationship of surface wettability with surface topography, structure, and chemistry. Accordingly, SNS polymer layer thickness and surface topography were altered, as controlled by the surface activation and graft polymerization conditions, in order to achieve a specific level of hydrophilicity. The atmospheric pressure plasma induced graft polymerization (APPIGP) method was utilized to generate a high density of surface activated sites on a PA surface for subsequent graft polymerization. Surface structuring via graft polymerization was then employed to synthesize a hydrophilic brush layer of polymeric chains that are terminally and covalently tethered onto the PA surface. The APPIGP method is

particularly advantageous because it results in high surface density of grafted polymer chains of low surface roughness and long-term stability. The effectiveness of the hydrophilic polymer brush layer in imparting biofouling resistance and cleaning effectiveness post-biofouling was demonstrated for SNS RO membranes. It is hypothesized that the hydrophilic SNS polymeric brush layer of these membranes can be effective in reducing biofoulant-surface affinity and screening the underlying PA-based RO membrane (Figure 1-2).
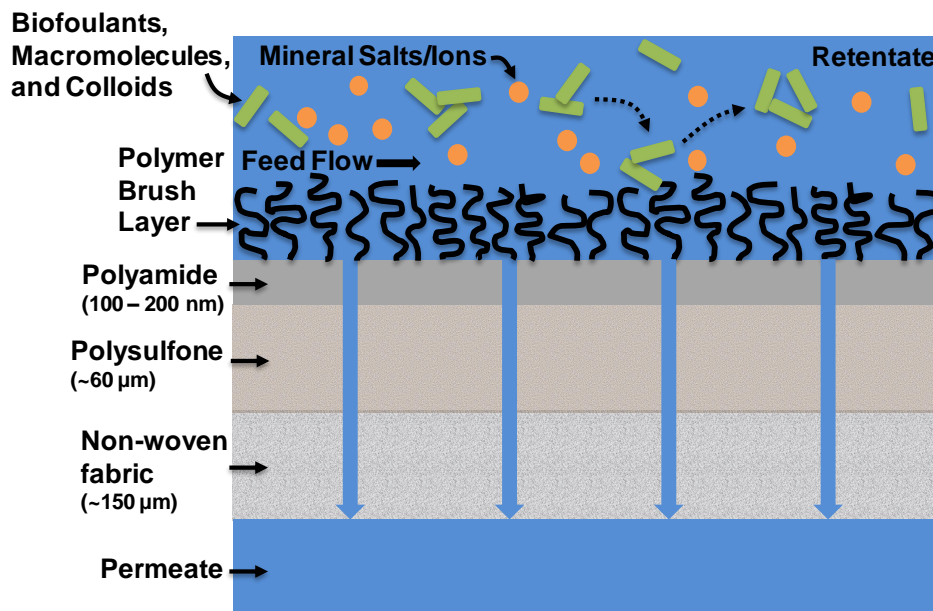
Figure 1-2. Schematic of a polyamide-polysulfone RO membrane with a nanostructured polymer brush layer imparting biofouling resistance by preventing adhesion of biofoulants onto the membrane surface.

1.2   Problem Statement

In order to investigate the dependence of surface wettability on surface topography, structure, and chemistry, SNS polymer layers were synthesized on a PA surface via APPIGP. Effective surface nanostructuring of the PA surface with hydrophilic polymers requires the use of monomers that are compatible with graft polymerization and have specific chemistries/functionalities that impart hydrophilicity. Systematic studies are then necessary to tune surface activation (via altering inlet gas composition for plasma generation) and graft polymerization conditions (e.g., polymerization time, monomer type and initial concentration). The above is essential in order to determine how APPIGP conditions affect the grafted polymer layer's surface topography at the nanoscale (e.g., roughness, polymer layer thickness and volume) and hydrophilicity. However, in order to ascertain the nanoscale changes in surface topography of the polymer brush layer, it is necessary to develop and evaluate the polymer brush layers on smooth PA-silicon surfaces. The effectiveness of the tethered hydrophilic polymer bush layer in promoting biofouling resistance and cleaning effectiveness post-biofouling (i.e., decreasing surface-solute affinity) to polymeric RO membranes can significantly enhance the performance of RO/nanofiltration (NF) membranes. Accordingly, it is critical to assess membrane performance (i.e., permeability, salt rejection, resistance to biofouling, and ease of cleaning) of SNS-PA RO membranes during desalination of source water of high biofouling propensity, and subsequent membrane cleaning.

1.3 Objectives of the Dissertation

The major goals for the dissertation were to: a) investigate the dependence of surface wettability of tethered hydrophilic polymer layers on surface topography (e.g., roughness, polymer layer thickness and volume), and b) demonstrate that hydrophilic SNS polymer layers can effectively impact membrane biofouling resistance. The above goals are rooted in the hypothesis that ***biofouling resistance of polyamide RO membranes can be achieved by tuning surface wettability and topography of a polymer brush layer tethered to the membrane surface***. The specific objectives of the research are listed below.

1. Investigate the relationship of surface topography, structure, and chemistry on surface wettability of a tethered hydrophilic polymer layer.

   - Develop a methodology to tune wettability and control surface roughness of a hydrophilic, semi-mobile, surface nanostructured polymer brush layer on a polyamide surface

     - Investigate and evaluate how plasma surface activation (e.g., plasma source gas) and graft polymerization (e.g., polymerization time, monomer type and initial concentration) conditions affect the number density of major end-grafted polymer features, polymer layer thickness, surface topography, and hydrophilicity

2. Demonstrate the effectiveness of the hydrophilic, SNS polymer layer on imparting biofouling resistance

- Develop high performance (i.e., >95% salt rejection and permeability >4 L/m^2·h·bar) surface nanostructured, polyamide, reverse osmosis membranes for use in brackish water and wastewater desalination

- Evaluate biofouling resistance during desalination of secondary wastewater and cleaning effectiveness post-biofouling for surface nanostructured RO membranes

1.4 Research Approach

In the present work, a detailed systematic study was performed in order to evaluate the relationship of surface topography, structure, and chemistry on the surface wettability of hydrophilic, SNS, tethered polymer surfaces. In order to accomplish this goal, SNS-PA surfaces, synthesized via APPIGP, were quantitatively analyzed with respect to surface topography, chemistry, and hydrophilicity. Surface chemistry was altered and topography and structure were tuned, depending on the surface activation and graft polymerization conditions, to achieve the desired level of surface wettability. The research approach was implemented in order to evaluate the impact of surface activation and graft polymerization conditions (e.g., plasma type, monomer type and initial concentration, graft polymerization time) on the resulting SNS-PA surface hydrophilicity.

The effectiveness of the SNS polymer layer on increasing hydrophilicity (and thus, decreasing surface-solute affinity) was demonstrated for the synthesis of low fouling PA-based RO membranes. These high performance membranes were developed based on SNS via APPIGP which was integrated with the interfacial polymerization method of synthesizing PA-TFC membranes. SNS-PA-TFC RO membranes were experimentally evaluated during the filtration of

secondary treated municipal wastewater effluent in a plate-and-frame RO system. The SNS polymer layer was capable of increasing the hydrophilicity of PA-TFC membranes to promote water permeability, while maintaining high salt rejection (>95%), and increasing biofouling resistance and cleaning efficiency post-biofouling compared to a commercially available membrane. A flow chart of the dissertation work is shown in Figure 1-3.

Evaluate the relationship of surface wettability of a hydrophilic, surface nanostructured, tethered polymer layer with surface topography, structure, and chemistry, and application to the synthesis of low fouling RO membranes

Determine the effectiveness of atmospheric pressure plasma conditions (e.g., plasma gas type) on surface activation of polyamide surfaces

Determine the impact of graft polymerization conditions (e.g., monomer type and initial concentration, polymerization time) on SNS-PA topography and hydrophilciity

Synthesis of SNS-PA-TFC RO membranes

Evaluate surface hydrophilicity and relationship to surface topography, structure, and chemistry for SNS-PA surfaces

Evaluate SNS membrane performance with respect to salt rejection and permeability

Demonstrate biofouling resistance and cleaning effectiveness post-biofouling of SNS-PA-TFC RO membranes

Figure 1-3. Research flow chart.

Chapter 3 focuses on the impact of surface topography, at the nanoscale, in relation to polymer-water affinity. Two candidate monomers were selected for the development of polymer surface nanostructured (SNS)-PA surfaces via atmospheric pressure plasma induced graft polymerization (APPIGP) onto a polyamide (PA) surface. The physiochemical characteristics (e.g., surface roughness and hydrophilicity) of the SNS-PA surfaces were modified to attain

9

varying degrees of surface hydrophilicity by altering surface topography and surface chemistry, which were controlled by polymerization reaction conditions. Subsequently, the dependence of surface wettability of the SNS-PA surface on surface topography was evaluated.

The impact of plasma type on the PA surface activation effectiveness, and the resulting polymer brush layer's topography and hydrophilicity is described in **Chapter 4**. Three different gas compositions were used to generate different plasma types. Three different vinyl monomers were used to synthesize nanostructured polymer brush layers. The grafted surfaces were evaluated with x-ray photoelectron spectroscopy (XPS) and contact angle to determine their surface chemistry and hydrophilicity, respectively. AFM and ellipsometry were employed to determine the polymer brush layer's surface topography and thickness, respectively. The effectiveness of plasma source gas on atmospheric pressure plasma (APP) PA surface activation was assessed by increase in surface hydrophilicity as quantified via analysis of water contact angle measurements. Subsequently, a systematic study was undertaken to quantify the change in surface wettability upon free radical graft polymerization at varying reaction conditions (e.g., plasma gas type, monomer type and initial concentration, temperature, polymerization time) which had a profound impact on surface topography.

The SNS approach was applied to the development of SNS-PA RO membranes for use in secondary treated wastewater desalination, as presented in **Chapter 5**. Four different SNS-PA RO membranes were examined for membrane performance with respect to permeability and salt rejection. Additionally, membrane surface properties were evaluated with respect to topography as evaluated by surface roughness, surface zeta potential, and hydrophilicity as quantified by free energy of hydration and polar component of surface energy.

In **Chapter 6**, the impact of the hydrophilic, SNS polymer brush layer on imparting biofouling resistance was experimentally evaluated in a plate-and-frame RO system. Two optimized (with respect to surface chemistry and topography) hydrophilic SNS membranes were examined for biofouling propensity and cleaning efficiency post-biofouling, and compared to a commercial PA RO membrane. The membranes were evaluated for biofouling resistance by monitoring permeate flux decline during RO treatment of secondary wastewater effluent. Also, the thickness and density of the biofouling layer were quantified by confocal laser scanning microscopy (CLSM), extracellular polymeric substances (EPS) analysis, and scanning electron microscopy (SEM). Membrane cleaning efficiency post-biofouling was determined by permeability recovery attained after DI water and chemical (Na$_2$·EDTA) cleaning, as well as biofilm removal as characterized by SEM.

Chapter 2.   Background and Literature Review

2.1   Importance of Surface Properties

Surface wettability (or surface hydrophilicity) is of considerable importance in a variety of applications such as membrane separations [11, 28], lubrication [29], fibers (e.g., textiles) [30-31], and biomedical applications [32-34]. There is considerable interest and benefit to modifying surfaces with respect to surface chemistry and topography in order to alter surface hydrophilicity [10-11, 24, 28, 32, 35], increasing [29, 35-36] or decreasing [11, 28, 32-34] the target solute affinity for the surface, decreasing surface adsorption of proteins (i.e., biofouling) [10, 24], decreasing friction [29], imparting biocompatibility [32-34], and increasing adhesion [30-31]. For example, previous studies have sought modify both inorganic and organic surfaces to mimic surface topographies found in nature such as the self-cleaning properties exhibited by cicada wings, gecko foot-hair, and the lotus leaf [37-39]. Indeed, the above studies illustrate the importance of interactions of surfaces with solutes, and how the interactions are impacted by surface properties.

In the present work, altering surface hydrophilicity is of particular importance for the application of reverse osmosis (RO) membranes. In the case of polymeric membranes, biofouling impedes membrane filtration performance [5]. Modifying the membrane surface for increased surface hydrophilicity is critical to decrease membrane surface biofouling (i.e., decrease surface-solute affinity) [9, 24, 40]. Thus, various approaches of modifying surfaces (and in particular polyamide-based RO membranes) are reviewed in the present chapter.

2.2   Strategies for Promoting Membrane Biofouling Resistance

The major methods of mitigating membrane biofouling include: (1) surface modification with suitable hydrophilic polymers containing negatively charged groups [11, 13, 21, 25, 40], (2) feed pretreatment including the use of chemical additives (e.g., UV, ozone, chlorination, chloramination), microfiltration (MF), and ultrafiltration (UF) [7, 41], and (3) cyclic membrane cleaning [26, 42-45]. As previously discussed (Chapter 1, Section 1.1), feed pretreatment does not effectively eliminate membrane biofouling. Therefore, periodic membrane cleaning is needed which adds to the cost of water treatment and may accelerate membrane damage [46]. Of the above three categories, membrane surface modification is widely regarded to be the most promising approach for combating membrane biofouling [9, 24, 40]. Over the last few decades, various approaches have been advanced for modifying membrane surface hydrophilicity and topography in order to decrease membrane biofouling propensity.

Membrane surface hydrophilicity, roughness, and surface charge are critical factors that control fouling propensity. Increasing membrane surface hydrophilicity is well known to promote biofouling resistance because most biofoulants are hydrophobic in nature [5, 24, 47]. Additionally, rough surfaces have increased surface area or valleys for foulants to become trapped or accumulate in. Therefore, smooth surfaces or surfaces with low surface roughness (R_{rms}) are known to decrease biofouling propensity [4-5, 24, 47]. Altering membrane surface charge can also be advantageous in order to increase electrostatic repulsion between biofoulants and the membrane surface. Since most biofoulants in natural waters (e.g., bacterial cells, proteins) are negatively charged, surfaces that have negatively charged groups reduce bacterial attachment and subsequent biofilm formation [5]. Therefore, surface modification that results in a smooth, hydrophilic, negatively charged membrane surface is ideal for promoting biofouling

resistance due to physical, hydrophilic-hydrophobic interactions [24], and electrostatic repulsion [26] between the polymer and the biofoulants, respectively.

Membrane surface modification can be accomplished via physical or chemical methods. Physical methods include membrane surface coating with polymers or surfactants [47-48] or embedding nanoparticles (e.g., TiO_2) within the polyamide (PA) matrix [49-51]. Although these methods have been shown to increase membrane performance (i.e., permeability and fouling resistance), the effects are often temporary due to gradual attrition (or leaching) of the surface coating additives [52]. A major deficiency with physical coating of the membrane surface (e.g., with polymers, surfactants, or other chemical modifiers) is the lack of long-term stability of such coatings. Chemical treatment methods include exposing the membrane to acids or plasma, or attaching polymer chains to the PA membrane surface. By exposing the PA membrane surface to acids such as hydrofluoric, hydrochloric, sulfuric, phosphoric and nitric acids, partial hydrolysis occurs resulting in increased hydrophilicity [47]; unfortunately, decreased salt rejection may occur due to uncontrolled acid exposure and biofouling propensity has not been investigated [47, 53]. Plasma treatment has also been known to hydrophillize (i.e., reduce contact angle) membrane surfaces to improve membrane permeability, fouling resistance, and flux recovery post-cleaning [54-57]. However, reduction in water contact angle due to plasma exposure is not permanent and over time (as first detected around 15 minutes) the contact angle generally rises back toward the value associated with the untreated surface [58]. Furthermore, some studies suggest that uncontrolled plasma treatment can lead to severe membrane etching (i.e., degradation) [54]. Therefore, surface modification by surface nanostructuring with suitable hydrophilic polymers is the preferred approach, as described in Section 2.3.

2.3 Surface Modification with Polymers

Altering surface properties in order to affect surface-solute interactions (e.g., improve membrane biofouling resistance) by attaching polymer chains (i.e., polymer "brush" layer) can be accomplished by polymer grafting or graft polymerization (Figure 2-1) [9]. Graft polymerization can be utilized to tailor-design surfaces for increased hydrophilicity, low surface roughness, and negatively charged groups, where the underlying surface is screened by end-grafted polymer chains. Moreover, the hydrophilic end-attached polymer chains swell and have partial mobility (due to Brownian motion of chain segments) when they come in contact with water [40, 59-61]. Therefore, the probability of solute (e.g., biofoulant) attachment to the surface is reduced.

Polymer grafting (or "grafting to") refers to covalent attachment of pre-formed hydrophilic polymer chains onto a surface at activated surface sites. In order to synthesize a polymer brush layer, the surface must possess activated (or reactive) sites for polymer chain anchoring. Activated sites are created via exposure to chemical initiators [13, 40, 62-63], gamma irradiation [64-67], UV irradiation [64, 68-70] or via plasma-based polymerization [21, 71-73]. However, in polymer grafting the ability to attain high surface graft density is limited due to steric hindrance, which reduces the ability of long polymer chains to reach the activated surface sites [74-75]. On the other hand, graft polymerization (or "grafting from"), whereby polymer chains are "grown" via sequential vinyl monomer addition from activated surface sites, allows for higher surface chain density and better control over surface properties (e.g., roughness) of the resulting polymer brush layer [9]. There are a variety of methods that have been used to create activated sites for subsequent graft polymerization: surface reactive initiators [25, 76] and monomers [77-79], and irradiation [13, 66-67] and plasma [21, 80] activation. When an initiator is used in bulk solution,

radicals in the monomer solution can form, leading to homopolymerization and polymer grafting (i.e., "grafting to"), yielding a broad molecular weight distribution of surface grafted chains (i.e., high polydispersity) [80]. Thus, graft polymerization (i.e., "grafting from") via monomer addition to activated surface sites is preferred since limited attachment of growing chains in solution via termination with surface chains (i.e., "grafting to") is ideal in order to create a polymer brush layer with higher surface polymer chain density and lower roughness [81-83]. Indeed, various studies have demonstrated that surface graft polymerization of hydrophilic polymers onto MF [84-86], UF [68, 72, 86] and RO/nanofiltration (NF) [12, 25, 40, 87] can be effective in reducing the extent of biofouling and protein adhesion.
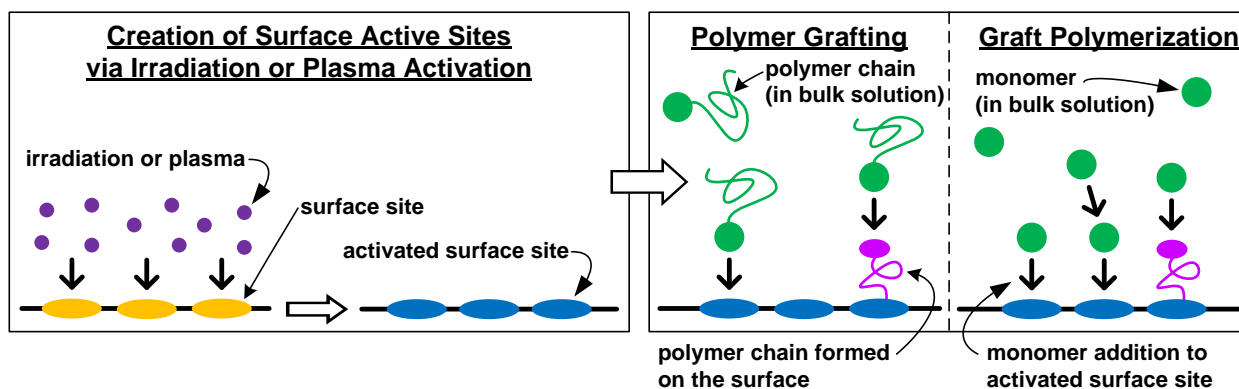
Figure 2-1. Methods for polymer brush layer synthesis: polymer grafting (i.e., "grafting to") and graft polymerization (i.e., "grafting from").

Various studies have shown that surface properties of polymer brush layers are dependent on the polymerization conditions (e.g., polymer grafting versus graft polymerization, grafting time, initial solution concentration, temperature, time, etc.). For example, when activated surface sites are formed via surface exposure to atmospheric pressure plasma followed by polymerization,

water contact angle decreases [32, 88-92] and surface roughness increases [76, 93] with increased graft yield of tethered hydrophilic polymer to different degrees depending on the polymerization conditions (Table 2-1). Therefore, it is critical to tune polymerization conditions in order to design surfaces of specific properties (e.g., roughness, hydrophilicity, surface charge), particularly for synthesizing membranes of low biofoulant-surface affinity that also achieve the target permeability and salt rejection.

Table 2-1. Polymer brush layer development via atmospheric pressure plasma induced polymerization [a].

Ref.	Surface	Plasma Initiation [b]	Polymerization					Grafted Polymer Layer Yield (GY),
			Method	Monomer or Polymer	$[M]_0$	Temp. (ºC)	Time (h) [c]	Contact Angle (θ_w), Roughness (R_{rms})
[94]	polystyrene	DBD Air $t_{exp} = 1 - 3000$ s (0.1 – 4.5 cm/s scan speed) Power = NR	"grafting to" with surface adsorbed monomer	diethylglycol monovinyl ether	90 – 220 µg/cm^2	ambient	≤0.83	$GY\downarrow$ as $[M]_0\uparrow$ (above 95 µg/cm^2) or $t_{exp}\uparrow$ (above 5 s) or energy density ↓ (below 2 J/cm^2) $t\downarrow$ as plasma distance ↑
				vinyl acid	NR			$t\downarrow$ as plasma distance ↑ (above 1 mm)
[32]	poly(vinylidene fluoride)	APPJ 10 L/min Ar $t_{exp} = 0 - 120$ s Power = 150 W	"grafting to" with surface absorbed polymer	poly(ethylene glycol) methacrylate	10 wt%	25	≤0.03	$GY\uparrow$ and $\theta_w\downarrow$ as $t_{exp}\uparrow$
[95]	polypropylene	APPJ 10 L/min Ar $t_{exp} = 15 - 120$ s Power = 150 W	"grafting from" followed by "grafting to" with surface adsorbed monomer	(2-(methacryloyloxy)-ethyl) dimethyl(3-sulfopropyl)-ammonium hydroxxide	30 wt%	25	~24	$GY\uparrow$ and $\theta_w\uparrow$ as $t_{exp}\uparrow$
[96]	50/50 cotton / polyethylene terephthalate	APGDP 40 L/min He $t_{exp} = 0 - 10$ s (before monomer exposure) + 5 – 10 s (after monomer exposure) Power = 600 W	"grafting to" with surface adsorbed monomer	1,1,2,2-tetrahydroperfluorodecyl acrylate (vapor)	1.42 – 2.83%	ambient	0.001 – 0.003	$\theta_w\uparrow$ as $t_{exp}\uparrow$
[97]	silicone elastomer	DBD NR t_{exp} = NR Power = 500 W	"grafting to" followed by "grafting to" with surface adsorbed polymer	poly(ethylene glycol) methyl ether methacrylate	10% wt/vol	50	~2	$R_{rms}\uparrow$, $\theta_w\downarrow$
[98]	cotton fabrics	DBD 10 L/min He $t_{exp} = 5 - 20$ min Power = NR	"grafting to" with surface adsorbed monomer	vinyl monomers synthesized with triethylamine and acryloyl chloride: contains OH groups or tertiary N groups	10 – 30 wt%	NR	0.08 – 0.33	$GY\uparrow$ as $t_{exp}\uparrow$ or $[M]_0\uparrow$

| Ref. | Surface | Plasma Initiation [b] | Polymerization | | | | | Grafted Polymer Layer Yield (GY), |
			Method	Monomer or Polymer	$[M]_0$	Temp. (ºC)	Time (h) [c]	Contact Angle (θ_w), Roughness (R_{rms})
[88]	polyethersulfone	APPJ 30 L/min He t_{exp} = NR (0.3 mm/s scan speed) Power = NR	"grafting to"	poly(ethylene glycol) methyl ether methacrylate	0.2 M	60	2	$GY\uparrow$, $\theta_w\downarrow$
[99]	polyethersulfone	APPJ 30 L/min He t_{exp} = NR (0.7 mm/s scan speed) Power = NR	"grafting from"	10 different amides	0.1 – 0.3 M	60	2	NR
[100]	polypropylene	plasma 6 L/min Ar t_{exp} = NR Power = 200 W	"grafting from"	glycidyl methacrylate	2 – 15 wt%	60 – 90	1 – 7	$GY\uparrow$ as $[M]_0\uparrow$ (up to 12 wt%) or $T\uparrow$ or $t_{exp}\uparrow$
[11]	polyamide-polyethyleneimine-silicon	APPJ 1/99 H$_2$/He t_{exp} = 10 s Power = 40 W	"grafting from"	methacrylic acid	5 – 20 vol%	60	~2	$R_{rms}\downarrow$ and $\theta_w\downarrow$ as $[M]_0\uparrow$
[101]	polytetrafluoro-ethylene	corona 30 L/min Ar + 3 L/min Ar bubbling through acrylic acid monomer t_{exp} = NR (1–20 mm/s scan speed) Power = 500 W	"grafting to" (plasma exposed to monomer in gas phase)	acrylic acid (vapor)	NR	NR	NR	NR
[102]	silicon	APPJ ~30 L/min 1/99 H$_2$/He t_{exp} = 10 s Power = 40 W	"grafting from"	styrene (in chlorobenzene)	10 – 50 vol%	70 – 100	8	$D\uparrow$ as $T\uparrow$ or $[M]_0\uparrow$ $t\uparrow$ as $[M]_0\uparrow$ (up to 30 vol% at T = 85ºC)
[80]	silicon	APPJ 30.4 L/min 1/99 H$_2$/He t_{exp} = 10 s Power = 20 – 60 W	"grafting from"	1-vinyl-2-pyrrolidone	10 – 50 vol%	80	8	$GY\uparrow$ as $[M]_0\uparrow$ (up to 30 vol%) $R_{rms}\uparrow$ as $[M]_0\uparrow$ (up to 40 vol%)
[103]	acrylic intraocular lens	APGDP Ar t_{exp} = 30 s (before monomer exposure) + 1 – 8 min (after monomer exposure) Power = 20 –23 W	"grafting to," followed by "grafting to" with surface absorbed polymer	poly(ethylene glycol) methacrylate	100%	NR	0.02 – 0.013	$R_{rms}\uparrow$ and $\theta_w\downarrow$ as $t_{exp}\uparrow$

Ref.	Surface	Plasma Initiation [b]	Polymerization					Grafted Polymer Layer Yield (GY), Contact Angle (θ_w), Roughness (R_{rms})
			Method	Monomer or Polymer	$[M]_0$	Temp. (ºC)	Time (h) [c]	
[12, 103]	polyamide-polysulfone	APPJ 1/99 H$_2$/He t_{exp} = 5 – 15 s Power = 40 W	"grafting from"	methacrylic acid	0.57 – 2.35 M	60	0.5	R_{rms}↑ as $[M]_0$↑
				acrylamide	0.1 – 0.3 M			no apparent trend (R_{rms} and θ_w reported)
[104]	50/50 nylon/cotton	APGDP He t_{exp} = 120 s Power = 800 W	"grafting to" with surface adsorbed monomer	diallyldimethyl-ammonium chloride	4 wt%	NR	NR	NR
[105]	50/50 nylon/cotton	APGDP 3 mL/min 99/1 He/O$_2$ t_{exp} = 120 s Power = 800 W	"grafting to" with surface adsorbed monomer	2-(perfluorohexyl)-ethyl acrylate (vapor)	5 mol%	NR	NR	θ_w↑
[106]	polypropylene	APGDP 99/1 He/O$_2$ t_{exp} = 0 – 120 s (before monomer exposure) + 60 – 120 s (after monomer exposure) Power = 400 – 800 W	"grafting from" followed by "grafting to" with surface absorbed monomer	diallyldimethyl-ammonium chloride	65 vol%	NR	0.02 – 0.03	NR
[107]	polyurethane	APPJ 5 L/min Ar with a max. of 5% O$_2$ t_{exp} = 30 – 180 s Power = 60 – 200 W	"grafting from"	acrylic acid	30%	70	3	GY↑ as t_{exp}↑ (up to 100 s) or power ↑ (up to 100 W)
					10 – 70%	30 – 80	1 – 5	GY↑ as $[M]_0$↑ or T↑ or t_{rxn}↑
[108]	polytetrafluoro-ethylene	APGDP 2 L/min He t_{exp} = 20 min Power = NR	"grafting to" with surface adsorbed monomer	acrylic acid	1 – 20%	ambient	0.17	θ_w↓ as $[M]_0$↑
[109]	polyester, 65% polyester, and 35% cotton	APPJ induced by DBD 10/2 He/Ar t_{exp} = NR (10 mm/min scan speed) Power = 770 or 1500 W	"grafting from"	acrylic acid (mist with N$_2$ carrier gas)	100 mL/h	24 – 26	NR	θ_w↓
[110]	polytetrafluoro-ethylene	APPJ induced by corona 30 L/min Ar + 3 L/min bubbling monomer vapor t_{exp} = NR Power = 500 W	"grafting to" (plasma exposed to monomer in gas phase)	acrylic acid (vapor)	NR	40 – 70	NR	θ_w↓
				acetic acid (vapor)		NR		
				1/1 acrylic acid/formic acid (vapor)				

Ref.	Surface	Plasma Initiation [b]	Polymerization Method	Monomer or Polymer	$[M]_0$	Temp. (ºC)	Time (h) [c]	Grafted Polymer Layer Yield (GY), Contact Angle (θ_w), Roughness (R_{rms})
[111]	polytetrafluoro-ethylene	APPJ 100 L/min Ar with 1200 ppm monomer vapor t_{exp} = 240 s Power = 500 W	"grafting to" (plasma exposed to monomer in gas phase)	acrylic acid (vapor)	~1200 ppm	45	0.07	NR
[31]	perfluoroalkoxy fluoro-plastics, polytetrafluoro-ethylene	APPJ induced by corona 100 L/min Ar t_{exp} = 75 s Power = 500 W	"grafting from"	acrylic acid	50 – 100%	45	0.5	$\theta_w\downarrow$ as $[M]_0\uparrow$
[112]	cotton	APGDP 40 L/min He + 0.5 – 2 L/min Ar t_{exp} = 420 s (0.37 m/min scan speed) Power = 750 W	"grafting to" with surface adsorbed monomer	2-(perfluorohexyl) ethyl acrylate (vapor) with di(ethyleneglycol) diacrylate (crosslinker)	10:1 – 20:1	100 – 160	0.07	$\theta_w\uparrow$ as $[M]_0\uparrow$ (up to 15:1 ratio between monomer:crosslinker) or $T\uparrow$ (up 130ºC) or Ar flowrate$\uparrow$ (up 1.25 L/min)
[113]	silicone hydrogel	APGDP 5 L/min He t_{exp} = 10 – 60 s Power = 60 W	"grafting from"	n-vinyl pyrrolidone	2 – 30 wt%	75	24	$\theta_w\downarrow$ as $[M]_0\uparrow$
			"grafting to"	poly(ethylene glycol) methyl ether methacrylate				
[114]	polyvinylidene-fluoride-hexafluoro-propylene	APGDP 5 L/min He t_{exp} = 30 s Power = 60 W	"grafting to"	poly(ethylene glycol) methyl ether methacrylate	2 – 20 wt%	75	24	$GY\uparrow$ as $[M]_0\uparrow$
[89]	polyethylene terephthalate	APPJ 20 – 38 L/min He + 0 – 0.2 O_2 t_{exp} = 30 – 180 s Power = 40 W	"grafting from"	acrylic acid	NR	50	1	$\theta_w\downarrow$ and $GY\uparrow$ as $t_{exp}\uparrow$ or He flowrate $\uparrow$ $GY\downarrow$ with the addition of O_2 gas
[90]	polyethylene terephthalate	APPJ 20 L/min He t_{exp} = 30 – 180 s Power = 40 W	"grafting from"	acrylic acid	NR	50	1	$\theta_w\downarrow$ and $GY\uparrow$ as $t_{exp}\uparrow$
[115]	polyacrilonitrile	DBD Air t_{exp} = 5 min Power = NR	"grafting to"	poly(ethylene glycol) methyl ether methacrylate (M_w = 300, 1100, 2080)	25%	60	3 – 12	$\theta_w\uparrow$ as $M_w\uparrow$

| Ref. | Surface | Plasma Initiation[b] | Polymerization | | | | | Grafted Polymer Layer Yield (GY), |
			Method	Monomer or Polymer	$[M]_0$	Temp. (ºC)	Time (h)[c]	Contact Angle (θ_w), Roughness (R_{rms})
[116]	polytetrafluoro-ethylene	DBD 5 L/min Ar + 10 L/min monomer vapor in Ar t_{exp} = 30 – 180 s Power = NR	"grafting to" (plasma exposed to monomer in gas phase)	acrylic acid (vapor)	100%	NR	0.003 – 0.07	θ_w↓ as t_{exp}/ t_{rxn}↑
[93]	polyethylene terephthalate	plasma 6 L/min t_{exp} = 1 min Power = 100 W	"grafting from"	acrylic acid	20 – 70%	60 – 90	1 – 5	GY↑ as $[M]_0$↑ or T↑ or t_{rxn}↑ (up to 3 h) R_{rms}↑ as GY↑
[117]	Kevlar	APPJ 40 L/min He t_{exp} = 5 – 60 s Power = 200 – 800 W	"grafting to" with surface adsorbed monomer	diallyldimethyl-ammonium chloride	10%	NR	0.001 – 0.017	GY↑ as t_{exp}↓ or power ↓ (above t_{exp} = 20s)
					30%			GY↑ as t_{exp}↑ (up to power = 500 W)
				3-(trimethoxysilyl)-propyldimethyl-octadecyl ammonium chloride	1%		0.001 – 0.013	GY↑ as power ↓ or t_{exp}↓
[118]	multi-walled carbon nanotubes	corona 1.5 L/min N_2 t_{exp} = NR Power = 300 W	"grafting from"	glycidyl methacrylate	95%	70	4	NR
[91]	polypropylene	DBD 0.24 L/min Ar t_{exp} = 30 – 180 s Power = 40 – 120 W	"grafting to" with surface absorbed monomer	n,n-dimethylamino ethyl methacrylate	1 – 43 wt%	NR	0.008 – 0.05	GY↑ as power ↑ (up to 100 W) or $[M]_0$↑ (up to ~28 wt%) or t_{exp}↑ (up to 130 s) GY↑ as θ_w↓
[92]	polypropylene	DBD 0.24 L/min Ar t_{exp} = 30 – 180 s Power = 40 – 120 W	"grafting to" with surface absorbed monomer	n-vinyl-2-pyrrolidone	4.61 – 28.27 wt%	NR	0.008 – 0.05	GY↑ and θ_w↓ as $[M]_0$↑

[a] Legend: NR – not reported; DBD – dielectric barrier discharge; APPJ – atmospheric pressure plasma jet; APGDP – atmospheric pressure glow discharge plasma; t_{exp} – plasma exposure time; $[M]_0$ – initial monomer or polymer concentration; T – polymerization reaction temperature; t_{rxn} – polymerization reaction time; ↑ – increases; ↓ – decreases; θ_w – water contact angle; R_{rms} – surface roughness; t – polymer layer thickness; D - polymer feature diameter; GY – grafted polymer layer yield as determined by either degree of grafting % = $[(W - W_0)/W_0] \times 100$ (where W_0 are W are the weight of substrate before and after grafting, respectively), grafting density, or absorbance ratio

[b] The first and second lines refer to the plasma source and feed gas, respectively

[c] Polymerization time only refers to the reaction time and does not include the total processing time

2.4 Free Radical Graft Polymerization

As previously described (Section 2.3), graft polymerization is a method of covalently attaching polymer chains (i.e., a polymer "brush" layer) directly to a polymeric surface. When the hydrophilic brush layer comes into contact with water, it swells away from the surface [10-11] with ensuing partial chain mobility (due to Brownian motion of chain segments [23]). As a consequence, solute (e.g., bacteria) attachment to the surface is retarded.

Synthesis of polymer chains that are end-grafted to the target surface via free radical graft polymerization (FRGP) [119-122] requires reactive surface sites present on the surface [119]. Surface sites can be free radicals or other surface active species created via surface exposure to an activating agent (e.g., plasma, and gamma or ultraviolet (UV) radiation) [19, 21, 68, 72, 123-124], a grafted vinyl monomer [12, 80, 125-126], or a grafted initiator [122]. The various methods that have been used to create activated surface sites are discussed in Sections 2.4.1 – 2.4.4. The active surface species provide anchoring sites for subsequent graft polymerization using a suitable vinyl monomer and, if required, additional bulk initiator.

The general reaction scheme for FRGP consists of the following 3 major steps: surface initiation, propagation (i.e., polymer chain growth), and termination (Figure 2-2) [127]. The mode of initiation is determined by surface activation method: a) irradiation or plasma exposure (Figure 2-2, Reactions 1-4), b) a grafted monomer (Figure 2-2, Reactions 5-7), or c) a grafted initiator (Figure 2-2, Reactions 8-10). In Figure 2-2, free initiator and monomer radicals are represented by $I \bullet$ and $M \bullet$, respectively; growing and terminated surface end-grafted (i.e., covalently bonded to a surface) polymer chains consisting of n monomers are given by $S_n \bullet$ and

G_n, respectively; growing and terminated homopolymer consisting of n monomers formed in the

bulk solution (i.e., not attached to the surface) are specified by $M_n\bullet$ and H_n, respectively.

Modes of Initiation for Different Surface Activation Methods	Propagation
	$S_n\bullet + M \rightarrow S_{n+1}\bullet$ (11)
a) $S \rightarrow S\bullet$ (1)	$M_n\bullet + M \rightarrow M_{n+1}\bullet$ (12)
$\quad S\bullet + O_2 \rightarrow SI$ (2)	
$\quad SI \rightarrow S\bullet$ (3)	Termination
$\quad S\bullet + M \rightarrow S_1\bullet$ (4)	$M_n\bullet + M \rightarrow H_n + M_1\bullet$ (13)
b) $I_2 \rightarrow 2I\bullet$ (5)	$S_n\bullet + M \rightarrow G_n + M_1\bullet$ (14)
$\quad I\bullet + M \rightarrow M_1\bullet$ (6)	$M_n\bullet + S \rightarrow H_n + S_1\bullet$ (15)
$\quad SM + I\bullet \rightarrow S_1\bullet$ (7)	$S_n\bullet + S \rightarrow G_n + S_1\bullet$ (16)
c) $SI_2 \rightarrow SI\bullet + I\bullet$ (8)	$M_m\bullet + M_n\bullet \rightarrow H_{m+n}$ (17)
$\quad I\bullet + M \rightarrow M_1\bullet$ (9)	$M_m\bullet + M_n\bullet \rightarrow H_m + H_n$ (18)
$\quad SI\bullet + M \rightarrow S_1\bullet$ (10)	$S_m\bullet + M_n\bullet \rightarrow G_{m+n}$ (19)
	$S_m\bullet + M_n\bullet \rightarrow G_m + H_n$ (20)
	$S_m\bullet + S_n\bullet \rightarrow G_{m+n}$ (21)
	$S_m\bullet + S_n\bullet \rightarrow G_m + G_n$ (22)

Figure 2-2. Reaction scheme for free radical graft polymerization [10]. Different modes of initiation can occur depending on the type of surface activation method: a) irradiation or plasma exposure that forms surface radicals ($S\bullet$); note that Reactions 1 and 2 are part of the plasma activation that lead to the formation of surface peroxides, b) a grafted monomer (SM), or c) a grafted initiator (SI_2). The subscripts n and m refer to differing number of monomers in growing or terminated chains.

Surface initiation by irradiation or plasma activation is carried out by exposure of a surface (S) to radiation or plasma to create a surface active site/radical ($S\bullet$) (Figure 2-2, Reaction 1). Upon

exposure to oxygen, peroxide activated surface sites (SI) are formed on the surface (Figure 2-2, Reaction 2) [12, 80], which can then decompose (Figure 2-2, Reaction 3) and react with a monomer (M) (Figure 2-2, Reaction 4). Surface initiation via a surface grafted monomer is carried out with a bulk initiator (I_2) that can decompose (Figure 2-2, Reaction 5) and react with a surface grafted monomer (SM) (Figure 2-2, Reaction 7). Surface initiation can also occur when a surface grafted initiator (SI_2) decomposes (Figure 2-2, Reaction 8) and reacts with a monomer (Figure 2-2, Reaction 10). Once polymer chain growth is initiated, propagation of polymer chains occurs by monomer addition to surface grafted (Figure 2-2, Reaction 11) and bulk ($M_n\bullet$) (Figure 2-2, Reaction 12) chains. Chain growth occurs until termination by chain transfer (Figure 2-2, Reactions 13-16) or combination (Figure 2-2, Reactions 17, 19, and 21) and disproportionation (Figure 2-2, Reactions 18, 20, and 22). FRGP results in the formation of end-grafted polymer chains that are tethered to the surface, G_n , and homopolymer chains in the bulk solution, H_n .

The kinetics of growth of surface chains (R_P) from active surface sites produced via plasma exposure (Section 2.4.4) typically follows a first order reaction, with respect to monomer concentration in solution ([M]) [102],

$$R_p = k_p \left(\frac{f_d k_d}{k_t}\right)^{1/2} [SI]^{1/2}[M] \tag{2-1}$$

where k_p, k_t, and k_d are the rate constants for surface chain propagation (via sequential monomer addition) (Figure 2-2, Reaction 11), chain termination (via combination and disproportionation, Figure 2-2, Reactions 21 and 22, respectively), and initiator decomposition (Figure 2-2, Reaction 3), respectively, f_d is the initiator thermal decomposition efficiency (for first order

25

decomposition), and $[SI]$ is the concentration of active surface species produced via plasma exposure (e.g., peroxides [12]). The grafted polymer yield (e.g., mg polymer/cm^2) and grafted polymer thickness are governed by the polymerization conditions (e.g., monomer type and concentration, grafting time, and temperature) [12, 128-129]. For example, higher polymer graft yield is expected with increasing temperature, initial monomer concentration, as well as reaction time. It has been reported that the above approach of surface graft polymerization enables the formation of a high chain surface density layer of terminally and covalently attached chains (i.e., "brush layer") at a reasonably low level of polydispersity [9]. It is noted, however, that if there is significant formation of free radical species and homopolymerization in solution (e.g., primarily due to thermal initiation at excessive high reaction temperatures), termination of surface chains can impede chain growth by monomer addition, thereby broadening the size distribution of the grafted polymer chains [80]. Therefore, controlling homopolymerization is paramount to in order to regulate the polydispersity of the grafted polymer layer [75, 130].

2.4.1 Surface Activation with Vinyl Monomers

Surface graft polymerization whereby the surface is activated with vinyl monomers has been shown to be effective for developing dense polymeric brush layers [12, 75, 77, 131]. This approach is particularly suitable for inorganic surfaces where vinyl group attachments can be easily accomplished via surface silylation [75, 77, 132]. Also, end-attached poly(vinylpyrrolidone) (PVP) chains (via surface graft polymerization), forming a robust brush polymer layer of terminally and chemically anchored macromolecular chains, were shown to be effective in reducing fouling in MF and UF treatment of oil-in-water microemulsions [133] and

reduction of protein adsorption [134] without attrition of the grafted modification layer, as is commonly encountered in physical membrane surface coating methods.

Graft polymerization kinetic studies [127] have suggested that the contribution of polymer grafting (Figure 2-2, Reactions 15, 19, 20) to the total polymer graft yield is more pronounced, relative to monomer addition (or "grafting from"), at high reaction temperatures and/or low initial monomer concentrations. This has been demonstrated for vinylpyrrolidone [127] and vinylpyridine [135] graft polymerization. Graft polymerization studies [75, 77-78, 132] have shown that graft polymer yield (mg/m^2) generally increases with increasing temperature and initial monomer concentration. Surface chain propagation was reported to be the dominant grafting process with higher reaction temperature promoting the formation of a denser layer of shorter grafted chains, whereas a higher initial monomer concentration enhances both graft density and average grafted chain length. While the above conclusions were derived based on graft polymerization onto surface anchored vinyl silanes, the general reaction scheme for graft polymerization (Figure 2-2, Reactions 11-22) should be applicable, without a loss of generality, to other graft polymerization systems irrespective of the surface anchoring scheme.

2.4.2   Surface Activation with Chemical Initiators

Surface activation via exposure of the surface to a solution containing chemical initiators or grafting or chemisorption of an initiator have been proposed specifically for modification of polymeric membranes (Table 2-2). In the first approach, the initiator reacts with certain surface functional groups to create reactive surface radicals, whereas in the second approach an initiator is first physisorbed, chemisorbed or grafted onto the polymeric surface. The decomposition of

27

the bulk initiator or fragments of surface-bound (or sorbed) initiator can promote the polymer initiation in the solution phase; thus, formed homopolymers can graft onto the surface thereby increasing surface chain polydispersity as well as grafted polymer yield (Figure 2-2, Reactions 19-20) [136]. Other important considerations also include initiator-surface-solvent compatibility and temperature required to carry out radical-forming reactions, especially when using thermal initiators.

The above approaches have been reported primarily for peroxide and azo compounds for surface nanostructuring of RO polyamide membranes [137], UF polyethersulfone membranes [138], and polyolefinic and polypropylene hollow fiber MF membranes [125, 139-140] at a temperature range of ~60 – 85°C. Such initiators generally produce two radicals per initiator due to thermal homolytic dissociation (Figure 2-2, Reaction 5) [141]. The homolytic decomposition of peroxide initiators involves the thermal cleavage of the weak O-O bond (bond dissociation energy = 154 kJ/mol) to produce radical species [142]. Whereas the dissociation energy of the C-N bond is high (approximately 290 kJ/mole [141]) for azo compounds which are typically used for activation of relatively hydrophobic polymer membranes surfaces (e.g., aromatic polyamide RO [137] membranes). Peroxide initiators have been used for graft polymerization of hydrophobic polypropylene MF [125, 140] and polyethersulfone UF [138] membranes with acrylic acid monomers. It has been proposed that for the above membranes, the initiator decomposes to form radicals which participate in hydrogen abstraction with the surface [137-138], thereby creating activated surface macroradical sites [138, 143]. However, it is noted that mere exposure of the membrane surface to an initiator does not ensure that the reactive initiator species would provide covalent anchoring of the grafted polymers with the membrane surface. Graft polymerization studies on modification of aromatic polyamide RO membranes

with 3-allyl-5,5,-dimethylhydantoin using 2,2'-azobisisobutyramidine dihydrochloride (AIBA) [137] reported that the positively charged AIBA in aqueous solutions [144] strongly associated (through electrostatic interactions) with the negatively charged membrane surface. Polyamide membranes modified with 3-allyl-5,5-dimethylhydantoin demonstrated reduction of microbial fouling as quantified by about a factor of three reduction in flux decline relative to the unmodified membrane [137]. MF and UF membranes modified with polyacrylic acid have demonstrated reduced protein surface adsorption (up to ~20% [140]) and improved resistance to protein biofouling. Membrane graft polymerization via simultaneous membrane surface exposure to a reaction mixture containing the initiator, monomer, and solvent has also been reported with the use of redox initiators [25, 87, 145-147]. Such approaches have been reported, for example, for modification of aromatic polyamide RO membranes with acrylic acids, acrylates and acrylamide type monomers [25, 63, 145]. Studies have also been reported on the modification of polyamide and polypiperazine-based NF membranes via graft polymerization of acrylic acids and methacrylates [87], polyethersulfone NF membranes with acrylamides, acrylic acids and acrylate monomers [46, 146-147].

Persulfate initiators and oxyacids of sulfur form efficient redox-systems [148], such as the commonly used potassium/sodium persulfate and potassium/sodium metabisulfite redox initiators ($K_2S_2O_8/K_2S_2O_8$ and $K_2S_2O_5/Na_2S_2O_5$), have been used for surface structuring of polyamide RO/NF, polypiperazine-based NF and polyethersulfone UF membranes. Graft polymerization has been achieved with acrylic acids, acrylate and acrylamide type monomers [46, 87, 145]. In the presence of $S_2O_5^{2-}$, the persulfate $S_2O_8^{2-}$ decomposes into two free radical species $SO_4^- \bullet$ [149]. In the ongoing debate [13] regarding the activity of the radical $SO_4^- \bullet$, some claim that $SO_4^- \bullet$ initially reacts with water to form an OH· radical, while others report that

the $SO_4^-\bullet$ reacts directly with the surface to produce surface radicals through hydrogen abstraction. An advantage of using redox initiators is that the rate of radical productions are reasonable at moderate temperatures [141] and these initiators can be used at room temperature. As a result, the rate of polymer termination is reduced [142]. Also, it is reported that reaction times to achieve a reasonable level of surface polymer coverage have been achieved over periods in the range of ~15 minutes to as long as 6 hours [87, 145, 147].

The performance of membranes modified via surface initiation induced graft polymerization has been shown to depend on the specific monomer used (e.g. monomer containing charged and/or hydrophilic groups) and its initial concentration, molar ratio of initiator components (oxidant:reductant), reaction conditions (e.g. temperature and pH), and reaction time [25, 87, 147]. Longer reaction time and higher initial monomer concentration are likely to reduce membrane permeability, although fouling resistance would generally increase with improved grafted surface polymer coverage. Membranes modified via graft polymerization with acrylic acid and acrylate monomers have typically demonstrated better fouling resistance characteristics relative to unmodified membranes in terms of a lower flux decline. For example, ~32% flux decline (in the course of 30 day desalting of brackish water) was reported for 3-sulfoproyl methacrylate grafted polyethersulfone NF membrane compared to greater flux decline (~54%) for the unmodified base polyethersulfone NF membrane [146]. Fouling resistance in desalting of brackish river water using polyamide RO membranes graft polymerized using the same monomer also demonstrated increased fouling resistance as verified by surface analysis via ATR-FTIR [145]. The above studies and others have shown that in general, graft polymerized RO membranes exhibit reduction in permeability (Section 2.8).

Although chemical initiated free radical graft polymerization can be applied to different polymeric surfaces activated with a variety of chemical initiators, there are several limitations to this approach. Chemical initiators can also initiate polymerization in the bulk solution (homopolymerization), hence resulting in polymer grafting (i.e., "grafting to"). A more serious concern is the relatively long reaction periods (up to ~18 h) reported in most studies, which is infeasible for large-scale commercial deployment. Membrane modification using the above approaches in-place (i.e., with prefabricated membrane elements in their pressure vessels) is feasible for specialized applications even with such long reaction periods; however, reproducibility of the approach would be important to demonstrate for wide-scale acceptance of this membrane surface structuring technology.

Table 2-2. Summary of chemically-initiated graft polymerization methods [a].

Ref.	Type of Initiator	Monomer	Membrane Support	Graft Polymerization Time [b]	Membrane Performance	Grafted Polymer Characterization Methods
[46]	$K_2S_2O_8$ and $K_2S_2O_5$	methacrylic acid, polyethyleneglycol methacrylate, sulfopropylmethacrylate	polyethersulfone (PES) (UF)	20 – 120 min (1 step)	NR	ATR-FTIR
[63]	potassium persulfate-sodium metabisulfite, $K_2S_2O_8$ and $Na_2S_2O_5$	methacrylic acid, polyethyleneglycol methacrylate, vinylsulfonic acid, 3-sulfopropyl-methacrylate k-salt, 2-acrylamido-2-methylpropane-sulfonic acid	polyamide composite (RO)	NR (1 step)	NR	ATR-FTIR
[25]	$K_2S_2O_8$ and $Na_2S_2O_5$	methacrylic acid, polyethyleneglycol methacrylate	polyamide composite (RO)	15 – 120 min (1 step)	$L_p \downarrow$, R_s ($\approx$)	ATR-FTIR, XPS, streaming potential
[87]	$K_2S_2O_8$ and $Na_2S_2O_5$ / $K_2S_2O_5$	acrylic acid, methacrylic acid, dimethyl-amino ethyl methacrylate, polyethylene-glycol ester of methacrylic acid, sulfopropyl methacrylate, hydroxyl-ethyl ester of methacrylic acid	polyamide and polypiperazine-based (NF)	15 – 60 min (1 step)	$L_p \downarrow$, $R_s \uparrow$, SR and CPFR $\uparrow$ (NR individually)	ATR-FTIR, EDX
[139]	4,4'-Azo-bis(4-cyanovaleryl chloride)	styrene, acrylic acid, 4-vinylpyridine, 4-vinylpyridine/1% divinylbenzene	polyethylene (PE) and polypropylene (PP) (MF)	6 – 18 hours (2 steps)	$L_p \downarrow$	SEM, EDX
[145]	potassium persulfate and potassium metabisulfite, $K_2S_2O_8$ and $K_2S_2O_5$	uncharged glycol ester of methacrylic acid, anionic sulfopropylmethacrylate, anionic 2-acrylamido-2-methyl propane sulfonate	aromatic polyamide (RO)	20 min (1 step)	$L_p \downarrow$, $R_s \uparrow$, BFR, SR, and CPFR $\uparrow$ (NR individually)	ATR-FTIR, contact angle
[146]	$K_2S_2O_8$-$K_2S_2O_3$	methacrylic acid, acrylamide, 3-sulfopropyl methacrylate	polyethersulfone (PES) (NF)	30 min (1 step)	$R_s \uparrow$, SR $\uparrow$	IR
[138]	benzoyl peroxide	methacrylic acid	polyethersulfone (PES) (UF)	2 – 8 hours (2 steps)	$L_p \downarrow$	graft yield, FTIR, XPS, contact angle, SEM
[147]	$K_2S_2O_8$ and Na_2SO_3	methylacrylic acid	phenolphthalein PES (UF/MF)	6 hours (1 step)	NR	ATR-FTIR, SEM, graft yield
[137]	2,2'-azobis (isobutyramidine) dihydrochloride	3-allyl-5,5-dimethylhydantoin	aromatic polyamide (RO)	10 – 100 min (multi-step)	$L_p \uparrow$, $R_s \downarrow$, BFR $\uparrow$	ATR-FTIR, XPS, contact angle, surface charge

[a] Legend: $\uparrow$ - increases; $\downarrow$ - decreases; ($\approx$) - less than 5% change; NR - not reported; L_p - permeability; R_s, R_c, R_p, and R_b are the rejection of salt(s), colloidal particle(s), protein(s), and biofoulant(s), respectively; SR - mineral salt(s) scaling resistance; CPFR, PFR, and BFR are the fouling resistance associated with colloidal particle(s), protein(s), and biofoulant(s), respectively; DG - degree of grafting.

[b] Graft polymerization time only refers to the reaction time and does not include the total processing time; the number of steps indicated does not include substrate cleaning.

2.4.3 Irradiation Induced Graft Polymerization

Polymeric surfaces can be directly modified via irradiation or activated by irradiation for subsequent graft polymerization. Gamma or ultraviolet (UV) radiation are the two most popular methods of surface irradiation for polymeric surface modifications and accordingly are discussed in Sections 2.4.3.1 and 2.4.3.2.

2.4.3.1 Gamma Induced Graft Polymerization

Gamma irradiation is typically employed using cobalt 60 (Co^{60}). This irradiation method has been reported for surface modifications of MF and UF membranes [19, 150-152] (Table 2-3). A variety of membranes have been modified via gamma radiation including polypropylene [19, 65, 151-152], polyethersulfone [150], and fluorinated Teflon [18]. Also, a variety of different monomers have been used for membrane graft polymerization via gamma-initiation such as styrene [150], acrylic acid [18-19], acrylonitrile [151-152], and 2-hydroxyethyl methacrylate (HEMA) [65].

Irradiation of surface molecules causes homolytic fission [13], which results in the formation of surface free radicals on the backbone of the polymeric chains of the membrane. Membrane surface irradiation in the presence of oxygen can lead to the formation of peroxides (i.e., activated surface sites) on the membrane surface [13]. Graft polymerization can be carried out during [18, 150, 153-154] or directly after [19, 151-152] surface activation by irradiation. The gamma dose is typically in the range of 0.5 – 20 Mrad [19, 150-153] with an exposure of 0.25 – 0.45 Mrad/h for 0.5 – 75 hours [19, 150-153]. Polymer membrane surface activation via gamma irradiation is typically accomplished in three different ways in order to create radicals to

33

initiate graft polymerization: (1) pre-irradiation, (2) peroxidation, and (3) mutual irradiation [19, 150-153] (Figure 2-3).

1. Pre-irradiation   2. Peroxidation   3. Mutual Irradiation

P $\leadsto$ P· + M → PM·   P $\overset{O_2}{\leadsto}$ P-O-O-H or P-O-O-P   P + M $\leadsto$ P· + M· → P-M·

                   $\leadsto$ P-O· + OH· or 2 P-O· $\overset{\Delta}{\rightarrow}$ P-O-M
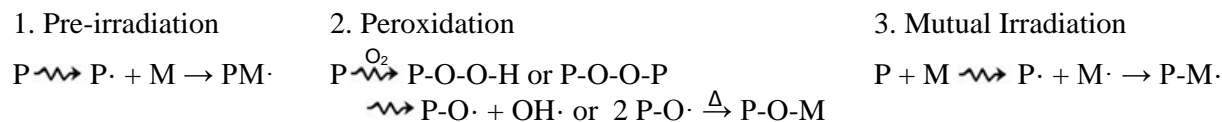
Figure 2-3. Gamma assisted grafted polymerization mechanisms where • is a free radical, *P* is the polymeric surface, *M* is the monomer, and $\leadsto$ indicates gamma irradiation.

In pre-irradiation, the polymeric surface is exposed to gamma rays in an inert environment, and free radicals are formed on the polymer backbone [13]. Subsequently, graft polymerization proceeds by exposing the activated surface to the desired monomer. The monomer can be in either a liquid (with or without solvent) or vapor phase. An advantage of the pre-irradiation method is that homopolymerization is limited since polymerization proceeds directly from surface active sites without the presence of initiators in solution. However, the above approach can result in polymer chain scission as well as surface etching and alteration of the surface pore structure [13]. In peroxidation, the polymeric surface is gamma irradiated in the presence of gaseous oxygen leading to the formation of hydroperoxides or diperoxides on the polymeric surface [13]. The surface peroxy groups are then exposed to the target monomer solution at an elevated temperature (60 − 100ºC) in order to decompose the peroxy groups to form surface radicals which serve to initiate free radical graft polymerization with a suitable vinyl monomer. An advantage of the peroxidation method is that the intermediate peroxy groups are relatively stable over several hours at 20ºC [13, 155]. Finally, in mutual irradiation, the surface is

34

simultaneously exposed to the monomer and gamma radiation [13]. Free radicals are formed on both the polymeric surface as well as in the monomer solution (or gas phase). This allows for graft polymerization via monomer addition to surface chains (i.e., "grafting from"), but also results in the formation of polymer chains in solution (or gas phase); the latter polymerization reaction leads to increased polydispersity of surface chains as well as potentially crosslinked surface chains.

The degree of grafting (i.e., percent of the monomer in solution added to the surface) is reported to generally increase with increasing gamma irradiation dose up to a plateau region [151-152]. The degree of grafting has also been reported to increase with initial monomer concentration and/or reaction time up to a maximum, and then decreases [151-152] as expected when the rate of chain termination and homopolymer formation increases faster than the rate of surface graft polymerization. Although the degree of grafting achieved via gamma surface activation has been reported in various studies [18-19, 150-152], limited characterizations have been provided regarding membrane permeability, rejection, and fouling resistance. Some partial success has been reported in imparting fouling resistance to polypropylene (MF/UF) membranes modified via gamma irradiation/graft polymerization; however, in most cases, gain in membrane rejection was at the expense of reduced permeability [65]. For example, work [65] on modifying polypropylene membranes (MF/UF) with 2-hydroxyethyl methacrylate (HEMA) (in solution) via the pre-irradiation method demonstrated a slight increase in membrane rejection of the protein bovine serum albumin (BSA) (from 28% up to ~34% for a 1g/L solution) with increased fouling resistance as indicated by over a factor of two flux decline reduction for the modified membrane.

Although moderate success has been achieved with surface modification via gamma radiation, this is not a low cost process and safety considerations are paramount [13]. Also,

gamma ray irradiation typically requires long exposure times (1 – 24 hours) to generate sufficient

radical concentration on polymeric surfaces [18-19, 151-154]; thus, this approach is not feasible

for large-scale membrane manufacturing.

Table 2-3. Summary of gamma initiated graft polymerization methods [a].

Ref.	Gamma Treatment	Monomer	Membrane Support	Graft Polymerization Time [b]	Membrane Performance	Grafted Polymer Characterization Methods
[150]	Radio nuclide Co^{60} Total Dose = 5 – 30 kGy Dose Rate = 4.2 kGy/h	styrene	polyethersulfone (PES) films	1.2 – 7.1 h (1 step)	NR	FTIR, SEM, TGA
[18]	Co^{60} Gamma Total Dose = 46.7 kGy Dose Rate = 0.18 kGy/h	acrylic acid	fluorinated ethylene propylene (FEP) films	0.5 – 8 h (2 step)	NR	% swelling, ion exchange capacity, FTIR, X-ray diffraction, TGA, DSC, DG
[19]	2100 Ci ^{60}Co Total Dose = 4 – 20 Mrad Dose Rate = 0.27 Mrad/h	acrylic acid, acrylamide	isotactic polypropylene (IPP) fibers	3 – 4 h (2 steps)	NR	IR, TGA, DSC, DG
[151]	2100 Ci ^{60}Co Total Dose = 4 – 11 Mrad Dose Rate = 0.27 Mrad/h	acrylonitrile	isotactic polypropylene (IPP) fibers	3 – 4 h (2 steps)	NR	IR, TGA, DTG, DTA, DG
[152]	2100 Ci ^{60}Co Total Dose = 0.5 – 12 Mrad Dose Rate = 0.35 Mrad/h	acrylonitrile	isotactic polypropylene (IPP) fibers	3 – 4 h (2 steps)	NR	IR, TGA, DG
[65]	^{60}Co Total Dose = 10 – 40 kGy Dose Rate = 4.51 kGy/h	2-hydroxyethyl methacrylate	polypropylene (PP) (MF/UF)	1 – 5 h (2 steps)	$L_p \downarrow$, $R_p \uparrow$, PFR $\uparrow$	FTIR, elemental analysis, contact angle, SEM, UV-VIS, DG

[a] Legend: ↑ - increases; ↓ - decreases; (≈) - less than 5% change; NR - not reported; L_p - permeability; $R_s, R_c, R_p,$ and R_b are the rejection of salt(s), colloidal particle(s), protein(s), and biofoulant(s), respectively; SR - mineral salt(s) scaling resistance; CPFR, PFR, and BFR are the fouling resistance associated with colloidal particle(s), protein(s), and biofoulant(s), respectively; DG - degree of grafting.

[b] Graft polymerization time only refers to the reaction time and does not include the total processing time; the number of steps indicated does not include substrate cleaning.

2.4.3.2 UV Induced Graft Polymerization

UV induced graft polymerization, otherwise known as photo-induced polymerization, has been primarily used for surface modification of polymer surfaces, including MF and UF membranes (Table 2-4) [16-17, 156-159]. UV-assisted graft polymerization can be accomplished via direct exposure of a UV photosensitive surfaces (e.g., polysulfone, polyethersulfone) to UV light [14, 156-157, 160-163] or with the use of a photoinitiator [17, 164-167]. In UV surface activation, the photoreactive chromospores (photosensitive sites that allow for bond rupture) enable the formation of free-radical sites on the polymeric backbone via photolysis [163]. Surfaces containing phenoxy-phenyl sulfone sites [163] such as polyaryl sulfone [161, 163], polysulfone [157], and polyether sulfone [14, 156, 160, 162] have been primary candidates for UV-induced graft polymerization. Accordingly, UF and MF membranes have been the popular target of surface modification by researchers, via the above approach. Exposure of photosensitive surface to UV light causes bond cleavage at the photoreactive chromospore sites, which results in the creation of free radical formation for subsequent initiation of graft polymerization. For example, UV exposure of the phenoxy-phenol sulfone group on the backbone of polyether sulfone (PES) leads to chain cleavage of the carbon-sulfur bond at the sulfone linkage (Figure 2-4; [163]). This results in the formation of two radicals (aryl radical and sulfonyl radical) at each end of the PES chain [163]. Also, an additional radical may be formed with the loss the sulfur dioxide on the sulfonyl radical site. The created surface radicals serve as both initiation and anchoring sites for vinyl monomer graft polymerization. UV surface exposure in the wavelength range of 200 – 500 nm is typically around 20 – 70 mW/cm^2 for a period from 1 min to 1 hour [17, 156, 160, 165-167]. The degree of graft polymerization typically increases with increasing initial monomer concentration and increasing irradiation dose [16, 157-158].

38
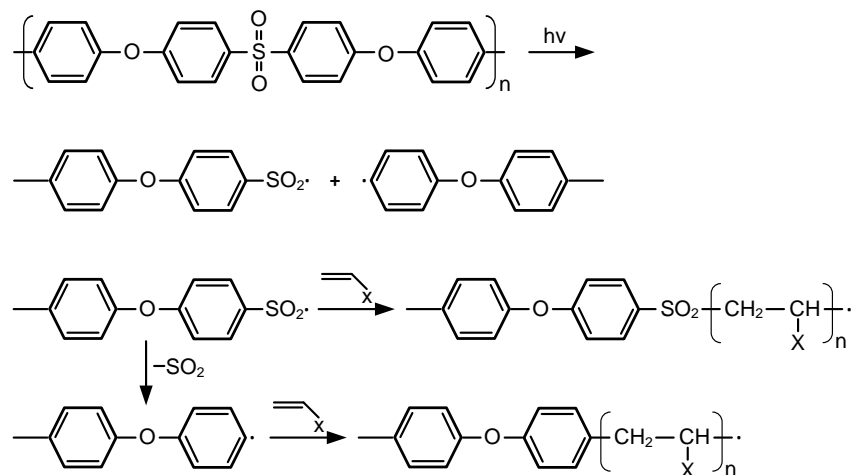
Figure 2-4. UV assisted graft polymerization mechanism of PES [13].

If the surface is not photosensitive, a photoinitiator has to be first adsorbed onto the surface or absorbed into the surface region. Upon exposure to UV the photoinitiator dissociates into free radicals that can then abstract hydrogen from the polymer backbone, forming polymeric radicals that can then be used to carry out polymerization [13, 168]. Common photoinitiators reported for polypropylene and poly(vinylidene fluoride) (MF/UF) surface modification with a variety of monomers (e.g., 2-hydroxyethyl methacrylate (HEMA), acrylamide, and 2-aminoethyl methacrylate (AEMA)) include benzoin ethyl ether [13, 164], xanthone [13], and benzophenone (BPO) [17, 164-167], the latter being particularly popular due to its peroxy group that can readily form free radicals [17, 165-167]. As described in Section 2.4.2 abstraction of hydrogen from the membrane surface polymer backbone also results in introduction of free radicals to the bulk monomer solution (during the graft polymerization process) and thus decreased grafting efficiency and grafted polydispersity of the grafted chains [168].

UV induced graft polymerization can be used with either photoactive membrane materials or with the use of photoinitiators. In the former case, prolonged surface exposure to UV can lead to membrane degradation [16, 158, 160] that can also be manifested by pore enlargement [160] due to polymer chain scission [16, 158, 160, 162]. Generally, polymer membrane surface structuring via UV-assisted graft polymerization, as with other techniques relying on chemical surface activation, leads to increased solute rejection at the expense of decreased permeability, in part due to pore blockage by the grafted polymer chains [16, 157-158] (Section 2.8). In some cases, however, reported slight increase in permeability (~3 − 5%) has been attributed to increasing surface hydrophilicity or pore widening as in the case of UF PES membrane graft polymerization with poly(ethylene glycol) methacrylate (PEGMA) [16]. It has also been shown [157] that hollow fiber polysulfone (PSf) UF membranes can be upgraded to NF membrane performance (e.g., with $CaCl_2$ rejection of 40 − 90%) via diallyl dimethyl ammonium chloride (DADMAC) surface nanostructuring. Modification of MF/UF polypropylene (PP) membranes with 2-aminoethyl methacrylate (AEMA) improved fouling resistance (quantified by ~7% lower flux decline and ~20% greater initial flux recovery after DI water cleaning of the fouled membranes), relative to the unmodified membranes, as during the filtration of 200x diluted activated sludge (350 mg/L COD) [166]. In general, fouling tests with BSA and model bacteria have shown that MF and UF membranes nanostructured with hydrophilic polymers demonstrated increased fouling resistance [14, 16, 156, 158, 160-161, 164, 169-170]. The latter is attributed to the increased negative surface charge imparted to the otherwise typically hydrophobic unmodified membranes enabling repulsion of negatively charged colloids and reduction of bacterial adhesion [16, 24, 161, 164, 171].

Table 2-4. Summary of UV initiated graft polymerization methods [a].

Ref.	UV Sensitive Membrane or Initiator [b]	Monomer	Membrane Support	Graft Polymerization Time [c]	Membrane Performance	Grafted Polymer Characterization Methods
[160]	Membrane: PES t_{exp} = 1 – 5 min λ = 365 nm Power = 21.7 mW/cm^2	acrylic acid, n-vinylpyrrlidone	PES (NF)	1 – 5 min (1 step)	$L_p \downarrow$, $R_c \uparrow$, CPFR $\uparrow$	ATR-FTIR, AFM
[157]	Membrane: PSf Energy = 16.3 – 22.8 J/cm^2	diallyl dimethyl ammonium chloride	hollow fiber PSf (UF)	NR (1 step)	$L_p \downarrow$, $R_s \uparrow$	NR
[158]	Membrane: PES, PSf λ = 300 nm Energy = 20 – 1946 mJ/m^2	n-2-vinyl pyrrlidone, 2-acrylamidoglycolic acid, 2-acrylamido-2-methyl-1-propanesulfonic acid	PES (UF) and PSf (UF)	3 – 60 s (multi-step)	$L_p \downarrow$, $R_p (\approx)$, PFR $\uparrow$	ATR-FTIR, contact angle, DG
[14]	Membrane: PES t_{exp} = 37.9 s λ = 365 nm Power = 16.57x10^4 mW/m^2	n-vinyl pyrrlidone	PES (NF)	36.70 s – 5 min (2 steps)	$L_p \downarrow$, $R_c \uparrow$ (L_p and R_c are not reported individually), CPFR $\uparrow$	NR
[164]	Photoinitiator: benzophenone (for PES) or ether ether of benzoin (for PVF) in methanol t_{exp} = 1 – 5 min	2-acrylamido-2-methyl-1-propanesulfonic acid, 2-hydroxyethyl methacrylate, and 2-(dimethylamino)ethyl methacrylate quaternized with methyl chloride	poly(vinylidene fluoride) (PVF) (MF) and PES (MF)	1 – 5 min (multi-step)	$L_p \downarrow$, BFR $\uparrow$	DG, AFM
[169]	Membrane: PES t_{exp} = 5 – 15 min λ = 300 nm Power = 25±1 mW/cm^2	(2-(acryloyloxy)ethyl) trimethyl ammonium chloride, acrylic acid	PES (NF)	5 – 15 min (1 step)	$L_p \downarrow$, BFR $\uparrow$	DG, ATR-FTIR, SEM, contact angle, zeta potential
[16]	Membrane: PES t_{exp} = 5 – 15 min λ > 300 nm Power = 60±10 mW/cm^2	poly(ethylene glycol) methacrylate	PES (UF)	1.5 – 3 min (1 step)	$L_p \downarrow$, $R_p \uparrow$, PFR $\uparrow$	DG, contact angle, ATR-FTIR, zeta potential
[162]	Membrane: PES t_{exp} = up to 60 s λ = 300 nm	n-2-vinyl pyrrlidone, 2-hydroxyethyl methacrylate, acrylic acid, 2-acrylamidoglycolic acid, 3-sulfopropyl methacrylate, 2-acrylamido-2-methyl-1-propanesulfonic acid	PES (UF)	up to 60 s (2 steps)	$L_p \downarrow$, $R_p \uparrow$, PFR $\uparrow$	DG, ATR-FTIR
[163]	Membrane: poly(arylsulfone) (PAS) t_{exp} = 2.5 – 10 min λ = 253.7 nm	2-hydroxyethyl methacrylate, glycidyl methacrylate, and methacrylic acid	PAS (UF)	2.5 – 10 min (1 step)	NR	ATR-FTIR, DG
[165]	Photoinitiator: benzophenone t_{exp} = 5 – 40 min λ = 300 nm	A-D-allyl glucoside	polypropylene (PP)	5 – 40 min (multi-step)	NR	XPS, ATR-FTIR, contact angle, grafting density

Ref.	UV Sensitive Membrane or Initiator [b]	Monomer	Membrane Support	Graft Polymerization Time [c]	Membrane Performance	Grafted Polymer Characterization Methods
[17]	Photoinitiator: benzophenone t_{exp} = 10 – 60 min λ = 350 – 450 nm	2-hydroxylethyl acrylate	PP (UF)	10 – 80 min (multi-step)	$L_p \uparrow$, $R_p \downarrow$, PFR $\uparrow$	XPS, SEM, DG
[167]	Photoinitiator: benzophenone t_{exp} = 5 – 30 min λ = 232 – 500 nm	acrylamide	PP (UF)	5 – 30 min (multi-step)	$L_p \uparrow$, BFR $\uparrow$	ATR-FTIR, DG, contact angle, SEM
[167]	Photoinitiator: benzophenone t_{exp} = 5 – 30 min λ = 232 – 500 nm	2-aminoethyl methacrylate	PP (UF)	5 – 30 min (multi-step)	L_p varies, $R_b \downarrow$, BFR $\uparrow$	ATR-FTIR, XPS, DG, SEM

[a] Legend: $\uparrow$ - increases; $\downarrow$ - decreases; ($\approx$) - less than 5% change; NR - not reported; L_p - permeability; R_s, R_c, R_p, and R_b are the rejection of salt(s), colloidal particle(s), protein(s), and biofoulant(s), respectively; SR - mineral salt(s) scaling resistance; CPFR, PFR, and BFR are the fouling resistance associated with colloidal particle(s), protein(s), and biofoulant(s), respectively; DG - degree of grafting.

[b] t_{exp} (exposure time), λ (UV source wavelength), and power and energy of UV source are listed as reported.

[c] Graft polymerization time only refers to the reaction time and does not include the total processing time; the number of steps indicated does not include substrate cleaning.

2.4.4 Surface Nanostructuring via Plasma Induced Graft Polymerization

In plasma induced graft polymerization, ionized gas (i.e., plasma) strikes a surface (and/or monomer adsorbed on a surface and/or monomer in gas phase) to create activated surface sites for subsequent graft polymerization (Table 2-1, Table 2-5). Plasma can be generated by flowing a neutral gas (e.g., nitrogen, oxygen, helium, hydrogen, and argon) through a plasma source containing electrons streaming through electrodes [172]. The electrons collide with the neutral gas, transferring kinetic energy, and creating ionized gas or plasma. Surface modification with plasma can be accomplished by three different approaches [10]. In the first approach, a surface with adsorbed monomer is exposed to plasma [94, 98, 108]. The second method employs exposing a surface to plasma along with a monomer (in gas phase) [101, 110, 116]. Both approaches result in the creation of active surface sites as well as monomer radicals in the bulk solution/gas [9]. Following monomer addition to active surface sites, polymer chains are tethered onto the surface. However, formation of monomer radicals results in partial cross-linking, and homopolymerization in solution/gas which can lead to polymer grafting (i.e., "grafting to") that negatively impacts polymer chain uniformity [9]. In the third approach, plasma is applied directly to the surface resulting in the formation of activated surface sites [12, 88, 173]. Subsequently, exposure of the surface to a monomer solution commences graft polymerization (i.e., "grafting from") via monomer addition from the activated surface sites, resulting in the formation of a layer of polymer chains that is covalently bonded to the surface. The above approach has been reported to enable the synthesis of graft polymer layers of high chain number density [81-82]. Therefore, the above is the preferred approach for creating surfaces with lower surface roughness.

When exposed to a polymeric surface, the activated species in plasma (electrons, ions, radicals, and photons [174]) induce hydrogen atom abstraction or break the C-C bonds [9]. In this process, plasma species bombard the carbon backbone on the polymeric surface to create surface radicals. After the surface is treated with plasma, it is also exposed to oxygen or air to allow for the formation of surface active sites (e.g., peroxides) [80]. When the surface is subsequently exposed to a vinyl monomer solution at a suitable temperature, monomer addition commences directly from the activated surface sites to form polymer chains that are covalently attached to the surface (Chapter 1, Figure 1-2). It is noted that plasma treatment alone can increase surface hydrophilicity; however, such a modification is temporary and degrades over time [58, 175]. Graft polymerization post-plasma surface activation results in permanent modification of surface properties (e.g., hydrophilicity) [9].

Plasma surface activation for surface modification has been extensively investigated over the last decade given its ability to create a high density of grafted polymer chains (average separation distance < 10 nm [80]) without the use of chemical initiators [10]. Most conventional plasma activation approaches, however, require operation under vacuum in order to increase plasma reactivity, which requires a low pressure gas chamber, limiting commercial scalability [20-21]. Also, it is noted that plasma surface treatment with high energy plasma (e.g., containing oxygen) can lead to surface etching, degrading the structural integrity of the exposed surface [54, 72, 176]. For example, in membrane applications etching would result in increased membrane permeability and decreased solute rejection [72]. The atmospheric pressure plasma (APP) approach, on the other hand, is particularly advantageous because it is operated under ambient conditions and is commercially scalable [10]. Furthermore, the APP settings (e.g., source gas, power, exposure time, etc.) can be tuned to prevent surface etching [72, 176].

APP sources for polymeric surface modification include corona discharge [177], dielectric barrier discharge (DBD) [91-92, 115], and atmospheric pressure plasma jet (APPJ) [11-12, 32, 88, 95, 99] (Figure 2-5). Although corona discharge is capable of generating a sufficient density of active plasma species, processing is limited due to the non-uniformity of the plasma discharge (due to drift to planar electrode) and restricted plasma area (around the metal tip) [172]. Generally, DBD is designed to have a parallel plate configuration, where the plasma exits the top electrode in many independent microarcs (100 μm in diameter, separation distance of ≤ 2 cm) which then travel to the second electrode located a few millimeters below. The heterogeneous distribution of microarcs results in a non-uniform plasma discharge. In addition, the DBD source cannot be moved to scan the surface during plasma treatment, and the parallel plates are fixed such that the electrode spacing cannot be changed, which inhibits the potential for scaling-up. Also, DBD requires a relatively high breakdown voltage $5 - 25$ kV and operates over an electron temperature range of $1 - 10$ eV, which results in a higher minimal voltage needed to sustain the plasma and a higher plasma gas temperature (~200ºC), respectively. Alternatively, APPJ employs a plasma jet with the source consisting of two concentric electrodes from which the plasma is discharged, resulting in a plasma discharge that is spatially and temporally uniform. In terms of potential scalability, the APP jet can be easily moved over surfaces for plasma treatment, and is operated at a breakdown voltage of $0.05 - 0.2$ kV and electron temperature range of $1 - 2$ eV (corresponds to a gas temperature of under 150ºC), both significantly lower than for the DBD source [172]. Furthermore, the density of the oxygen atoms for the APP jet discharge is four times higher (10^{16} particles/cm^3) compared to the DBD and corona sources (10^{12} particles/cm^3). The significant increase in plasma density enables the generation of active sites of high surface density (i.e., #/area).
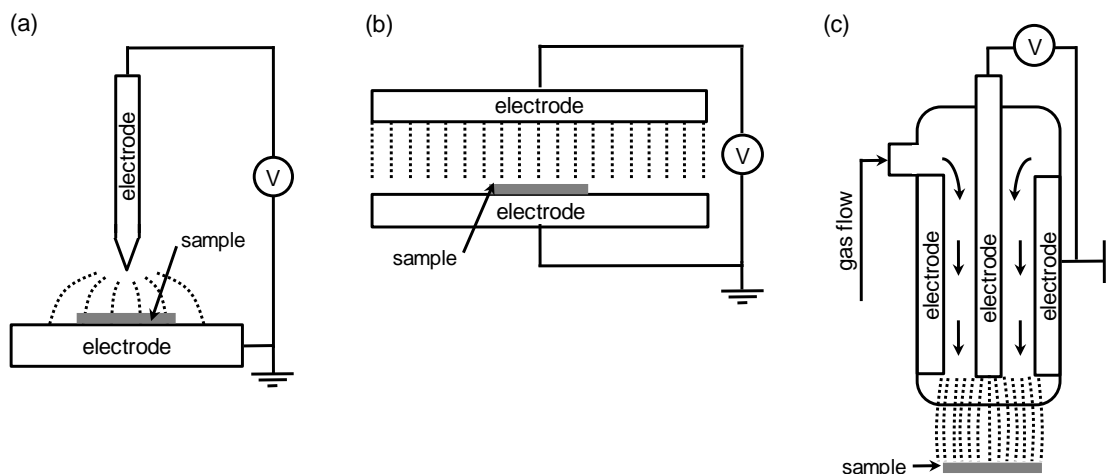
Figure 2-5. Atmospheric pressure plasma sources: (a) corona discharge, (b) dielectric barrier discharge, and (c) plasma jet (vertical cross-section of cylindrical jet).

Numerous previous studies have focused on membrane surface nanostructuring via low pressure plasma induced graft polymerization [21, 55, 68, 72, 86, 124, 178-183]. However, the recent success of APP membrane surface modification with vinyl monomers [12, 88] showed that it is feasible to utilize APP to create polymer chains on a membrane surface to impart protein fouling resistance. The above success provides incentive and support for extending the application of APP to design RO membrane surfaces with polymer chains that impart biofouling resistance. However, it is critical to determine how plasma induced polymerization reaction conditions (e.g., plasma source gas, power, and exposure time, initial monomer type and concentration, and graft polymerization time and temperature, etc.) affect the physicochemical characteristics (e.g., surface topography and hydrophilicity) of the nanostructured RO membranes. Such knowledge would provide the basis for tailor-designing membranes of specific surface hydrophilicity and topography to retard surface-solute affinity (e.g., decreased biofouling propensity).

Table 2-5. Summary of methods of plasma initiated graft polymerization on membrane surfaces [a].

Ref.	Plasma Treatment [b]	Monomer	Membrane Support	Graft Polymerization Time [c]	Membrane Performance	Grafted Polymer Characterization Methods
[178]	Ar t_{exp} = 60 s Power = NR Pressure = 75 Torr	2-methoxyethylacrylate	polyethylene (PE)	(1 step)	$L_p \downarrow$, $R_p \downarrow$, PFR $\uparrow$	ATR-FTIR, graft yield, SEM
[173]	Ar t_{exp} = 180 s Power = NR Pressure = 760 Torr	acrylic acid	polyvinylidene difluoride (PVDF) and PES (MF/UF)	20 min (1 step)	NR	ATR-FTIR, SEM
[179]	Ar t_{exp} = 60 s Power = 60 W Pressure = 113 mTorr	styrene	polyacrylonitrile (PAN) (UF)	1 – 2 h (2 steps)	$L_p \downarrow$, $R_{oil} \uparrow$	ATR-FTIR, contact angle, pore size
[72]	He t_{exp} = 10 – 90 s Power = 25 W Pressure = 200 mTorr	n-vinyl-2-pyrrolidone	PES (UF)	1 h (3 steps)	$L_p \uparrow$, PFR $\uparrow$	contact angle, ATR-FTIR, XPS, graft density
[55]	Ar t_{exp} = 15 – 600 s Power = 30 – 120 W Pressure = 0.45 – 1.13 Torr	acrylic acid	PS (UF)	1 – 15 h (3 steps)	$L_p \downarrow$, $R_p \downarrow$, PFR $\uparrow$	contact angle, ATR-FTIR, pore size, graft yield, AFM
[88]	He t_{exp} = 103 s Power = NR Pressure = 760 Torr	45 different monomers (polyethylene glycol's, strong & weak acids, basic & zwitterionics hydroxyls, amines)	PES (UF)	2 h (1 step)	$L_p \uparrow$, $R_p \uparrow$, PFR $\uparrow$	contact angle, ATR-FTIR, graft yield
[99]	He t_{exp} = NR (0.7 mm/s scan speed) Power = NR Pressure = 760 Torr	10 different amide monomers	PES (UF)	2 h (1 step)	$L_p \uparrow$, $R_p \uparrow$, PFR $\uparrow$	graft yield discussed but not quantified
[181]	Ar t_{exp} = 120 s Power = 60 W Pressure = 75 mTorr	methacryloxyethyl benzyl dimethyl ammonium chloride	PE (MF/UF)	2 h (1 step)	$L_p \uparrow$, $R_b (\approx)$, BFR $\uparrow$	contact angle, ATR-FTIR, XPS, pore size, SEM
[12]	H$_2$/He t_{exp} = 10 – 40 s Power = 40 W Pressure = 760 Torr	methacrylic acid, acrylamide	polyamide TFC (NF)	0.5 – 2 h (3 steps)	$L_p \uparrow$, $R_s \uparrow$, SR $\uparrow$, PFR $(\approx)$	contact angle, ATR-FTIR, AFM

Ref.	Plasma Treatment [b]	Monomer	Membrane Support	Graft Polymerization Time [c]	Membrane Performance	Grafted Polymer Characterization Methods
[184]	He/O$_2$ t_{exp} = NR (6 mm/s scan speed) Power = NR Pressure = 760 Torr	9 monomers synthesized by reacting a thiol linker with a maleimide containing various different functional groups	PES (UF)	2 h (1 step)	L$_p$ ↑ (5 monomers) and ↓ (4 monomers), PFR ↑ (6 monomers) and ↓ (3 monomers)	contact angle
[180]	Ar t_{exp} = 30 – 120 s Power = 30 W Pressure = 275 mTorr	methacrylic acid	PVDF (MF)	1 h (1 step)	L$_p$ ↓	contact angle, ATR-FTIR, pore size, graft density
[185]	Ar t_{exp} = NR Power = NR Pressure = NR	hydroxylethyl-metacrylic acid	PES (UF)	2 h (1 step)	L$_p$ ↑	contact angle, bubble point, MWCO, AFM
[124]	Ar t_{exp} = 20 – 120 s Power = 10 W Pressure = 5 mTorr	acrylic acid	PAN (UF)	1 – 5 min (1 step)	L$_p$ ↑, R$_s$ ↓	contact angle, ATR-FTIR
[68]	He t_{exp} = 30 s Power = 25 – 50 W Pressure = 100 – 200 mTorr	2-hydroxy-ethyl-methacrylate, acrylic acid, methacrylic acid	PAN and PSf (UF)	1 – 4 h (3 steps)	L$_p$ ↑, R$_p$ ↑, PFR ↑	ATR-FTIR, contact angle, XPS, graft yield
[182]	NR t_{exp} = 30 – 120 s Power = 750 W Pressure = 300 mTorr	2-acrylamido-2-methylpropanesulfonic acid	PSf (NF)	30 min + 30 – 110 s (2 step)	L$_{p,0}$ and R$_{s,0}$ NR	ATR-FTIR, contact angle, pore size, SEM, graft yield
[21, 86]	Ar t_{exp} = 1 – 10 min Power = 40 W Pressure = 160 mTorr	acrylamide, acrylic acid	PES (MF/UF)	1 h (2 steps)	L$_p$ ↑, PFR ↑	ATR-FTIR, XPS, contact angle, graft yield
[183]	Ar t_{exp} = 60 s Power = 30 – 40 W Pressure = 113 – 150 mTorr	n-vinyl-pyrrolidone	PAN (UF)	1 – 15.5 h (2 steps)	L$_p$ ↓, R$_s$ ↑	ATR-FTIR, XPS

[a] Legend: ↑ - increases; ↓ - decreases; (≈) - less than 5% change; NR - not reported; L$_p$ - permeability; R$_s$,R$_c$, R$_p$, R$_b$, and R$_{oil}$ are the rejection of salt(s), colloidal particle(s), protein(s), biofoulant(s), and oil(s), respectively; SR - mineral salt(s) scaling resistance; CPFR, PFR, and BFR are the fouling resistance associated with colloidal particle(s), protein(s), and biofoulant(s), respectively; DG - degree of grafting.

[b] The first line refers to the plasma gas, t_{exp} - plasma exposure time.

[c] Graft polymerization time only refers to the reaction time and does not include the total processing time; the number of steps indicated does not include substrate cleaning.

2.5   Fundamentals of the Reverse Osmosis Process

Altering reverse osmosis (RO) membrane surface topography and wettability by surface attachment of hydrophilic polymer chains via atmospheric pressure plasma induced graft polymerization (APPIGP) is a promising approach for decreasing membrane biofouling propensity (Section 2.4.4). In the reverse osmosis (RO) desalination process, a feed solution flows tangentially across a semipermeable membrane. Pressure is applied to a saline solution, resulting in water passage through the membrane but rejection of mineral salt ions, resulting in a low salinity product water stream (i.e., permeate) and a high salinity retentate (or concentrate) stream. In order for permeate production to occur, the applied pressure must be equal to or greater than the osmotic pressure difference between the retentate exit and permeate streams [186]. Current RO membranes used for water desalination are thin film composite (TFC) membranes based on a selective polyamide (PA) layer (100 − 200 nm thick), which is responsible for solute (e.g., salt) rejection [10]. The active PA separation layer is typically structurally supported by a porous polysulfone (PSf) layer (~60 μm thick) and a non-woven fabric layer (~150 μm thick) (Figure 2-6) [187-188].
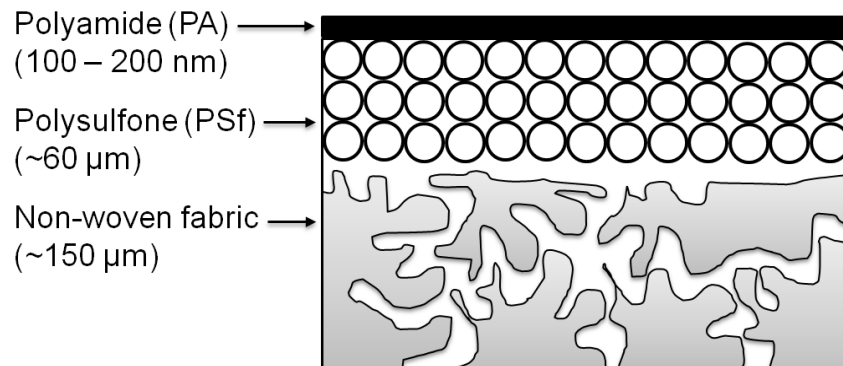
Figure 2-6. Cross-section illustration of a conventional PA-based RO membrane [187-188].

RO desalination is conventionally carried out in cross-filtration with the feed water flowing tangentially across the membrane surface (Figure 2-7). The feed stream with a feed flowrate, Q_f, concentration, C_f, and pressure, P_f, enters the membrane at one end. The pressure drives a solute lean permeate flowrate, Q_p, stream through the membrane with a solute concentration, C_p, and pressure, P_p. The solute rich retentate stream is rejected from the membrane with a flowrate, Q_r, concentration, C_r, and pressure, P_r. The concentration of solutes in the bulk solution and at the membrane surface are represented by C_b and C_m, respectively.
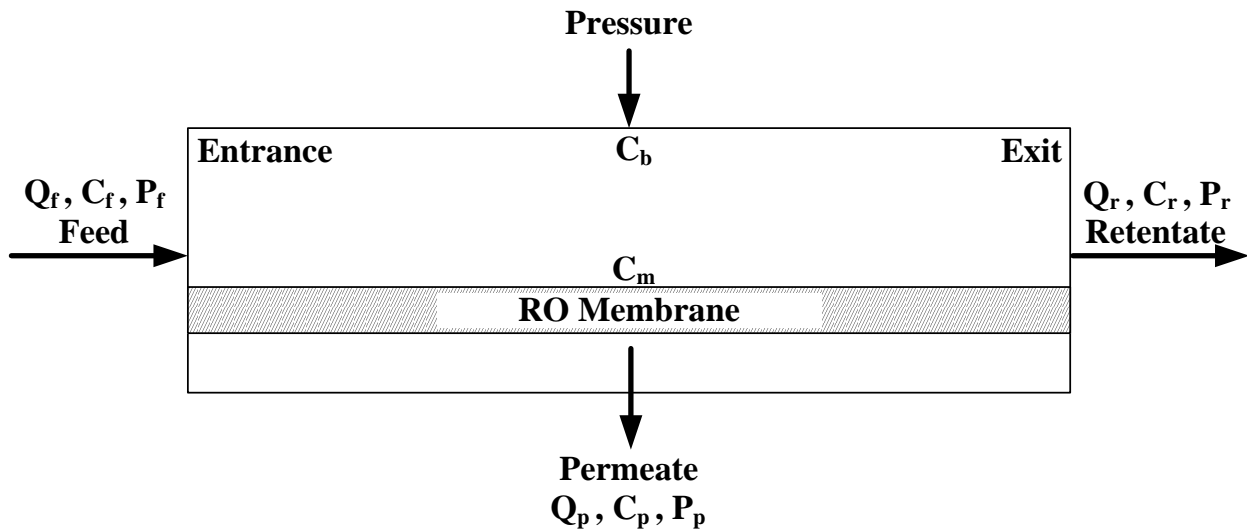
Figure 2-7. Illustration of the RO process, where Q_f, Q_r, and Q_p are the flowrates of the feed, retentate, and permeate, respectively, C_f, C_r, C_p, C_b, and C_m are the solute concentrations at the feed, retentate, permeate, bulk solution, and at the membrane surface, respectively, and P_f, P_r, and P_p are the pressures of the feed, retentate, and permeate, respectively.

The performance of RO membranes is characterized in terms of salt rejection and membrane water permeability. Salt rejection is a measure of a membrane's ability to prevent salt passage through the membrane into the fresh water permeate stream. A higher salt rejection indicates that less salt passes through the membrane into the permeate stream. The observed and intrinsic membrane salt rejections, R_o and R_i, respectively, are defined as

$$R_o = 1 - \frac{C_p}{C_b} \tag{2-2}$$

$$R_i = 1 - \frac{C_p}{C_m} \tag{2-3}$$

where C_p, C_b, and C_m are the solute concentrations of the permeate stream, bulk solution, and at the membrane surface, respectively. Water permeability denotes the efficiency of fresh water production. The permeate flux through the membrane (L/m^2·h), J_p, is expressed by [189]

$$J_p = L_p(\Delta P - \sigma \Delta \pi) \tag{2-4}$$

where $\Delta \pi$ is the osmotic pressure difference between the feed solution at the membrane surface and the permeate, ΔP is the applied pressure, L_p (L/m^2·h·psi) is the membrane permeability, and σ (~1 for RO membranes) is the reflection coefficient. The applied pressure, ΔP, is given as

$$\Delta P = P_f - \left(\frac{P_f - P_r}{2}\right) - P_p \tag{2-5}$$

where P_f, P_r, and P_p are the pressures of the feed, retentate, and permeate, respectively. The osmotic pressure, π, is proportional to the salt concentration, and for dilute solutions it is typically expressed in terms of the Van't Hoff's equation

$$\pi = iMRT \tag{2-6}$$

where i is the Van't Hoff's factor, M is the molar concentration of salt in solution (mol/L), R is the ideal gas constant (8.314 L·kPa/mol·K), T is temperature (K). Lastly, RO membrane process productivity can be characterized in terms of water recovery, Y, which is a ratio of permeate and feed flowrates (i.e., Q_p and Q_r, respectively):

$$Y = \frac{Q_p}{Q_f} = 1 - \frac{Q_r}{Q_f} \tag{2-7}$$

2.6   Synthesis of the RO Membrane Polyamide Active Separation Layer

In RO membranes, a thin layer ($100 - 200$ nm thick) of polyamide (PA) serves as the semi-permeable layer that rejects monovalent salts from the permeate/product water [10]. It is often referred to as the active layer of the reverse osmosis membrane. The aromatic PA film is synthesized onto a membrane support layer (e.g., polysulfone) via conventional interfacial polymerization between m-phenylenediamine (MPDA) and trimesoyl chloride (TMC) (Figure 2-8) [190]. First, aqueous MPDA is exposed to the membrane support (e.g., polysulfone) to allow for surface adsorption. After an allotted time period (typically on the order of minutes to hours; see Table 2-6), the MPDA solution is removed from the surface by draining [11-12, 191], rolling with a rubber roller [49, 192-194], or by air knife [195-197]. Subsequently, the MPDA adsorbed surface is exposed to an organic solution of TMC for a period of time (typically on the order of seconds; see Table 2-6), which immediately commences interfacial polymerization. Next, the excess organic solution is drained and the PA membrane is cured in an oven.

Thereafter, the PA membrane is typically rinsed with DI water before being immersed in DI water and stored away from light [11, 191].
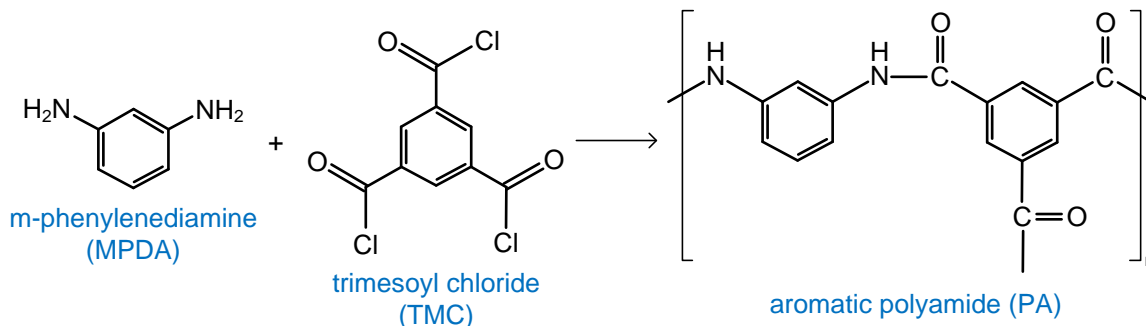
Figure 2-8. Polyamide thin film composite membrane synthesized by interfacial polymerization between m-phenylenediamine and trimesoyl chloride.

The desired membrane permeability and rejection are achieved through adjustment of the interfacial polymerization reaction conditions (e.g., MPDA concentration and absorbance time, and TMC solvent, interfacial polymerization reaction time, cure temperature, and time) (Table 2-6). There is a trade-off between membrane permeability and rejection; usually higher water permeability results in decreased solute rejection (Figure 2-9). Low water permeability (and hence, higher salt rejection) is attributed to inordinately low free volume and overly dense crosslinking of the PA layer structure [191].

Table 2-6. Interfacial polymerization of polyamide [a].

Ref.	Surface	MPDA [b]	TMC [c]	Cure [d]	L_p (L/m²·h·bar)	Rejection R (%)	Solute	Pressure (bar)	Comments
[198]	polysulfone	2 wt%; t_{MPDA} = NR; rubber roller	0.1 wt%; hexane; t_{ip} = 6 – 100 s	ambient 30 min	0.67 – 1.27	97.2 – 98.5	2000 ppm NaCl	15.5	$L_p\downarrow$ and $R\uparrow$ as $t_{ip}\uparrow$ (with the exception of t_{ip} = 20 s)
[191]	polysulfone	1% w/v 0.25/1 – 4/1 MPDA/SPES-NH$_2$; t_{MPDA} = 2 h; drained	0.25 – 1.5% w/v; cyclohexane; t_{ip} = 120 – 300 s	70ºC NR	1.60 – 4.80	42 – 97	2000 ppm NaCl	20	$L_p\downarrow$ and $R\uparrow$ as [MPDA]$\uparrow$; $L_p\downarrow$ and $R\uparrow$ as $t_{ip}\uparrow$; $L_p\downarrow$ and $R\uparrow$ as [TMC]$\uparrow$
[192]	polyether-sulfone	2% w/v; t_{MPDA} = 2 min; rubber roller	0.1% w/v; hexane; t_{ip} = 60 s	70ºC 6 min	0.16 – 1.23	55 – 85	2000 ppm NaCl	12	lag time before exposure to TMC affects L_p and R
[195]	polysulfone	NR; t_{MPDA} = 0.25 min; air knife	NR; hexane, heptane, cyclohexane, Isopar G; t_{ip} = 15 s	45 – 90ºC 10 min	0.08 – 0.20	93.0 – 98.4	2000 ppm NaCl	15.5	$L_p\downarrow$ and $R\uparrow$ as $T\uparrow$; TMC solvent ranking with $\uparrow L_p$: Isopar G < cyclohexane < heptane < hexane; TMC solvent ranking with $\uparrow R$: cyclohexane < hexane < Isopar G < heptane
[199]	polyacrylo-nitrile	2 wt%; t_{MPDA} = 30 min; removed	1 wt%; toluene; t_{ip} = 180 s	70ºC 60 min	N/A				N/A
[193]	polysulfone	1 wt% 8/2 – 9/1 w/w; piperazine /MPDA; t_{MPDA} = 1 min; rubber roller	0.05 wt%; hexane; t_{ip} = 10 s	ambient 120 min	6.65 – 7.25	78 – 90	1000 ppm PEG	13.8	$L_p\downarrow$ and $R\uparrow$ as [MPDA]$\uparrow$
[49]	polysulfone	2% w/v; t_{MPDA} = 2 min; rubber roller	0.1% w/v; hexane; t_{ip} = 60 s	NR NR	0.78	93.4	2000 ppm NaCl	12.4	N/A
[11]	polysulfone	2.5 wt%; t_{MPDA} = 3 min; draining	0.13 wt%; hexane; t_{ip} = 20 s	80ºC 0.5 min	187	30	1000 ppm NaCl	3.5 – 20.7	N/A
[12]	polysulfone	2.5 wt%; t_{MPDA} = 3 min; draining	0.13 wt%; hexane; t_{ip} = 15 – 20 s	80ºC 0.5 min	187	30	1000 ppm NaCl	3.5 – 20.7	N/A
[194]	polyether-sulfone	1 wt%; t_{MPDA} = 3 min; rubber roller	0.2 wt%; hexane; t_{ip} = 40 s	80ºC 3 min	1.8, 2.4	64, 67	1000 ppm NaCl	5, 10	N/A
[200]	polysulfone	2% w/v; t_{MPDA} = NR; none	0.1% w/v; hexane; t_{ip} = 60 s	60 – 62ºC 7 min	3.1	94 – 96	2000 ppm NaCl	17.2	N/A
[196]	polysulfone	3.4 wt%; t_{MPDA} = 2 min; air knife	0.15 wt%; Isopar-G; t_{ip} = 60 s	95ºC 2 min	1.0	95.8 – 97.2	2922 ppm NaCl	27.6	variability in membrane performance is due to underlying polysulfone surface casting conditions
[197]	polysulfone	3.4 wt%; t_{MPDA} = 2 min; air knife	0.15 wt%; Isopar-G; t_{ip} = 60 s	95ºC 2 min	1.1	97.4	2922 ppm NaCl	27.6	N/A

[a] Legend: NR – not reported; t_{MPDA} – MPDA adsorption time; t_{ip} – interfacial polymerization time; T – curing temperature; L_p – water permeability; R – solute rejection; $\uparrow$ – increases; $\downarrow$ – decreases
[b] Reported values: MPDA concentration; adsorption time onto the surface (t_{MPDA}); method used to remove the excess MPDA solution
[c] Reported values: TMC concentration; solvent; interfacial polymerization reaction time (t_{ip})
[d] The first and second lines refer to the curing temperature and time, respectively

Figure 2-9. Variation of membrane permeability with rejection for the polyamide membranes presented in Table 2-6 [11-12, 49, 191-200].

2.7 Concentration Polarization and Membrane Fouling

In RO desalination, salt molecules accumulate near the membrane surface, which is commonly known as concentration polarization (CP). In this stage, permeate flow convects the salt ions toward the membrane surface, forming a concentration gradient between the membrane surface and the bulk flow (Figure 2-10) [201-205]. The salt species concentrations within the concentration boundary layer is often approximated using the film model (Equation (2-8)), where C_m, C_b, and C_p are the concentrations (mg/L) of the mineral salts at the membrane surface, bulk solution, and permeate, respectively, R_0 is the observed rejection ($R_0 = 1 - C_p/C_b$), J is the permeate flux (L/m^2·s), and k (m/s) is the solute mass transfer coefficient of the feed solution.

$$CP = \frac{C_m}{C_b} = (1 - R_0) + R_0 exp(J/k) \qquad (2\text{-}8)$$

In the RO process, the CP layer increases along the membrane surface, with the highest CP modulus at the tail end of the membrane channel. Operating RO membranes at high recovery (Section 2.5, Equation (2-7)) increases the concentration of solutes in the retentate stream, which can result in the concentration of sparingly soluble salt to exceed the solubility limits. As a consequence, these sparingly soluble salts can precipitate, resulting in membrane scaling that reduces permeate flux [206-207] and can shorten membrane lifetime [170].
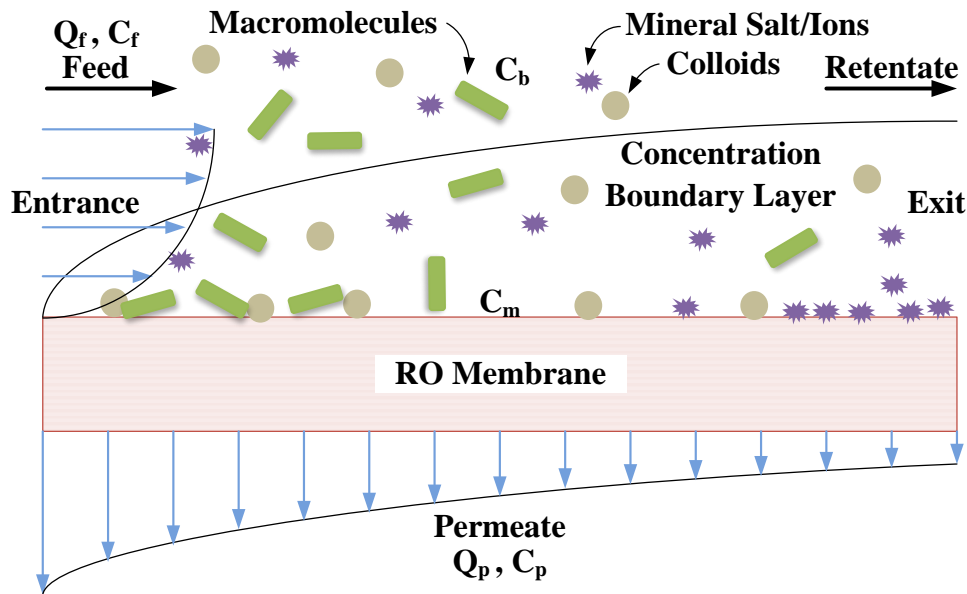
Figure 2-10. Illustration of a concentration polarization boundary layer formed across a membrane surface due to solute accumulation where Q_f and Q_p are the volumetric flow rates of the feed and permeate solutions, respectively, and C_f, C_p, C_m, and C_b are the solute concentrations of the feed, permeate, at the membrane surface, and bulk solution, respectively.

Unlike mineral scaling, biofouling occurs primarily at the entrance of the membrane channel due to the higher mass transfer coefficient/deposition velocity at the entrance region [208]. While various foulants are encountered in the process of water desalination, this research focuses on biofoulants. There are a variety of biofoulants such as humic acid, polysaccharides, proteins, bacteria, and microorganisms (most of which are negatively charged between pH 6.5 – 7.8) that can irreversibly foul the membrane [195]. During the RO desalination process, macromolecule species interact with the membrane surface through Van der Waals forces, electrostatics, hydrophobic and hydrogen bonding, thereby adsorbing and colonizing onto the membrane surface. Subsequently, the bacterial colonies metabolize and produce extracellular polymeric substances (EPS) forming a biofilm, which results in membrane biofouling [48]. In the initial stages of biofouling, the biofoulants attach to the membrane surface, causing a decrease in permeate flux. As the biofoulants colonize on the membrane surface, significant flux decline can occur [209]. Once biofilms form, they can be difficult to remove and require aggressive membrane cleaning which leads to additional energy and maintenance costs and can quicken the need for membrane replacement [6]. Additionally, strong foulant-surface adhesion force may resist removal, resulting in irreversible fouling.

2.8   Effects of Membrane Surface Structuring on Membrane Permeability

Membrane surface modification by nanostructuring with hydrophilic polymer chains often promotes increased surface hydrophilicity and fouling resistance [10]. However, membrane permeability can be negatively impacted (i.e., freshwater production efficiency decreases) due to surface or pore blockage. Indeed, the majority of previous studies have reported a decrease in membrane permeability post surface nanostructuring with polymers [10]. In select studies where

the membrane permeability did not decrease, membrane selectively was compromised (i.e., rejection decreased) [137, 158]. As previously discussed in Section 2.6, there is a trade-off between membrane permeability and rejection. Higher water permeability results in decreased solute rejection, and vice versa. Unfortunately, the selection of commercial membranes with respect to performance and polymeric material is limited, and thus it is often difficult to optimize the graft polymerization process to arrive at the target performance. An approach to overcome the above dilemma is to optimize the permeability and rejection of the starting membrane material (e.g., PA) such that, upon surface nanostructuring, membrane performance is upgraded to the target level. Therefore, it is imperative to tune both PA interfacial polymerization (Section 2.6) as well as the FRGP conditions to target high monovalent salt rejection (> 95%) while maximizing membrane permeability.

Chapter 3. Wettability of Terminally Anchored Polymer Brush Layers on a Polyamide Surface

3.1 Introduction

Surface activation by atmospheric pressure plasma (APP) is typically accomplished by exposure of the surface to plasma (e.g., using argon, helium, nitrogen, oxygen or other suitable gas) for a short duration (order of seconds to minutes) [31, 89]. Graft polymerization post-APP treatment is typically preformed with vinyl monomers with reported initial monomer concentrations typically in the range of 1 – 30% v/v [11, 108, 113], although concentrations as high as 70% v/v have been reported [93]. Graft polymerization is generally carried out at mild temperatures (50 – 80ºC, [11-12, 80, 89, 102]), but higher temperatures have been reported for grafting in non-aqueous solvents [102, 210]. Studies have shown that APP, followed by either graft polymerization (i.e., "grafting from") [11-12, 31, 89] and polymer grafting (i.e., "grafting to") [32, 113] using hydrophilic monomers enabled synthesis of terminally anchored polymer brush layers with reported water contact angles in the range of 5 – 75º. The degree of polymer grafting is quantified in most studies in terms of grafting mass density which has been reported to be in the range of 0.01 – 3.0 mg/cm^2 [32, 93, 95, 114]. Although published studies concerned with atmospheric pressure plasma induced graft polymerization (APPIGP) have generally reported on wettability and grafting density, few have provided information regarding surface topography (e.g., via AFM analysis) which suggests a range of root-mean-square surface roughness, R_{rms}, of 0.18 – 220 nm [11, 32, 80, 93, 102, 210].

In addition to the importance of surface chemistry, surface topography at the nanoscale [11-12, 80, 93, 102, 210] and sub-micron scale [32] can have a measurable impact on surface wettability (or hydrophilicity). Accordingly, this chapter focused on evaluating the impact of

surface topography at the nanoscale/sub-micron range, for a hydrophilic polymer brush layer, on surface wettability (i.e., hydrophilicity). The brush layer was synthesized on a thin polyamide surface created on a smooth silicon wafer substrate (Figure 3-1).
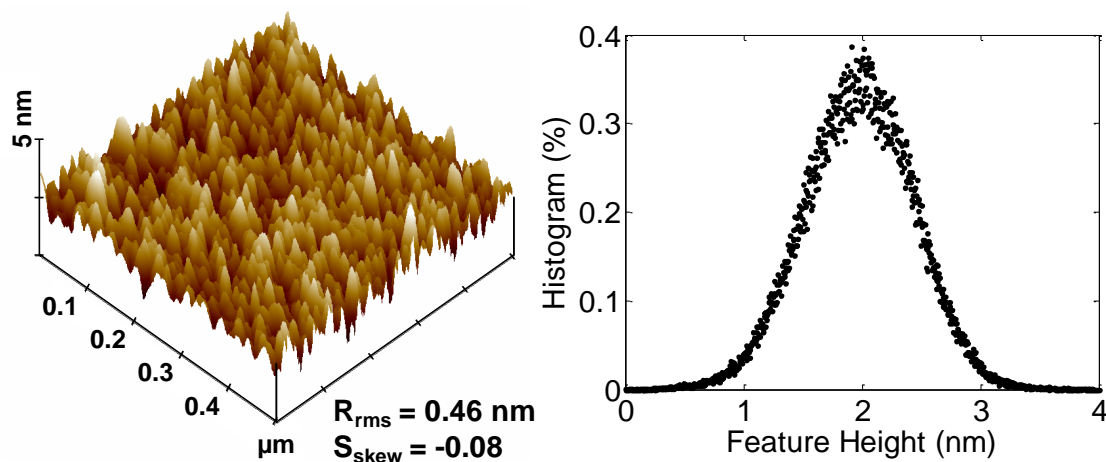
Figure 3-1. AFM imaging and feature height distribution graph of the PA-Si surface.

A polyamide (PA) substrate, which has a hydrophobic character relative to the hydrophilic brush layer, was selected for brush layer anchoring given the popularity of this polymer as a membrane material for nanofiltration (NF) and reverse osmosis (RO) membranes as well as in various other applications [11-12]. In particular, it is noted that there have been increasing efforts over the last decade to modify the surfaces of PA membranes in order to increase both surface hydrophilicity and resistance to biofouling and fouling by organics and colloidal matter. Indeed, using the APPIPG approach, previous work [12] has demonstrated that hydrophilic polymer brush layers can be effective in increasing local membrane surface hydrophilicity. In the present chapter, brush layers were synthesized by a two-step process consisting of surface activation by an APP source (via surface impingement) followed by surface graft polymerization with two different

60

water soluble vinyl monomers. The effect of surface activation and graft polymerization conditions on the resulting surface topography (e.g., surface feature height distribution and surface roughness) was assessed and subsequently surface wettability was quantified with the aim of elucidating the impact of topography of the hydrophilic brush layer.

3.2   Materials and Methods

3.2.1   Materials

Prime-grade silicon <100> wafers (Wafernet, Inc., San Jose, CA) of 100 mm in diameter and 0.050 – 0.055 mm in thickness were used as substrates to facilitate surface analysis. Concentrated H_2SO_4 (Fisher Scientific, Pittsburgh, PA) and reagent grade H_2O_2 (Sigma-Aldrich, St. Louis, MO) were used to prepare the piranha solution (3:1 mixture of sulfuric acid and 30% hydrogen peroxide) for silicon wafer cleaning. The polyamide surface for anchoring the hydrophilic brush layers was prepared using poly(ethyleneimine) (PEI, M_w = 750,000 g/mol), 1, 3-phenylenediamine (MPDA, ≥ 99%), and trimesoyl chloride (TMC, 98%) (Sigma-Aldrich, St. Louis, MO). The monomers for graft polymerization were 1-vinyl-2-pyrrlidone (nVP) (>99%, Aldrich, St. Louis, MO), and acrylamide (AAm) (Fisher Chemicals, 99%, Fair Lawn, NJ). Solutions of PEI, nVP, and AAm were all prepared using ultra-pure deionized water produced by filtering the distilled water through a Milli-Q filtration system (Millipore Corp., San Jose, CA). Hexane (Sigma-Aldrich, St. Louis, MO), was the solvent for preparing the TMC solution. Monomer solutions were degassed using industrial grade nitrogen (97%, Air Liquide, Los Angeles, CA).

61

3.2.2 Surface Nanostructured Polyamide Surfaces

Surface nanostructured-polyamide-silicon (SNS-PA-Si) surfaces were synthesized in three sequential steps: (1) surrogate surface preparation, (2) plasma surface activation, and (3) graft polymerization. The silicon wafers, which served as smooth substrates for the PA surfaces, were first immersed in a piranha bath (3:1 mixture of concentrated sulfuric acid to 30 wt. % hydrogen peroxide) for 10 min at 90ºC to remove organic residues, and rinsed for three cycles in a DI water dump rinser (South Coast Enterprises, Fullerton, CA). The substrate samples were then oven dried (~75ºC) and cut into 1.2 cm x 1.2 cm squares. Thereafter, ~0.5 mL of 0.3 wt% aqueous PEI (polyethyleneimine) solution was dispensed onto the center of the silicon wafer surface using a syringe, and then cast spun (spin-coater model PWM32, Headway Research Inc., Garland, TX) at 2500 rpm for 30 s; the above process was repeated in order to ensure a fully covered surface. PEI served as an adhesion layer and for absorbing MPDA (*m*-phenylenediamine) to enable interfacial polymerization with TMC. Following the addition of the adhesive PEI layer, ~0.5 mL of an aqueous solution of 2.5 wt% MPDA was dispensed (using a syringe) onto the PEI-Si surface to provide for complete surface coverage. After about 2 minutes (allowing for absorption of MPDA into the PEI-Si), the substrate was cast spun at 500 rpm for 30 s, followed by spinning at 3000 rpm for 30 s. Immediately afterward, ~0.5 mL of 0.13 wt% TMC (trimesoyl chloride or 1,3,5-benzenetricarbonyl trichloride) in hexane was dispensed (using a syringe) onto the MPDA-PEI-Si surface, such that the entire surface was covered, to initiate TMC-MPDA interfacial polymerization. Polymerization was allowed to proceed for 30 s and then the substrate was spun at 3000 rpm for 30 s to yield the polyamide-polyethyleneimine-silicon (PA-PEI-Si) surface used for graft polymerization (Figure 3-2). The PA-PEI-Si substrate was subsequently triple rinsed with DI water to remove any unreacted

monomer, blown dry with a nitrogen gas gun, oven dried (80ºC) for 1 h, and then stored in a dark chamber until further use.
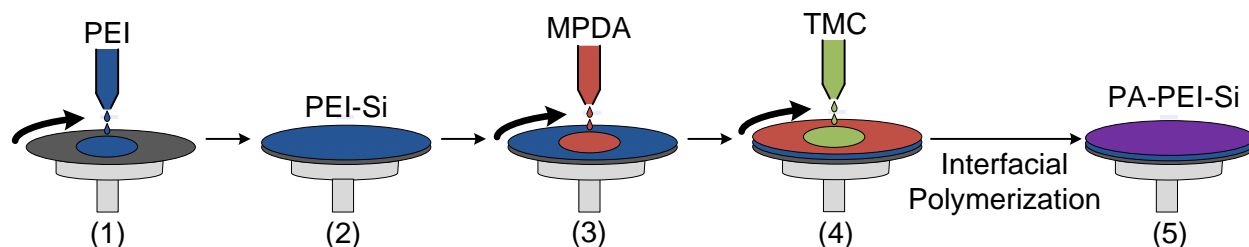
Figure 3-2. Schematic of the synthesis of silicon-polyamide surfaces: 1) coat the Si surface with PEI and cast spin, 2) resulting PEI-Si surface, 3) coat the PEI-Si surface with MPDA and cast spin, 4) coat the MPDA-PEI-Si surface with TMC and cast spin, 5) interfacial polymerization between MPDA and TMC results in the PA-PEI-Si surface.

The second step consisted of exposing the PA-PEI-Si surface to an impinging jet of atmospheric pressure plasma (using the apparatus described elsewhere [172]); explicit operational details are given in Appendix C.1. Briefly, the plasma was produced using a mixture of 1 vol% ultra-high purity H_2 (99.999%, Air Liquide, Los Angeles, CA) and 99 vol% He (99.999%, Airgas, Los Angeles, CA) at 30 L/min at 40 W for a period of 10 s [9, 12, 80]. Subsequently, the PA-PEI-Si surface was exposed to a pure oxygen (99%, Airgas, Los Angeles, CA) stream for 2 minutes to allow for the formation of surface active sites (e.g., peroxides) [9, 80]. Thereafter, in the third step, the plasma treated substrate was immediately immersed in degassed (using nitrogen gas) aqueous monomer solutions and graft polymerization was allowed to proceed. Graft polymerization (Figure 3-3) was accomplished with either vinylpyrrolidone

(nVP) or acrylamide (AAm) at initial monomer concentrations in the ranges of 0.94 − 1.87 M and 0.1 − 0.3 M, respectively, in 40 mL glass vials. Graft polymerization was carried out at 70ºC, with the vials in a constant temperature water bath, for a period of 0.5 − 2 hours. At the end of the set graft polymerization period, the SNS-PA-Si substrates were washed with DI water and stored in a vacuum chamber until further use. The resulting polyvinylpyrrolidone (PVP)-PA-Si and polyacrylamide (PAAm)-PA-Si surfaces consisted of PVP and PAAm chains that are terminally anchored to the polyamide surface. It has been previously demonstrated [11-12] via attenuated total reflection-Fourier transform infrared (ATR-FTIR) spectroscopy that the APPIGP process results in covalent and terminal surface attachment (onto the PA surface) of polymer chains formed by radical polymerization of vinyl monomers.
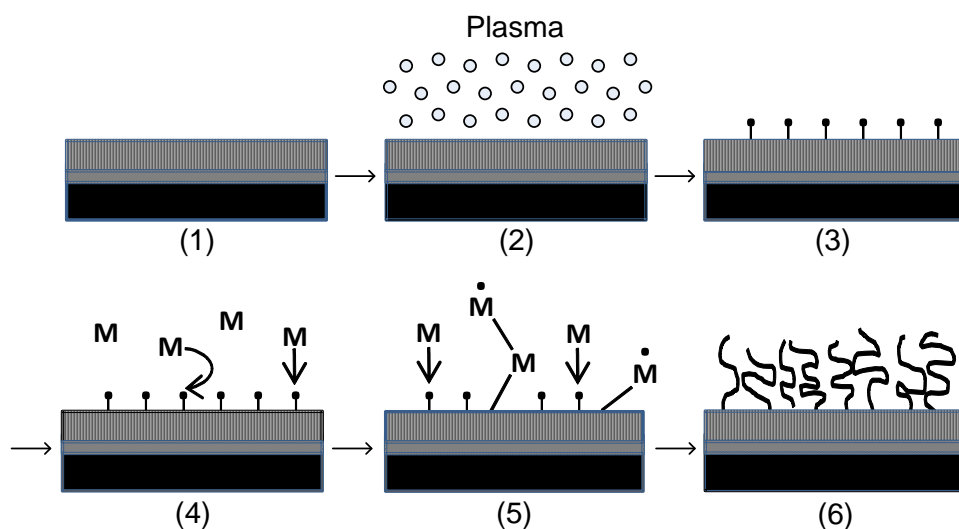
Figure 3-3. Illustration of the multi-step atmospheric pressure plasma induced graft polymerization process: 1) polyamide surface, 2) atmospheric pressure plasma exposed to the surface, 3) activated surface sites (·), 4) monomer (M) exposed to the activated surface, 5) polymer chains are grown from activated surface sites, 6) resulting nanostructured surface.

3.2.3 Surface Characterization

Surface topography was evaluated by tapping mode atomic force microscopy (AFM) (Multimode AFM with Nanoscope IIIa SPM controller, Digital Instruments, Santa Barbara, CA). All AFM scans were taken in ambient air using NSC15 silicon nitride probes (Digital Instruments, Veeco Metrology Group, Santa Barbara, CA) with a force constant in the range of $20 - 70$ N/m, a nominal radius of curvature of $5 - 10$ nm and a side angle of 20°. AFM scans were taken at a scan rate of $0.8 - 0.9$ Hz for $3 - 6$ locations on the substrate surface; scans were replicated at the same location at 0° and 90° to verify that the AFM images were free of directional errors.

The root-mean-square surface roughness (R_{rms}) was determined from the AFM feature height distribution data,

$$R_{rms} = \sqrt{\frac{\Sigma(Z_i - Z_{avg})^2}{N}} \tag{3-1}$$

where Z_i is the surface feature height of the ith sample out of N total samples, and Z_{avg} is the average feature height. Asymmetry of the feature height distribution was quantified in terms of skewness (S_{skew}) of the height distribution data,

$$S_{skew} = \frac{\Sigma(Z_i - Z_{avg})^3}{(N - 1)\sigma^3} \tag{3-2}$$

in which σ is the standard deviation. The exposed polymer volume, V, for the polymer surfaces was determined by volume integration over the z-height profile of the polymer surface features. It should be noted that AFM surface analysis was performed in air, which is a poor solvent for

the polymeric surfaces. Thus, the AFM measured surface feature heights and separation (a surrogate for chain separation) represent lower and higher limit estimates, respectively, since the hydrophilic brush layer chains are expected to swell (i.e., extend away from the surface) in water (a good solvent for both PAAm and PVP) [10-11].

Contact angle measurements were conducted by the sessile drop method (Kruss Model DSA 100, Hamburg, Germany) at 22°C with a liquid volume of 1 μL for both water and diiodomethane. Each reported contact angle represents the average of at least three replicate measurements. Relative hydrophilicity was expressed in terms of the free energy of hydration (ΔG_{iw}), calculated from the Young-Dupree equation [211],

$$\Delta G_{iw} = -\gamma_w (1 + \cos \theta_w) \qquad (3\text{-}3)$$

where γ_w is the liquid surface energy of water, and θ_w is the water contact angle. It has been suggested that the shift from hydrophobicity ($\Delta G_{iw} > \Delta G_{iw,ref}$) to hydrophilicity ($\Delta G_{iw} < \Delta G_{iw,ref}$) can be reasonably assigned at $\Delta G_{iw,ref} = $ -113 mJ/m². It has been reported that free energy of hydration typically ranges from about -40.0 mJ/m² for a highly hydrophobic to about -142.0 mJ/m² for highly hydrophilic levels [212]. It is interesting to note that $\Delta G_{iw,ref} = $ -113 mJ/m² corresponds to a water contact angle of about 56.5°, with water contact angles below considered truly hydrophilic.

Surface wettability can also be analyzed in terms of the relative contributions of the polar, γ_s^p (affected by dipole/dipole, hydrogen bonding, and π-cloud/π-cloud interactions), and dispersive, γ_s^d (governed by van der Waals interactions), components of the solid surface energy (γ_s) [213]. The solid surface energy quantifies the adhesion of the surface (a polymer substrate in the present study) to other substances due to attractive forces (e.g., intermolecular interactions) that

exist between all atoms or molecules [213]. Accordingly, wetting should be favored by high solid surface energy (i.e., increased attractive forces). The surface energy of a solid, γ_s, is given as

$$\gamma_s = \gamma_s{}^d + \gamma_s{}^p \qquad (3\text{-}4)$$

where the polar ($\gamma_s{}^p$) and dispersive ($\gamma_s{}^d$) components can be determined following Owens and Wendt [213],

$$\gamma_L(1 + \cos\theta) = 2\sqrt{\gamma_s{}^d\gamma_L{}^d} + 2\sqrt{\gamma_s{}^p\gamma_L{}^p} \qquad (3\text{-}5)$$

where γ_L is the surface energy of a liquid, θ is the contact angle made by a drop of liquid that is deposited upon a flat, horizontal, solid surface, and $\gamma_L{}^p$ and $\gamma_L{}^d$ represent the polar and disperse components of the liquid surface energy, respectively. Given values of $\gamma_L{}^p$ and $\gamma_L{}^d$, the polar and dispersive components of the solid surface energy for both the native and polymer grafted surfaces were determined, using Equations (3-4) and (3-5), based on contact angle measurements for two liquids of different polarities (water [214], polar; diiodomethane [215], apolar) (Table 3-1).

Table 3-1. Liquid surface tension and its dispersive and polar components at 22°C (mJ/m²) [214-215].

Liquid	$\gamma_L{}^d$	$\gamma_L{}^p$	γ_L
Water	21.7	50.8	72.5
Diiodomethane	50.4	0	50.4

3.3 Results and Discussion

3.3.1 Surface Topography

Surface topography, as determined from AFM surface analysis of the PA-Si and SNS-PA-Si (graft polymerized with vinylpyrrolidone (nVP) or acrylamide (AAm)) substrates are depicted in Figure 3-1 and Figure 3-4, respectively. The root-mean-square (RMS) surface roughness of the SNS-PA-Si substrates was $1.2 - 13$ times greater than for the underlying PA-PEI-Si surface (0.46 nm) (Table 3-2). The PVP-PA- Si and PAAm-PA- Si R_{rms} roughness was in the range of $0.55 - 2.89$ nm and $1.54 - 5.84$ nm, respectively, increasing both with increasing grafting time and initial monomer concentration (Figure 3-5 and Table 3-2). Increased surface roughness would be expected with increased rate of chain termination, k_t, relative to chain propagation, k_p; indeed the ratio k_t/k_p is about a factor of 27 times higher for AAm [216] relative to nVP [127] polymerization. This implies that longer chains with fewer shorter (terminated) chains will be formed for the grafted PAAm relative to the PVP brush layer.

0.5 h

1 h

2 h

0.94 M

8 nm

$R_{rms} = 0.55$ nm
$S_{skew} = 1.03$

10 nm

$R_{rms} = 0.85$ nm
$S_{skew} = 0.33$

20 nm

$R_{rms} = 1.27$ nm
$S_{skew} = 3.39$

1.40 M

10 nm

$R_{rms} = 0.63$ nm
$S_{skew} = 0.81$

15 nm

$R_{rms} = 1.04$ nm
$S_{skew} = 0.87$

30 nm

$R_{rms} = 2.62$ nm
$S_{skew} = 1.98$

1.87 M

10 nm

$R_{rms} = 0.83$ nm
$S_{skew} = 1.61$

20 nm

$R_{rms} = 1.69$ nm
$S_{skew} = 1.77$

30 nm

$R_{rms} = 2.89$ nm
$S_{skew} = 2.31$
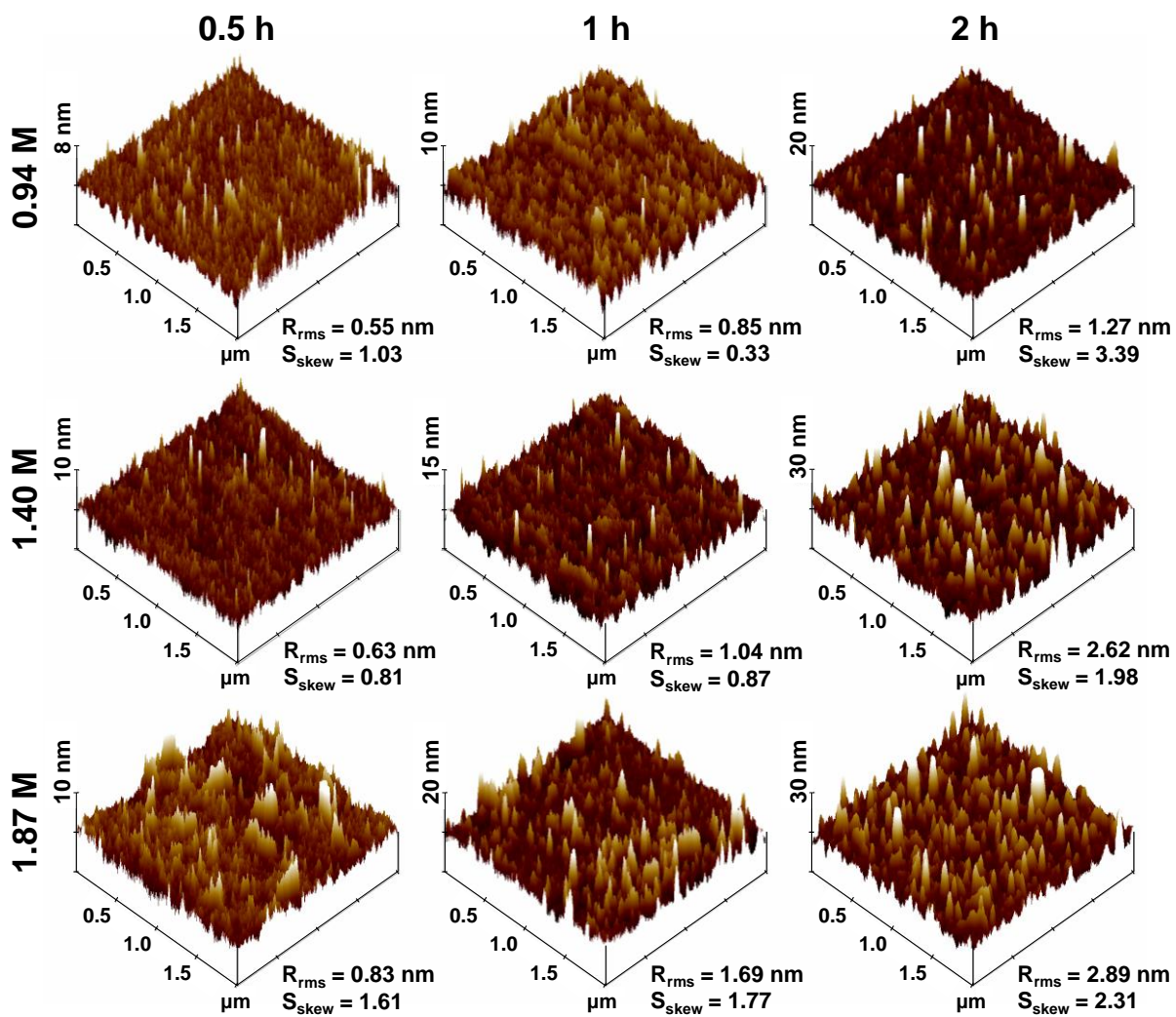
Figure 3-4a. Tapping mode AFM images of SNS surfaces graft polymerized for $0.5 - 2$ h for PVP-PA-Si at $[M]_0 = 0.94 - 1.87$ M.

	0.5 h	1 h	2 h
0.1 M	R_{rms} = 1.54 nm, S_{skew} = 1.41	R_{rms} = 2.07 nm, S_{skew} = 2.51	R_{rms} = 2.67 nm, S_{skew} = 2.36
0.2 M	R_{rms} = 1.76 nm, S_{skew} = 2.87	R_{rms} = 2.76 nm, S_{skew} = 1.70	R_{rms} = 3.65 nm, S_{skew} = 1.29
0.3 M	R_{rms} = 2.04 nm, S_{skew} = 1.52	R_{rms} = 3.12 nm, S_{skew} = 0.99	R_{rms} = 5.84nm, S_{skew} = -0.91
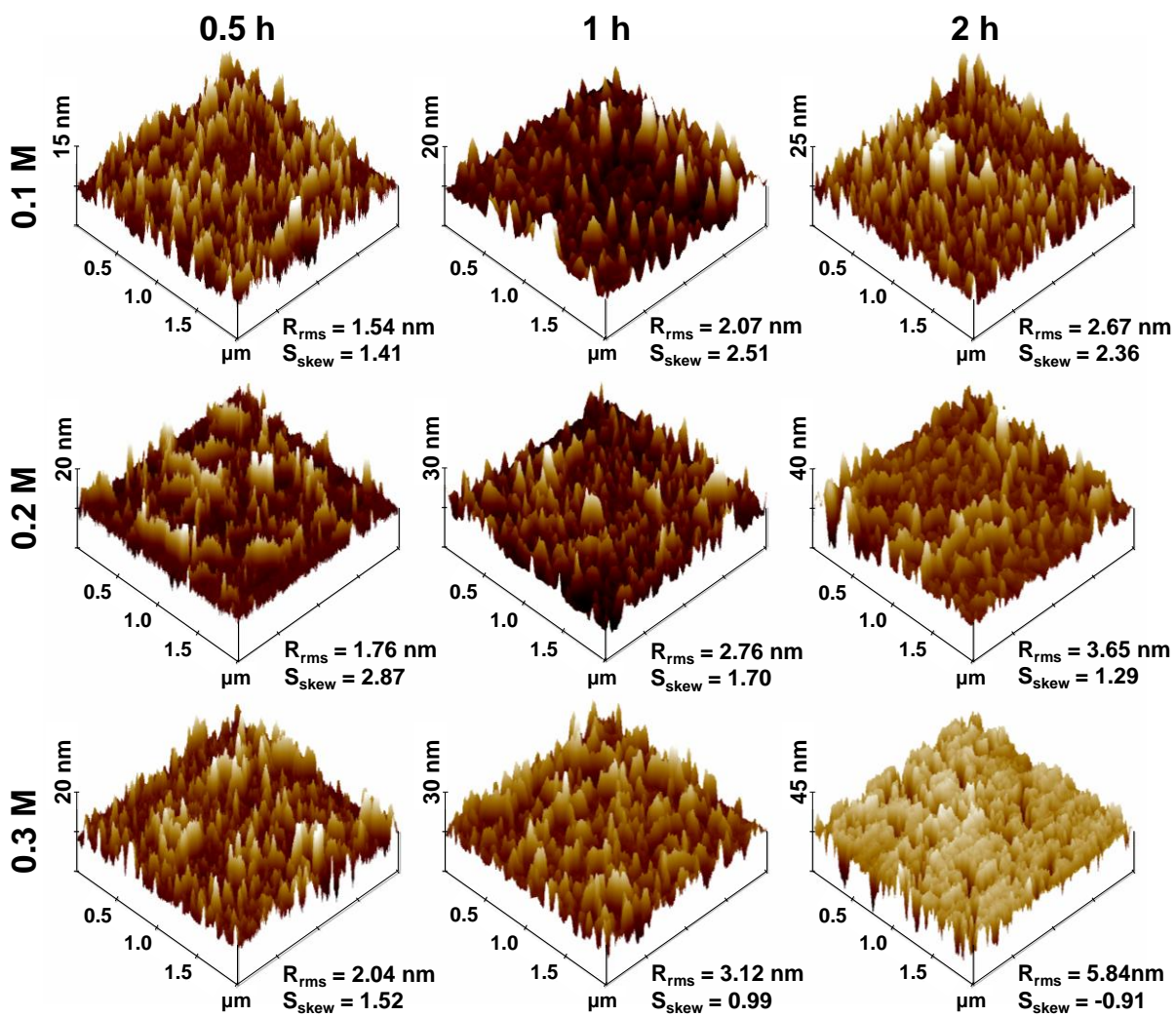
Figure 3-4b. Tapping mode AFM images of SNS surfaces graft polymerized for $0.5 - 2$ h for PAAm-PA-Si at $[M]_0 = 0.1 - 0.3$ M.

Table 3-2. PA-Si and SNS-PA-Si surface properties.

Surface	$[M]_0$	Time (h)	R_{rms} (nm)	S_{skew} (%)	Avg. Feature Height (nm)	$V (10^5)$ $(nm^3/\mu m^2)^a$	θ_w (°)	θ_d (°)	ΔG_{iw} (mJ/m^2)	γ_s (mJ/m^2)
PA-Si	0	0	0.46	-0.08	1.97	9.72	76.5	35.2	-89.4	45.8
PVP-PA-Si	0.94	0.5	0.55	1.03	2.35	13.5	66.5	41.4	-101.4	47.8
	0.94	1.0	0.85	0.33	2.75	17.5	61.6	39.1	-107.0	51.1
	0.94	2.0	1.27	3.39	4.04	30.4	59.5	38.1	-109.3	52.5
	1.40	0.5	0.63	0.81	2.32	13.2	62.2	37.4	-106.3	51.3
	1.40	1.0	1.04	0.87	3.12	21.2	61.0	34.2	-107.6	52.9
	1.40	2.0	2.62	1.98	6.90	59.0	57.8	32.5	-111.1	55.1
	1.87	0.5	0.83	1.61	3.04	20.4	61.7	37.0	-106.9	51.7
	1.87	1.0	1.69	1.77	4.55	35.5	59.2	33.9	-109.6	53.9
	1.87	2.0	2.89	2.31	8.30	73.0	57.6	31.8	-111.3	55.4
PAAm-PA-Si	0.10	0.5	1.54	1.41	4.27	32.7	62.4	49.7	-106.1	47.2
	0.10	1.0	2.07	2.51	4.34	33.4	56.2	45.2	-112.8	52.2
	0.10	2.0	2.67	2.36	8.26	72.6	51.8	42.7	-117.3	55.5
	0.20	0.5	1.76	2.87	4.27	32.7	58.6	48.1	-110.3	49.9
	0.20	1.0	2.76	1.70	6.06	50.6	51.3	45.1	-117.8	55.1
	0.20	2.0	3.65	1.29	16.2	152	48.4	39.5	-120.6	58.4
	0.30	0.5	2.04	1.52	6.63	56.3	57.4	46.6	-111.1	51.0
	0.30	1.0	3.12	0.99	11.2	102	50.1	43.6	-119.0	56.2
	0.30	2.0	5.84	-0.91	29.3	283	46.5	35.6	-122.4	60.5

[a] exposed polymer volume as determined by AFM

Skewness (S_{skew}) of the feature height distribution (FHD) for the grafted polymer surfaces was in the range of -0.91 – 3.4 (Table 3-2). Additionally, there was an observed shift in the FHD from about 0 – 13 nm toward 0 – 44 nm size chains (accompanied by a shift in R_{rms} surface roughness from 0.55 to 5.8 nm) with increasing grafting time and initial monomer concentration as shown in Figure 3-6. The mean surface height was in the range of 2.3 – 8.3 nm and 4.3 – 29 nm for the PVP and PAAm grafted surfaces, respectively. It is expected that, for free radical polymerization, the occurrence of thermal initiation in solution (i.e., formation of monomer radicals) may lead to formation of homopolymer chains that may subsequently graft to active surface sites or growing active surface chains. As a consequence, a bimodal surface

feature height distribution can result as observed in the FHDs for the PAAm surfaces that were synthesized at high initial monomer concentration ($[M]_0 = 0.3$ M) and increased grafting time (1 – 2 h) (Figure 3-6f).
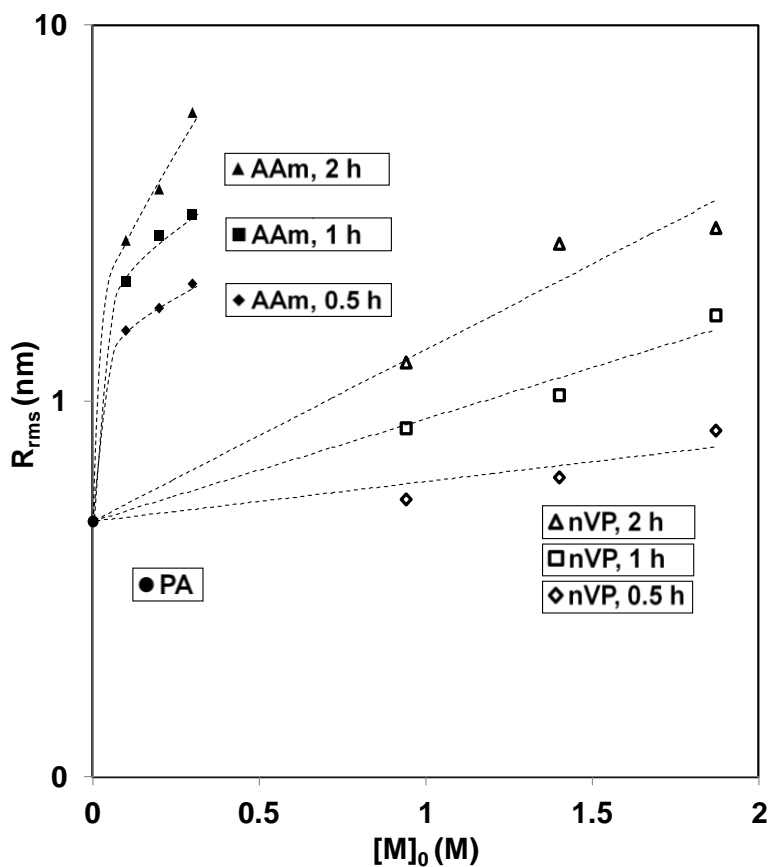
Figure 3-5. Variation of surface roughness for PVP-PA-Si and PAAm-PA-Si surfaces with initial monomer concentrations at $[M]_0 = 0.94 - 1.87$ M and $[M]_0 = 0.1 - 0.3$ M, respectively (over a graft polymerization period in the range of 0.5 – 2 h).
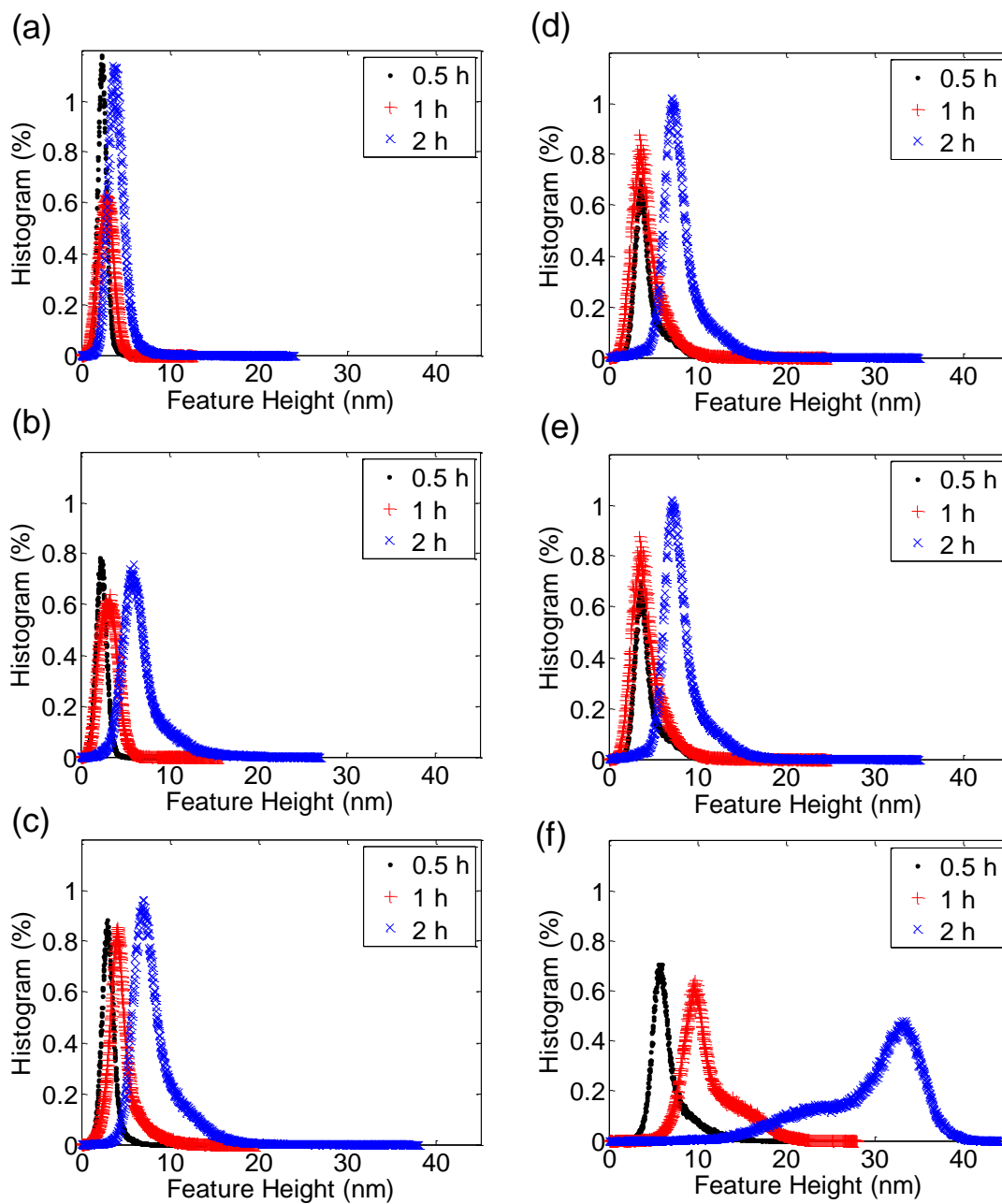
Figure 3-6. AFM feature height distributions for PVP-PA-Si surfaces at initial monomer concentrations of (a) 0.94 M, (b) 1.40 M, and (c) 1.87 M, and for PAAm-PA-Si at (d) 0.1 M, (e) 0.2 M, and (f) 0.3 M, for different reaction periods as indicated in the legend.

Inspection of the surface FHDs for the SNS-PA-Si surfaces reveals that the R_{rms} surface roughness increases with higher average surface feature height (Figure 3-7). Further analysis of the surface FHDs and AFM image cross-section along linear paths, as illustrated in the examples shown in Figure 3-8 (PVP-PA-Si: $[M]_0$ = 1.40 M, 2 h and PAAm-PA-Si: $[M]_0$ = 0.2 M, 2 h), reveal average major peak separation (dictating the geometry of surface "valleys", e.g., between peaks at linear positions of 0.2 μm and 0.45 μm, Figure 3-8c) distances of ~70 − 115 nm and feature heights of 2.3 − 8.3 nm for the PVP-PA-Si surfaces (Table 3-2). The above PVP surfaces are denser than the PAAm-PA-Si surfaces which have major peak separation distances of ~140 − 220 nm (Figure 3-8) and feature heights in the range of 4.3 − 29 nm (Table 3-2). It noted, when comparing the PVP and PAAm grafted surfaces, that greater peak separation distance correlates with higher feature heights and the relatively broader FHD, which is consistent with the observation of previous studies employing APPIGP with vinyl monomers [217].
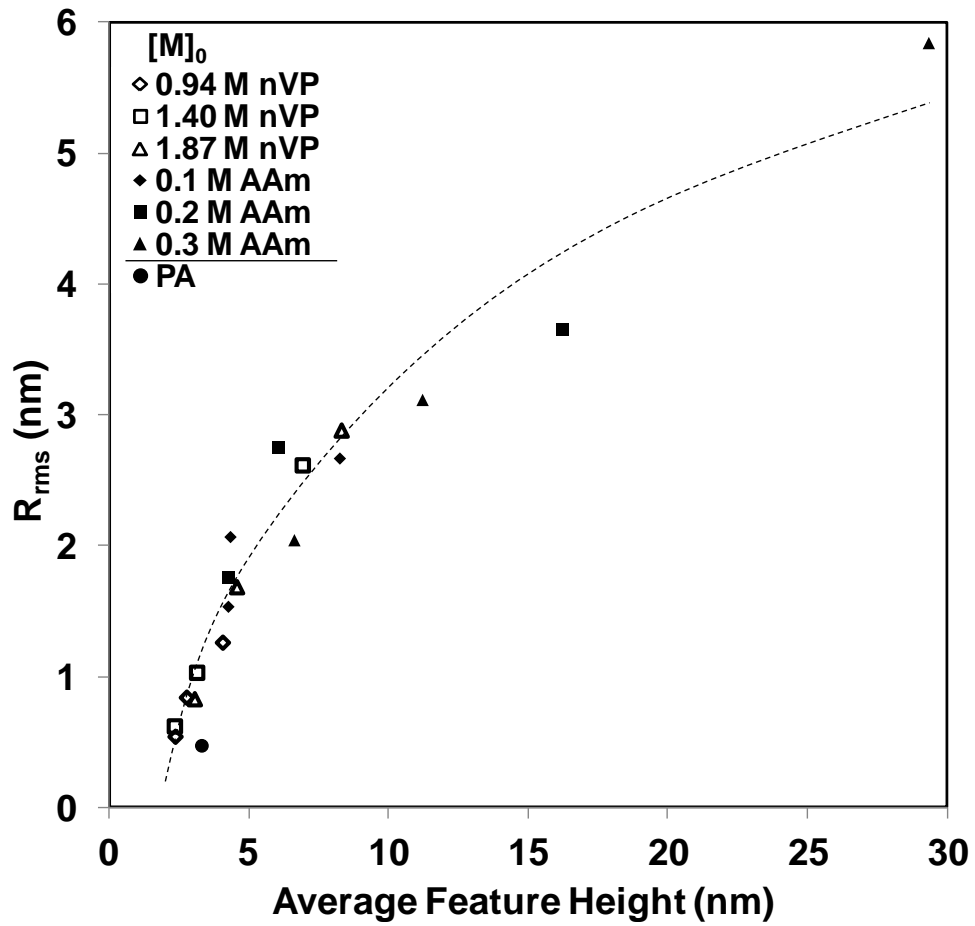
Figure 3-7. Correlation of polymer feature height with surface roughness for the PA-Si surface and SNS-PA-Si surfaces graft polymerized with nVP and AAm (surfaces synthesized over a graft polymerization period in the range of 0.5 – 2 h).
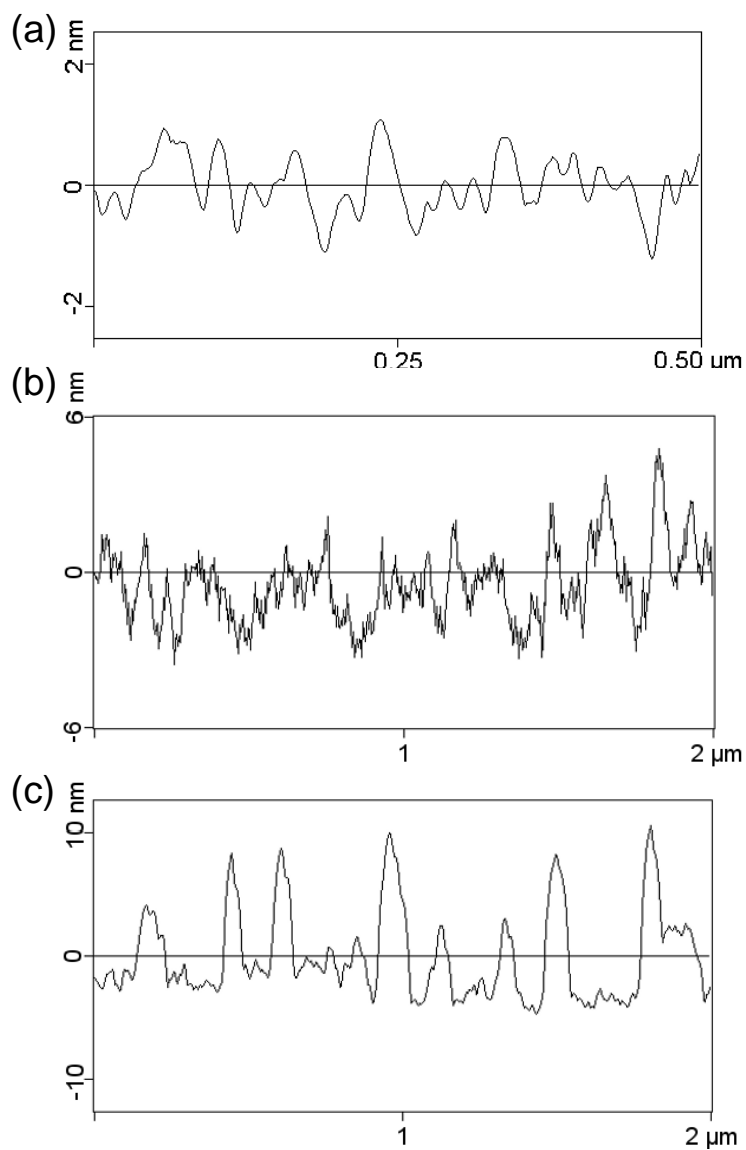
Figure 3-8. Surface feature height profiles for (a) PA-Si, (b) PVP-PA-Si (1.40 M, 2 h), and (c) PAAm-PA-Si (0.2 M, 2 h) surfaces.

3.3.2 Surface Wettability

The water contact angle decreased with increased graft polymerization time (of the AAm and nVP monomers) and increased initial monomer concentration (up to a maximum), as previous

studies have shown [80, 218-219]. For PVP and PAAm brush layers, the water contact angle deceased by 13 – 25% (76.5º to 66.5 – 57.6º) and 18 – 39% (76.5º to 62.4 – 46.5º), respectively, for initial monomer concentrations in the ranges of 0.94 – 1.87 M nVP and 0.1 – 0.3 M AAm over a graft polymerization period in the range of 0.5 – 2 hours at 70ºC (Figure 3-9).
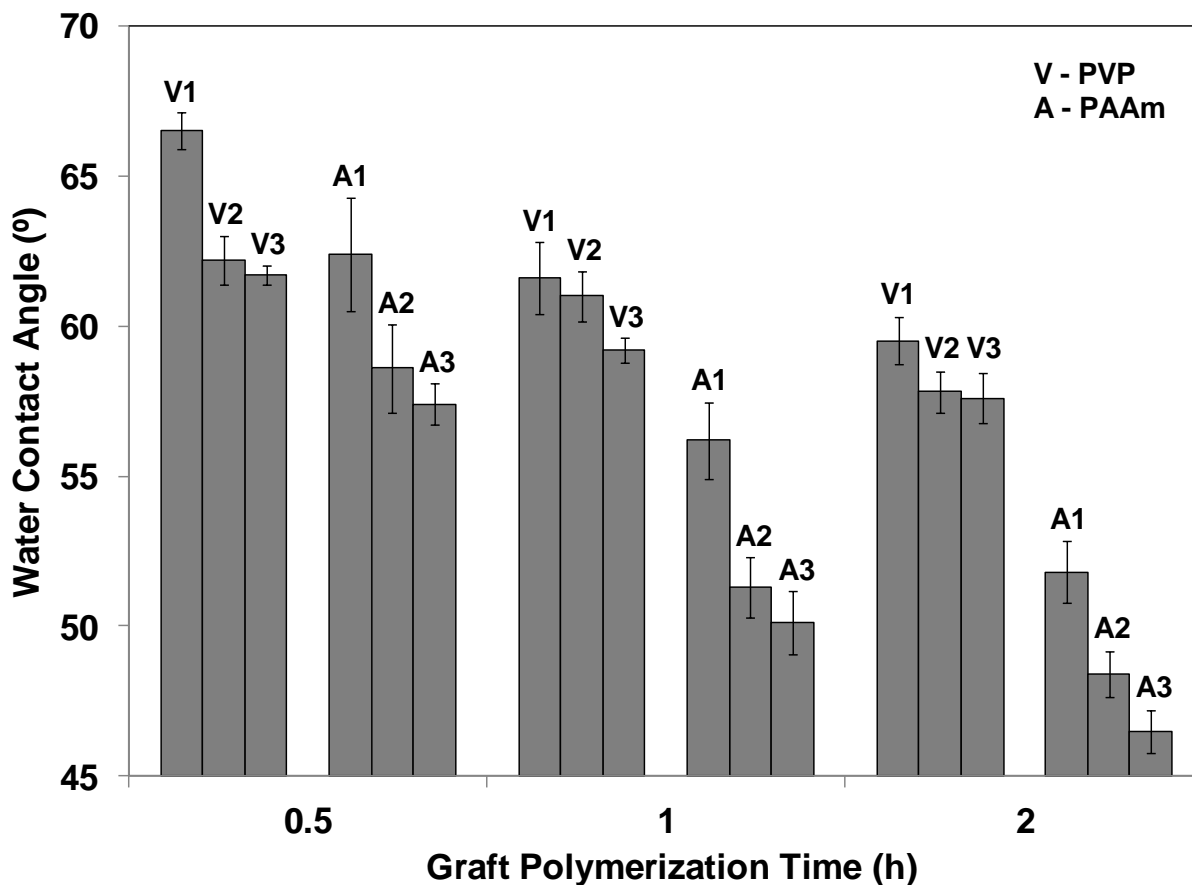
Figure 3-9. Water contact angles for SNS-PA-Si substrates structured with vinylpyrrolidone (nVP) and acrylamide (AAm). V1, V2, and V3 are for PVP-PA-Si surfaces synthesized at initial monomer concentrations of 0.94 M, 1.40 M, and 1.87 M, respectively, and A1, A2, and A3 are for PAAm-PA-Si surfaces synthesized at initial monomer concentrations of 0.1 M, 0.2 M, and 0.3 M, respectively. Note: water contact angle for the PA-Si surface = 76º.

While water contact angle provides an indication of relative surface hydrophilicity, the free energy of hydration (ΔG_{iw}) [211] enables a quantitative demarcation between hydrophilicity and hydrophobicity. Accordingly, when considering the free energy of hydration (Figure 3-10 and Table 3-2), only the PAAm brush layer surfaces, synthesized at reaction time $\geq$2 h or at initial monomer concentrations of 0.2 – 0.3 M AAm at reaction time $\geq$1 h, can be considered to be truly hydrophilic (i.e., ΔG_{iw} < -113 mJ/m^2, Section 3.2.3). Overall, in terms of free energy of hydration, the relative hydrophilicity of the PA-Si surface (ΔG_{iw}= -89 mJ/m^2) was increased via APPIGP by 24% and 37% for the PVP-PA-Si and PAAm-PA-Si surfaces, respectively.

Previous studies have reported that increase in surface roughness amplifies hydrophilicity (i.e., decreases water contact angle) of intrinsically hydrophilic surfaces [220-221]. It has been argued [221] that, for an intrinsically hydrophilic surface, the wetted area has a lower surface energy than the area around it; therefore, a water drop tends to spread spontaneously causing a net energy decrease. Also, for the hydrophilic brush layers, increased surface roughness provides greater available surface area that leads to greater net surface energy decrease which further induces water drop spreading, thus leading to greater wetting. Indeed, as shown in Figure 3-11, the free energy of hydration decreases with increased roughness, although the correlations for the PVP and PAAm surfaces are somewhat different owing to the different surface chemistries of these polymers. For example, for the PVP and PAAm surfaces ΔG_{iw} decreases by 10% and 15%, respectively, for a corresponding increase of surface roughness by 2.3 nm and 4.3 nm.
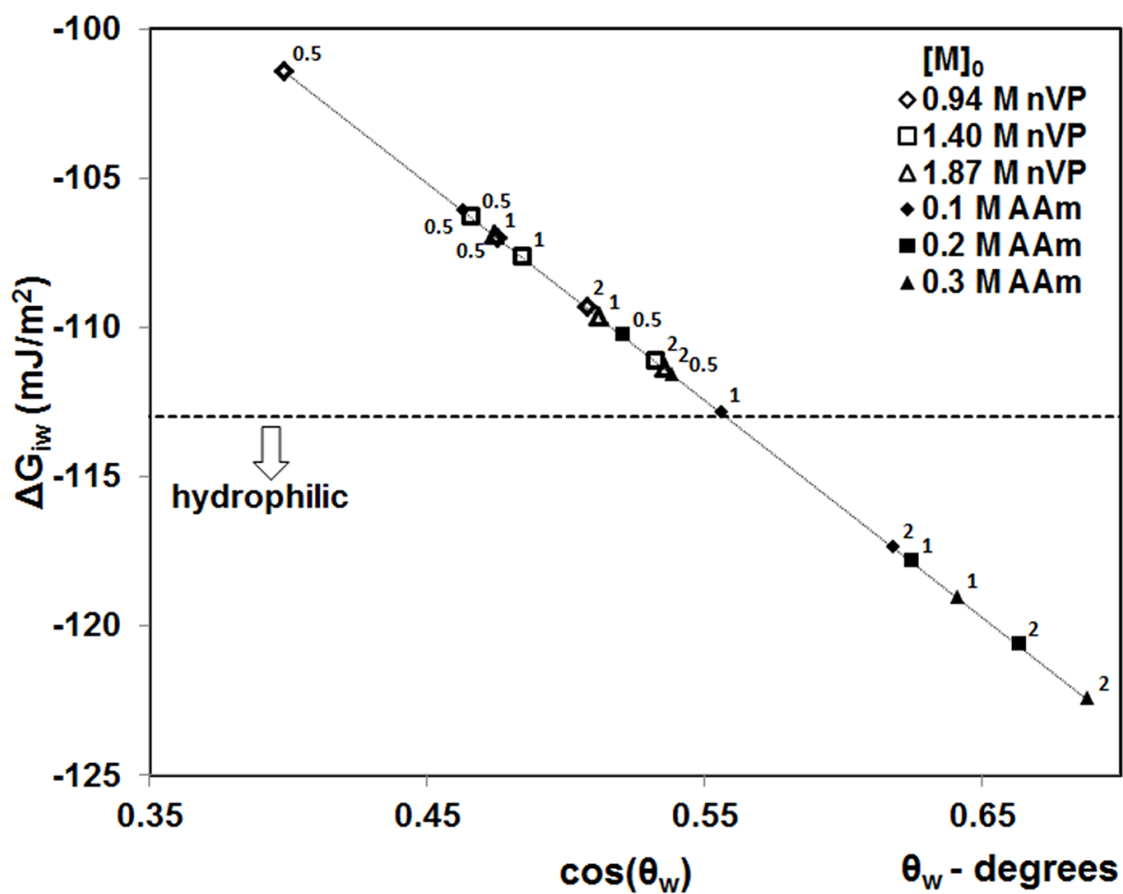
Figure 3-10. Relative hydrophilicity of PVP and PAAm polymer brush layers on a PA-Si surface. Note: free energy of hydration (ΔG_{iw}) for the PA-Si surface = -89 mJ/m^2 (i.e., $\cos(\theta_w)$ = 0.23). Also, the numbers next to the data points represent the graft polymerization time in hours.
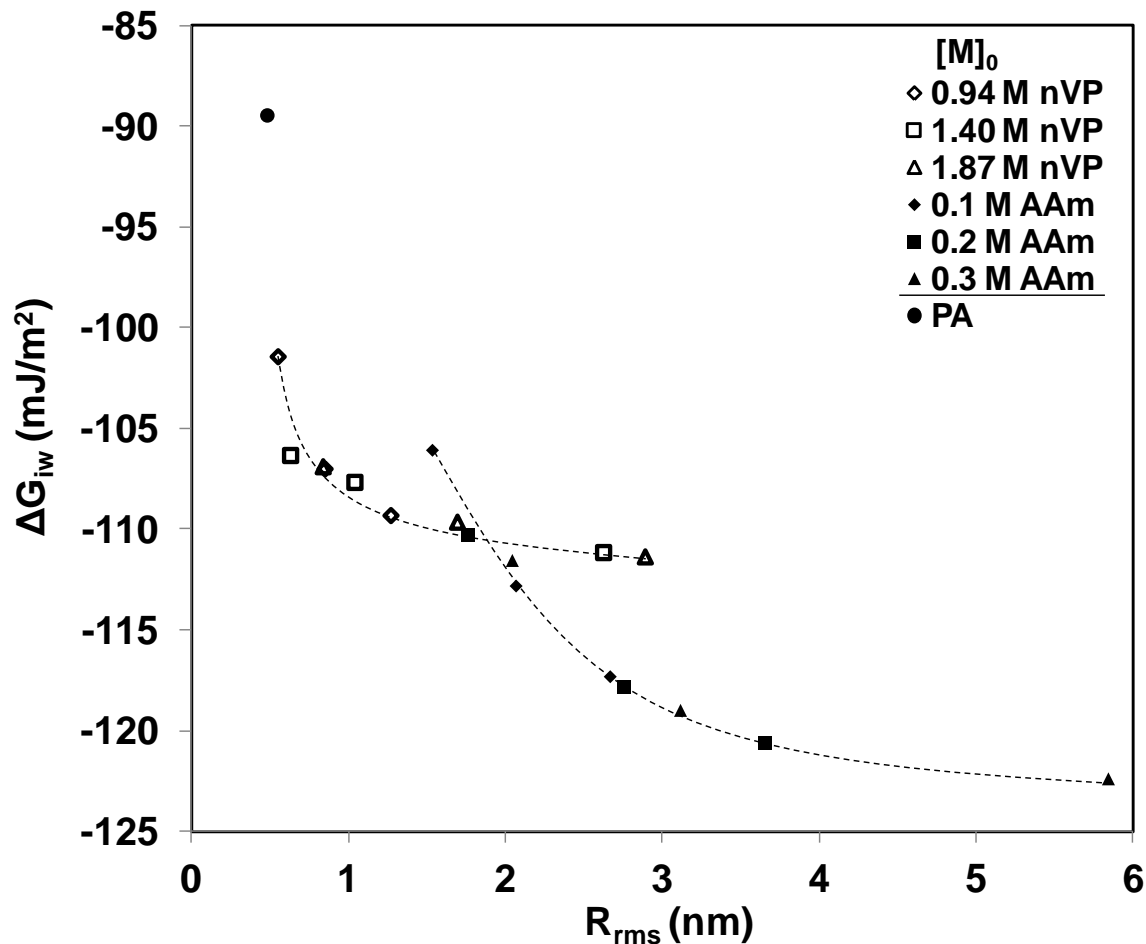
Figure 3-11. Free energy of hydration (ΔG_{iw}) and surface roughness (R_{rms}) of the PA-Si surface and SNS-PA-Si surfaces graft polymerized with vinylpyrrolidone and acrylamide (surfaces synthesized over a graft polymerization period in the range of $0.5 - 2$ h).

Surface hydrophilicity for the hydrophilic brush layer surfaces, relative to the polyamide surface, can also be assessed by comparing the relative magnitudes of the polar and dispersive components of the solid surface energy (Section 3.2.3). As shown in Figure 3-12, the polar component of the solid surface energy increases significantly, by $2.2 - 2.9$ times and $3.1 - 4.5$ times, for the PVP-PA-Si and PAAm-PA-Si substrates, respectively, relative to the polyamide

surface (γ_s^p = 4.2 mJ/m^2). In comparison, for the PA-Si surface the dispersive component was the overwhelming contributor to the total solid surface energy (91%), with the polar component contributing only 9%. It is interesting to note that the polar component of solid surface energy for the hydrophilic brush layers are qualitatively consistent with the order of the absolute difference between the solubility parameters of water (30.1 MPa$^{1/2}$ [222]) and the PAAm (28.0 MPa$^{1/2}$ [223]) and PVP (25.6 MPa$^{1/2}$ [223]) polymer brush layer. Specifically, the observation of $(\gamma_s^p)_{PAAm}$ > $(\gamma_s^p)_{PVP}$ (Figure 3-12) is consistent with the fact that $|\delta_w - \delta_{PAAm}|$ < $|\delta_w - \delta_{PVP}|$ which suggests greater affinity between water and PAAm as opposed to PVP. The above also implies greater water sorption by the polymer brush layer with increased polymer surface volume. Indeed, for both the PVP and PAAm polymer brush layers, the free energy of hydration decreases with increased polymer volume (Table 3-2). It is also apparent that owing to the greater water-PAAm affinity and generally higher polymer volume attained for the this polymer, relative to the PVP-PA-Si substrate, the PAAm brush layer surface also exhibited greater wettability as quantified by the free energy of hydration (Table 3-2).

The above results clearly demonstrate that wettability of hydrophilic polymeric surfaces, as quantified by the free energy of hydration, is impacted by both surface structure (in terms of surface roughness and polymer volume), as well as by the polymer-water affinity as quantified by the solubility parameters. Swelling of the brush layers in aqueous solutions could be affected by both ionic-strength and pH, albeit impact of the latter is likely to be less pronounced given that PAAm [224] and PVP [225] are non-ionic. Overall, the results illustrate that measurable control over surface wettability is feasible through adjustment of surface graft polymerization conditions (e.g., surface activation, monomer type and initial concentration in solution, temperature, and graft polymerization time). Clearly, surface structuring at the nanoscale with

hydrophilic polymers can profoundly impact surface wettability, and past work has shown such brush layers to be effective in reducing the fouling propensity of ultrafiltration [133] and RO membranes [12].
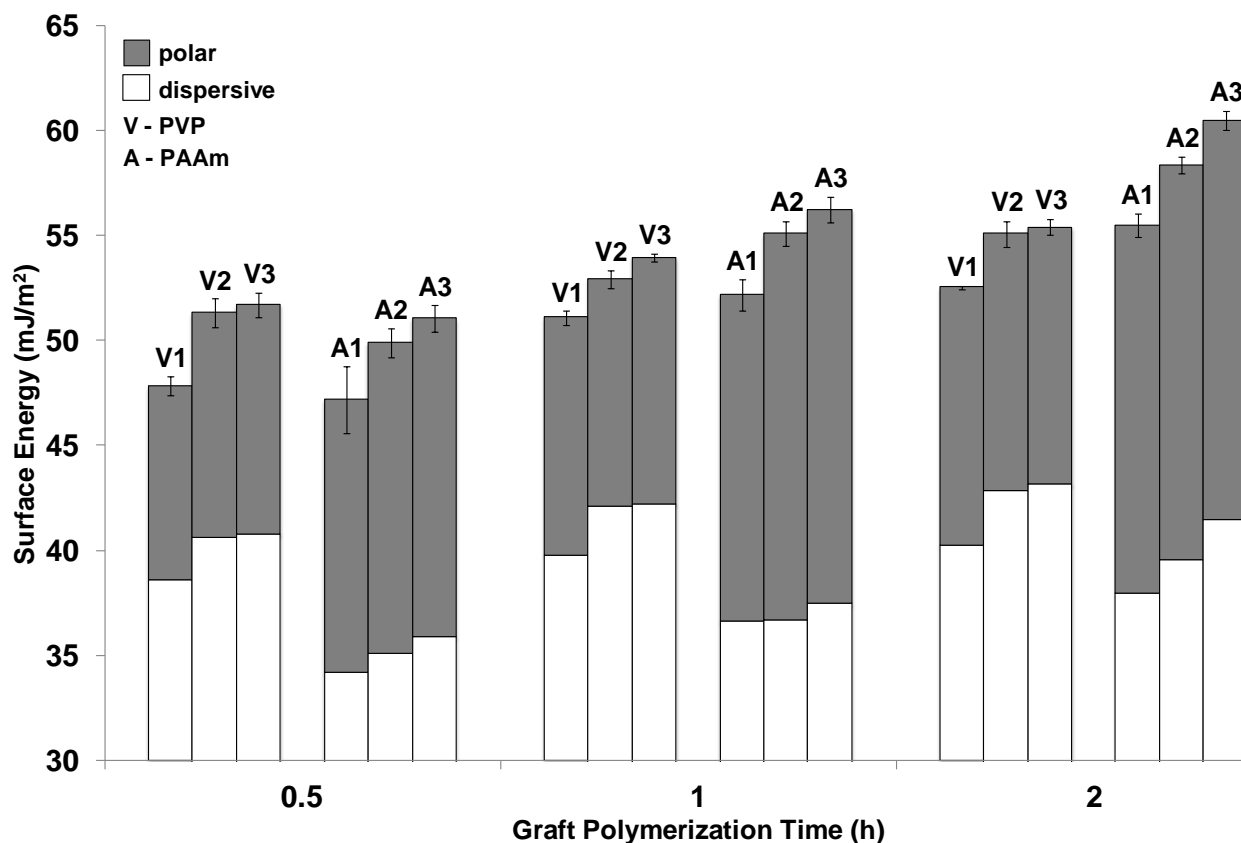
Figure 3-12. Solid surface energy (γ_s) of PA-Si surfaces structured with terminally anchored brush layers of PVP and PAAm. V1, V2, and V3 are for PVP-PA-Si surfaces synthesized at initial monomer concentrations of 0.94 M, 1.40 M, and 1.87 M, respectively, and A1, A2, and A3 are for PAAm-PA-Si surfaces synthesized at initial monomer concentrations of 0.1 M, 0.2 M, and 0.3 M, respectively. Note: solid surface energy, γ_s, for the PA-Si surface = 46 mJ/m^2, where $\gamma_s^p = 4.2$ mJ/m^2 and $\gamma_s^d = 42$ mJ/m^2.

3.4   Conclusions

Surface wettability of hydrophilic polymer brush layers was evaluated with a focus on elucidating the impact of surface topography, at the nanoscale, and polymer-water affinity. Hydrophilic polyvinylpyrrolidone (PVP) and polyacrylamide (PAAm) brush layers were synthesized onto a polyamide surface, via graft polymerization induced by polyamide (PA) surface activation with atmospheric pressure plasma. PAAm brush layers were found to be more effective than PVP brush layers in being able to increase surface hydrophilicity as quantified via contact angle, free energy of hydration, and surface energy. Hydrophilicity (or wettability) of the PA substrate, as quantified by the free energy of hydration, decreased by $13 - 24\%$ and $19 - 37\%$ for the PVP and PAAm brush layers relative to the PA substrate. Surface hydrophilicity increased with both increasing surface roughness and volume of polymer in the brush layer, the latter showing a strong correlation (i.e., increased polymer volume with increased surface roughness). Over the range of root-mean-square surface roughness of $0.55 - 2.89$ nm and $1.54 - 5.84$ nm, for the PVP and PAAm brush layers, respectively, the free energy of hydration correspondingly decreased by 10% and 15%. The present study suggests that the physicochemical characteristics (e.g., surface roughness and wettability) of the polymer grafted layer can be tailor-designed by adjusting surface topography and surface chemistry, which are controlled by polymerization reaction conditions, to attain a specific level of surface wettability. It is envisioned that structuring of various surfaces with hydrophilic brush layers could be of benefit in improving surface wettability in biomedical applications, lubrication, as well in reducing membrane fouling in water treatment applications.

Chapter 4.   Hydrophilicity of Tethered Polymers Synthesized by Atmospheric Pressure Plasma Induced Graft Polymerization onto a Polyamide Surface

4.1   Introduction

Atmospheric pressure plasma (APP) induced graft polymerization is a useful approach to surface nanostructure (SNS) with a polymer brush layer in order to alter surface properties of inorganic and organic materials [10]. Surface activation and modification via APP in ambient air has been typically accomplished by arcs [172], plasma torch [172], corona discharge [118], dielectric barrier discharge (DBD) [94] and impinging plasma stream [12, 80] (Chapter 2, Figure 2-5). Arcs and plasma torch sources are not suitable for treatment of polymer substrates due to high electron temperature (>3000ºC) which can result in significant etching of the organic substrate [172]. Discharge of atmospheric pressure plasma as an impinging jet (i.e., APPJ) is preferable to corona and DBD sources due to the relatively high density, homogenous distribution of plasma discharge, and its ability to be conveniently utilized over complex geometries of varying sizes (Chapter 2, Section 2.4.4). It is noted that previous studies have argued that the surface density of active sites (e.g., peroxide) formed via APPJ in ambient air for subsequent graft polymerization is impacted by the plasma source gas, surface exposure time, and the radio frequency (RF) power of the plasma generator [80].

Once a surface has been treated by plasma, surface structuring with a polymer brush layer can be accomplished via graft polymerization by exposing the surface to a solution of a suitable vinyl monomer. The rate of graft polymerization for the sequential addition of vinyl monomers from activated surface sites (R_p) is given in Chapter 2, Equation (2-1). Termination of surface chains can occur by chain transfer between a growing grafted chain with a monomer, and

combination and disproportionation between a growing homopolymer chain and a growing grafted chain [127]

$$R_t = k_{tr}[S\cdot][M] + k_t[S\cdot][M\cdot] \tag{4-1}$$

in which R_t is the rate of surface chain termination, k_{tr} and k_t are the overall chain transfer (with monomer) and termination rate constants for the tethered surface chains, and $[M]$, $[S\cdot]$, and $[M\cdot]$ are the concentrations of the monomer in solution, and surface-bound and homopolymer growing chains. As the concentrations of monomer (in solution) and surface active sites increase so do the rates of both graft polymerization ("grafting from") and polymer grafting ("grafting to"), consistent with reported experimental data provided by previous studies [11, 75, 102, 127]. Therefore, one would expect that the resulting tethered layer distribution of chain sizes (i.e., polydispersity) [80, 102], and thus roughness and uniformity, would vary depending on the density of surface active sites and the polymerization conditions. Indeed, results of Chapter 3 reveal that both chemistry and topography of tethered polymer structured substrate surfaces impact surface hydrophilicity/hydrophobicity. Accordingly, it is critical to optimize the plasma surface treatment [80] in conjunction with the conditions for graft polymerization in order to achieve the desired surface wettability.

This chapter presents an investigation of the impact of APPJ surface activation and graft polymerization conditions on surface wettability of a polyamide substrate afforded by a tethered layer of hydrophilic polymers. Specifically, comparison is provided regarding the effectiveness of He and H_2 plasma for PA surface activation utilizing the free energy of hydration as a metric to assess the level of surface hydrophilicity achieved for different SNS conditions. Three different vinyl monomers, acrylic acid, 2-hydroxyethyl methacrylate, and vinylsulfonic acid,

were evaluated with respect to the achievable level of tunable PA surface hydrophilicity via SNS to synthesize surfaces of tethered chains of poly(acrylic acid) (PAA), poly(2-hydroxyethyl methacrylate) (PHEMA), and poly(vinylsulfonic acid) (PVSA). The above three polymers were selected given their reported potential as effective anti-foulant surface modifiers [226-228]. Surface topography (e.g., roughness, number density of major surface polymer features, and separation) and tethered polymer layer thickness were quantified for the above polymer surfaces and evaluated with respect to the free energy of hydration and its polar and dispersive surface energy components.

4.2 Experimental

4.2.1 Materials

The silicon substrates served as smooth supports for the PA surfaces were <100> oriented, boron doped, p-type silicon wafers of 100±0.5 mm in diameter, 500±50 μm thickness and resistivity range of 1 – 100 Ω cm (waf-001, Semiconductor Solutions LLC, Alhambra, CA). Polyamide (PA) surfaces were synthesized onto silicon wafer supports using materials described in Chapter 3, Section 3.2.1. Aqueous monomer solutions of acrylic acid (AA, 99%), 2-hydroxyethyl methacrylate (HEMA, ≥99%), and vinylsulfonic acid, sodium salt solution (VSA, 25 wt. % in H_2O) (Aldrich, St. Louis, MO) were used for graft polymerization. Aqueous solutions of AA, HEMA, and VSA were prepared using ultra-pure deionized water (resistivity = ~15 MΩ cm), produced via filtering distilled water through a Milli-Q filtration system (Millipore Corp., San Jose, CA). Monomer solutions were degassed described in Chapter 3, Section 3.2.1. Atmospheric pressure plasma was generated using ultra high purity hydrogen (99.999%, Air

Liquide, Los Angeles, CA) and helium (99.999%, Airgas, Los Angeles, CA) gases. Oxygen gas (99%, Airgas, Los Angeles, CA) was also used for surface treatment.

4.2.2 Synthesis of Hydrophilic Surface Nanostructured Polymer - Polyamide Surfaces

Surface nanostructured-polyamide-silicon (SNS-PA-Si) surfaces were prepared via a sequential process consisting of: (1) polyamide surface preparation, (2) plasma surface activation, and (3) graft polymerization. In this chapter, the polyamide surface (PA-Si) was synthesized, as described in Chapter 3, Section 3.2.2, without spinning at 3000 rpm for 30 s after interfacial polymerization. The PA-Si surface was relatively smooth (root-mean-square surface roughness below ~0.5 nm; Figure 4-1) which allowed quantification of surface topography of the graft polymerized PA surface (Section 4.2.3.2).
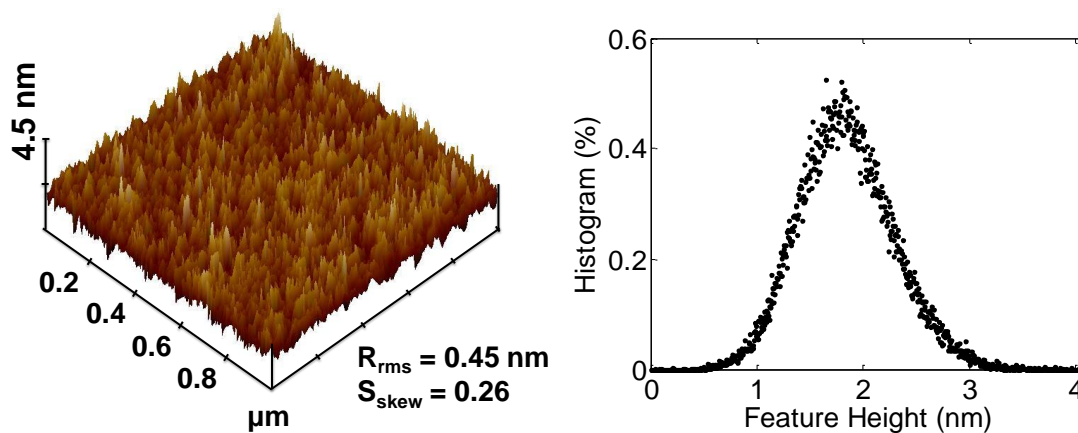
Figure 4-1. AFM image and corresponding feature height distribution for the PA-Si surface.

In the second process step, the PA-Si surface was exposed to an APPJ generated using hydrogen or helium for a period of ~10 s. This treatment period was selected based on preliminary evaluation of treatment effectiveness for exposure times over the range of 5 – 20 s.

The plasma source system, consisting of a Surfx Atomflo™ 300 Series (Surfx Technologies, Redondo Beach, CA) and a custom plasma applicator is described elsewhere [80, 172]; explicit operational details are given in Appendix C.2. Hydrogen APP was generated using a mixture of gases of 1.2 vol% hydrogen in helium at power of 50 W which was determined to be optimal as assessed based on water contact angle measurements (Figure 4-2a). Helium APP was generated with only helium gas also at 50 W (Figure 4-2b). The PA-Si surface was exposed to a pure oxygen stream (1 − 2 minutes), post plasma treatment, to allow for the formation of surface peroxides [58, 80]. As has been documented in previous work [58], the reduction in water contact angle due to plasma exposure is not permanent and over time the contact angle generally rises (typically first detected at ~15 minutes) back toward the untreated value. Accordingly, for substrate samples designated for assessing the impact of plasma treatment, the water contact angles were measured, at most, within 5 minutes of plasma treatment.

Graft polymerization followed immediately (typically within ~5 − 10 s) after surface activation, whereby the plasma treated substrate was immersed in a 40 mL glass vial containing a degassed aqueous monomer solution. Graft polymerization occurred over a period of 0.5 − 2 hours using either acrylic acid (AA), vinylsulfonic acid (VSA), or 2-hydroxyethyl methacrylate (HEMA) at initial monomer concentrations in the ranges of 0.73 − 2.92 M, 0.09 − 1.81 M, and 0.08 − 1.24 M, respectively, at corresponding temperatures of 70ºC, 60ºC, and 50ºC. The ranges of initial monomer concentrations were selected so as to avoid excessively high solution viscosity due to homopolymerization. Homopolymerization could ensue due to excessive thermal initiation of monomer and chain transfer reactions that would then also lead to termination of growing surface chains [127]. The resulting poly(acrylic acid) (PAA)-PA-Si, poly(2-hydroxyethyl methacrylate) (PHEMA)-PA-Si, or poly(vinylsulfonic acid) (PVSA)-PA-Si

surfaces consisted of a grafted layer of PAA, PHEMA, or PVSA chains that are terminally and covalently bound (i.e., tethered) to the PA surface. The above SNS-PA-Si substrates were washed with DI water and stored in a vacuum chamber until further use.
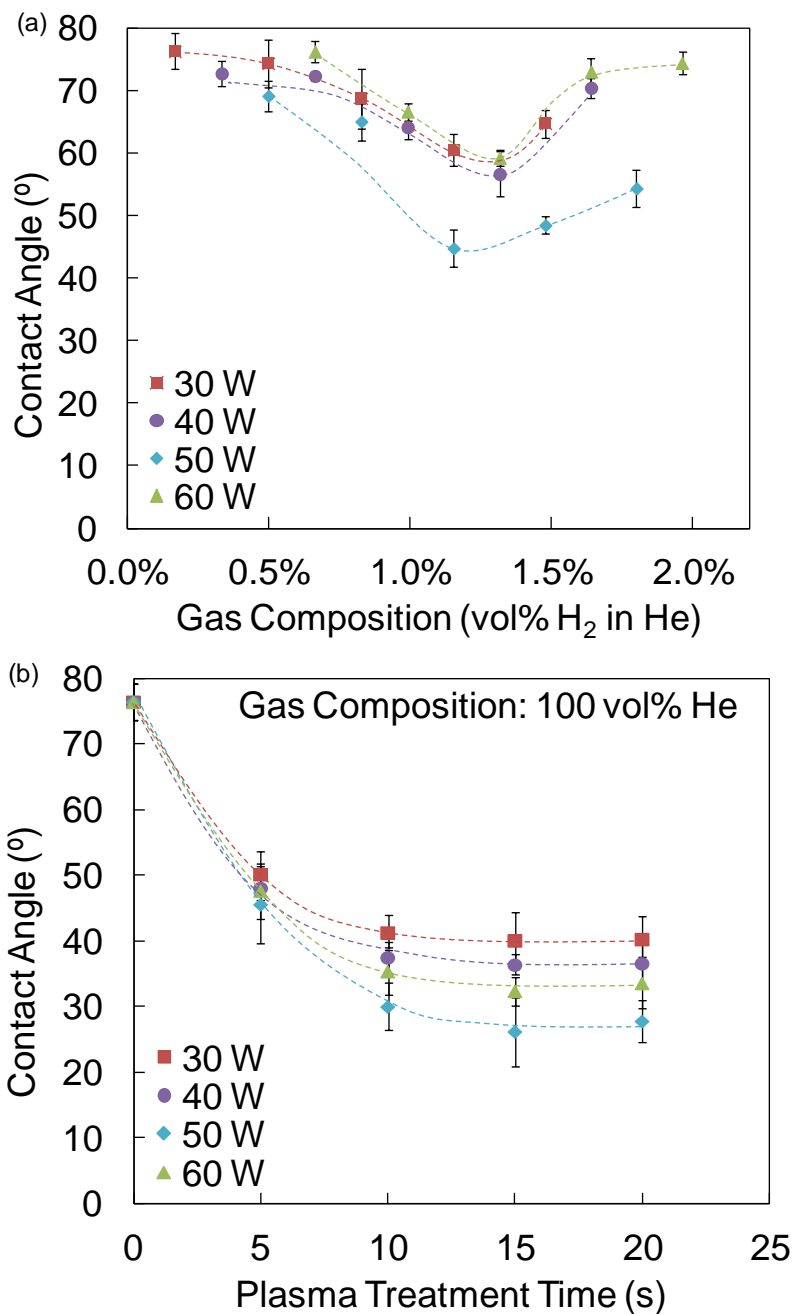
Figure 4-2. Change in contact angle of PA-Si due to surface exposure to (a) H_2/He plasma for 10 s at different levels of RF power, and (b) He plasma at different levels of RF power.

4.2.3 Surface Characterization

4.2.3.1 Surface Chemistry and Thickness

The formation of tethered hydrophilic polymers by surface graft polymerization was confirmed via x-ray photoelectron spectroscopy (XPS) (AXIS Ultra Delay-Line Detector (DLD), Kratos Analytical Ltd, Manchester, UK). XPS was operated with concentric hemispherical analyzers in an ultra-high vacuum chamber ($<1\text{x}10^{-8}$ Torr) while conducting charge neutralization. Excitation was achieved using a monochromatic Al Kα x-ray source (hν = 1486.6 eV). The binding energy scale was referenced to the hydrocarbon C 1s at 284.8 eV for all spectra [229].

The average thickness of the graft polymerized layer was measured in ambient air by ellipsometry (LSE Stokes 7109-C-351A, Gaertner Scientific Corporation, Skokie, IL) using a HeNe laser with a 632.8 nm wavelength and 1 mm beam diameter at an incidence angle of 70º. The grafted polymer layer thickness was calculated as the difference between the average thicknesses before atmospheric pressure plasma induced graft polymerization (i.e., PA-Si surface) and that of the grafted SNS-PA-Si polymer surface. The SNS polymer layer thickness was determined based on an average of 5 – 10 measurements. These thickness measurements represent lower limit estimates, since the tethered hydrophilic polymer chains are expected to swell (i.e., extend away from the surface) when immersed in a good solvent, such as water [22].

4.2.3.2 Surface Topography

Surface topography of both the unmodified PA surface and graft polymerized PA substrate was examined via tapping mode atomic force microscopy (AFM) (Multimode AFM with a

Nanoscope IIIa SPM controller, Digital Instruments, Santa Barbara, CA). The analysis was performed in ambient air using NSC15/noAl silicon cantilevers (MikroMasch USA, San Jose, CA) with a force constant in the range of $20 - 75$ N/m, resonance frequency in the range of $265 - 400$ kHz, probe tip radius of < 10 nm, and full tip cone angle $< 20º$. AFM analysis was conducted at a scan rate of 0.8 Hz and scan size of 2 μm x 2 μm for $3 - 6$ locations on the substrate surface. Replicate scans were performed at 0º and 90º in the same location to verify that the AFM images were free of directional errors. The root mean square (RMS) roughness (R_{rms}) and skewness (S_{skew}) of the surfaces was calculated from the AFM feature height distribution data, given in Chapter 3, Equations (3-1) and (3-2), respectively. Here also, as with ellipsometric measurements, the feature height represents a lower limit since air is a poor solvent for the hydrophilic polymers. The graft polymerized polymer volume, V, was determined by means of volume integration (relative to the underlying PA surface) over the height distribution data of the polymer surface.

The surface number density and average peak-to-peak separation distance for the major polymer surface features were determined by expectation-maximization (EM) image segmentation algorithm from the 2D AFM images [230]. The EM method regards an image as a data clustering scenario and iteratively estimates the maximum log-likelihood of the function (clusters of foreground as major polymer surface features and background as valleys) and finds the clusters resulting in that maximum likelihood. Each pixel is assigned a partial probability of belonging to a cluster at each iteration and final/posterior probability is assigned upon convergence. The convergence threshold for log-likelihood was set to 10^{-4} as validated in the literature [231-232]. The above approach typically identifies the major features, for a given substrate, as those above ~30% of the maximum peak height.

4.2.3.3 Surface Hydrophilicity

Water and diiodomethane contact angle measurements for the modified and unmodified PA surfaces were performed using a Kruss Model DSA 100 (Hamburg, Germany) contact angle measurement system as described in Chapter 3, Section 3.2.3 at 20°C. Hydrophilicity was evaluated with respect to free energy of hydration (ΔG_{iw}) (Chapter 3, Equation (3-3)), and solid surface energy (γ_s) and its polar ($\gamma_s^{\,p}$) and dispersive ($\gamma_s^{\,d}$) contributions (Chapter 3, Equations (3-4) and (3-5)) as described in Chapter 3, Section 3.2.3. In this chapter, the liquid surface tension values (mJ/m^2) (described in Chapter 3, Section 3.2.3) at 20ºC for water and diiodomethane were taken to be $\gamma_L^{\,p} = 51$, $\gamma_L^{\,d} = 21.8$, and $\gamma_L = 72.8$, and $\gamma_L^{\,p} = 0$, $\gamma_L^{\,d} = 50.8$, and $\gamma_L = 50.8$, respectively [211].

Polymer-water affinity (or compatibility) can also be assessed based on the polymer solubility parameters [222, 233]. Accordingly, polymer-water affinity increases as their Euclidean distance in the solubility parameter space decreases [222],

$$Ra = \sqrt{4\left(\delta_{d,i} - \delta_{d,w}\right)^2 + \left(\delta_{p,i} - \delta_{p,w}\right)^2 + \left(\delta_{h,i} - \delta_{h,w}\right)^2}.$$ In the above, the solubility parameter components that represent "non-polar" (i.e., dispersion), permanent dipole-permanent dipole (i.e., polar), and hydrogen bonding interactions are designated by $\delta_{d,i}$, $\delta_{p,i}$, $\delta_{h,i}$, respectively, for the polymer and correspondingly as $\delta_{d,w}$, $\delta_{p,w}$, and $\delta_{h,w}$ for water [222]. The polymer solubility parameter components were calculated by a group contribution method [233-234] (Table 4-1) resulting in Ra values of 8.8 MPa$^{1/2}$ and 11.2 MPa$^{1/2}$ for PAA and PHEMA, respectively, suggesting that a SNS surface of the former polymer would be expected to be more hydrophilic. It is noted that the group contributions were not available for PVSA and thus comparisons with PHEMA and PAA were on the basis of experimental determination of free energy of hydration.

Table 4-1. Solubility parameter values (MPa$^{1/2}$) of water and selected polymers.

	δ_d	δ_p	δ_h	Ra
Water	18.1	17.1	16.9	-
PAA	20.3	9.7	15.2	8.8
PHEMA	21.7	8.6	18.3	11.2

4.3 Results and Discussion

4.3.1 Polyamide Surface Activation via Atmospheric Pressure Plasma Treatment

Previous studies have shown that atmospheric plasma treatment of inorganic and polymeric surfaces can reduce the water contact angle which was attributed to the increased presence of surface hydrophilic groups such as peroxides [58, 80]. Accordingly, the effectiveness of plasma source gas on PA surface activation can be assessed via the increase in surface hydrophilicity [58] as quantified by the water contact angle change (Section 4.2.3.3). Indeed, as shown in Figure 4-3, after 10 s of exposure to H_2, He and O_2 based plasmas (Section 4.2.2), the water contact angle for the polyamide surface (76.5±0.7°) decreased by 41%, 61%, and 82%, respectively, indicating increased surface hydrophilicity. Contact angle decrease due to exposure to H_2 and He plasmas tapered off at about at $10 - 12$ s plasma treatment time, whereas the water contact angle was reduced to ≲5° (i.e., approaching complete wetting) after ~20 s of exposure to O_2 plasma. Although surface exposure to oxygen plasma resulted in the greatest water contact angle reduction, the PA surface thickness (as measured by ellipsometry) was reduced by up to ~9% after only 5 s of exposure to this plasma. This reduction of polymer surface layer thickness due to plasma etching is detrimental to applications of such modified PA surfaces. For example, PA surface etching can result in loss of integrity of PA based membranes leading to suboptimal

or unacceptable membrane performance (e.g., in terms of reduced solute rejection). Given the above concern, surface activation with H_2 or He plasmas should be preferable; thus, these plasmas were subsequently selected for evaluating their suitability for effective PA surface activation necessary for surface graft polymerization (Section 4.3.2). Comparison of He versus H_2 plasma activation was carried out for 10 s treatment time, since longer exposure times yielded marginal additional reduction ($<4°$) in water contact angle (i.e., hydrophilicity increase) for these plasmas (Figure 4-3).
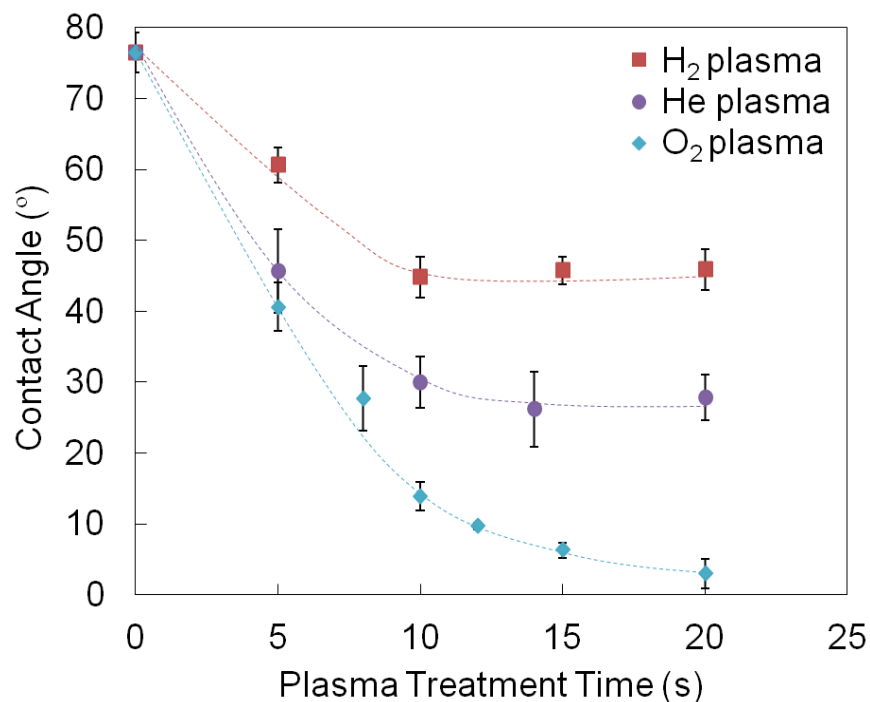
Figure 4-3. Change in water contact angle of PA-Si surface after $5 - 20$ s exposure to H_2, He, and O_2 atmospheric pressure plasmas.

4.3.2   Surface Characterization of Polymer Brush Layer

4.3.2.1   XPS Analysis

SNS-PA-Si surfaces characterized by XPS indicate a shift in C, O, and N composition (compared to the native PA-Si surface) which was expected upon graft polymerization (Table 4-2). As illustrated for the PAA surface prepared at $[M]_0$ = 2.92 M, 2 h reaction time at 70ºC, there was a 78% increase in O atom abundance compared to the native PA-Si surface; this result is consistent with increased oxygen composition for PAA (40.0 At %) compared to PA (12.5 – 19.0 At % [235]). Additionally, the O/N ratio shift from 1.6 to 7.9 and 7.8 for the PAA surfaces, activated with He and H_2 APPs, respectively, is indicative of the presence of PAA (which does not contain nitrogen) on the PA surface (where the PA chains have a nitrogen containing backbone). The presence of PVSA on the PA-Si surface was confirmed, as illustrated for graft polymerization at $[M]_0$ = 1.81 M, 2 h, 60ºC, by the existence of sodium (~1 At %) and sulfur (1.6 – 2.5 At %) which are located on the PVSA side chains. Furthermore, the O/N ratio increase, from 1.6 to 2.7 and 2.9, for the surfaces prepared via He and H_2 plasma activation, respectively, is also indicative of the presence of PVSA (which does not contain nitrogen) on the PA-Si surface. Confirmation of the existence of PHEMA chains on the PA surface (Table 4-2) is shown in the example of surface graft polymerization at $[M]_0$ = 1.24 M, 2 h reaction time at 60ºC, for which the O/N ratio increased, from 1.6 to 3.2 and 3.1, for the surfaces activated with He and H_2 plasma, respectively, due to the presence of PHEMA (which does not contain nitrogen).

Table 4-2. Elemental composition of the PA and polymer grafted PA surfaces.

Surface	Plasma	Atomic %					Atomic Ratio	
		C	O	N	Na	S	O/N	O/C
PA	-	73.7	16.2	10.1	0.0	0.0	1.61	0.22
PAA [a]	He	67.6	28.8	3.6	0.0	0.0	7.92	0.43
	H_2	67.5	28.8	3.7	0.0	0.0	7.78	0.43
PVSA [b]	He	65.6	23.3	8.7	0.9	1.6	2.69	0.36
	H_2	66.0	22.9	8.0	0.7	2.5	2.89	0.35
PHEMA [c]	He	68.7	23.8	7.5	0.0	0.0	3.19	0.35
	H_2	68.1	24.1	7.8	0.0	0.0	3.09	0.35

[a] graft polymerization at $[M]_0 = 2.92$ M, 2 h, 70ºC
[b] graft polymerization at $[M]_0 = 1.81$ M, 2 h, 60ºC
[c] graft polymerization at $[M]_0 = 1.24$ M, 2 h, 50ºC

4.3.2.2 Grafted Polymer Layer Thickness

The grafted polymer layer thickness (determined by ellipsometry) increased with reaction time as well as with initial monomer concentration (Figure 4-4), as expected for free radical graft polymerization (Chapter 2, Equation (2-1)). As polymerization proceeds, chain transfer (of monomer with growing surface chains; Equation (4-1)) will lead to increased rate of formation of growing chain radicals in solution and ensuing termination of growing surface chains [236]. As a consequence, the rate of grafted polymer growth decreases with reaction time. Additional reasoning for the decreased grafted polymer growth is the increased steric hindrance for monomer diffusion within the grafted layer as surface chain density increases in the surface grafting zone. Given the above, the grafted polymer layer thickness tends toward a plateau at sufficiently long reaction time which is particularly evident for VSA graft polymerization, relative to the AA and HEMA graft polymerized surfaces. The above trend is not surprising

given that VSA is reported to have the lower $k_p/k_t^{1/2}$ (~0.4 (L/mol·s)$^{1/2}$ [237]) ratio (see Chapter 2, Equation (2-1)) relative to AA and HEMA; in other words, termination of growing chains is more significant for polymerization of VSA relative to the other two monomers.

The polymer layer thickness increased in the order of PVSA>PAA>PHEMA (Table 4-3). Greater thicknesses was attained for the PAA layer (~10 − 90 nm at $[M]_0$ = 0.73 − 2.92 M, 0.5 − 2 h, 70ºC), compared to the PHEMA layer (~2.5 − 40 nm at $[M]_0$ = 0.08 − 1.24 M, 0.5 − 2 h, 50ºC). Given the higher k_p (Chapter 2, Equation (2-1)) value for AA (~1.2x10^5 L/mol·s [238]) compared to HEMA (~400 L/mol·s [239]), one should expect that at a similar monomer concentration a higher grafted layer thickness would be obtained for PAA. Indeed, even the highest PHEMA initial monomer concentration (1.24 M) yielded a lower grafted layer thickness than for PAA at the lowest initial monomer concentration (0.73 M) for SNS-PA-Si surfaces synthesized via the same reaction time and plasma treatment.

The grafted polymer layer thickness was consistently higher when surface activation was with He as opposed to H_2 plasma (Figure 4-4). Overall, a grafted polymer layer thickness, after the 0.5 − 2 h polymerization step, was in the range of 8.0 − 97 Å was attained for PA surface graft polymerization post surface activation with He plasma; the above range of grafted layer thickness was significantly greater than achieved for PA surfaces graft polymerized post activation with H_2 plasma (2.5 − 33 Å). The above trend is hypothesized to be due to a greater number density of surface active sites on the PA surface achieved for surface treatment with He compared to H_2 plasma. This postulate is inferred from the lower water contact angle (i.e., greater degree of hydrophilicity; Section 4.3.1) measured for the He relative to H_2 plasma treated PA surfaces (Figure 4-3). One should note that polymer surface chain growth by monomer addition, for a given monomer and reaction conditions, should be similar irrespective of the

surface number density of growing chains (as long as there is no significant steric hindrance). Therefore, one may argue that similar chain length should be expected for graft polymerization of the PA surfaces achieved post either He or H_2 plasma surface treatment. However, it is stressed that ellipsometric polymer layer thickness measurements represent grafted polymer layer thickness averaged over the measurement area (~0.8 mm^2). Therefore, lower measured average thickness would result from sparser surface coverage (i.e., lower chain number density as expected for H_2 plasma activated surface); this trend is expected even if such chains are of the same length as for a surface of higher surface chain density (i.e., as expected for He treated PA surface).
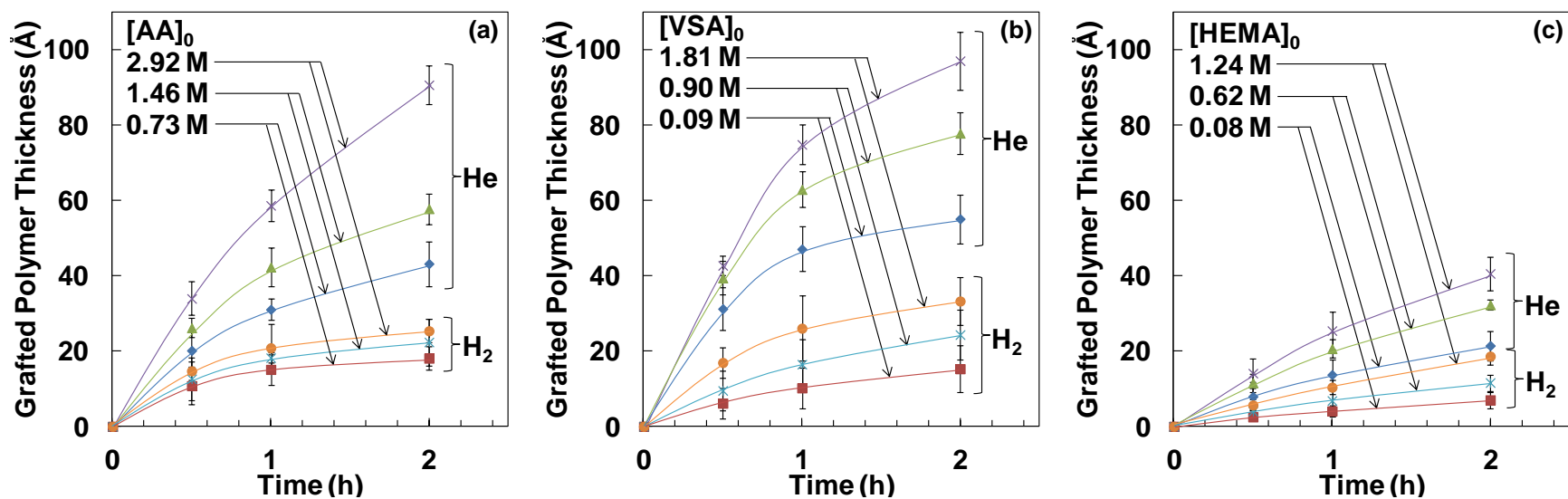
Figure 4-4. Thickness of the graft polymerized layers of (a) PAA, (b) PVSA, and (c) PHEMA. Graft polymerization was for a period of 2 hours at reaction temperatures of 70ºC, 60ºC, and 50ºC for AA, VSA and HEMA, respectively.

Table 4-3. Range (and average) surface topography values for SNS-PA-Si surfaces.

Surface	Plasma	R_{rms} (nm) [d]	Polymer Volume (10^5 nm^3/μm^2) [d]	Grafted Polymer Layer Thickness (Å) [e]	Surface Feature Density (# peaks/μm^2) [f]	Avg. peak-to-peak distance (nm) [f,g]
PAA [a]	He	1.09–2.28 (1.51)	16.1–38.2 (33.1)	20.2–90.8 (44.9)	2.00–58.5 (31)	72.4–551 (165)
	H$_2$	0.70–1.93 (1.17)	2.82–41.9 (27.3)	10.8–25.4 (17.6)	0.75–40.3 (13)	82.8–441 (211)
PVSA [b]	He	0.69–3.00 (1.17)	3.91–95.5 (33.8)	31.3–97.2 (58.8)	2.75–119 (47)	54.7–338 (129)
	H$_2$	0.57–1.48 (1.04)	5.74–21.8 (27.2)	6.15–33.3 (17.6)	0.50–12.8 (9.0)	169–1380 (342)
PHEMA [c]	He	0.95–3.63 (2.23)	6.02–74.0 (47.7)	7.96–40.6 (20.9)	11.8–95.0 (44)	66.4–173 (106)
	H$_2$	0.82–1.93 (1.31)	10.2–37.1 (28.4)	2.51–18.7 (7.88)	5.75–22.0 (15)	136–280 (181)

[a] graft polymerization at $[M]_0 = 0.73 - 2.92$ M, $0.5 - 2$ h, 70ºC
[b] graft polymerization at $[M]_0 = 0.09 - 1.81$ M, $0.5 - 2$ h, 60ºC
[c] graft polymerization at $[M]_0 = 0.08 - 1.24$ M, $0.5 - 2$ h, 50ºC
[d] determined by AFM
[e] measured via ellipsometry
[f] determined via AFM of major surface polymer features (Section 4.2.3.2)
[g] measured from midpoint to midpoint of neighboring major surface polymer features (Section 4.2.3.2)

4.3.2.3 Surface Topography

Surface topography varied depending on the graft polymerization conditions as illustrated by the AFM images of PA, PAA, PVSA, and PHEMA (Figure 4-1, Figure 4-5a-d and Table 4-3) with additional details in Figure 4-12a-f and Table 4-4 in Section 4.5. Longer graft polymerization periods resulted in higher surface roughness (R_{rms}) and mean surface feature height (Figure 4-5a with details Figure 4-12a-f and Table 4-4 in Section 4.5) due to increased formation of homopolymer chains and their termination with surface chains (Chapter 2, Equation (2-1) and Equation (4-1)). Surface roughness for the PAA, PVSA, and PHEMA layers, formed on the He plasma activated PA substrate, increased by a factor of $2.4 - 5.1$, $1.5 - 6.7$, and $2.1 - 8.1$, respectively, over the reaction period of $0.5 - 2$ h, for the corresponding initial

monomer concentration ranges of 0.73 – 2.92 M, 0.09 – 1.81 M, and 0.08 – 1.24 M (Figure 4-12a-f and Table 4-4 in Section 4.5). Synthesis of PAA, PVSA, and PHEMA grafted layers onto the He APP treated PA surfaces, relative to H_2 APP, for the above same conditions generally resulted in greater surface roughness (R_{rms}) and feature heights on average by factors of 1.3, 1.1, 1.6 and 1.2, 1.1, 1.5, respectively. It is noted that, in all cases, the increase in surface roughness was accompanied by taller grafted polymer surface feature heights (Figure 4-12a-f and Table 4-4 in Section 4.5). This trend is consistent, as also reported in Chapter 3, Section 3.3.1 on poly(vinylpyrrolidone) and poly(acrylamide) graft polymerized surfaces, with the expectation of longer chain length for the higher conditions of initial monomer concentration and reaction time due to increased surface chain termination with homopolymers (i.e., "grafting to").

Compared to the PA-Si surface having surface roughness of $R_{rms} = 0.5$ nm and short surface feature heights $\lesssim$ 4 nm (Figure 4-1), all SNS-PA-Si surfaces had greater surface roughness ($R_{rms} = 0.57 – 3.6$ nm) and a broader polymer feature height distribution (FHD) (Figure 4-12a-f and Table 4-4 in Section 4.5). In general, longer reaction time and higher initial monomer concentration resulted in a broader FHD and presence of taller surface features. For example, for PA surface activated with He plasma, synthesis of grafted PVSA at $[M]_0 = 1.81$ M, the tall feature heights (i.e., at the FHD tail) increased from ~12 nm to ~24 nm as the reaction time increased from 0.5 h to 2 h (Figure 4-5a). Likewise, increased monomer concentration resulted in a rise in feature height (Table 4-4 in Section 4.5). Such a behavior is illustrated for the PAA layer, grafted onto the He plasma activated PA surface, revealing a rise of tall surface features from ~21 nm to ~44 nm as the initial monomer concentration increased from 0.73 M to 2.92 M for a reaction period of 2 h (Figure 4-5b).

Although individual grafted polymer chains were not discernible via AFM analysis, the number density of major surface polymer features (determined via AFM, Section 4.2.3.2) can be regarded as an indirect indication of the density of the grafted polymer chains (Figure 4-13 in Section 4.5). For example, the grafted polymer surfaces synthesized onto the He plasma activated PA surface resulted in average number density of major polymer features that was a factor of $2.3 - 5.3$ higher and average peak-to-peak separation being a factor of $1.3 - 2.7$ lower than for surface graft polymerized onto PA post H_2 plasma treatment (Figure 4-6, Table 4-3). Along with the number density of major surface polymer features, the grafted polymer layer thickness also increased for SNS-PA-Si surfaces grafted post He APP treatment compared to the H_2 APP activated surfaces (Figure 4-7). The above trends are consistent with the assertion that higher density of activated surface sites was achieved on the PA surface via He relative to H_2 APP surface activation (Section 4.3.1). A wide range of number density of polymer surface features was obtained for the different polymers (depending on the graft polymerization conditions) yielding average low to high chain-chain separation ranges of ~$275 - 1380$ nm and ~$15 - 150$ nm at average peak densities of 0.5 #/μm^2 and 120 #/μm^2, respectively. The above results suggest that the design of end-grafted polymer layers for specific applications (e.g., surface screening to retard or enhance solute-surface affinity) should consider optimization of surface activation and graft polymerization conditions relative to the desirable surface topography.
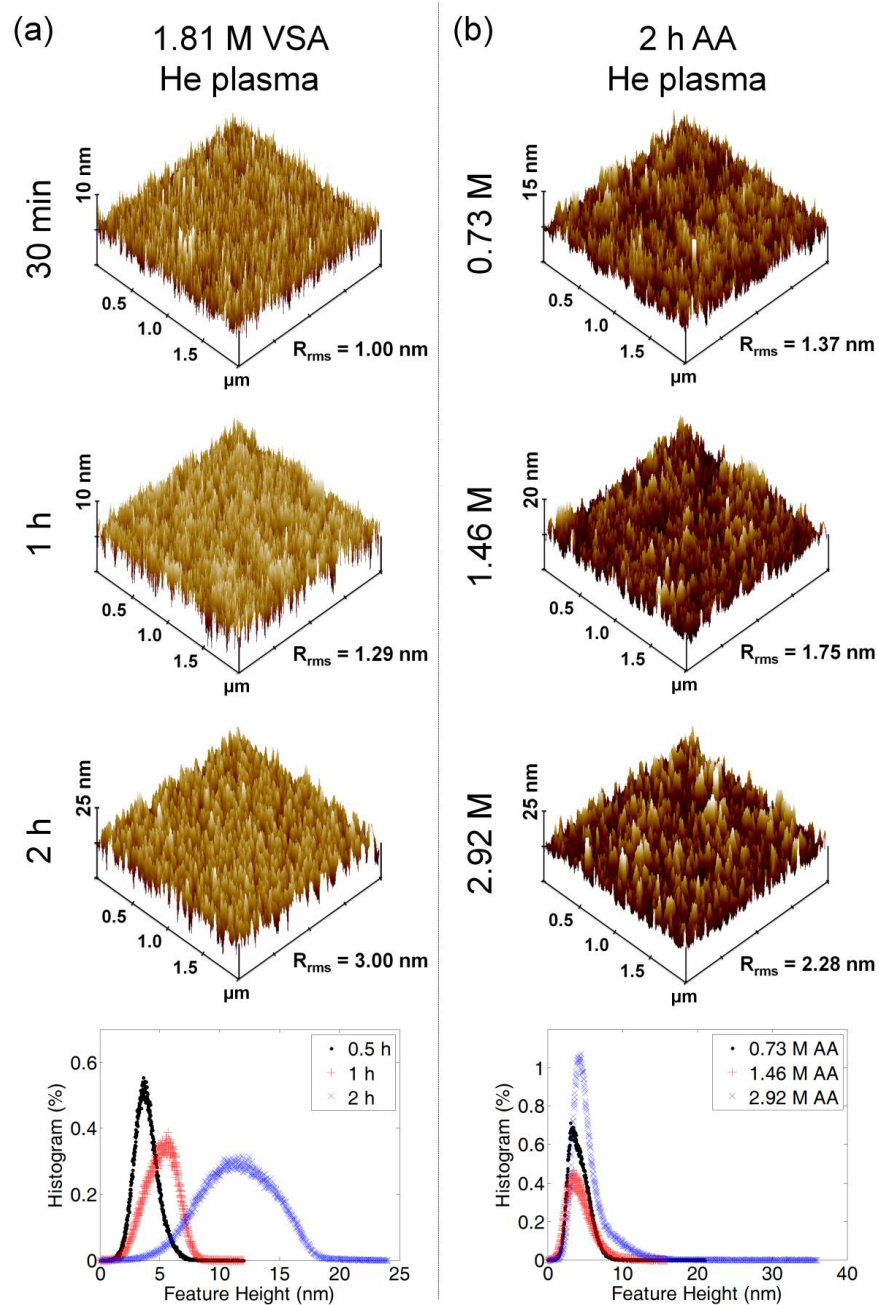
Figure 4-5ab. AFM images and polymer feature height distributions of SNS surfaces graft polymerized onto a PA surface activated with He plasma. (a) PVSA synthesized at $[VSA]_0 =$ 1.81 M over a reaction time scale of 0.5 − 2 h, and (b) AA graft polymerization to form tethered PAA at a reaction time of 2 h over an initial monomer concentration range of $[AA]_0$ = 0.73 − 2.92 M.
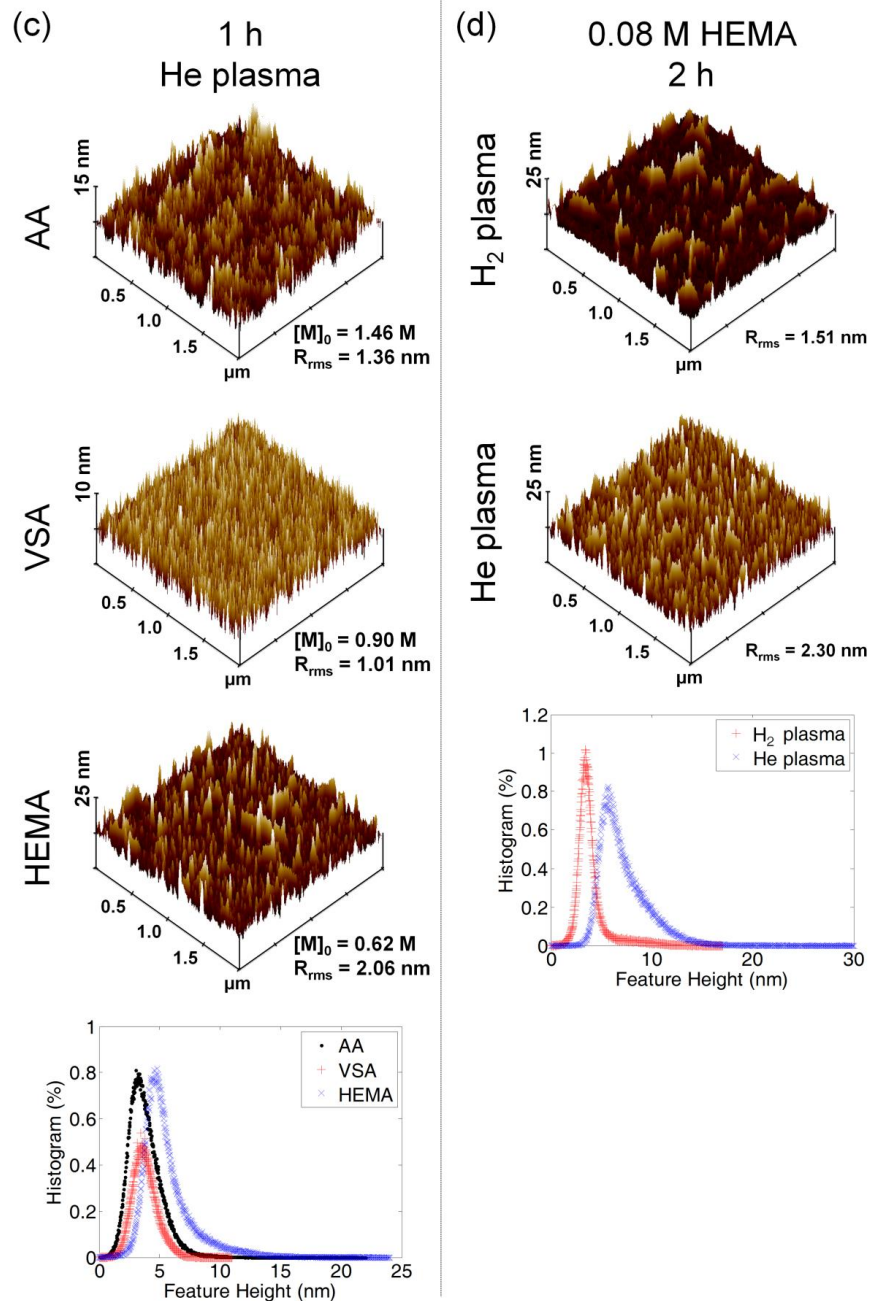
Figure 4-5cd. Examples of AFM images and polymer feature height distributions of SNS surfaces formed by (c) graft polymerization of AA, VSA and HEMA (at different initial monomer concentrations and 1 h reaction time) onto a PA surface activated via He plasma, and (d) PHEMA SNS surfaces formed by graft polymerization of HEMA ([HEMA]$_0$ = 0.08 M at 2 h reaction time) onto PA surfaces activated by He and H$_2$ plasmas.
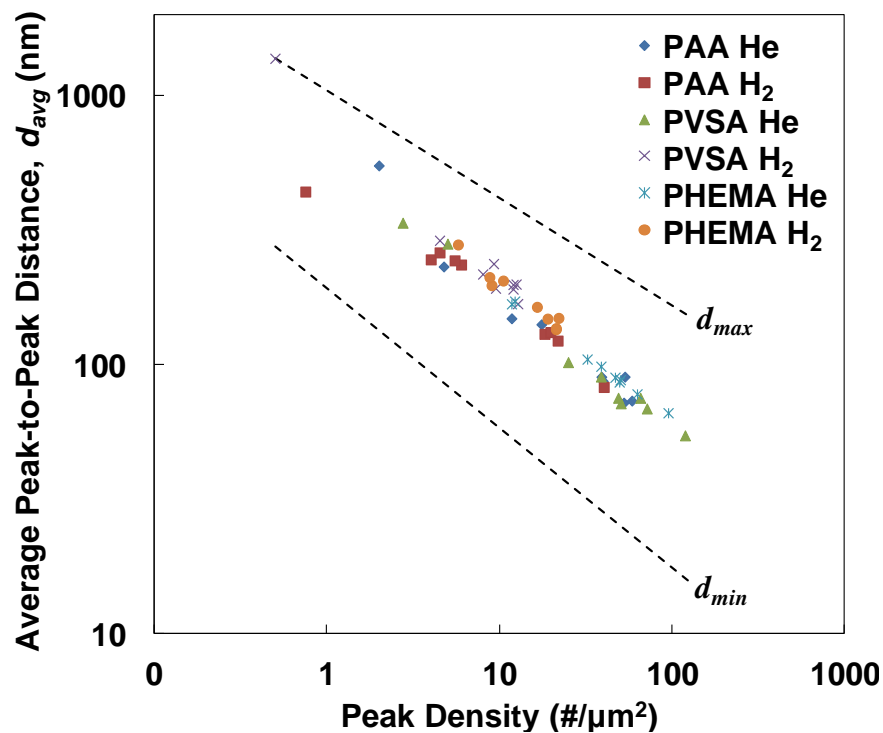
Figure 4-6. Correlation of the number density of major polymer feature peaks with the average peak-to-peak distance for the SNS-PA-Si surfaces graft polymerized with AA ($[M]_0$ = 0.73 − 2.92 M), VSA ($[M]_0$ = 0.09 − 1.81 M), and HEMA ($[M]_0$ = 0.08 − 1.24 M). SNS surfaces were synthesized via He and H_2 APP surface activation followed by a 0.5 − 2 h graft polymerization period. The upper and lower dashed lines indicate the range of average minimum and maximum peak-to-peak separation for the major peaks (defined as being above ~30% of the maximum peak height for each substrate, Section 4.2.3.2).
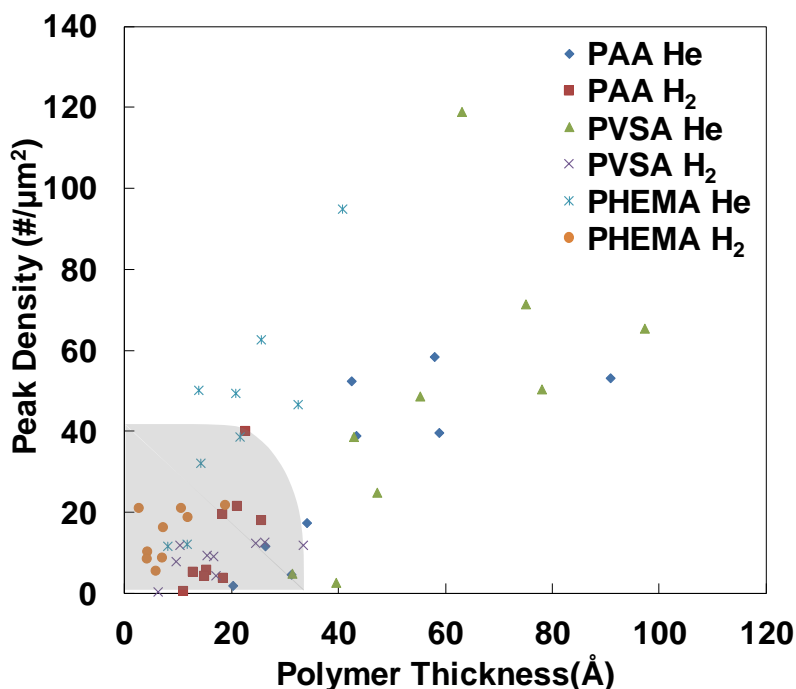
Figure 4-7. Map showing grafted polymer layer thickness versus number density of major grafted polymer feature peaks. The shaded area encompasses the range of polymer thicknesses and average major peak density that were reached for SNS-PA-Si surfaces graft polymerized post PA surface activation with H_2 plasma, and with He plasma at low initial monomer concentration and/or short graft polymerization times. The region outside the shaded area exclusively represents the range of polymer thickness and average major peak density for SNS surfaces grafted on PA post surface activation with He plasma.

4.3.2.4 Surface Hydrophilicity

Grafting the PA surface with hydrophilic polymers increased the surface hydrophilicity as quantified by the decrease in free energy of hydration (ΔG_{iw}) of the grafted surfaces (Figure 4-8a). The decrease in ΔG_{iw} correlated with increased reaction time (Figure 4-8a), initial monomer concentration (Figure 4-8a), polymer layer thickness (Figure 4-9a), surface roughness

(Figure 4-9b) and grafted polymer volume (Figure 4-14a in Section 4.5). All the PVSA-PA-Si and PAA-PA-Si surfaces treated with He APP were considered as truly hydrophilic (i.e., ΔG_{iw} < -113 mJ/m^2; Chapter 3, Section 3.2.3) over the range of 0.5 – 2 h and 0.09 – 1.81 M and 0.73 – 2.92 M, respectively (Figure 4-8a). For the H$_2$ APP initiated surfaces, only the PVSA-PA-Si surfaces synthesized at a reaction time ≥1 h (for $[M]_0$ = 0.09 – 1.81 M) and PAA-PS-Si surfaces synthesized at initial monomer concentration of 2.92 M AA (for 0.5 – 2 h) could be considered hydrophilic beyond experimental uncertainty. Graft polymerization onto PA surfaces initiated with He APP exhibited increased -ΔG_{iw} compared to those activated with H$_2$ APP. It is postulated that a higher number density of activated surface sites was achieved with He relative to H$_2$ plasma surface treatment (Section 4.3.1). As a consequence, for a given monomer, a higher grafted polymer layer thickness (which also correlated with higher surface roughness) resulted in higher polymer surface volume (Table 4-3 and Figure 4-14b-c in Section 4.5). A greater volume of surface grafted hydrophilic polymer would in turn provide higher capacity for water absorption into the surface layer and thus increased hydrophilicity as quantified by higher -ΔG_{iw} (Figure 4-14a in Section 4.5). For example, polymer volume increases by a factor of ~14 (from 2.8 x10^5 nm^3/μm^2 to 3.8 x10^6 nm^3/μm^2) for PAA and ~17 (from 5.7 x10^5 nm^3/μm^2 to 9.6 x10^6 nm^3/μm^2) for PVSA were accompanied by 24% and 20% increase in -ΔG_{iw}, respectively. It is noted that the pK$_a$ of PAA and PVSA which are both < 5 [240], whereas the pK$_a$ of hydroxyl groups on PHEMA is reported in the range of ~11 – 12 [241]. Therefore, one should expect that the free energy of hydration of PHEMA would not be as low as for PAA and PVSA since these polyacids are ionized in water at pH ~6 – 8. Indeed, the PHEMA-PA-Si surfaces could not be considered to be truly hydrophilic even though various studies have promoted this polymer due to its biocompatibility, hydrophilicity, and anti-fouling properties [228, 242].
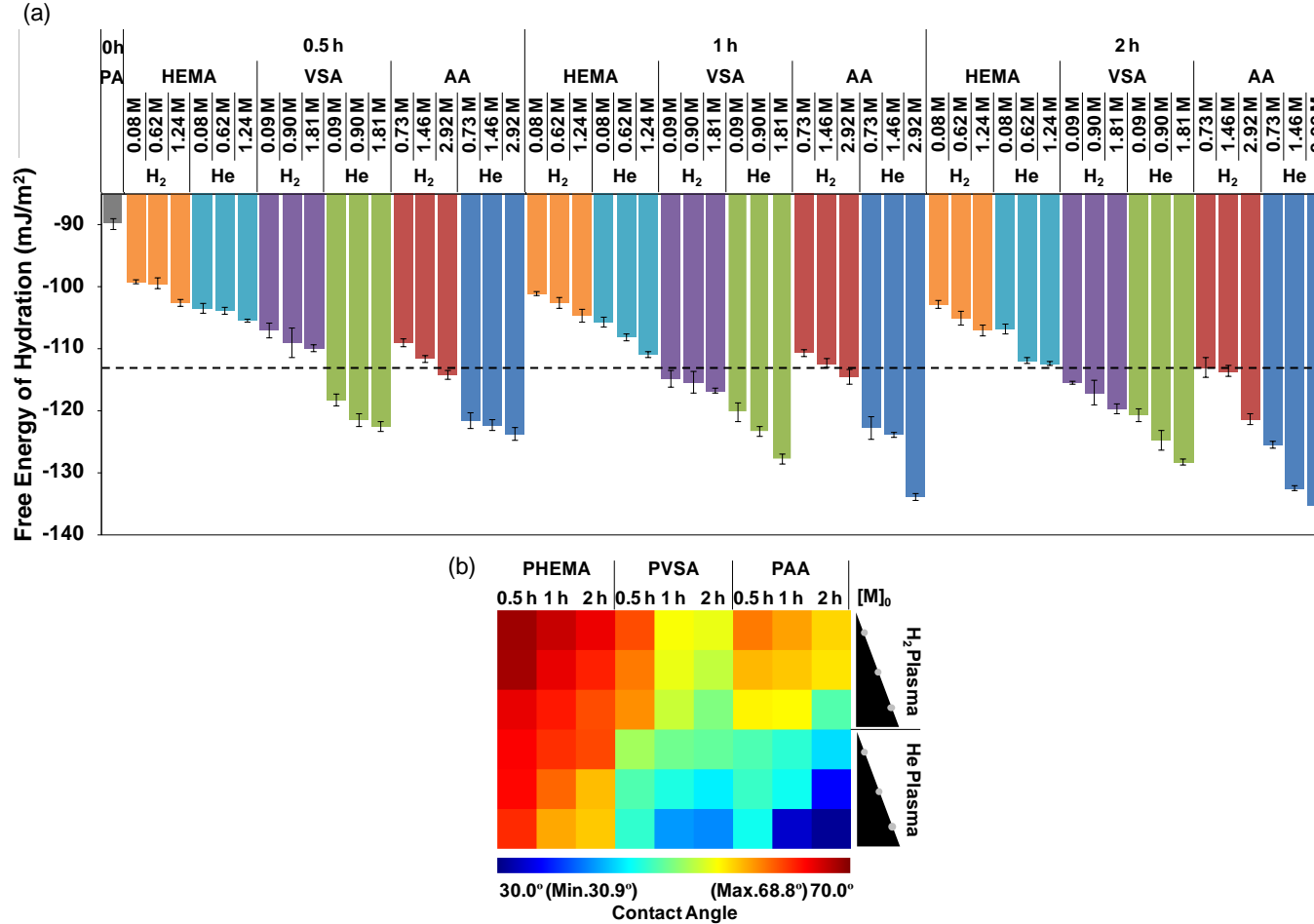
Figure 4-8. Summary of the hydrophilicity of tethered PAA, PVSA, and PHEMA polymer layers on a PA-Si surface as quantified by (a) free energy of hydration (ΔG_{iw}), calculated from (b) water contact angle data shown in the heat map summary (also see data in Table 4-4 in Section 4.5). Note: Tethered polymer layers with ΔG_{iw} values below the horizontal dashed line are designated as hydrophilic.
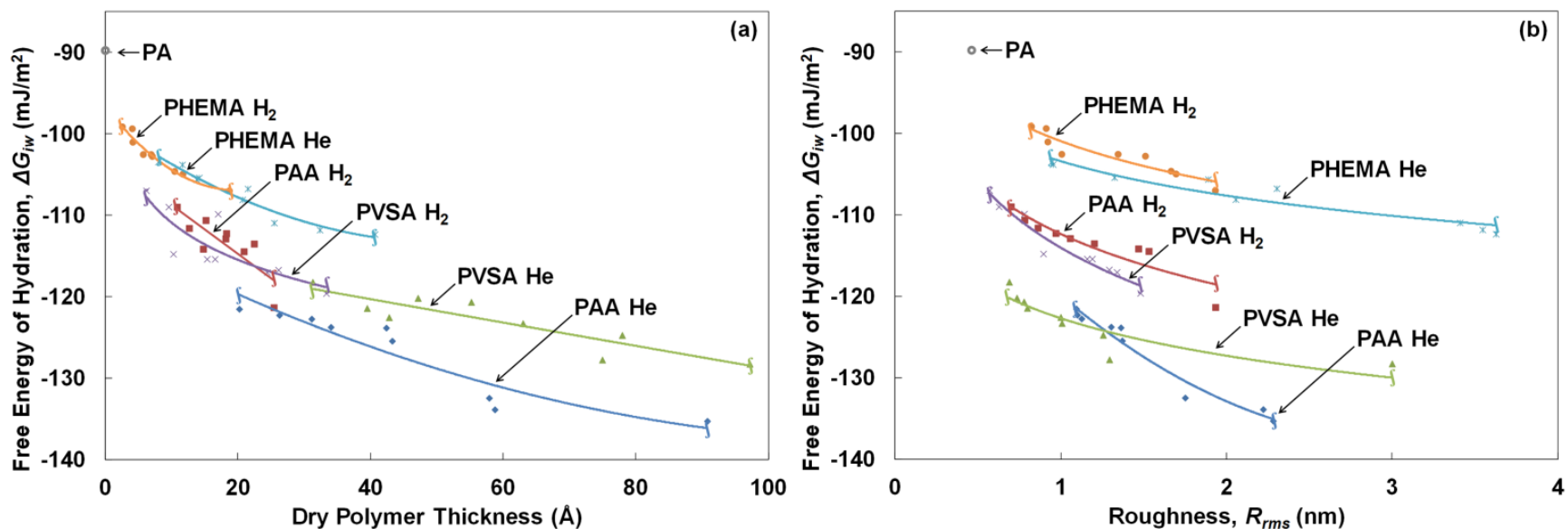
Figure 4-9. SNS-PA-Si surface hydrophilicity, as quantified by the decrease in free energy of hydration, increased with (a) increasing grafted polymer layer thickness, and (b) increasing surface roughness. The different grafted polymer surfaces were synthesized post PA surface activation with He or H_2 APP, for initial AA, VSA and HEMA monomer concentrations of 0.73 – 2.92 M, 0.09 – 1.81 M, and 0.08 – 1.24 M, respectively, over a polymerization period of 0.5 – 2 h.

Further insight with respect to the influence of monomer type on surface hydrophilicity achieved for the graft polymerized PA surfaces can be assessed based on comparison of the polar (γ_s^p) and dispersive (γ_s^d) components of the surface energy (Figure 4-10 and Chapter 3, Equations (3-4) and (3-5)). Over the present range of monomers and graft polymerization conditions γ_s^d was in the range of 39.9±3.3 mJ/m^2, while γ_s^p was 17.6±9.1 mJ/m^2. The increase in γ_s^p correlated with increased reaction time (Figure 4-10), initial monomer concentration (Figure 4-10), polymer layer thickness (Figure 4-11a), surface roughness (Figure 4-11b) and grafted polymer volume (Figure 4-14d in Section 4.5). Clearly, the hydrophilic polymers significantly altered the polar component of the surface energy. For example, upon graft polymerization of the PA surface γ_s^p increased by a factor of 4.7 – 6.5 and 4.2 – 5.4 for the PAA and PVSA surfaces, respectively, that were synthesized post He surface activation. For the PHEMA grafted layer synthesized post He surface treatment, γ_s^p increased, relative to the PA surface, by a factor of 2.5 – 3.0 over the range of which was significantly lower than for the former hydrophilic polymers. It is noted that Ra (i.e., the Euclidean distance in the solubility parameter space, Section 4.2.3.3) for PAA is lower than for PHEMA, consistent with the finding that on average $(\gamma_s^p)_{PAA} > (\gamma_s^p)_{PHEMA}$; the above both imply greater affinity between water and PAA compared to PHEMA and thus greater wettability of the PAA surface. Clearly, the polymer type is a governing factor in establishing surface wettability. This is illustrated by the difference in γ_s^p values for He treated PA surfaces of ~20 mJ/m^2, ~24 mJ/m^2, and ~10 mJ/m^2 for PAA, PVSA and PHEMA, respectively, at about the same surface roughness of ~1.3 nm (Figure 4-11b).
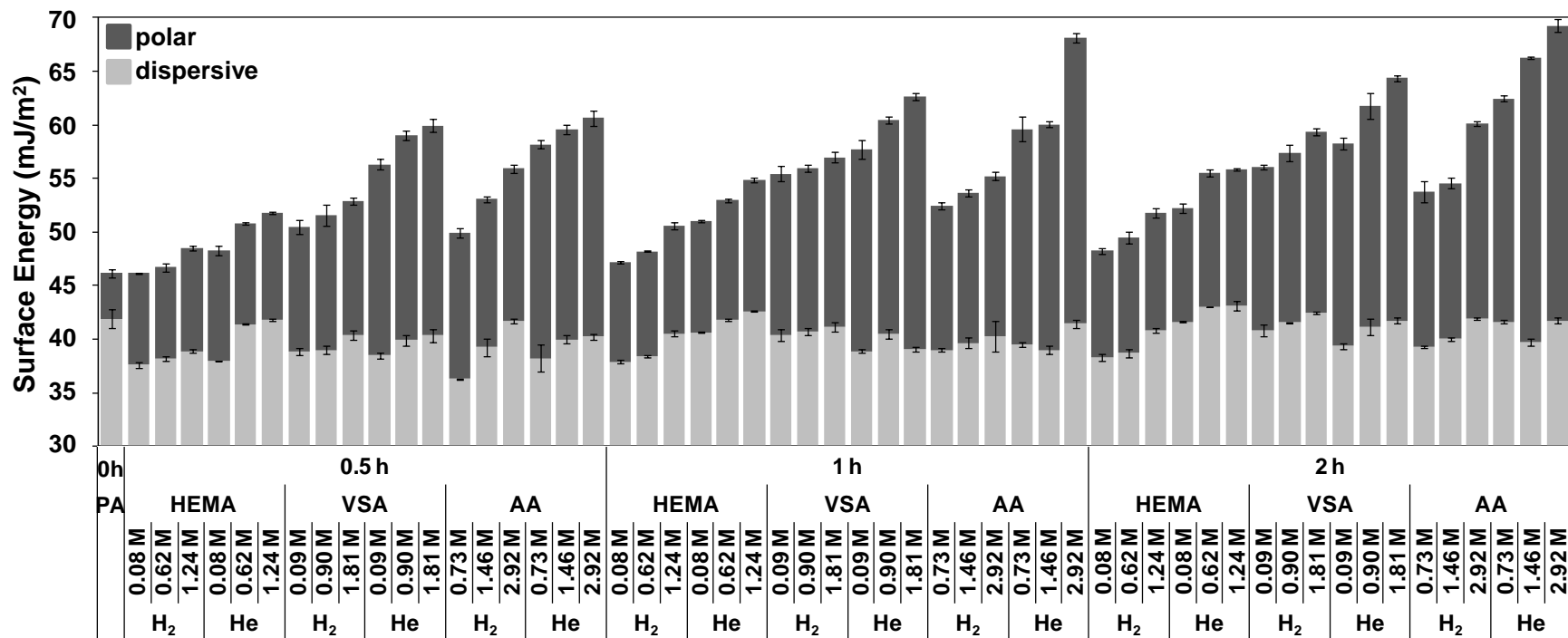
Figure 4-10. Solid surface energy (γ_s) and its dispersive (γ_s^d) and polar (γ_s^p) components for the PA-Si and SNS-PA-Si surfaces consisting of tethered PAA, PVSA, and PHEMA chains.
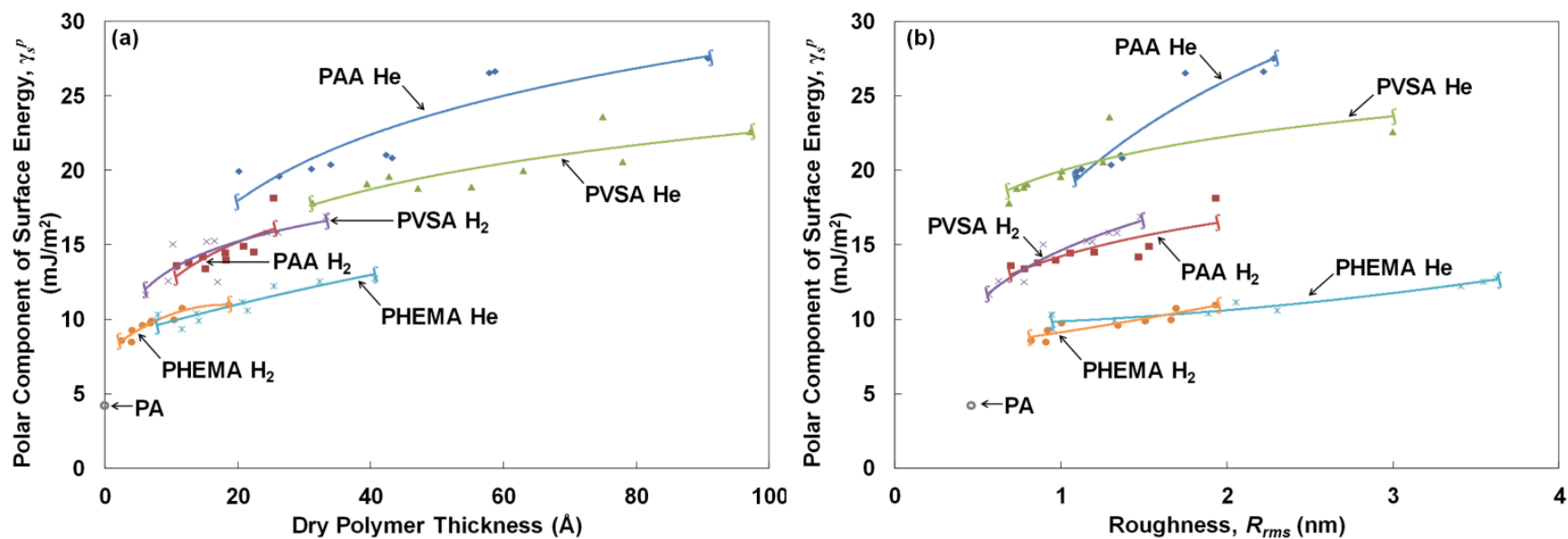
Figure 4-11. Polar component of surface energy for tethered polymer surfaces (SNS-PA-Si) increased with (a) increasing polymer layer thickness, and (b) increasing surface roughness. Graft polymerization was carried out post PA surface activation with He or H_2 APP, over a graft polymerization period of 0.5 – 2 h and initial monomer concentrations of 0.73 – 2.92 M, 0.09 – 1.81 M, and 0.08 – 1.24 M for PAA, PVSA, and PHEMA, respectively.

4.4   Conclusions

Surface nanostructuring (SNS) with terminally anchored (tethered) hydrophilic polymers (PAA, PVSA and PHEMA) was shown to enable alteration of surface hydrophilicity as demonstrated using a polyamide surface. The tethered hydrophilic polymer surfaces were synthesized by surface graft polymerization (in a monomer solution) post activation of the polyamide surface via atmospheric pressure plasma. Use of He or H_2 plasmas was preferable to O_2 plasma given that the latter resulted in excessive substrate etching. Surface activation by He plasma was found to be more effective, relative to H_2 plasma, in enabling the formation of a thicker grafted polymer layer of higher density of major surface polymer features. Greater degree of surface water wettability (or hydrophilicity), as quantified by lower free energy of hydration and increased polar component of the surface energy, was attained for grafted polymer layers synthesized at higher initial monomer concentration and longer reaction time. Surface hydrophilicity increase, for a given polymer type, correlated with increased grafted polymer layer thickness and surface roughness, demonstrating that tuning of surface hydrophilicity can be achieved through adjustment of surface polymerization conditions as well as monomer selection.

4.5   Addendum

This section presents detailed AFM images of all of the SNS-PA-Si surfaces (reaction time 0.5 – 2 h) examined in this chapter: PAA surfaces grafted via He APP PA-Si surface activation (Figure 4-12a), PAA surfaces grafted via H_2 APP PA-Si surface activation (Figure 4-12b), PVSA surfaces grafted via He APP PA-Si surface activation (Figure 4-12c), PVSA surfaces grafted via H_2 APP PA-Si surface activation (Figure 4-12d), PHEMA surfaces grafted via He APP PA-Si

113

surface activation (Figure 4-12e), and PHEMA surfaces grafted via H_2 APP PA-Si surface activation (Figure 4-12f). Figure 4-12a-f demonstrates that for the array of grafted surfaces investigated, increasing graft polymerization time from $0.5 - 2$ h, increasing initial monomer concentration, or surface activation by He APP, relative to H_2 APP, resulted in greater surface roughness and feature heights. Detailed surface properties of the above mentioned SNS-PA-Si surfaces are presented in Figure 4-13 and Table 4-4. Lastly, the relationships between polymer volume and ΔG_{iw}, polymer layer thickness, roughness, and γ_s^p are presented in Figure 4-14a-d. Figure 4-14a-d suggests that a greater volume of SNS hydrophilic polymer (which correlates with polymer layer thickness and roughness) provides a higher capacity for water absorption into the surface layer, therefore, increasing hydrophilicity.
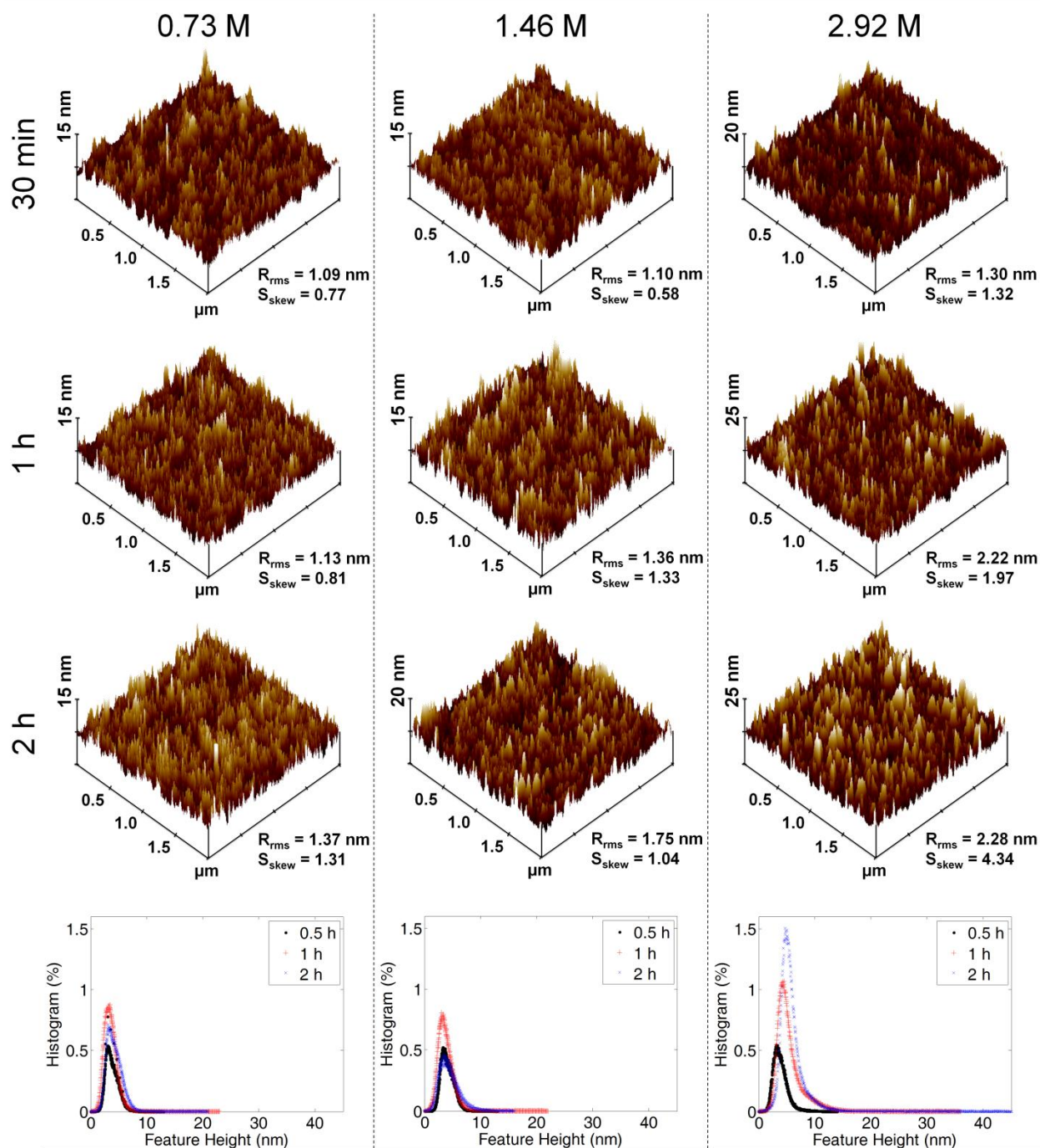
Figure 4-12a. AFM images and corresponding polymer surface feature height distributions for grafted PAA surfaces synthesized on PA-Si surfaces activated via He plasma. Graft polymerization was carried out at an initial monomer concentration range of $[M]_0 = 0.73 - 2.92$ M for a period of $0.5 - 2$ h at 70ºC.
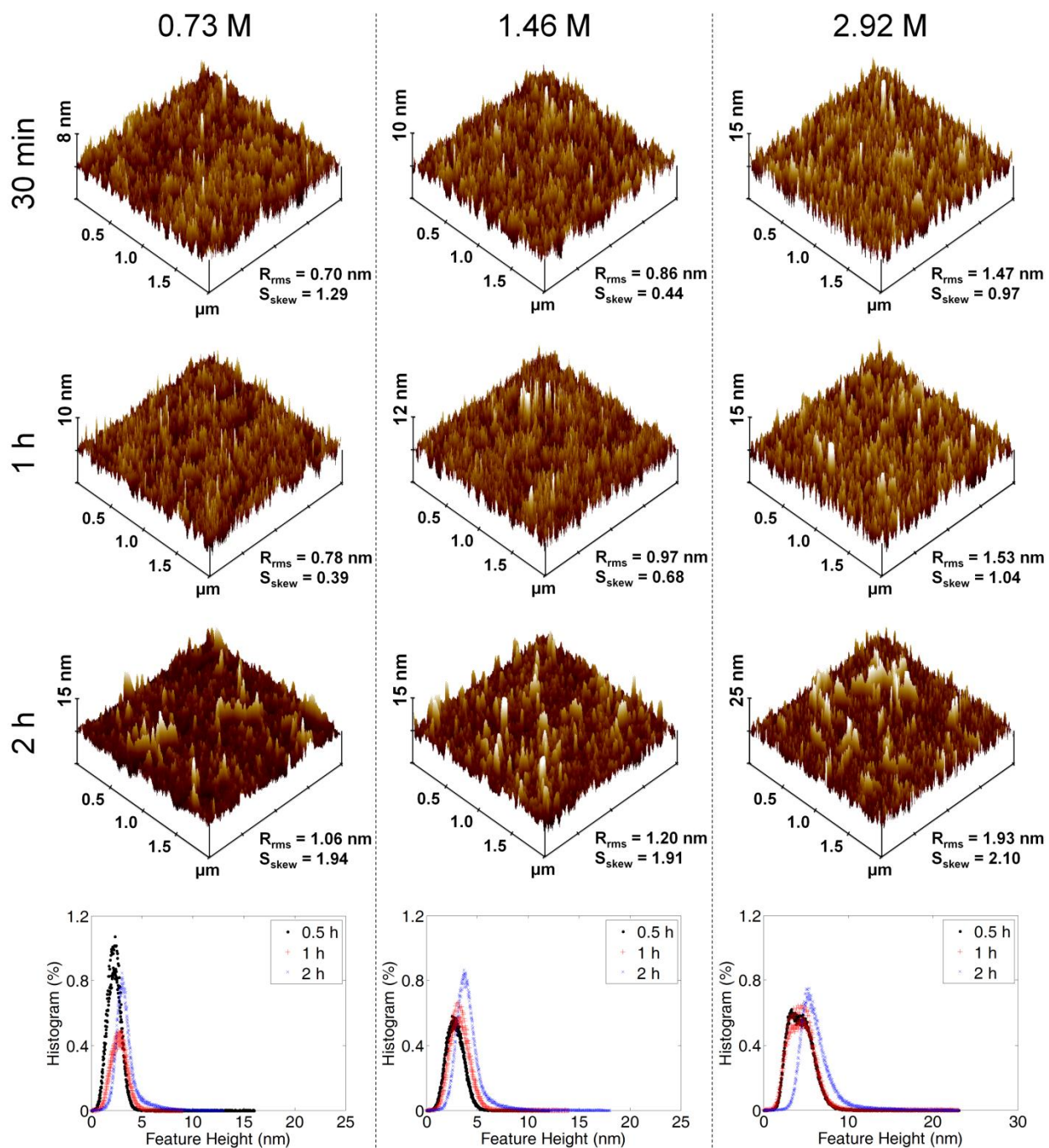
Figure 4-12b. AFM images and corresponding polymer surface feature height distributions for grafted PAA surfaces synthesized on PA-Si surfaces activated via H_2 plasma. Graft polymerization was carried out at an initial monomer concentration range of $[M]_0 = 0.73 – 2.92$ M for a period of $0.5 – 2$ h at 70ºC.
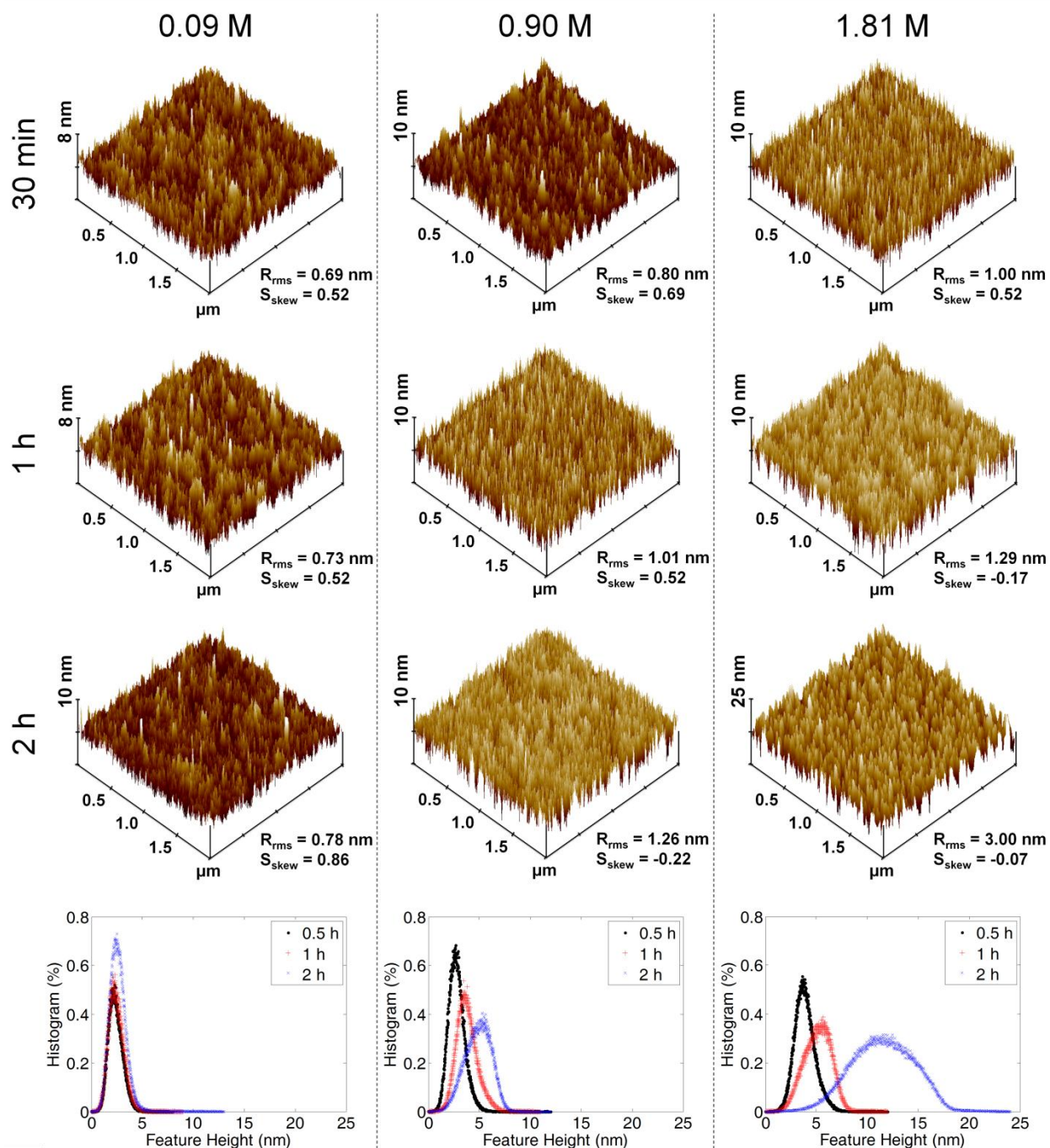
Figure 4-12c. AFM images and corresponding polymer surface feature height distributions for grafted PVSA surfaces synthesized on PA-Si surfaces activated via He plasma. Graft polymerization was carried out at an initial monomer concentration range of $[M]_0 = 0.09 - 1.81$ M for a period of $0.5 - 2$ h at 60ºC.
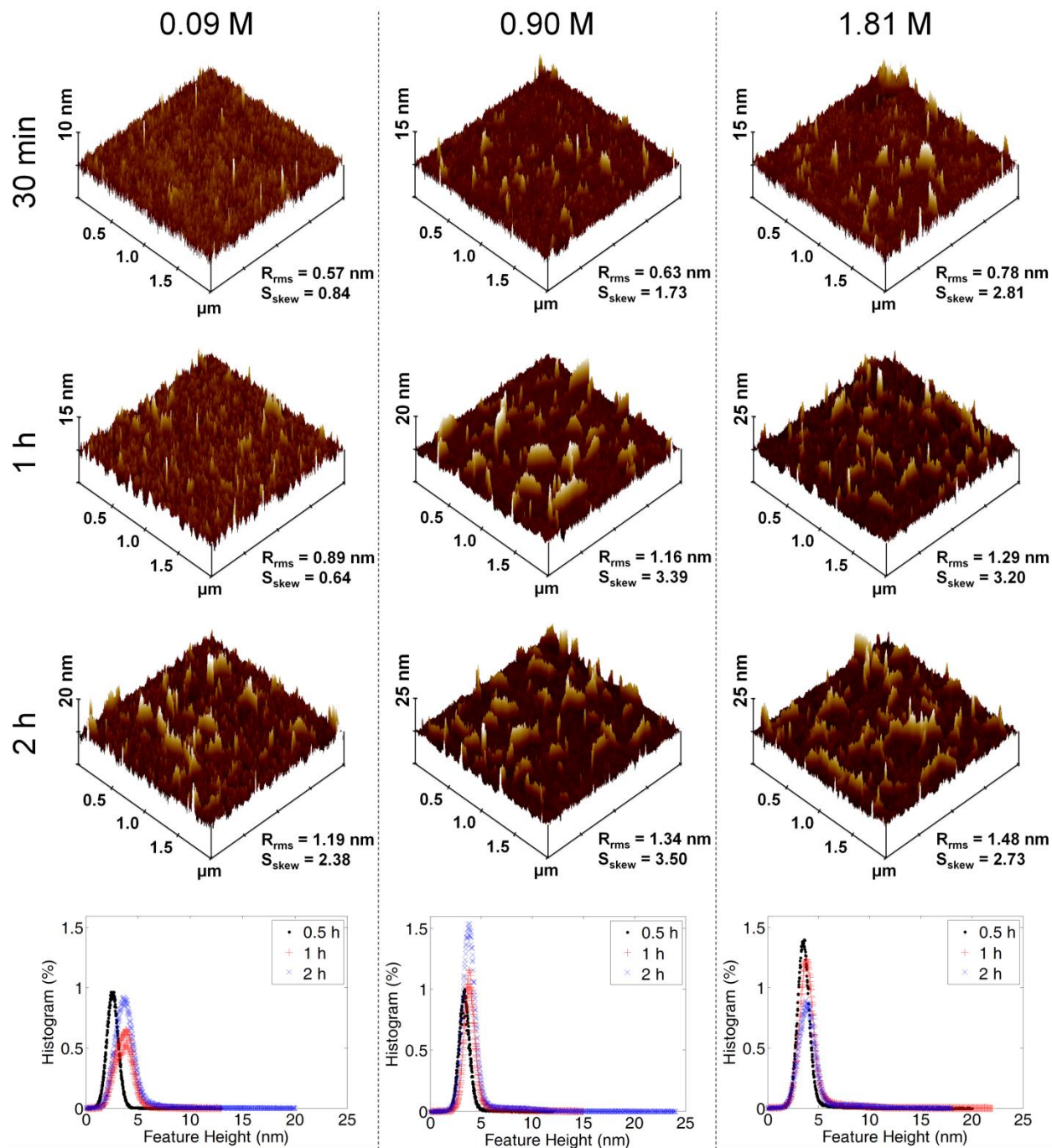
Figure 4-12d. AFM images and corresponding polymer surface feature height distributions for grafted PVSA surfaces synthesized on PA-Si surfaces activated via H_2 plasma. Graft polymerization was carried out at an initial monomer concentration range of $[M]_0 = 0.09 - 1.81$ M for a period of $0.5 - 2$ h at 60ºC.
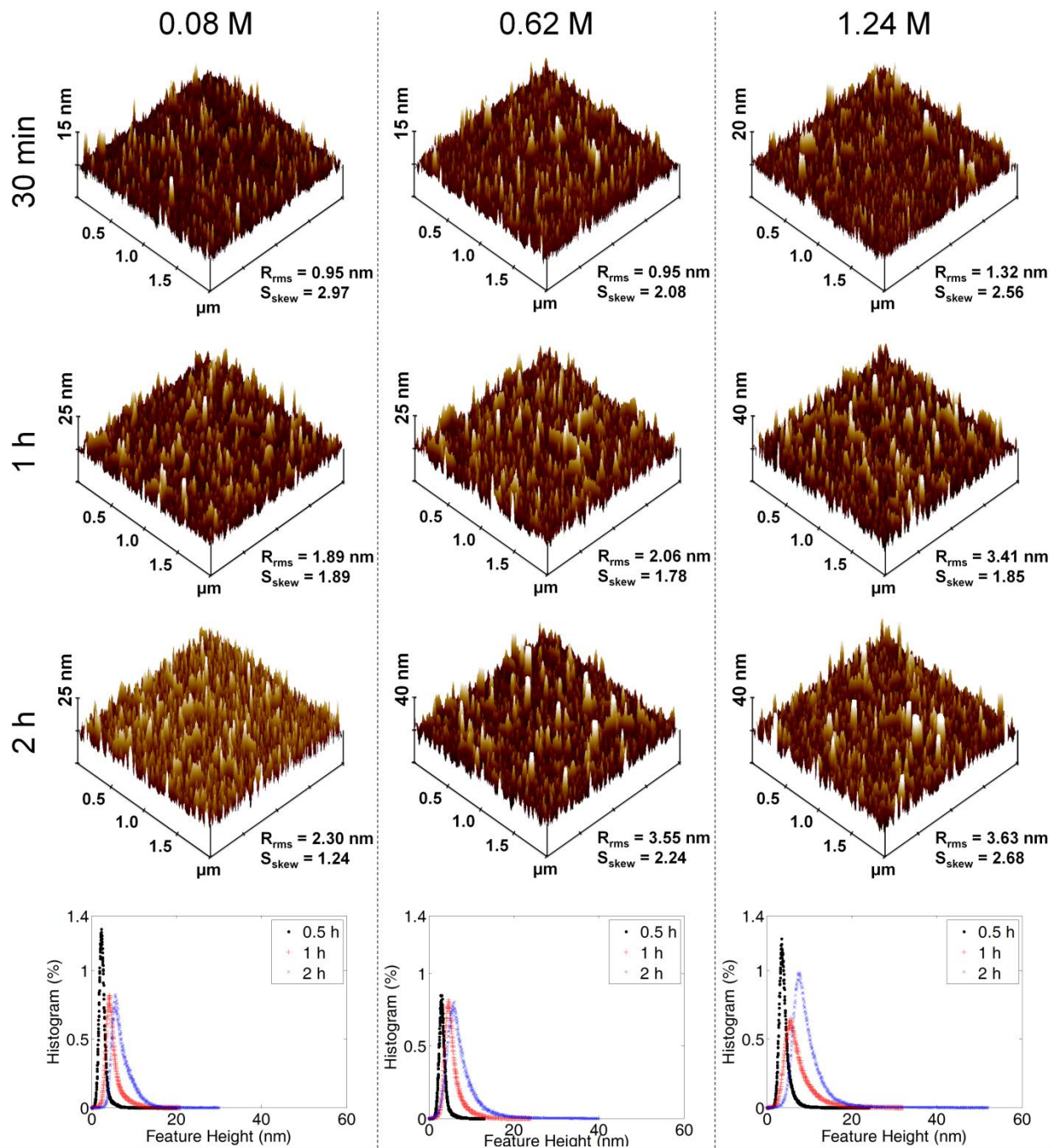
Figure 4-12e. AFM images and corresponding polymer surface feature height distributions for grafted PHEMA surfaces synthesized on PA-Si surfaces activated via He plasma. Graft polymerization was carried out at an initial monomer concentration range of $[M]_0 = 0.08 - 1.24$ M for a period of $0.5 - 2$ h at 50ºC.
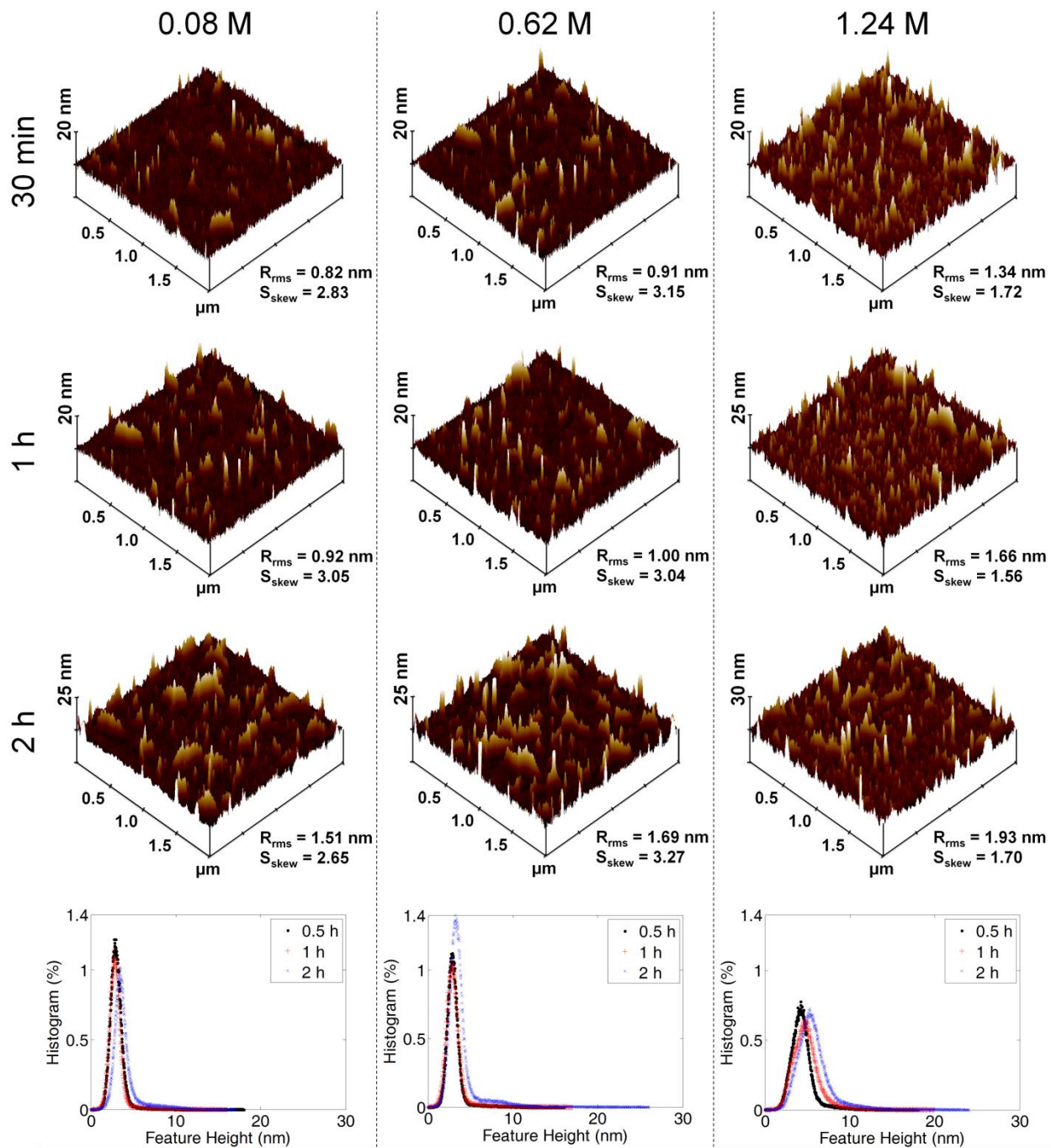
Figure 4-12f. AFM images and corresponding polymer surface feature height distributions for grafted PHEMA surfaces synthesized on PA-Si surfaces activated via H_2 plasma. Graft polymerization was carried out at an initial monomer concentration range of $[M]_0 = 0.08 - 1.24$ M for a period of $0.5 - 2$ h at 50ºC.
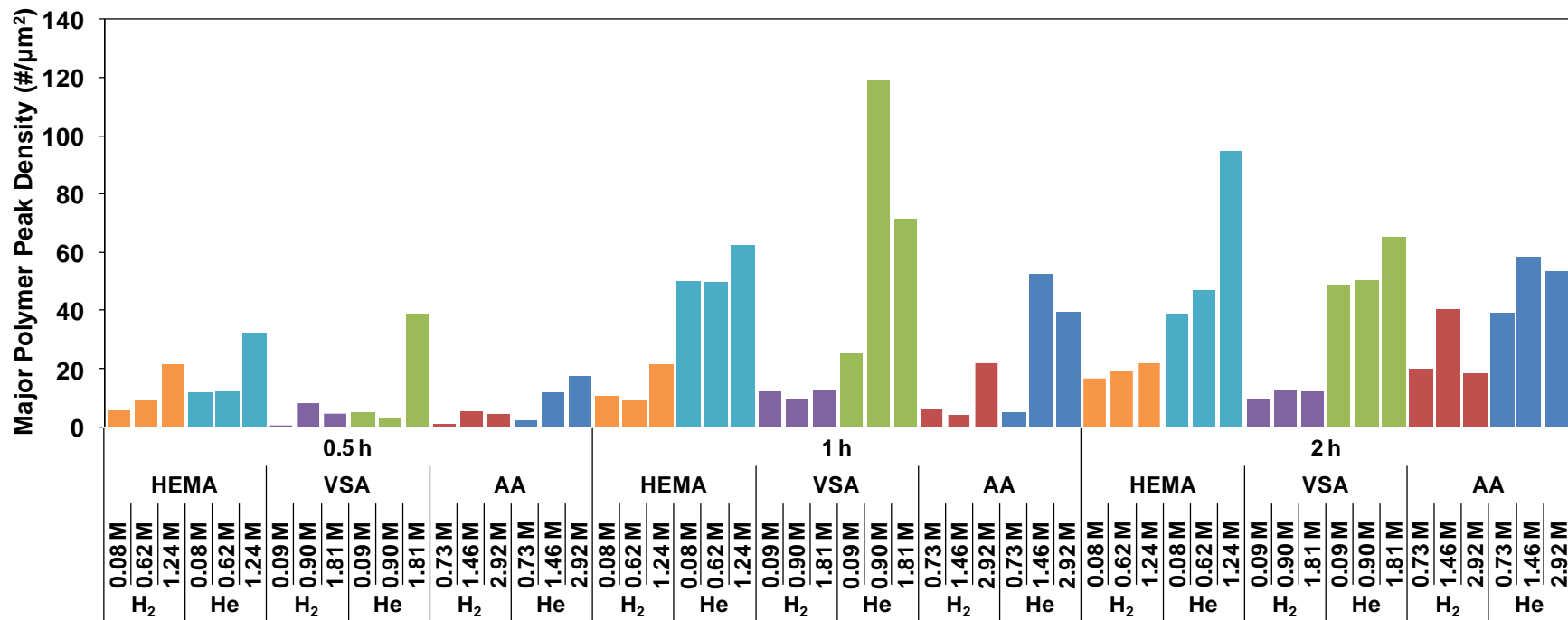
Figure 4-13. Number density of major polymer feature peaks for graft polymerized PAA, PVSA, and PHEMA on PA-Si surfaces synthesized at varying grafting conditions. Generally, grafted polymer layers were of higher density when synthesized on PA surfaces activated via He relative to H_2 plasma. Note: major peaks were defined as being above ~30% of the maximum peak height for each substrate.
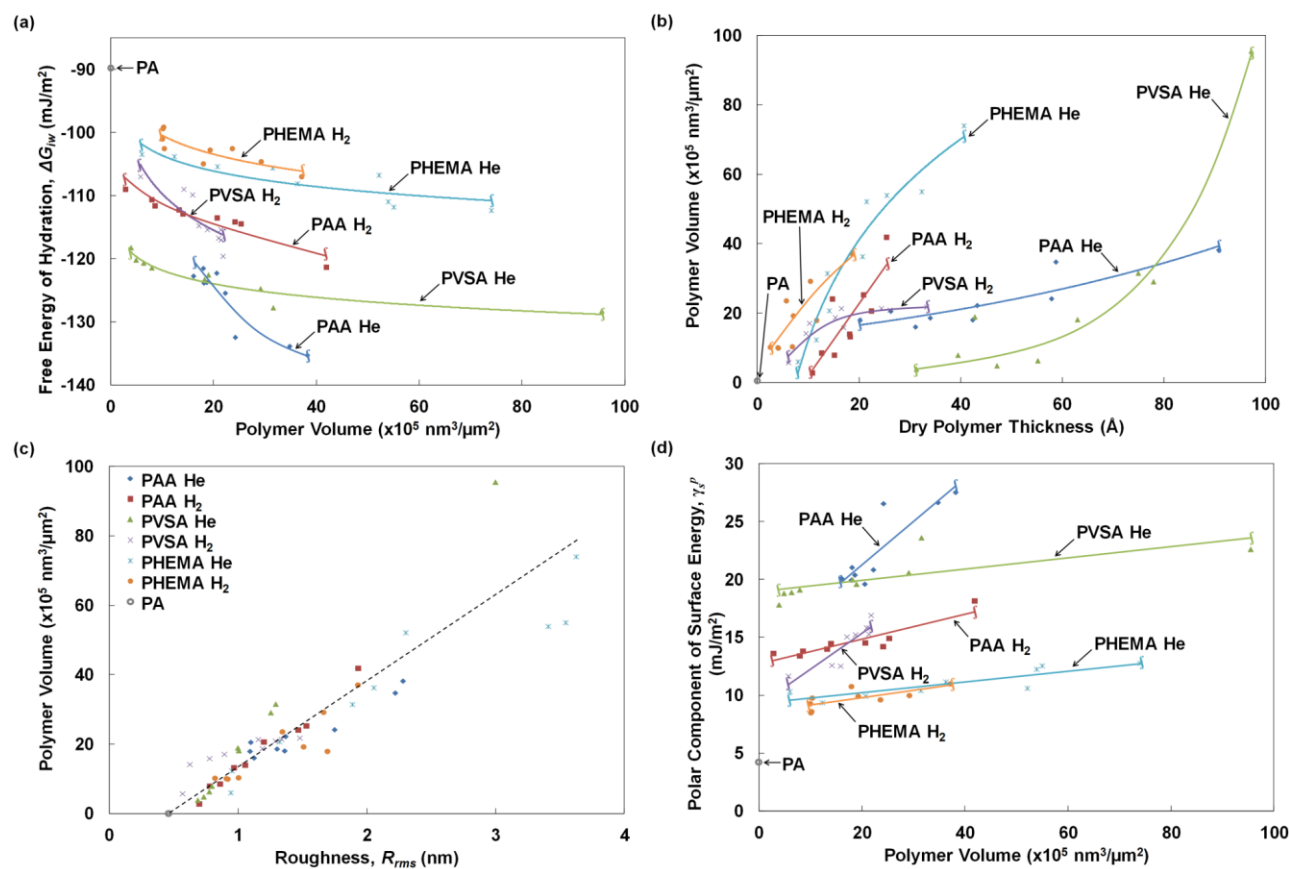
Figure 4-14. The grafted polymer layer volume increased with (a) decreasing free energy of hydration (i.e., increasing hydrophilicity), (b) increasing grafted polymer layer thickness, (c) increasing surface roughness, and (d) increasing polar component of surface energy. The SNS polymer surfaces were synthesized on PA surfaces (activated via He or H_2 APP) over a graft polymerization period of $0.5 - 2$ h and initial monomer concentrations of $0.73 - 2.92$ M, $0.09 - 1.81$ M, and $0.08 - 1.24$ M for PAA, PVSA, and PHEMA, respectively.

Table 4-4. SNS-PA-Si surface properties.

Surface	Plasma	Time (h)^a	$[M]_0$	R_{rms} (nm)	S_{skew} (%)	Avg. Feature Height (nm)	V (x10^5 nm^3/μm^2)^b	Grafted Polymer Layer Thickness (Å)	θ_w (°)^c	θ_d (°)^d	ΔG_{iw} (mJ/m^2)	γ_s^d (mJ/m^2)	γ_s^p (mJ/m^2)	γ_s (mJ/m^2)
PAA	He	2	2.92	2.28	4.34	5.79	38.2	90.8	30.9	35.6	-135.3	41.7	27.5	69.3
		2	1.46	1.75	1.04	4.39	24.2	57.9	35.0	39.8	-132.4	39.7	26.5	66.3
		2	0.73	1.37	1.31	4.20	22.2	43.2	43.7	35.9	-125.4	41.6	20.8	62.4
		1	2.92	2.22	1.97	5.45	34.8	58.7	33.0	36.2	-133.9	41.5	26.6	68.1
		1	1.46	1.36	1.33	3.78	18.1	42.3	45.5	41.2	-123.8	39.0	21.0	60.0
		1	0.73	1.13	0.81	3.58	16.1	31.1	46.7	40.2	-122.7	39.5	20.1	59.6
		0.5	2.92	1.30	1.32	3.84	18.6	34.0	45.6	38.7	-123.7	40.3	20.4	60.6
		0.5	1.46	1.10	0.58	4.03	20.6	26.2	47.2	39.3	-122.3	40.0	19.6	59.6
		0.5	0.73	1.09	0.77	3.77	18.0	20.2	48.0	42.7	-121.5	38.2	19.9	58.2
PAA	H$_2$	2	2.92	1.93	2.10	6.16	41.9	25.4	48.2	35.2	-121.3	41.9	18.2	60.1
		2	1.46	1.20	1.91	4.04	20.7	22.4	56.0	39.2	-113.5	40.0	14.5	54.5
		2	0.73	1.06	1.94	3.37	14.0	18.1	56.6	40.6	-112.9	39.3	14.5	53.8
		1	2.92	1.53	1.04	4.50	25.3	20.9	55.1	38.6	-114.5	40.3	14.9	55.2
		1	1.46	0.97	0.68	3.30	13.2	18.2	57.2	39.9	-112.2	39.7	14.0	53.7
		1	0.73	0.78	0.39	2.77	7.9	15.1	58.7	41.2	-110.6	39.0	13.4	52.4
		0.5	2.92	1.47	0.97	4.38	24.1	14.7	55.4	35.7	-114.1	41.7	14.2	55.9
		0.5	1.46	0.86	0.44	2.83	8.6	12.6	57.8	40.7	-111.6	39.3	13.8	53.1
		0.5	0.73	0.70	1.29	2.25	2.8	10.8	60.2	46.3	-109.0	36.3	13.6	49.9
PVSA	He	2	1.81	3.00	-0.07	11.52	95.5	97.2	40.4	35.6	-128.2	41.7	22.6	64.4
		2	0.9	1.26	-0.22	4.88	29.1	77.9	44.5	36.8	-124.7	41.2	20.6	61.8
		2	0.09	0.78	0.86	2.61	6.34	55.2	48.9	40.5	-120.7	39.4	18.9	58.2
		1	1.81	1.29	-0.17	5.13	31.6	74.9	41.0	41.1	-127.7	39.1	23.6	62.7
		1	0.9	1.01	0.52	3.79	18.2	63.0	46.1	38.2	-123.3	40.5	20.0	60.5
		1	0.09	0.73	0.52	2.46	4.9	47.1	49.4	41.4	-120.2	38.9	18.8	57.7
		0.5	1.81	1.00	0.52	3.87	19.0	42.8	46.9	38.5	-122.5	40.4	19.6	59.9
		0.5	0.9	0.80	0.69	2.77	7.9	39.5	48.1	39.4	-121.4	39.9	19.1	59.0
		0.5	0.09	0.69	0.52	2.36	3.9	31.3	51.4	42.2	-118.2	38.5	17.8	56.3

Surface	Plasma	Time (h)[a]	$[M]_0$	R_{rms} (nm)	S_{skew} (%)	Avg. Feature Height (nm)	V (x10^5 nm^3/μm^2)[b]	Grafted Polymer Layer Thickness (Å)	θ_w (°)[c]	θ_d (°)[d]	ΔG_{iw} (mJ/m^2)	γ_s^d (mJ/m^2)	γ_s^p (mJ/m^2)	γ_s (mJ/m^2)
PVSA	H$_2$	2	1.81	1.48	2.73	4.15	21.8	33.3	50.0	34.0	-119.6	42.5	16.9	59.4
		2	0.9	1.34	3.50	4.11	21.4	24.4	52.6	36.0	-117.0	41.6	15.8	57.4
		2	0.09	1.19	2.38	3.85	18.8	15.3	54.2	37.6	-115.4	40.8	15.2	56.0
		1	1.81	1.29	3.20	4.07	20.9	26.1	52.9	36.9	-116.7	41.1	15.8	57.0
		1	0.9	1.16	3.39	4.11	21.4	16.5	54.2	37.8	-115.4	40.7	15.3	56.0
		1	0.09	0.89	0.64	3.68	17.1	10.2	54.8	38.4	-114.8	40.4	15.0	55.5
		0.5	1.81	0.78	2.81	3.56	15.9	17.0	59.4	38.5	-109.9	40.4	12.5	52.9
		0.5	0.9	0.63	1.73	3.39	14.2	9.5	60.2	41.2	-109.0	39.0	12.6	51.6
		0.5	0.09	0.57	0.84	2.55	5.7	6.1	62.0	41.5	-107.0	38.8	11.7	50.5
PHEMA	He	2	1.24	3.63	2.68	9.37	74.0	40.6	57.1	32.6	-112.3	43.1	12.8	55.9
		2	0.62	3.55	2.24	7.47	55.0	32.3	57.6	32.9	-111.8	43.0	12.5	55.5
		2	0.08	2.30	1.24	7.19	52.1	21.5	62.2	35.9	-106.8	41.6	10.6	52.2
		1	1.24	3.41	1.85	7.37	53.9	25.4	58.4	33.7	-110.9	42.6	12.2	54.9
		1	0.62	2.06	1.78	5.60	36.3	20.7	61.0	35.5	-108.1	41.8	11.2	53.0
		1	0.08	1.89	1.89	5.12	31.4	13.7	63.2	37.9	-105.6	40.7	10.4	51.1
		0.5	1.24	1.32	2.56	4.04	20.7	14.1	63.4	35.4	-105.4	41.8	9.9	51.8
		0.5	0.62	0.95	2.08	3.20	12.3	11.6	64.8	36.3	-103.8	41.4	9.4	50.8
		0.5	0.08	0.95	2.97	2.57	6.0	8.0	65.1	43.2	-103.5	38.0	10.3	48.3
PHEMA	H$_2$	2	1.24	1.93	1.70	5.68	37.1	18.7	62.0	37.6	-107.0	40.8	11.0	51.8
		2	0.62	1.69	3.27	3.77	18.0	11.6	63.8	41.8	-104.9	38.7	10.8	49.5
		2	0.08	1.51	2.65	3.90	19.3	7.0	65.7	42.5	-102.8	38.3	9.9	48.2
		1	1.24	1.66	1.56	4.89	29.2	10.4	64.1	38.1	-104.6	40.6	10.0	50.5
		1	0.62	1.00	3.04	3.01	10.4	6.9	65.9	42.3	-102.5	38.4	9.8	48.2
		1	0.08	0.92	3.05	2.97	10.0	4.1	67.2	43.3	-101.0	37.9	9.3	47.2
		0.5	1.24	1.34	1.72	4.33	23.6	5.7	65.9	41.4	-102.5	38.9	9.6	48.5
		0.5	0.62	0.91	3.15	2.98	10.1	4.0	68.6	42.7	-99.4	38.2	8.5	46.7
		0.5	0.08	0.82	2.83	3.00	10.2	2.5	68.8	43.9	-99.1	37.6	8.6	46.2

[a] graft polymerization reaction time; [b] exposed polymer volume (V) as determined by AFM; [c] $\theta_{w=}$ water contact angle; [d] $\theta_{d=}$ diiodomethane contact angle

Chapter 5. Synthesis of End-Grafted Polymer Chains on Polyamide Reverse Osmosis Membranes

5.1 Introduction

Water desalination via reverse osmosis (RO) membrane technology is critical for producing (post-secondary treatment) potable water from municipal, industrial and agricultural wastewater, and seawater. However, biofouling on RO membrane surfaces inhibits the economic feasibility of widespread commercial use (Chapter 2, Section 2.7). Membrane surface modification with the aim of increasing surface hydrophilicity and decreasing membrane fouling propensity has achieved increased attention over the past several years [9, 40, 59-61].

In particular, surface modification can be carried out via free radical graft polymerization (FRGP) to surface nanostructure RO membranes with polymer chains (Chapter 2, Section 2.4). In the FRGP approach of modifying PA-thin film composite (TFC) membranes, the monomers used must be nontoxic, water soluble, commercially and economically feasible, have a vinyl group, and a low free radical polymerization reaction temperature. Furthermore, specific chemical functionalities such as hydrophilic or negative groups would be potentially desirable for reducing the membrane surface biofouling propensity. The candidate monomers that were selected from the above criteria were acrylic acid, vinylsulfonic acid, methacrylic acid, and acrylamide. Acrylic acid and vinylsulfonic acid monomers were chosen because of their superior surface properties in terms of hydrophilicity (ΔG_{iw} = -135 $-$ -107 mJ/m^2) and controlled surface roughness ($R_{rms} \lesssim 3$ nm) after atmospheric pressure plasma induced FRGP onto PA-Si substrates (Chapter 1 and Chapter 4, Section 4.3). Methacrylic acid and acrylamide selected due to their resistance to mineral salt and organic fouling [12]. Accordingly, this chapter presents the

approach of synthesizing surface nanostructured polyamide thin film composite (SNS-PA-TFC) RO membranes with the above monomers. Membrane performance was evaluated and surface properties (e.g., hydrophilicity, topography, and surface charge) were examined to identify functionalities that would be suitable for imparting biofouling resistance.

5.2   Materials and Methods

5.2.1   Materials

The base polyamide membrane was synthesized, on 200 μm polysulfone support (Hydranautics, Oceanside, CA; Koch, Wilmington, MA), with 1,3-phenylenediamine (MPDA, 99%) and 1,3,5-benzenetricarboxylic chloride (TMC, 98%) (Sigma-Aldrich, St Louis, MO). Hexane (≥99%, Sigma-Aldrich, St Louis, MO) was the organic solvent for the TMC solution. Atmospheric pressure plasma was generated using ultra high purity hydrogen (99.999%, Air Liquide, Los Angeles, CA) and helium (99.999%, Airgas, Los Angeles, CA) gases. Oxygen gas (99%, Airgas, Los Angeles, CA) was also used for surface treatment. Acrylic acid (AA, 99%, Aldrich, St. Louis, MO), vinylsulfonic acid, sodium salt solution (VSA, 25 wt. % in H_2O, Aldrich, St. Louis, MO), methacrylic acid (MAA, 98%, Fluka, Ronkonkoma, NY) and acrylamide (AAm, 99%, Fisher Chemicals, Fair Lawn, NJ) monomers were used for aqueous free radical graft polymerization. Ultra-pure deionized (DI) water produced by filtering distilled water through a Milli-Q filtration system (EMD Millipore, Temecula, CA) was the aqueous solvent used in monomer solutions. Surface characterization and performance of the nanostructured polyamide thin film composite membranes were compared to a commercial RO

membrane (ESPA2, Hydranautics, Oceanside, CA) which is utilized for RO desalination of treated wastewater prior to aquifer recharge [243].

5.2.2 Membrane Synthesis

The surface nanostructured polyamide thin-film composite (SNS-PA-TFC) membranes were synthesized by atmospheric pressure plasma induced graft polymerization (APPIGP), a sequential process consisting of: (1) polyamide surface preparation, (2) plasma surface activation, and (3) graft polymerization [11-12] (Figure 5-1). First, a polyamide thin film composite (PA-TFC) membrane was created by polyamide interfacial polymerization onto a polysulfone (PSf) sheet (200 μm thick) [187, 244]. In this process, an aqueous solution of 2.5 wt% MPDA was exposed to one side of the PSf support layer. After a 3 min adsorption period, the excess MPDA solution was removed with a rubber roller (NC9638424, Fisher Chemicals, Fair Lawn, NJ). Subsequently, the MPDA adsorption side of the membrane was exposed to 0.13 wt% TMC in hexane. After a 15 − 30 s interfacial polymerization reaction time, the excess TMC solution was drained and the PA-TFC was cured in a vacuum oven for 30 s at 80°C. The PA-TFC was then placed in a dark compartment before further use. Atmospheric pressure plasma jet (APPJ) PA surface activation was performed with pure helium gas at a power of 50 W (for the poly(acrylic acid) (PAA) and poly(vinylsulfonic acid) (PVSA) PA-TFC membranes; Appendix C.2) or with a mixture of gases of 1 vol% hydrogen and 99 vol% helium (for poly(methacrylic acid) (PMAA) and polyacrylamide (PAAm) PA-TFC membranes; Appendix C.1). All surfaces were treated with APPJ for 5 − 20 s followed by exposure to an impinging oxygen gas stream for 1 − 2 min. Lastly, the activated PA-TFC surfaces underwent graft polymerization for 30 minutes with aqueous vinyl monomer solutions of acrylic acid,

vinylsulfonic acid, methacrylic acid, or acrylamide at initial monomer ($[M]_0$) concentrations of 1.81 M at 60°C, 2.92 M at 70°C, 1.17 M at 60°C, and 0.3 M at 70°C, respectively. It is noted that the above reaction conditions were previously determined to be optimal for creating surfaces of low free energy of hydration (i.e., high level of hydrophilicity) while maintaining relatively low surface roughness ($R_{rms} \leq 3$ nm) for the synthesis of SNS-PA-silicon surfaces with AA and VSA (Chapter 4, Section 4.3), and for the synthesis of SNS-TFC membranes that demonstrated increased mineral scaling resistance for MAA and AAm [12]. At the termination of the graft polymerization period, the SNS-PA-TFC membranes were thoroughly washed with DI water to remove any un-grafted material and stored in DI water until use. The resulting PAA-PA-TFC, PVSA-PA-TFC, PMAA-PA-TFC, or PAAm-PA-TFC membranes consisted of a grafted layer of PAA, PVSA, PMAA, or PAAm chains that are terminally and covalently tethered to the PA-TFC surface.
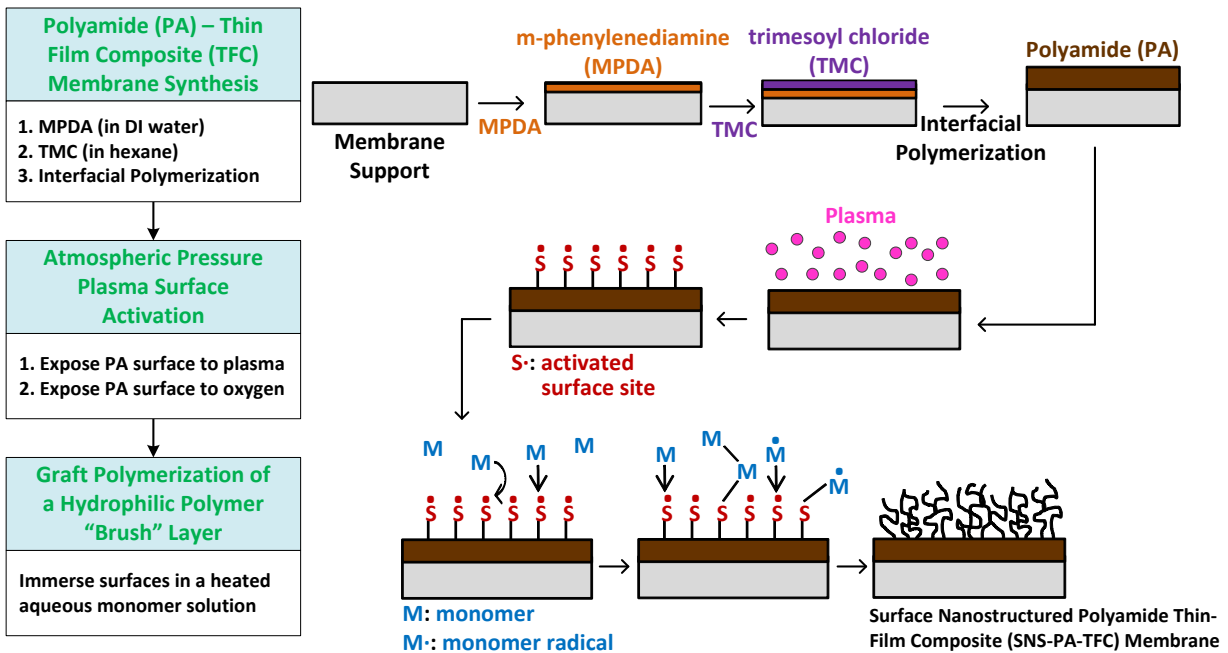
Figure 5-1. Atmospheric pressure plasma induced graft polymerization (APPIGP) process for synthesis of surface nanostructured RO PA membranes.

5.2.3   Plate-and-Frame Reserve Osmosis Systems

Two similar plate-and-frame RO (PFRO) membrane systems were used (Figure 5-2). For both systems, water was fed to the PFRO membrane channel using a high pressure 1/2 hp (373 W) positive displacement feed water pump (Hydra-Cell Pump Model No. M03XRSGSHEP, Wanner Engineering Inc., Minneapolis, MN). The transmembrane pressure and feed water flow rate were regulated by adjusting the pump variable frequency drive (VFD) (L100, Hitachi, Tokyo, Japan), and bypass and backpressure valves. The permeate flowrate was measured with a FlowCal 5000 digital flow meter (Tovatech, South Orange, NJ) for both systems. The first PFRO system (Figure 5-2a) consisted of a flow channel having dimensions of 1.65 cm (width) x 2.92 cm (length) x 0.238 cm (height) with an active flat sheet membrane area of 4.82 cm^2. The feed side pressure was monitored with a digital gauge pressure (PGP-25B-300, Omega, Stamford, CT) and a digital flow meter (S-112, Georgetown, TX) was used to monitor the feed flow rate (Appendix E). This system configuration was designed for automated operation and data acquisition via Labview (Appendix E, Section E.2.2). Automation enabled the VFD and valve settings to be accurately set through the appropriate control action to attain the desired transmembrane pressure and feed water flow rate. An earlier PFRO system (Figure 5-2b) relied on manual manipulation of the VFD and valve settings. This system had a flow cell of dimensions 1.63 cm (width) x 3.2 cm (length) x 0.215 cm (height) with a 5.22 cm^2 active membrane area. Feed flow rate and pressure were monitored using a PMRI – 010747 digital flow meter (Cole-Parmer, Vernon Hills, IL) and a digital pressure gauge (Achcroft, Milford, CT), respectively.
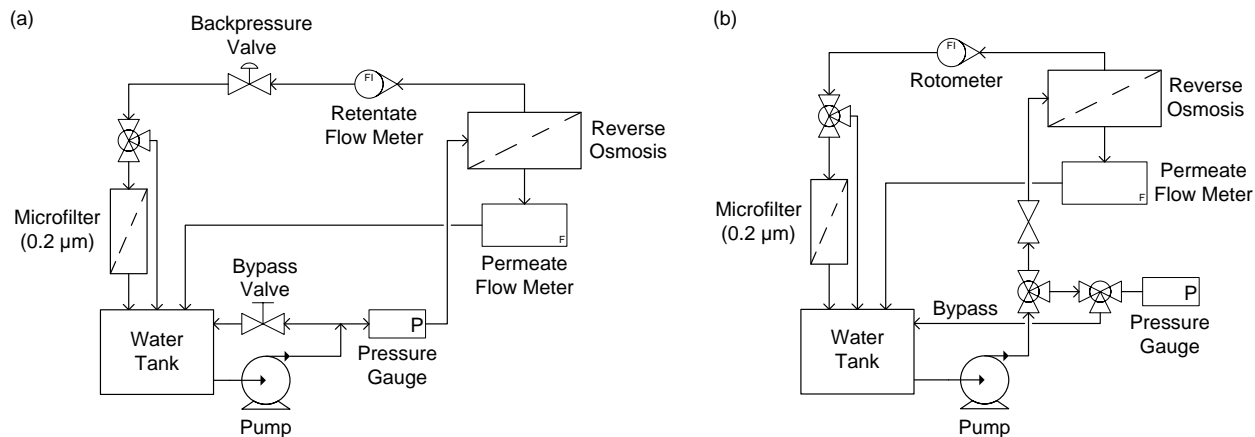
Figure 5-2. PFRO systems used to evaluate the performance of the following nanostructured membranes: (a) PAA-PA-PSf and PVSA-PA-PSf, and (b) PMAA-PA-PSf and PAAm-PA-PSf.

5.2.4   Membrane Characterization

Surface topography of the SNS-PA-PSf and commercial membranes was analyzed by tapping mode Atomic Force Microscopy (AFM) (Veeco MultiMode Nanoscope IIIa AFM; Digital Instruments, Santa Barbara, CA) as previously described in Chapter 3, Section 3.2.3. AFM scans were scans taken in a 10 μm x 10 μm area. Membrane surface hydrophilicity was assessed by captive bubble contact angle measurements (Kruss Model DSA 100, Germany) with 6 μL air bubbles while the membrane was submerged in DI water at 22°C. Each reported contact angle represents the average of at least three replicate measurements. The zeta potential, or the electrical potential at the surface of shear, was used to characterize the electrical charge of the membrane surface [245]. The streaming potential was measured across the membrane surface using a SurPASS Electro-kinetic Analyzer (Anton-Paar KG, Graz, Austria) equipped with a flat-plate measuring cell (55 mm × 25 mm). The streaming potential was determined in a 10 mM KCl

solution at pH 7.6 (by dosing with 0.1 M KOH) from 0 – 600 mbar. The zeta potential (ζ) was determined from the Helmholtz-Smoluchowski equation (Equation (5-1)) [246]

$$\zeta = \frac{E_s}{\Delta P}\frac{\eta}{\varepsilon\varepsilon_0}\frac{L}{A}\frac{1}{R} \tag{5-1}$$

where E_s is the streaming potential, ΔP is the applied transmembrane pressure, η is the liquid viscosity, ε is the liquid permittivity, ε_0 is the permittivity of vacuum/free space, R is the electrical resistance across the medium, and L and A are the length and cross sectional area of the flow channel, respectively.

Membrane intrinsic permeability was determined with DI water over a feed pressure range of 120 – 300 psi (~ 825 – 2070 kPa) and crossflow velocity of 0.07 – 0.15 m/s. The observed salt rejection was calculated from conductivity measurements (CON 11 Economy Meter, Oakton Instruments, Vernon Hills, IL) assessed during the filtration of a 1000 ppm NaCl feed solution at 225 psi.

5.3   Results and Discussion

The PAA-PA-TFC ($[M]_0$ = 1.81 M at 60°C), PVSA-PA-TFC ($[M]_0$ = 2.92 M at 70°C), PMAA-PA-TFC ($[M]_0$ = 1.17 M at 60°C), and PAAm-PA-TFC ($[M]_0$ = 0.3 M at 70°C) membranes had surface roughnesses (R_{rms}) of 54.8 nm, 59.0 nm, 38.2 nm, and 27.4 nm, respectively (Table 5-1, Figure 5-3, and Figure 5-4). It is noted that the lowest surface roughness was achieved for the SNS-PA-TFC membrane synthesized at 0.3 M AAm at 70°C and reaction time of 30 min. Surface roughness varied depending on the interfacial polymerization reaction time for the underlying PA-TFC. In particular, ranking of the surface roughness was in the order

of PAAm-PA-TFC < PMAA-PA-TFC < PAA-PA-TFC < PVSA-PA-TFC, which is congruent with the increasing interfacial polymerization time for their underlying PA-TFC layers of 15 s, 17 s, 25 s, and 27 s, respectively. For example, lower surface roughness of the underlying PA-TFC for the PAAm (R_{rms} ~ 20 nm) membrane compared to the PMAA (R_{rms} ~32 nm) membrane enabled lower surface roughness for the graft polymerized PAAm-PA-TFC (R_{rms} = 27.4 nm) compared to PMAA-PA-TFC (R_{rms} = 38.2 nm).

Although the PMAA-PA-TFC membrane did not have the lowest surface roughness, it achieved the lowest contact angle (42.2^{o}) in comparison to the PAA-PA-TFC (50.3^{o}), PVSA-PA-TFC (58.4^{o}), PAAm-PA-TFC (60.1^{o}), and ESPA2 (61.3^{o}) membranes. The above results suggests that the carboxylic groups of the grafted poly(methacrylic acid) induce a lower the negative surface charge for PMAA-PA-TFC, as shown by zeta potential measurements (Table 5-1), causing decreased contact angle (i.e., increased surface hydrophilicity). The effect of surface charge on increasing surface hydrophilicity proves to be paramount, notwithstanding studies that suggest increased surface roughness of PMAA-PA-TFC, relative to PAAm-PA-TFC, would lead to increase surface hydrophobicity [247]. Also, it is suggested the relatively high hydrophilicity of the PMAA-PA-TFC membrane would promote decreased biofouling during water filtration due to increased replusion of hydrophobic boifoulants (Chapter 2, Section 2.2).

The efficiency of RO desalination in term of membrane permeability was found to be significantly higher for the SNS-PA-TFC membranes ($13 - 58\%$) compared to the commercial ESPA2 membrane (Table 5-1). The PMAA-PA-TFC membrane had the highest permeability, which is hypothesized to be attributed to, in part, the relatively high level of surface hydrophilicity (as measured by contact angle). Lastly, the ability of the membrane to reject

monovalent salt for all the SNS-PA-TFC membranes was slightly greater by 1.2 – 2.7% compared to the ESPA2 membrane.

Table 5-1. Membrane surface properties and performance.

Membrane	Surface Roughness (nm)	Contact Angle (º)	Zeta Potential (mV)	Permeability (x 10^{-11} m/s·Pa)	Rejection [a] (%)
PAA-PA-TFC	54.8	50.3	-44.6	1.64	95.6
PVSA-PA-TFC	59.0	58.4	-33.9	1.32	96.6
PAAm-PA-TFC	27.4	60.1	-18.3	1.41	95.8
PMAA-PA-TFC	38.2	42.2	-44.3	1.85	95.2
ESPA2	52.6	61.3	-27.8	1.17	94.1

[a] Salt rejection measured with 1000 ppm NaCl

(a) **PAA-SNS-PA-TFC ([M$_0$] = 2.92 M)**

R$_{rms}$ = 54.8 nm
S$_{skew}$ = 0.619

(b) **PVSA-SNS-PA-TFC ([M$_0$] = 1.81 M)**

R$_{rms}$ = 59.0 nm
S$_{skew}$ = 0.932
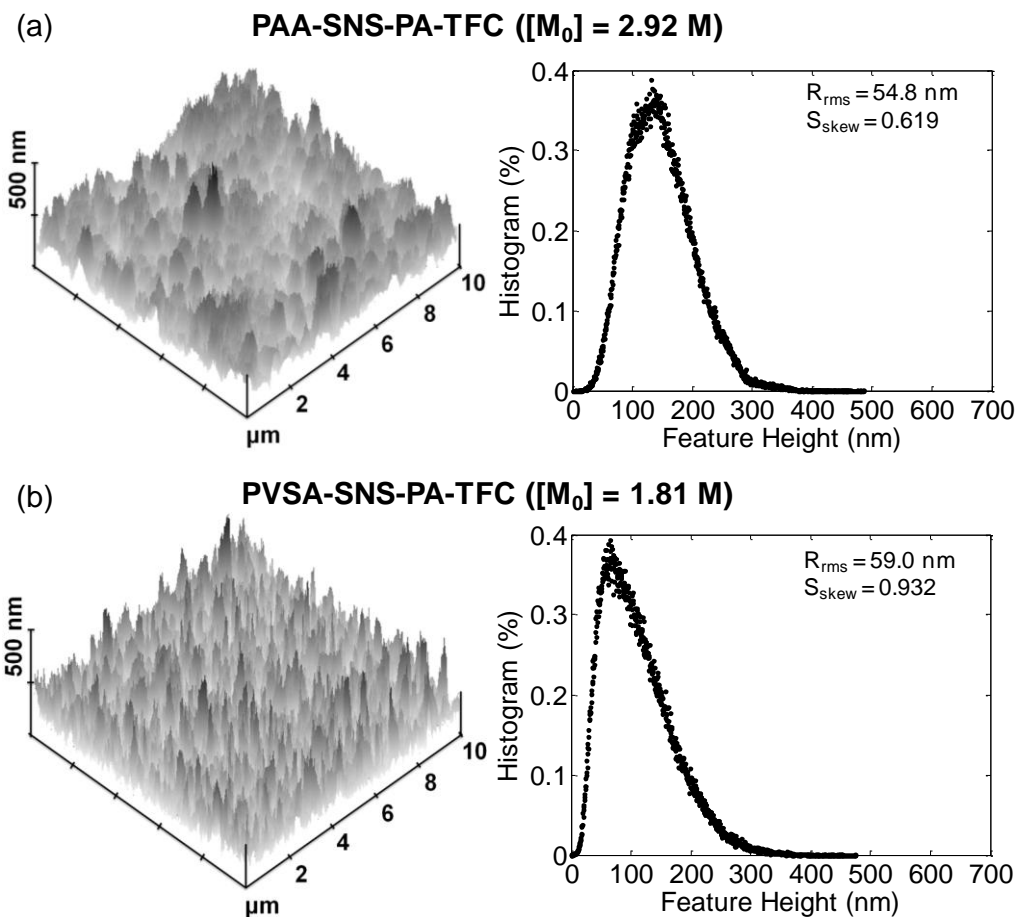
Figure 5-3. Membrane AFM images: (a) PAA-PA-TFC membrane synthesized at an initial monomer concentration of 2.92 M at 70°C and reaction time of 30 min, and (b) PVSA-PA-TFC membrane synthesized at an initial monomer concentration of 1.81 M at 60°C and reaction time of 30 min.
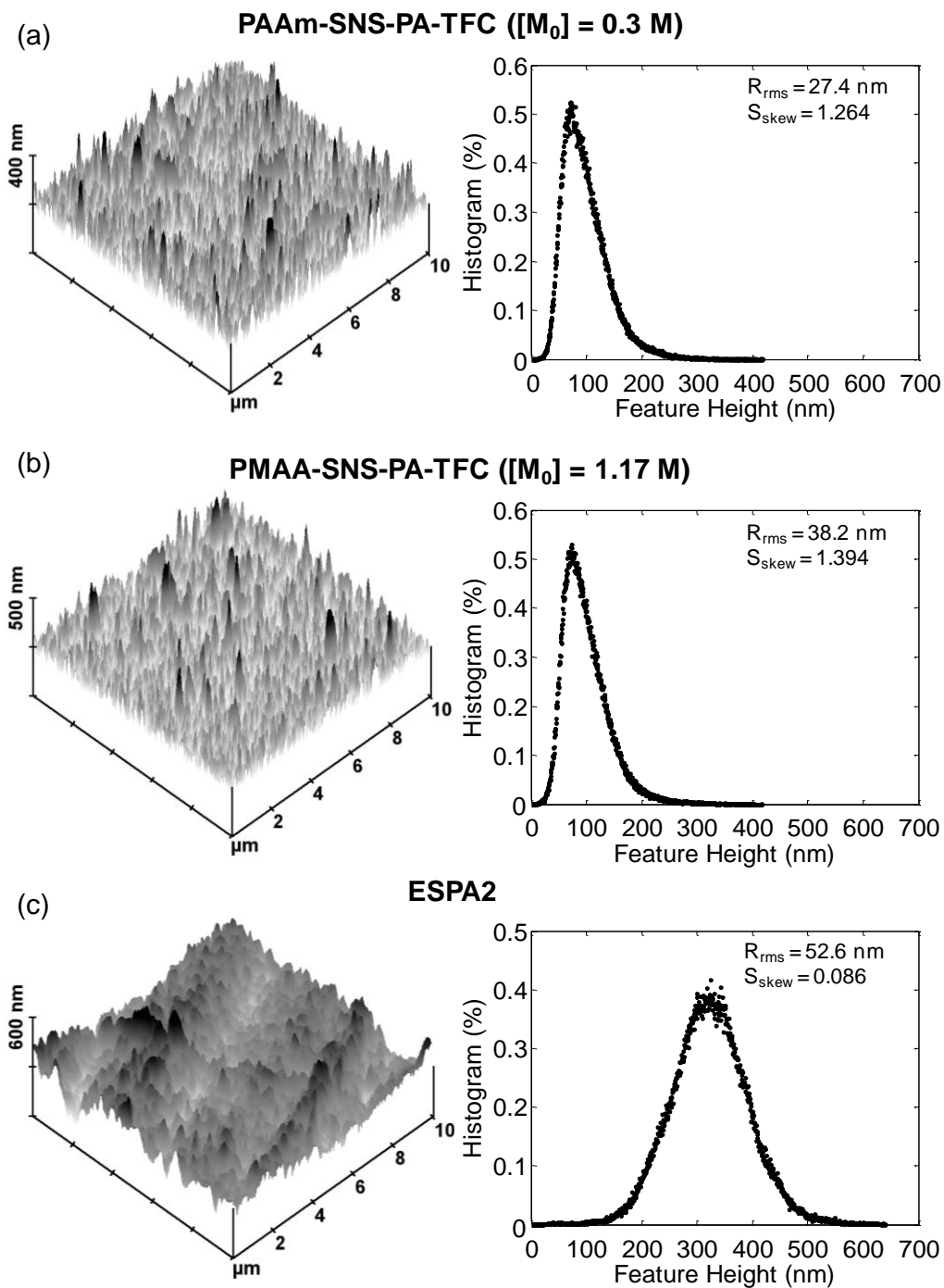
Figure 5-4. Membrane AFM images: (a) PMAA-PA-TFC membrane synthesized at an initial monomer concentration of 0.3 M at 70°C and reaction time of 30 min, (b) PAAm- PA-TFC membrane synthesized at an initial monomer concentration of 1.17 M at 60°C and reaction time of 30 min, and (c) ESPA2.

5.4   Conclusions

A new class of RO membranes was developed with hydrophilic polymer chains of poly(acrylic acid) (PAA), poly(vinylsulfonic acid) (PVSA), poly(methacrylic acid) (PMAA), or polyacrylamide (PAAm) that were terminally and covalently bonded to a polyamide-thin film composite (PA-TFC) membrane surface. It was shown that the surface nanostructured (SNS)-PA-TFC membranes, owing to their hydrophilic surface brush layer, were of improved performance in terms of their higher permeability. The PAAm-PA-TFC membrane, which had the lowest surface roughness (27 nm), was the most promising membrane for imparting surface biofouling resistance. Furthermore, the PMAA-PA-TFC membrane proved to have both the highest permeability and lowest contact angle (i.e., highest hydrophilicity). The relatively high hydrophilicity observed on the PMAA-PA-TFC membrane would be expected to assist in reducing biofoulant-surface affinity. Accordingly, the PAAm-PA-TFC and PMAA-PA-TFC membranes were selected for subsequent biofouling studies of RO membranes.

Chapter 6.   Biofouling and Cleaning Effectiveness of Surface Nanostructured Reverse Osmosis Membranes

6.1   Introduction

Membrane fouling remains a major challenge in the operation of RO plants [248]. In particular, membrane biofouling [2, 209, 249], which is commonly referred to the unwanted bacterial deposition and growth of biofilms, is of major concern in water reuse applications of RO desalting. Biofouling increases membrane's resistance to water permeation and can reduce membrane longevity. Although pretreatment and chemical cleaning methods have been used to combat membrane biofouling, bacteria attachment and biofilm formation on RO membranes still occurs due to the self-replicating capability of the minuscule amount (~0.01%) of microorganisms that evade the pretreatment process (Chapter 1, Section 1.1 and Chapter 2, Section 2.2) [4, 8]. Furthermore, pretreatment methods are costly and may result in membrane damage.

Surface nanostructuring of RO membranes by attaching layer of polymer chains (i.e., "brush layer") to the membrane surface can increase surface hydrophilicity to facilitate decreased membrane mineral scaling and organic fouling [10, 40, 59-61]. A particular study [11-12] reported that surface nanostructuring of polyamide thin film composite (PA-TFC) RO membranes with hydrophilic poly(methacrylic acid) (PMAA) and poly(acrylamide) (PAAm) brush layers resulted in increased membrane permeability, greater mineral scaling resistance, and comparable fouling resistance for model organic scalants (i.e. BSA and alginic acid) compared to a commercial RO membrane with high productivity and salt rejection. It has been hypothesized [11-12] that the hydrophilic brush layer chains, which were covalently bonded to the membrane surface, employ Brownian motion and sufficiently screen the underlying PA surface. Thus, the

probability of attachment of mineral scalants and organic macromolecules to the surface of nanostructured (SNS) PA-TFC membranes was reduced. In this same regard, it is envisioned that the SNS-PA-TFC membranes would have a lower biofouling propensity.

The present chapter explores the biofouling resistance of the SNS-PA-TFC class of membranes, as well as the effectiveness of cleaning the biofouled membranes. Biofouling resistance of synthesized SNS-PA-TFC-RO membranes was examined during desalination of secondary wastewater effluent (Orange County Water District (OCWD) Groundwater Replenishment System (GWRS), Fountain Valley, CA). Real-time monitoring of biofilm growth, carried out using OCWD water, was performed with a small transparent plate-and-frame RO cell [11-12]. The biofouled membrane was imaged by confocal laser scanning microscopy (CLSM) and scanning electron microscopy (SEM), and the biofilm density was quantified by extracellular polymeric substances (EPS) analysis. Membrane performance was monitored in terms of monovalent salt (NaCl) rejection and permeate flux decline during biofilm growth and effectiveness of permeability recovery by DI water and chemical cleaning with a $Na_2 \cdot EDTA$ solution.

6.2   Experimental

6.2.1   Materials and Reagents

The feed water used in the biofilm filtration study was unchlorinated secondary municipal wastewater effluent obtained from the OCWD-GWRS facility. This water source consisted of 80% activated sludge and 20% trickling filter effluents (Table 6-1). For chemical cleaning of the membrane system, an aqueous solution of disodium ethylenediamine-tetraacetic acid

(Na$_2$·EDTA, Fisher Scientific, Pittsburgh, PA) used. Membranes were exposed to aqueous solutions of glutaraldehyde and phosphate buffered saline (PBS) (Sigma Aldrich, St. Louis, MO) to preserve the biofilm on the membrane surface.

Table 6-1. Water analysis of the OCWD secondary wastewater effluent [a].

Parameter	Quantity	Units
pH	7.6	dimensionless
Total dissolved solids	990	mg/L
Suspended Solids	6.42	mg/L
Total Coliform	1001	MPN [b]/100 mL
Fecal Coliform	113	MPN/100 mL
Enterococcus	237	CFU [c]/100 mL
E. *coli*	77	CFU/100 mL
Total Hardness (as CaCO$_3$)	281	mg/L
Boron	0.39	mg/L
Calcium	75.9	mg/L
Phosphate phosphorous	0.19	mg/L
Potassium	16.7	mg/L
Sodium	219	mg/L
Silica	21.7	mg/L
Sulfate	227	mg/L
Total nitrogen	11.7	mg/L
Total organic carbon	10	mg/L
Calcite (CaCO$_3$) saturation index	$< 4.8 \times 10^{-4}$	dimensionless
Calcium Orthophosphate (Ca$_3$(PO$_4$)$_2$) saturation index	0.155	dimensionless
Gypsum (CaSO$_4$·2H$_2$O) saturation index	0.041	dimensionless

[a] Source: Orange County Water District (OCWD) Groundwater Replenishment System (GWRS) treatment facility, Orange County Water District Research Center, Fountain Valley, CA
[b] MPN/100mL - most probable number per 100 mL solution
[c] CFU/100mL - colony forming units per 100 mL solution

Poly(methacrylic acid) (PMAA) and poly(acrylamide) (PAAm) SNS-PA-TFC membranes were synthesized as described in Chapter 5. Briefly, the PMAA and PAAm membranes achieved high observed salt rejection (1000 ppm NaCl) and exceptional water permeability of 95.2% and 95.8%, and 1.85 x 10^{-11} m/s·Pa and 1.41 x 10^{-11} m/s·Pa, respectively. Biofouling resistance of the

SNS membranes was compared to a commercial RO membrane (ESPA2, Hydranautics, Oceanside, CA) with a similar observed salt (NaCl) rejection (94.1%) and lower water permeability (1.17 x 10^{-11} m/s·Pa). It is important to note that ESPA2 was chosen for comparison of membrane performance with respect to biofouling resistance because it was utilized for RO desalination in the same water treatment plant (OCWD-GWRS) where the source water for this investigation was from [243].

6.2.2 Membrane Biofilm Characterization

At the termination of each experiment, the membrane sheets were removed from the cell and preserved for surface analysis. The biofilms on the membrane surfaces were preserved by first immersing the membrane coupon in an aqueous solution of 4 wt% glutaraldehyde for 30 min at 4ºC [243]. The membrane was drip dried, followed by exposure to 1x phosphate buffered saline (PBS) at pH = 7.2 for 1 min. Afterwards, the membrane was again drip dried and stored in a 40 mL glass vial filled with an aqueous solution of 50 vol% ethanol at 4ºC. The biofouled membranes were cut into a 0.5 cm x 0.5 cm segment for confocal laser scanning microscopy (CLSM) analysis, and into 2.5 cm x 1 cm segments for extracellular polymeric substances (EPS) analysis. CLSM and EPS analyses followed the basic protocols reported by [250] and [251-252], respectively.

CLSM analysis (Leica Confocal SP1 MP-inverted, Leica, Buffalo Grove, IL) enabled observation of the distinct morphology and thickness of the hydrated biofilm matrix [243]. The membrane preparation protocol involved of first staining the membrane samples using propidium iodide from LIVE/DEAD BacLight Bacterial Viability Kits (L13152, Molecular Probes, Eugene,

OR) in accordance with manufacturer's specifications. The contents of one pipette of propidium iodide (Component B; excitation = 490 nm, emission = 635 nm) from the kit were dissolved in 2.5 mL of DI water to obtain a 30μM propidium iodide solution. Subsequently, 1 mL of the propidium iodide solution was pipetted onto the surface of the biofouled membrane and placed in the dark for 15 minutes. After draining the excess solution, the stained membrane was mounted on a glass slide, using the above kit's BacLight mounting oil (Component C). In order to image the biofilm vial CLSM, a thin cover slide (0.16 – 0.19 mm) was carefully and lightly placed in between the oil on top of the biofilm and the objective lens to prevent the lens from contacting the mounting oil.

EPS analysis [251-252] provides a quantitative assessment or indication of the proteins and polysaccharides contained in the biofilm matrix and thus a measure of the extent of biofouling. Analysis for the above proceeded by first immersing the membrane samples in 3-6 mL of DI water in a 10 ml test tube, followed by sonication in a temperature controlled sonicator bath (B2510, Branson, Danbury, CT) for 1 hour in order to detach the biofilm from the membrane surface. The test tube containing the membrane sample was then centrifuged for 5 min at 7500 rpm to allow the bacteria to settle to the bottom. Afterwards, 1 mL of the suspended solution was withdrawn from the test tube and placed into each of three 5 mL tubes for proteins and polysaccharides analyses in triplicates. Protein concentration was determined at an absorbance of 595 nm following the Bradford method [251, 253] and bovein casein as a standard [254] over the concentration range of 0 – 500 μg/L. The analysis proceeded by withdrawing 50 μL of the sample solution (containing the extracted EPS) and adding to a 5 mL tube containing 1.5 mL of a coomassie protein assay reagent (Thermo Scientific, # 1856209, Rockford, IL), gently swirling the resulting mixture and then allowing to stand for 20 minutes

prior to determining the protein concentration via absorbance analysis (NanoDrop 2000c Spectrophotometer, Thermo Scientific, Wilmington, DE). Polysaccharide concentration was determined at an absorbance of 490 nm following the method of Dubois [252] using d-glucose as a standard [253] over a concentration range of 0 – 140 mg/L. The analysis proceeded by withdrawing 0.2 mL of the sample solution (containing the extracted EPS) and adding (while gently swirling) to a 5 mL tube containing 5 μL of 80% phenol. Subsequently, 0.5 mL sulfuric acid was added to the above solution with gentle swirling. The test tubes were then heated (10 minutes) to 30°C in a water bath prior to determining the polysaccharide concentration via absorbance analysis.

SEM imaging of the clean and biofouled membranes were obtained, post vacuum drying at room temperature (~ 22 °C), with a dual-beam FIB-SEM (Focus Ion Beam - Scanning Electron Microscopy) (Nova 600, FEI Company, Hillsboro, OR). Membrane samples (2 cm x 2 cm) were gold sputtered for 2 min at 70 mTorr and 15 mA (Anatech Hummer 6.2 Sputtering System, Hayward, CA), to achieve a gold film thickness of ~10 nm. SEM analysis was performed at an average working distance of 5 mm and 52° angle with an electron beam voltage of 10 keV. In order to generate membrane cross-sections to measure the relative change in biofilm thickness after 24 hour biofilm growth and membrane cleaning, the membrane surface was first coated with platinum. Then, a Ga-ion beam (focused ion beam or FIB) at voltage of 30kV and current range of 100-1000 pA was used to generate membrane cross-sections. The FIB-SEM biofilm thickness measurements, which were measured for the dried membranes, are therefore significantly lower than those obtained from CLSM analysis of the hydrated membranes. Nevertheless, FIB-SEM measurements do offer a relative quantification of the extent of residual biofouling when comparing different membrane cleaning protocols.

6.2.3   Membrane Biofouling

A plate-and-frame RO (PFRO) membrane system, as described in Chapter 5, Section 5.2.3 (Figure 5-2b), was used for the biofouling and cleaning studies. During filtration, the system was operated in total recycle such that the permeate, retentate, and bypass lines were fed back to the feed water tank. In preparation of biofilm growth, the membrane sheets were rinsed with DI water for ~5 minutes, followed by submersion in ~ 22°C DI water for 30 minutes. Subsequently, the membrane sheet was placed in the PFRO cell, without a feed spacer, and conditioned with DI water at ~ 1370 kPa for 6 – 12 hours.

Biofilm growth was carried out by exposing the membrane in the RO test cell to secondary wastewater effluent obtained from the Orange County Water District (OCWD) (Fountain Valley, CA) that operates a 26.5×10^{4} m^3/day RO plant as part of a Groundwater Replenishment System (GWRS) (Table 6-1). Biofilm growth commenced on the same day in which the secondary wastewater effluent was obtained from the OCWD-GWRS. A biofilm layer was developed on the membrane surface following the protocol adapted from Krafft and Herzberg [243, 255] for laboratory biofilm growth. The initial step involved inoculation, were 1.5 L of secondary wastewater effluent (source water directly from OCWD, un-filtered) and 3.5 L of tertiary wastewater effluent were combined to form a 5 L water source. Tertiary wastewater effluent was created by filtering the secondary wastewater effluent through a 0.2 μm cartridge filter (Gelman Science, Ann Arbor, MI). The 5 L water source was filtered through the membrane feed flow channel in total recycle for 1 h at a cross flow velocity of 7.14×10^{-2} m/s and same initial volumetric permeate flux (for all membranes) of 8.17×10^{-6} m/s. In the subsequent step of biofilm growth, secondary wastewater effluent (from the feed reservoir) was fed via a 0.2 μm cartridge filter to the PFRO cell (in a total recycle mode). The PFRO was operated also at a cross

flow velocity of 7.14 x 10^{-2} m/s and transmembrane pressure set to yield an initial permeate flux of 1.02 x 10^{-5} m/s for the biofilm growth period of 24 hours; the corresponding transmembrane pressures were 1517, 1241, and 1100 kPa for the ESPA2, PAAm-SNS-PA-TFC, and the PMAA-SNS-PA-TFC membranes, respectively. The biofilm was allowed to form over a period of 24 h in order to allow for the observation of sufficiently significant flux decline (>30%) [5, 243]. It is important to note that in the current study, evaluation of the biofouling tendencies for different membranes, for a given feed, was done at the same crossflow velocity and initial permeate flux [12, 243, 248, 256] such that all comparisons were at the same initial concentration polarization level (Section 6.3).

Once an adequate level of biofilm growth was attained (as indicated by flux decline), the membranes were conditioned (at a crossflow velocity of 7.14 x 10^{-2} m/s) by dosing the feed solution (tertiary wastewater effluent) with 0.1 g/L of both dextran and ammonium chloride (NH_4Cl) in order to prevent bacterial detachment by sustaining nutrient supplement for the biofilm growth. Increased resistance to permeate flow due to biofilm formation was monitored via permeate flux decline. The present biofilm formation protocol resulted in a biofilm thickness (measured via CLSM) in the range of 7.5 – 35 μm which is consistent with recent RO biofouling studies [243, 257-258]. It is noted that the biofilm thickness, as determined via FIB-SEM, in the dry state was significantly lower (0.26 – 0.81 μm) relative to the hydrated thickness as measured via CLSM. Nonetheless, the dry-state biofilm thickness can serve as a useful measure, along with the determination of membrane residual permeability, for assessing the effectiveness of membrane cleaning.

6.2.4   Membrane Cleaning

The biofouled membranes were cleaned by DI water and subsequently with an aqueous solution of 2mM $Na_2 \cdot EDTA$ (at pH 11) to determine the effectiveness of different cleaning methods and efficiency of biofilm layer removal for both SNS and the commercial membranes. After the 24 h biofilm growth period, each membrane was cleaned with DI water at a cross flow velocity of 0.143 m/s and transmembrane pressures of 1380 kPa, 1200 kPa, and 1034 kPa for the ESPA2, PAAm-SNS-PA-TFC, and the PMAA-SNS-PA-TFC membranes, respectively. The above transmembrane pressures were slightly below the pressures deployed in the biofilm growth step (by $3 - 9\%$) to avoid further biofilm compaction. Subsequently, the membrane was cleaned with DI water at a lower transmembrane pressure (138 kPa) (with no water permeation) and a cross flow velocity of 0.143 m/s for ~ 1 h, such that there was no significant permeate flux recovery ($< 5\%$).

Immediately after DI water cleaning, a two-step cleaning process with 2mM $Na_2 \cdot EDTA$ solution at pH 11 was performed for the different membranes. This process was carried out, for all the membranes, at a constant transmembrane pressure of 1034 kPa for 1 h, followed by cleaning with the same solution at a lower transmembrane pressure of ~ 138 kPa (with no water permeation) for 1 h. For cleaning regiment with permeation through the membrane (i.e., at elevated transmembrane pressure), permeate flux was monitored and the permeability again measured post chemical cleaning (2mM $Na_2 \cdot EDTA$ solution at pH 11).

6.3 Analysis of Membrane Resistance

RO membrane permeate flux (J_v), on the basis of membrane resistance (R_T), is given by [6, 259-260]

$$J_v = \frac{\Delta P - \sigma \Delta \pi}{\mu R_T} \tag{6-1}$$

where ΔP is the transmembrane pressure difference, σ is the reflection coefficient (equal to 1.0 for high rejection RO membranes), $\Delta \pi$ is the solution osmotic pressure, and μ is the permeate viscosity. The total resistance (R_T) is the sum of intrinsic membrane (R_m) and fouling (R_f) resistances. The fouling resistance (R_f) in turn is considered to be the sum of the reversible (R_{rev}) and irreversible (R_{irr}) biofouling resistances. Irreversible fouling is typically quantified as the residual resistance to permeation of the solvent determined after non-chemical cleaning (i.e., water cleaning in this chapter). In this chapter, the applied transmembrane pressure difference (1100 − 1517 kPa) during membrane biofouling (Section 6.2.3) was much greater than the wastewater effluent osmotic pressure (73 kPa) or the cleaning solutions (0 kPa for DI water and 22 kPa 2mM Na$_2$·EDTA). The above osmotic pressures were calculated via a multi-electrolyte thermodynamic simulator [248, 261]. The solute concentration at the membrane surface was estimated by means of the concentration polarization (CP) modulus (Chapter 2, Equation (2-8)) in the membrane flow channel, determined using a numerical computational fluid dynamics (CFD) model applied to the PFRO channel [208, 262].

Increase in permeation resistance during biofouling or decrease in resistance during cleaning can be analyzed using Equation (6-1) where R_m is obtained from independent flux measurements for the native (clean membrane) with water (or the cleaning solution). Alternatively, one can take

the time derivative of Equation (6-1), knowing that $dR_m/dt = 0$ (where t is time), and integrating

to get the fouling resistance, $R_f(t) = \dfrac{(\Delta P - \sigma \Delta \pi)}{J_0 \mu} \int_0^t \dfrac{d}{dt}\left(\dfrac{J_0}{J_v(t)}\right) dt$, where A is the active

membrane area and J_0 is the initial water permeate flux. It is noted that in the above approach, the calculated fouling resistance for the biofilm growth period is essentially the total resistance (R_T) less the sum of the intrinsic membrane resistance and the resistance at the end of the inoculation period (i.e., $t = 0$ for the biofilm growth period).

The degree of membrane permeability recovery (*MPR*), for the three different membranes and cleaning protocols, was also determined from permeate flux measurements. Membrane permeability (L_p) was calculated from $L_p = J_v / (\Delta P - \sigma \Delta \pi)$ with the fraction of recovered permeability (*MPR*) quantified as $MPR = L_{p,i} / L_{p,0}$ where $L_{p,0}$ and $L_{p,i}$ are the initial and final permeabilities, respectively, for each of the membrane cleaning steps.

6.4 Results and Discussion

6.4.1 Membrane Biofouling

The CLSM (Figure 6-1) and SEM images (Figure 6-2) of the biofouled membranes (after 24 h growth period) revealed the presence of bacterial fouling. The observed bacteria of rod-like geometry belong to the Gram-negative bacteria family [263], which is consistent with the bacteria species known to exist in the municipal wastewater used in the study (Table 6-1). The hydrated biofilm thicknesses (Table 6-2) on the PMAA-SNS-PA-TFC (7.5 µm) and PAAm-SNS-PA-TFC (14.4 µm) membranes were lower by a factor of 4.7 and 2.4, respectively, compared to the commercial ESPA2 membrane (35 µm). Proteins and polysaccharides surface

mass density (as determined by EPS analysis, Section 6.2.2) on the biofouled membrane was lower by factors of 2.9 and 2.2 for the PMAA-SNS-PA-TFC and PAAm-SNS-PA-TFC membranes, respectively, relative to ESPA2 (Figure 6-3). The level of biofouling for the SNS-PA-TFC membranes, as quantified by the level of surface proteins and polysaccharides was $5.8 - 8.2$ µg/cm^2 and $33.1 - 45.0$ µg/cm^2, respectively, with the above foulant levels being somewhat higher for ESPA2. It is noted that the above results are consistent with the proteins and polysaccharides levels reported in recent studies on biofouling of a polyethersulfone membrane [257]. Due to the negative surface charge of the PMAA grafted layer (Table 5-1), it is hypothesized that electrostatic repulsion of negatively charged bacteria, in combination with partial Brownian mobility of the tethered polymer chains [9, 11-12], contributed to a lower degree of biofouling on the membrane surface.
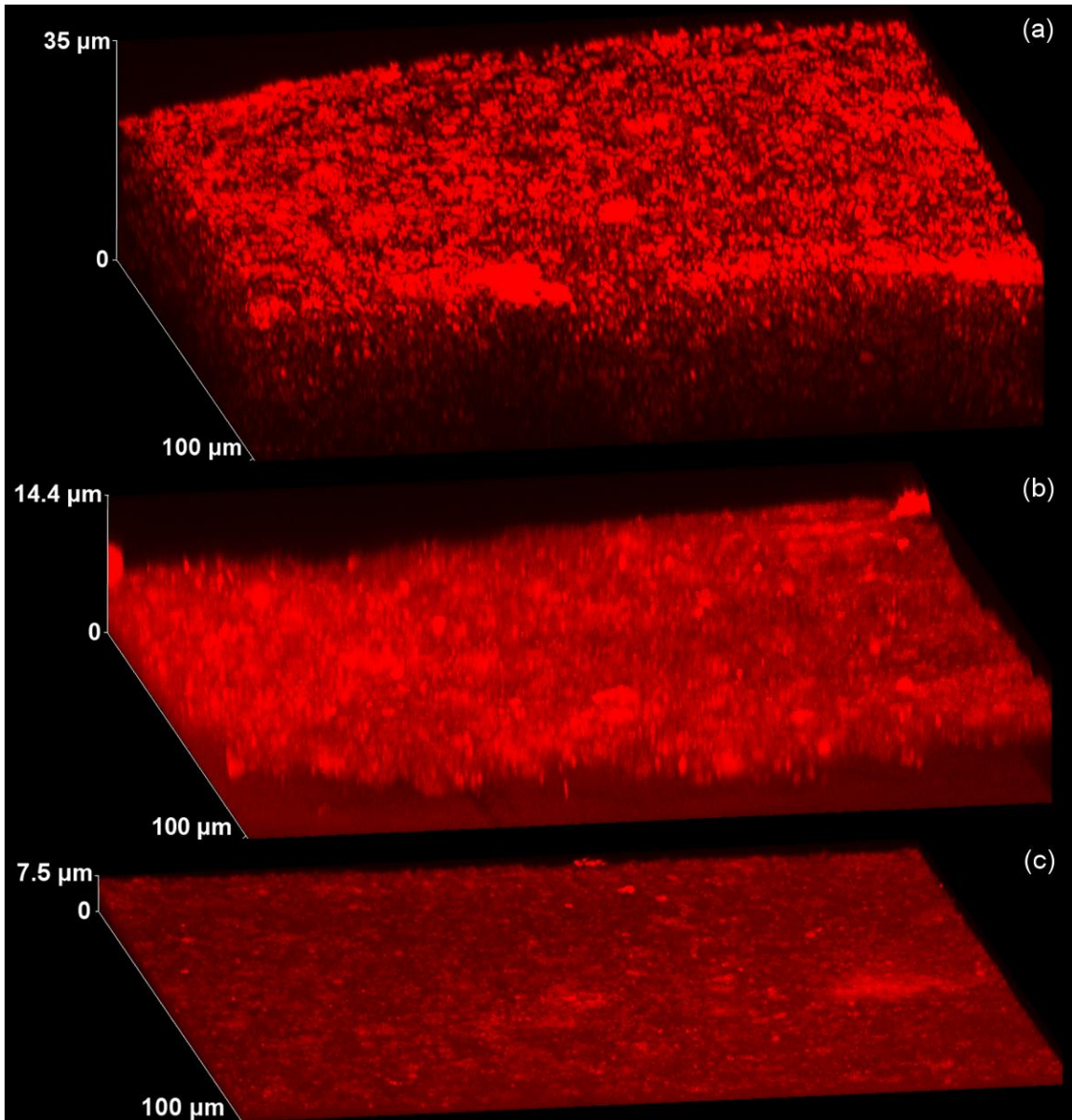
Figure 6-1. Membrane CLSM images of the biofilm layer after 24 h biofilm growth: (a) ESPA2, (b) PMAA-SNS-PA-TFC, (c) PAAm-SNS-PA-TFC. All tests were carried out at initial permeate flux of 1.02×10^{-5} m/s and a crossflow velocity of 7.14×10^{-2} m/s.
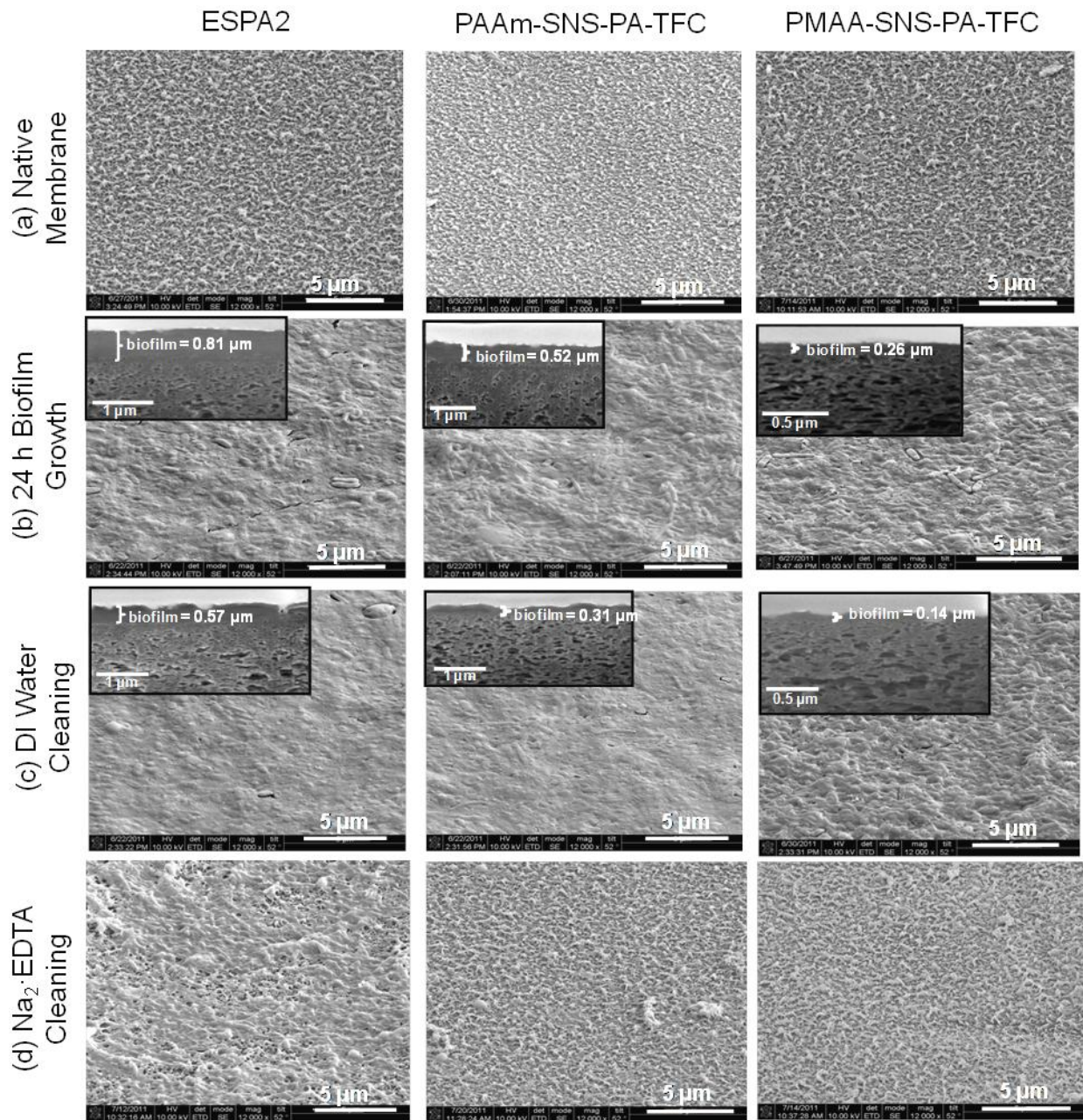
Figure 6-2. Membrane SEM images of (a) native membrane surfaces, (b) after biofilm growth, (c) after DI water cleaning, and (d) after Na$_2$·EDTA cleaning.

Table 6-2. Membrane permeability (L_p) and the biofilm thickness (δ) after biofilm growth and membrane cleaning stages.

Biofilm Growth & Cleaning Stages	ESPA2	PAAm-SNS-PA-TFC	PMAA-SNS-PA-TFC
	Permeability x 10^{-11} (m/s·Pa)		
Native membrane	1.17	1.41	1.85
24 h biofilm formation	0.68	0.95	1.34
1 h cleaning with DI water at high pressure [a]	0.75	1.07	1.52
1 h cleaning with DI water at low pressure [b], no permeation	0.88	1.19	1.65
1 h cleaning with 2 mM Na_2·EDTA at high pressure [c]	0.93	1.25	1.73
1 h cleaning with 2 mM Na_2·EDTA at low pressure [d], no permeation	1.25	1.53	1.89
	CLSM Biofilm Thickness (μm)		
24 h biofilm formation	35	14.4	7.5
	FIB-SEM Biofilm Thickness [e] (μm)		
24 h biofilm formation	0.81	0.52	0.26
1 h cleaning with DI water at low pressure [b], no permeation	0.57	0.31	0.14

[a] 1034 – 1380 kPa; [b] 138 kPa; [c] 1034 kPa; [d] 138 kPa; [e] biofilm thickness in dry-state.
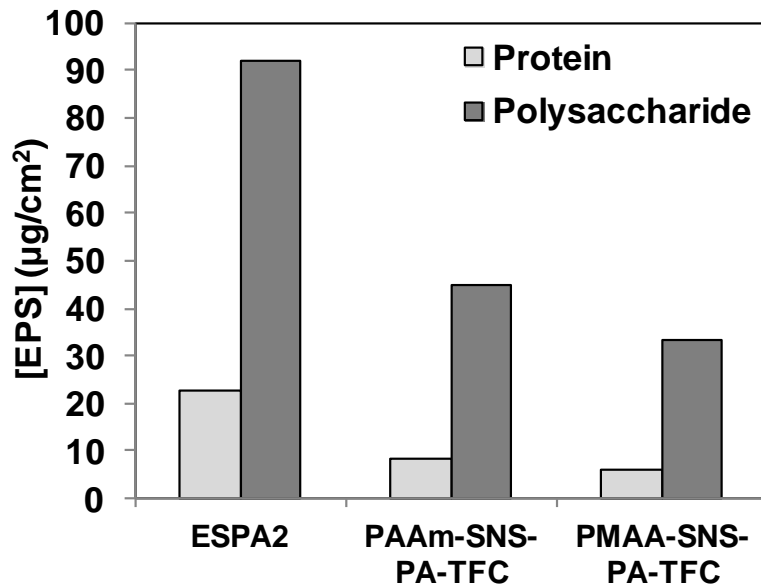
Figure 6-3. EPS measurements after 24 h biofilm growth. All tests were carried out at initial permeate flux of 1.02 x 10^{-5} m/s and a crossflow velocity of 7.14 x 10^{-2} m/s.

The progression of biofouling of the ESPA2 and the SNS-PA-TFC membranes was evaluated by observing the progression of permeate flux decline during the 24 h biofilm growth period. The above experiments were carried out in multiplicity, with permeability and flux decline measurements scatter within 5%. The apparent onset of permeate flux decline was observed at t = 2.5, 3 and the 5.5 h for the ESPA2, PAAm-SNS-PA-TFC, and PMAA-SNS-PA-TFC membranes, respectively (Figure 6-4a). In all cases, permeate flux decline was consistent with progressive biofilm growth (Section 6.2.3). Bacteria that adhere and colonize the membrane surface (by means of EPS) [209, 249, 264-265] lead to both increased hydraulic resistance to permeate flow in addition to surface blockage [249]. ESPA2 exhibited a significantly greater degree of biofouling compared to the PAAm-SNS-PA-TFC and PMAA-SNS-PA-TFC membranes as quantified by permeate flux decline at t = 24 h that reached ~ 46%, 40% and 34%, respectively. The ESPA2 and PAAm-SNS-PA-TFC membranes have similar water contact angles (~60º), but ESPA2 has a lower negative surface charge (-27.8 mV) compared to the PAAm-SNS-PA-TFC membrane (-18.3 mV) (Table 5-1). Therefore, one would be tempted to suggest that the ESPA2 should be more resistant to biofouling. However, it should be noted that the PAAm-SNS-PA-TFC has a 48% lower surface roughness relative to ESPA2, and is equipped with a polymeric brush layer of water soluble but terminally anchored polymer chains. As a result, segments of the tethered PAAm chains are capable of measurable degree of Brownian motion, thereby providing the advantage of reducing the propensity of foulant attachment to the brush layer [11], compared to the rigid ESPA2 membrane surface.

Progression of the biofilm resistance during the 24 h filtration period was assessed for the different membranes via the analysis presented in Section 6.3. The results (Figure 6-4b) illustrate that the fouling resistance-time profile is concave upward (with respect to t), which suggests that

surface blockage is predominantly responsible for permeate flux decline versus a concave down profile which would be indicative of resistance due to cake filtration [266]. Upon detection of biofilm resistance, the PMAA-SNS-PA-TFC membrane had the lowest rate of biofilm resistance rise (dR_f/dt), as quantified by a factor of 3.0 and 1.6 lower than for the ESPA2 and PAAm-SNS-PA-TFC membranes, respectively. Additionally, at the end of the 24 h biofilm growth period, the resistance due to the biofilm layer on the PMAA-SNS-PA-TFC membrane surface significantly lower compared to the ESPA2 and PAAm-SNS-PA-TFC membranes by a factor of 4.2 and 2.2, respectively. It should be recognized that the fouling resistance as depicted in Figure 6-4b represents the added biofouling resistance post the inoculation period. The above results indicate that the SNS-PA-TFC membranes were less prone to biofouling compared to the ESPA2 membrane, with the lowest biofouling propensity for the PMAA-SNS-PA-TFC.

FIB-SEM sectioning (Figure 6-2) uncovered dry biofilm thickness for the different membranes, which was quantified to be about 3.1 and 1.6 times higher for the ESPA2 membrane compared to the PMAA-SNS-PA-TFC and PAAm-SNS-PA-TFC membranes, respectively. Although the FIB-SEM images are for the biofilm in the dry state, the thickness measurements obtained from these images provide a relative comparison of the severity of biofouling among the tested membranes. Indeed, the above ranking of the biofilm thickness was qualitatively consistent with the order of the extent of permeate flux decline (Figure 6-4a).
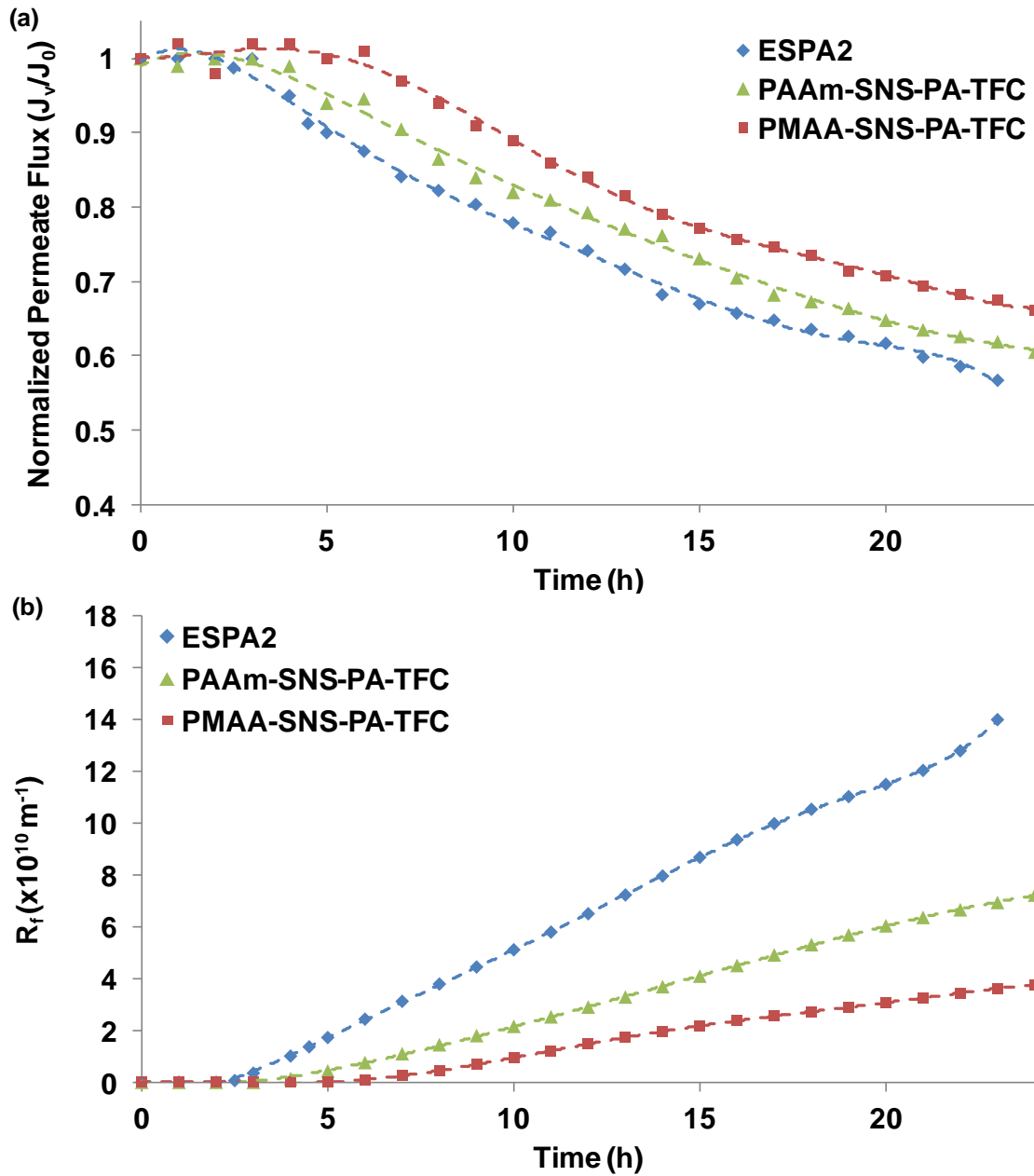
Figure 6-4. (a) Normalized permeate flux and (b) resistance due to fouling ($R_{fouling}$) during biofilm growth period. All tests were carried out at initial permeate flux of 1.02×10^{-5} m/s and a crossflow velocity of 7.14×10^{-2} m/s. (It noted that the fouling resistances at the termination of the inoculation period (i.e., initial resistance for the biofilm growth step) were 9.8×10^{10} m^{-1}, 4.3×10^{10} m^{-1} and 1.9×10^{10} m^{-1} for the ESPA2, PAAm-SNS-PA-TFC, and the PMAA-SNS-PA-TFC membranes, respectively.)

154

6.4.2   Membrane Cleaning

The membrane cleaning efficiency for the different membranes was initially assessed by cleaning with DI water for 1 h at a transmembrane pressure slightly below the pressure carried out during the 24 h biofilm growth period (1034 – 1380 kPa). This initial membrane cleaning step was performed in order to determine the degree of permeability recovery (*MPR*), achievable by removing the loosely bound/attached biofilm by fluid shear, while maintaining sufficient permeate flux (and *ΔP*) to avoid significant lifting (or detachment) of the biofilm layer. DI water cleaning at elevated pressure resulted in a partial reduction of the hydraulic resistance attributed to the biofilm (R_f) where the cleaning effectiveness diminished at ~ 30 min for all of the membranes (Figure 6-5). Also, the permeability recovery (relative to the clean membrane) was merely 64% for ESPA2, and 76% and 82% for the PAAm-SNS-PA-TFC and PMMA-SNS-PA-TFC membranes, respectively. It is reasonable to deduce that the biofilm on the SNS-PA-TFC membranes was more loosely bonded/attached to the surface (due to the partial mobility [9, 11-12, 267] and surface functionalities of the polymer brush layer), compared to ESPA2, and therefore greater *MPR* was attained by pressurized cleaning with DI water. As expected, the above cleaning protocol was unable to restore the membrane permeability back to the native state as low pressure water cleaning without permeation through the membrane is the preferred approach [268].
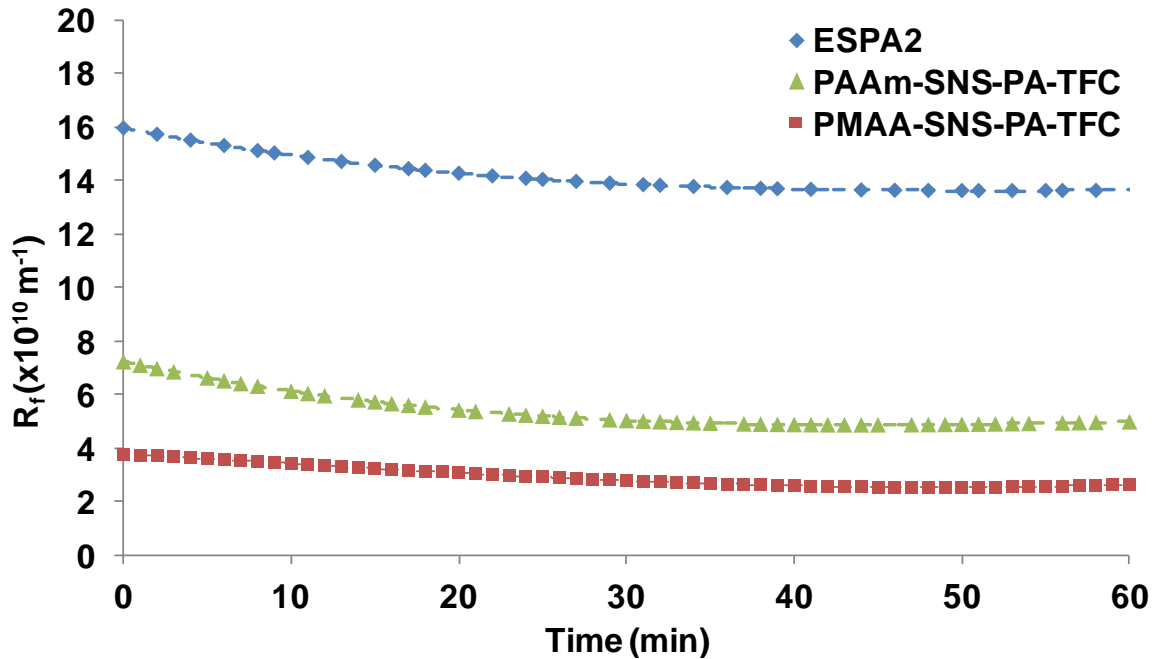
Figure 6-5. Resistance due to the fouling layer (R_f) during DI water cleaning at transmembrane pressures of 1380 kPa, 1200 kPa, and 1034 kPa (with initial corresponding permeate fluxes of 4.6×10^{-9} m^3/s, 5.8×10^{-9} m^3/s, 7.7×10^{-9} m^3/s) for ESPA2, PAAm-SNS-PA-TFC, and the PMAA-SNS-PA-TFC membranes, respectively.

Additional biofilm removal was achieved in the second cleaning step, where the biofouled membranes were washed at a crossflow velocity of 0.143 m/s (surface shear rate of ~400 s^{-1}) for 1 h with no permeation (i.e., low transmembrane pressure = 138 kPa). Biofilm removal was quantified by both the SEM images (Figure 6-2) that indicated a decrease in biofilm thickness and the accompanied increase in permeability recovery (Table 6-2). Permeability recovery for the second cleaning step was ~ 75%, 84% and 89% for ESPA2, PAAm-SNS-PA-TFC and PMAA-SNS-PA-TFC, respectively. Irreversible fouling resistance (R_{irr}) after the above water cleaning protocol was highest for ESPA2 (3.2×10^{10} m^{-1}) followed by PAAm-SNS-PA-TFC

(1.5×10^{10} m^{-1}) and PMAA-SNS-PA-TFC (7.6×10^9 m^{-1}). The somewhat greater effectiveness of the DI water cleaning regimen for the nanostructured membranes suggests that the biofilm formed on the SNS-PA-TFC surfaces were less compacted compared to the ESPA2 membrane, and thus, easier to remove by DI water cleaning. Still, a more aggressive cleaning regimen was needed to restore the membrane permeability to its native state.

Accordingly, chemical cleaning with a low concentration of aqueous Na$_2$·EDTA solution at high pH (~ 11), which is known to successfully clean RO membranes [269-271], was performed. The third step for cleaning the biofouled membranes was completed by filtration of aqueous 2 mM Na$_2$·EDTA at pH ~ 11 for 1 h at $\Delta P = 1034$ kPa and a crossflow velocity of 0.143 m/s. This cleaning regimen reduced the biofilm resistance (Figure 6-6) with cleaning effectiveness that diminished in about 25 min and 20 min for the ESPA2 and SNS-PA-TFC membranes, respectively. Membrane permeability recovery (relative to the native/clean membranes) was highest for the PMAA-SNS-PA-TFC membrane at 93% compared to the PAAm-SNS-PA-TFC and ESPA2 membranes at 89% and 80%, respectively. Subsequently, a final chemical cleaning step was performed at low transmembrane pressure (138 kPa), which enabled operation without permeation, resulted in permeabilities that were slightly higher (by ~2.2 – 8.5%) relative to the native/clean membranes (Table 6-2). This behavior is possibly due to increased membrane surface hydrophilicity by Na$_2$·EDTA as suggested in previous studies [269]. Yet, upon examination of membrane surface images (Figure 6-2), residual traces of biofilm remained on the ESPA2 membrane surface even after full permeability recovery was achieved by chemical cleaning. In contrast, there was no observed residual biofilm the SNS-PA-TFC membrane surfaces (Figure 6-2).
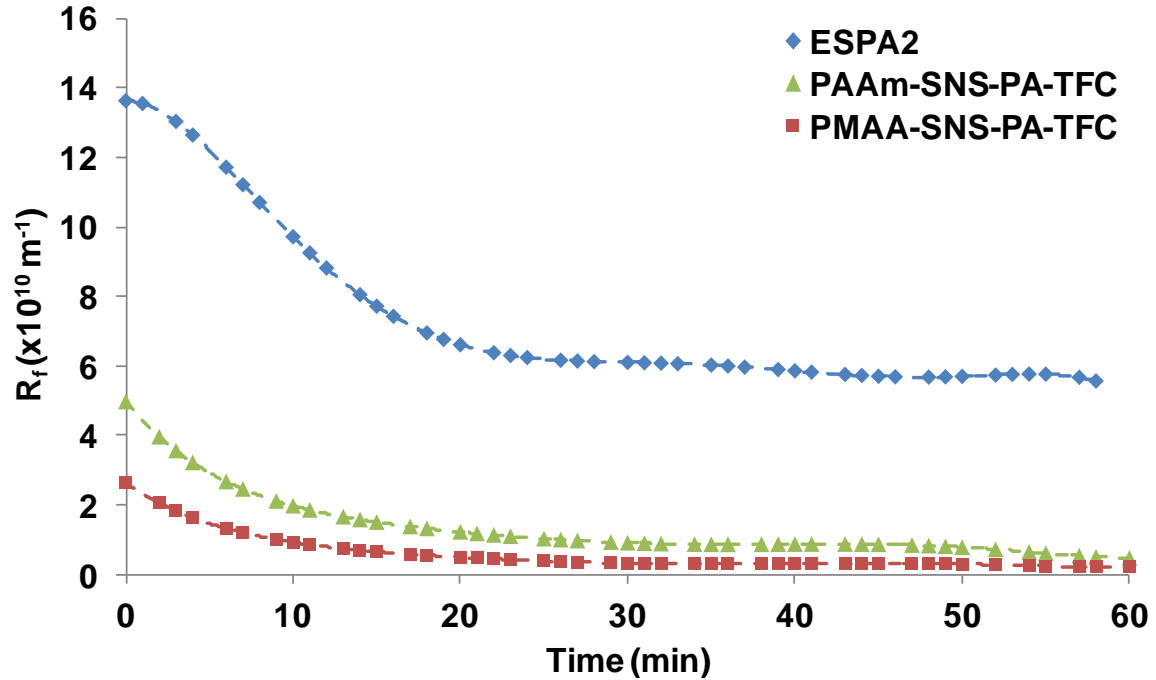
Figure 6-6. Resistance due to the fouling layer (R_f) during chemical cleaning with 2 mM Na$_2$·EDTA solution at a transmembrane pressure of 1034 kPa.

6.5 Conclusions

Poly(methacrylic acid) (PMAA) and polyacrylamide (PAAm) surface nanostructured (SNS) RO membranes were evaluated for their biofouling resistance during secondary wastewater (from a municipal wastewater treatment plant (MWTP)) filtration and cleaning effectiveness post biofouling. The SNS-PA-TFC membranes achieved significantly lower biofouling propensities, as quantified by a 2.4 – 4.7 times lower hydrated biofilm thickness, compared to the commercial membrane of similar salt rejection (95±0.9%) that was used in the MWTP. Greater resistance to biofouling was observed for the SNS-PA-TFC membranes, as quantified by fouling resistance for the SNS-PA-TFC membranes that was lower by a factor of 2.2 – 4.2, and permeability recovery, via water cleaning, was a factor of 1.1 – 1.2 greater relative to the commercial

membrane used in the OCWD MWTP. Chemical cleaning enabled complete restoration of membrane permeability for all membranes. This chapter suggests that the SNS-PA-TFC membranes, owing to their hydrophilic surface nanostructured polymer brush layer, were effective in reducing biofouling propensity and increasing cleaning efficiency due to decreased biofilm adhesion.

Appendix A **Candidate Monomers for Atmospheric Pressure Plasma Induced Graft Polymerization (APPIGP)**

The monomers selected for graft polymerization onto a PA surface were selected since they had the following attributes: (a) high water solubility, (b) capable of polymerizing at relatively low temperatures, and (c) specific chemical functionality for reducing biofouling propensity. In the present research the following monomers were examined: 2-hydroxyethyl methacrylate (HEMA) [68], acrylamide (AAm) [12, 21, 86], acrylic acid (AA) [21, 55, 68, 86, 124, 173], n-vinylpyrrolidone (nVP) [72, 183], methacrylic acid (MAA) [12, 68, 180], and vinylsulfonic acid (VSA) [88] (Chapter 2, Table 2-5). The polymerization reaction resulted in the formation of poly(2-hydroxyethyl methacrylate) (PHEMA), polyacrylamide (PAAm), poly(acrylic acid) (PAA), polyvinylpyrrolidone (PVP), poly(methacrylic acid) (PMAA), and poly(vinylsulfonic acid) (PVSA) grafted brush layers.
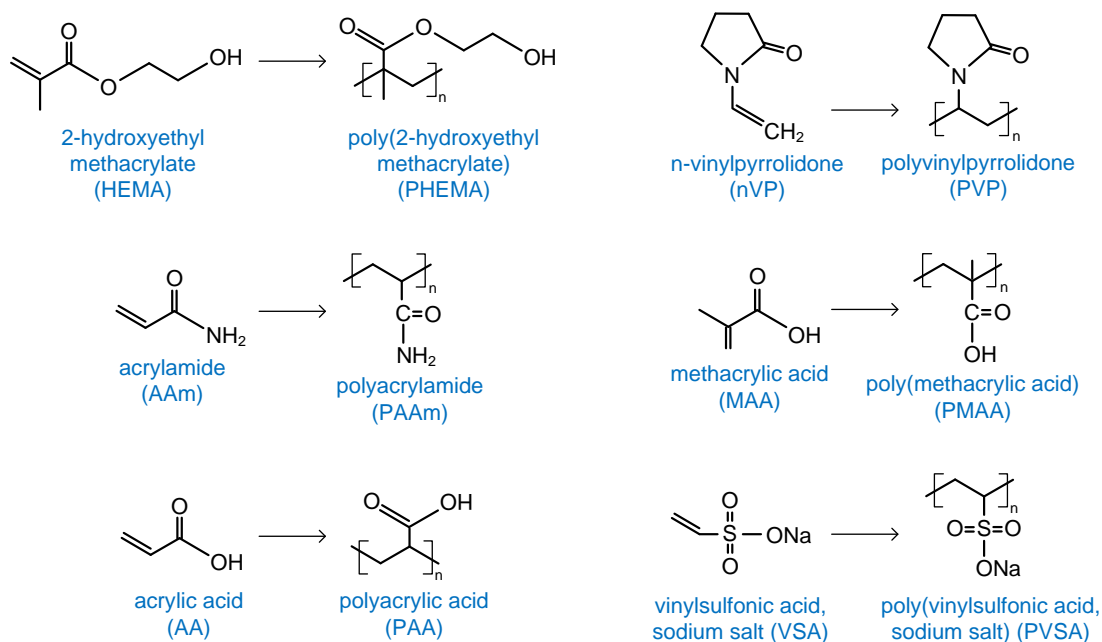
Figure A-1. Monomers and associated polymer chains tethered to PA surfaces synthesized via atmospheric pressure plasma induced graft polymerization (APPIGP).

Appendix B   Spin Coating Procedure

The PWM32 Spin Controller (Headway Research, Inc., Garland, Texas) is used for PA-Si surrogate surface preparation.

1. Cut the clean silicon wafer (Prime-grade silicon <100> wafers, Wafernet, Inc., San Jose, CA) into 1 cm x 1 cm pieces/substrates.

2. Blow clean each substrate with the N_2 gun.

3. Place the substrate pieces in a 4" petri dish.

4. Insert the 0.5" diameter center piece chuck (total diameter of the chuck is ~2") in the spin coater.

5. Program spin casting recipes:

    1. press STEP, press 0 to be in the READY state

    2. press RECIPE, press CLEAR, and enter the recipe number (e.g., $0 - 9$)

    3. press STEP, press 1 (in order to program Step 1 of the spin casting program)

    4. press SPEED/RAMP, and enter the desired speed ($0 - 10,000$ rpm), press ON or ENTER

        • Note: OFF or CLEAR can be used as a backspace key

    5. press SPEED/RAMP, and enter the desired acceleration/deceleration (e.g., $0 - 20,000$ rpm), press ON or ENTER

    6. press STEP TERMINATOR, and enter the time duration (e.g. $0 - 999.9$ s), press ON or ENTER

7. press STEP, press the subsequent step number (e.g., 2 in order to program Step 2 of the spin casting program)

8. repeat steps 4 – 7, and continue until all steps have been programmed

9. press STEP, press 0 to be in the READY state

6. Place a 1 cm x 1 cm silicon piece onto chuck and turn on the vacuum.

7. Using a disposable pipet, cover the surface of the silicon wafer with 0.3 wt% PEI (M_w = 750,000 g/mol, Sigma–Aldrich, St. Louis, MO) (make sure there are no air bubbles).

8. Use the green foot-pedal on the floor to begin the spin casting program: 2500 rpm for 30 s (1000 rpm ramp change), repeated twice.

- Note: to stop/abort the spin casting program, step on the red foot-pedal and reset the spinner by stepping on the green-foot pedal.

9. Using a disposable pipet, cover the surface with 2.5 wt% MPDA (≥99%, Sigma–Aldrich, St. Louis, MO) solution and allow for 2 min absorption.

10. Use the green foot-pedal on the floor to begin the spin casting program: 500 rpm for 30 s (1000 rpm ramp change) followed by 3000 rpm for 30 s (1000 rpm ramp change).

11. Using a disposable pipet, cover the surface with 0.13 wt% TMC (98%, Sigma–Aldrich, St. Louis, MO) in hexane (Sigma–Aldrich, St. Louis, MO) and let the solution absorb onto the surface for 30 seconds.

12. Use the green foot-pedal on the floor to begin the spin casting program: 3000 rpm for 30 s (1000 rpm ramp change).

13. Turn off the vacuum, remove substrate from spin coater, rinse with triple DI water, blow dry with N_2 gun, place into a new in a 4" petri dish

14. Seal petri dish with all surrogate surfaces, bring back to lab, place in 80ºC vacuum chamber for 1 h

Appendix C   Operating Protocol for the Atmospheric Pressure Plasma Systems

C.1   UCLA Plasma System

The UCLA plasma system consisted of a plasma generator (Part No. 232190-03, Model Ctr. DPM 1 PS, Serial 9804-3007, Rev A), matching network (Part No. 9900-0003-30A, Model RFS 3000, Serial 9804-3011, Rev A), and controller (Model RF-5, Serial 560-07304C) all from RF Services, Inc. (Sunnyvale, CA). The above was used in conjunction with a custom UCLA plasma applicator.

C.1.1 Plasma System Inspection

1. Fill the glove-bag with nitrogen gas and examine to see if there are any holes. Patch any visible holes with transparent tape.

2. Examine tubing for leaks by filling tubing with nitrogen gas and squirting connections with a soapy water solution. If the water starts bubbling there is a leak. Replace tubing and/or connections if holes exist.

3. Check gas cylinders; if they are empty, request new cylinders by calling Cylinder Management (x 51127); request UHP (ultra high purity) helium, oxygen and hydrogen tanks or industrial nitrogen (Air Liquide, Los Angeles, CA).

4. Open helium, oxygen, and hydrogen gas valves and set their pressure regulators to ~ 40 psi, ~ 44 psi, and ~ 34 psi, respectively.

5. Close plasma gas valves at plasma station.

C.1.2 Operation of Plasma Source

1. Use nitrogen gas to degas a prepared monomer solution in 40 mL glass vials (03-340-47E, Fisher Scientific, Pittsburgh, PA) for 10 min at ~ 0.5 psig.

2. Turn on the plasma generator and matching network. Allow the system to stabilize for ~5 minutes.

3. Transfer prepared sample substrate, degassed monomer solution, and tweezers into the glove-bag.

4. Turn on vacuum pump and open the vacuum valve so that the gas is evacuated from the glove-bag.

5. At once, close the vacuum valve and open the nitrogen gas valves to fill the glove-bag.

6. Open plasma gas valve and ensure that the flow rates of helium, hydrogen, and oxygen are 450 cm^3/min, 10 cm^3/min, and 17 cm^3/min, respectively by examining the rotometer (Model 150 MM, Part GF-5546-2827, Gilmont Instruments, Barrington, IL)

7. Position a silicon wafer (Prime-grade silicon <100> wafers, Wafernet, Inc., San Jose, CA) below the plasma source. Turn on the plasma by pressing the black "RF off" button and then the red "RF on" button on the plasma generator. Turn the RF power to 40 W by manipulating the "power adjust" knob on plasma generator.

8. Tune the matching network until the reflected power is zero by manipulating the "tune" knob. Note that the matching network switch must be set to "manual".

9. Once the reflected power is zero at 40 W, ensure that the color of the plasma discharge emitted onto the silicon wafer is light blue. If plasma does not ignite (no color emitted), the following problems may be occurring: plasma source needs to be tuned, plasma gas valves are closed, and/or the matching network or generator (i.e., power) is not working properly.

10. Press the green "RF off" button to turn off the plasma.

11. Place the sample substrate on top of an inverted 50 mL glass beaker, and position directly under the plasma source/applicator.

12. Turn on the plasma by pressing the black "RF off" button and then the red "RF on" button on the plasma generator for exactly 10 s.

13. Press the green "RF off" button to turn off the plasma.

14. Open the oxygen valve to allow oxygen gas to impinge upon the sample surface for 2 min at 500 cm^3/min.

15. Remove the sample substrate and inverted 50 mL glass beaker from under plasma source.

C.1.3 Graft Polymerization

1. Place the plasma treated sample into the monomer solution vial (with the sample surface facing upwards for substrates or inwards for membrane surfaces) and screw on vial cap.

2. Place capped vial in a 50 – 70°C water bath for a 0.5 – 2 h graft polymerization reaction time.

3. Remove vial from water bath and properly dispose of monomer solution.

4. Remove the sample from the vial and thoroughly rinse with DI water, then

- for substrates, dry with N_2 and place in petri dish and place in vacuum oven (~40ºC) overnight.

- for membranes, submerge in DI water and store in a 4ºC fridge.

C.2   AtomFlow 250C Plasma System

The AtomFlow 250C Plasma System (Surfx Technologies Inc., Redondo Beach, CA) was used in conjunction with a custom UCLA plasma applicator.

C.2.1 Operation of Plasma Source

1. Use nitrogen gas to degas a prepared monomer solution in 40 mL glass vials (03-340-47E, Fisher Scientific, Pittsburgh, PA) for 10 min at ~ 0.5 psig.

2. Turn on power source (power button) and matching network (flip to on switch, make sure it's on manual); warm up for ~30 minutes.

3. Ensure all plasma gas valves at plasma station are closed. Open N_2, He, O_2, and H_2 gas tanks and set their pressure regulators to 30 psi, 30 psi, 44 psi, and 30 psi, respectively. Make sure there is enough gas left in the tanks to complete the experiment (400 psig of He). If gas cylinders are empty, request new cylinders by calling Cylinder Management (x 51127); request UHP (ultra high purity) helium, oxygen and hydrogen tanks or industrial nitrogen (Air Liquide, Los Angeles, CA).

4. Open the He/secondary gas valve (at exit of RF box).

5. Select "AtomFlow 250C" and hit the start button (green).

6. Hold the purge button (on the back side of the plasma box) for ~30s to clear out any moisture/impurities in the line.

7. Tune the flowrates and RF power to the cold start conditions: 60 W, He: 30 L/min, H_2: 0.2 L/min.

8. Turn on the plasma by pressing the start button. Check the plasma discharge seen in the silicon wafer under the plasma exit region. Notes:

    - It takes ~6 s to ignite the plasma.

    - Ensure that the RF power and gas flowrates are within 10% of the setpoint.

    - Ensure that the reflective power is below 100 bit counts.

    - If the plasma does not ignite properly hit the reset button and it will reset the system to original set up conditions and brings you to the main menu.

    - The color of plasma discharge should be a light blue and the color intensity will change with RF power; if plasma does not have a color, either the source is not properly tuned, the plasma gas valve is not opened, the matching network is not working properly, or the RF power is not sufficient to ionize the gas.

9. Turn off plasma by pressing the stop button.

10. Tune the flowrates and RF power to the plasma conditions desired.

    - Maintain a 30 L/min He flowrate.

    - Increase the secondary gas (e.g. H_2, O_2) flowrate before increasing the RF power.

    - Decrease the RF power before reducing the secondary gas (e.g. H_2, O_2) flowrate.

11. Turn on the plasma by pressing the start button. Check the plasma discharge seen in the silicon wafer under the plasma exit region.

12. Turn off plasma by pressing the stop button.

13. Repeat 12 – 13 three times to ensure plasma quality.

14. Place the sample in the center of an inverted 50 mL glass beaker.

15. Turn on plasma source (green start button) and wait for the plasma to stabilize.

16. Slide the sample/50 mL glass beaker 2 mm under the plasma source for 10 s.

17. Promptly slide the sample/50 mL glass beaker out from under the plasma source.

18. Turn off plasma by pressing the stop button and close He/ secondary gas valve (at exit of RF box).

19. Open O_2 gas valves such that the rotometer (Model 150 MM, Part GF-5546-2827, Gilmont Instruments, Barrington, IL) reads ~500 cm^3/min.

20. Slide the sample/50 mL glass beaker back under the plasma source and allow oxygen to flow over surface for 1 min.

21. Slide the sample/50 mL glass beaker out from under the plasma source.

22. Close O_2 gas valves.

C.2.2 Graft Polymerization

Graft polymerization was conducted using the same protocol described in Section C.1.3 with the addition of N_2 bubbling through the monomer solution throughout the graft polymerization period (Figure C-1). The graft polymerization setup was comprised N_2 that was fed through

1/4" ID, 3/8" OD, 1/16" wall thickness Masterkleer PVC tubing (5233K56, McMaster-Carr, Santa Fe Springs, CA) to a 10-way splitter (10 Way – 10 outlets with shutoffs with 1/4" barbed fittings, Missouri Malt Supply, Fenton, MO) and then to 18 gauge, .033" ID, .050" OD, 4" long reusable type 304 SS dispensing needles (6710A44, McMaster-Carr, Santa Fe Springs, CA) attached by male X barb 1/4" tube ID plastic quick-turn (Luer-Lok) coupling nylon (51525K126, McMaster-Carr, Santa Fe Springs, CA). The N_2 then fed into monomer solutions contained in 40 mL glass vials with PTFE/silicone septa and open-top polypropylene closure (03-340-47E, Fisher Scientific, Pittsburgh, PA) and exited through disposable straight needles (14-826-5G, Fisher Scientific, Pittsburgh, PA). The vials were partially submerged in a circulator water bath (MGU C12, Lauda, Delran, New Jersey) to maintain constant temperature. The needles were secured in place by feeding through worm-drive hose clamp (5388K14, McMaster-Carr, Santa Fe Springs, CA) which are attached to a wood frame.
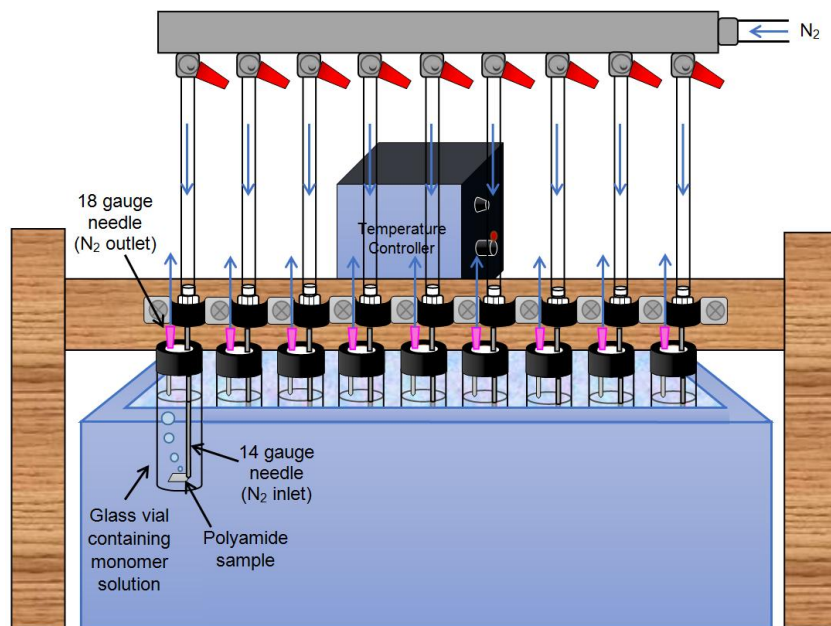
Figure C-1. Schematic of the experimental graft polymerization setup.

Appendix D   Analytical Techniques

This appendix describes the procedures for analytic techniques used in Chapter 3, Chapter 4, Chapter 5, and Chapter 6. Surface characterization was performed with Atomic Force Microscopy (AFM), Contact Angle, X-ray Photoelectron Spectroscopy (XPS), and Ellipsometry.

D.1   Atomic Force Microscopy (AFM)

The AFM (Multimode AFM with Nanoscope IIIa SPM controller, Digital Instruments, Santa Barbara, CA) is pictured in Figure D-1, Figure D-2, and Figure D-3.

(3) adjusts laser y-axis position (top/bottom); adjust to align laser

(4) adjusts photodetector mirror (up/down); adjust to attain the maximim signal when focusing laser and to adjust RMS/ VERT, adjust (4) first before (5)

(5) adjusts photodetector mirror (left/right) (positioned on the back of the device); adjust to attain the maximum signal when focusing laser and to adjust RMS/ VERT

(6) adjusts reflectance angle of mirror (positioned on the back of the device); adjust to attain the maximum signal

(7) moves stage left/right

(8) moves stage up/down

(2) adjusts laser x-axis position (left-right); adjust to align laser

(1) clamping screw (positioned on the back of the device); adjust to secure the tip holder

Figure D-1. Picture of AFM system (front view, top).

(12) changes the display; keep switch to the middle option 'AFM'

STM
AFM & LFM
TM AFM

Down

Up

(11) moves canteliver up/down (up = away from sample, down = toward sample)

(10) moves viewing window left/right

(9) moves viewing window up/down
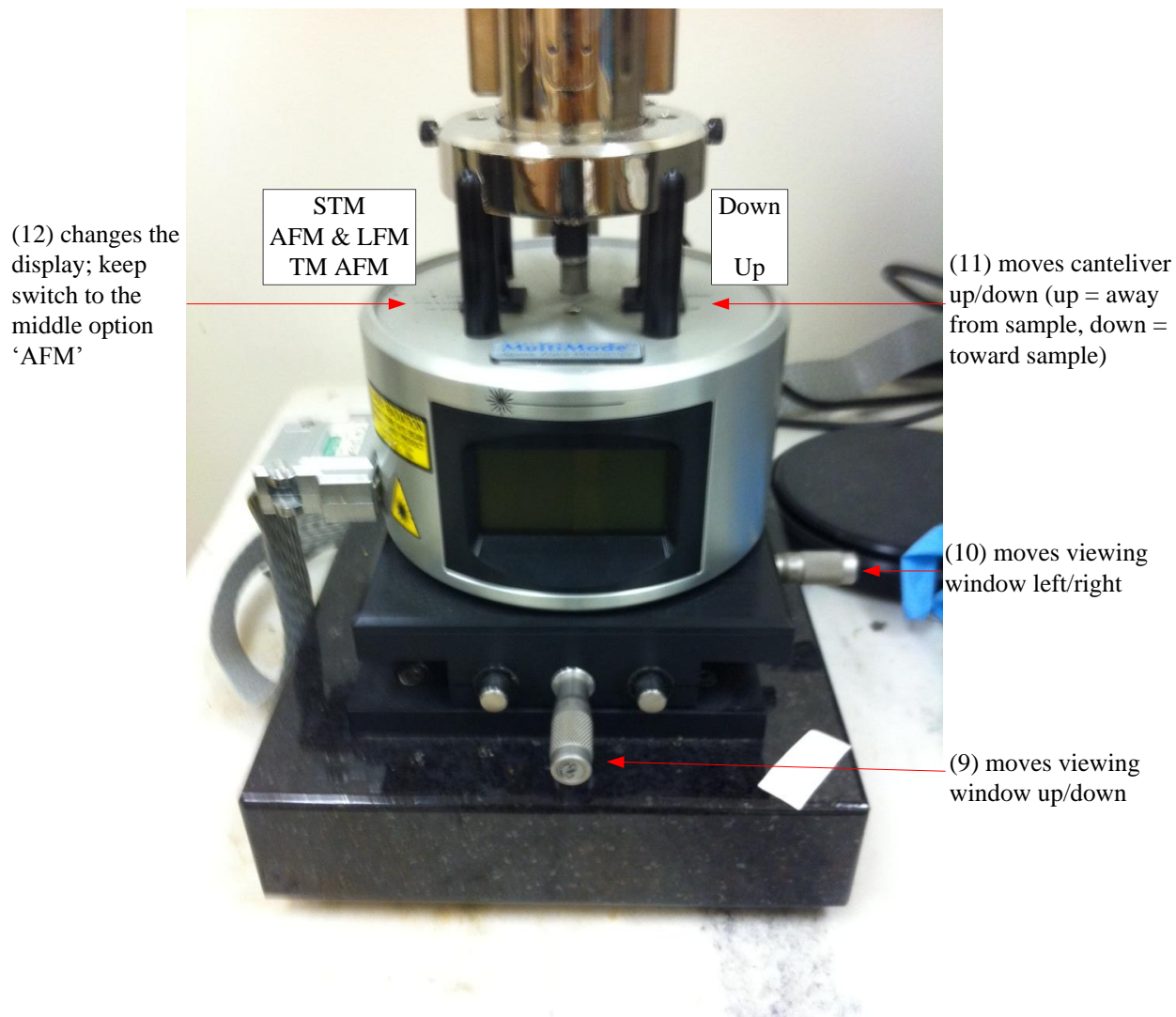
Figure D-2. Picture of AFM system (front view, bottom).
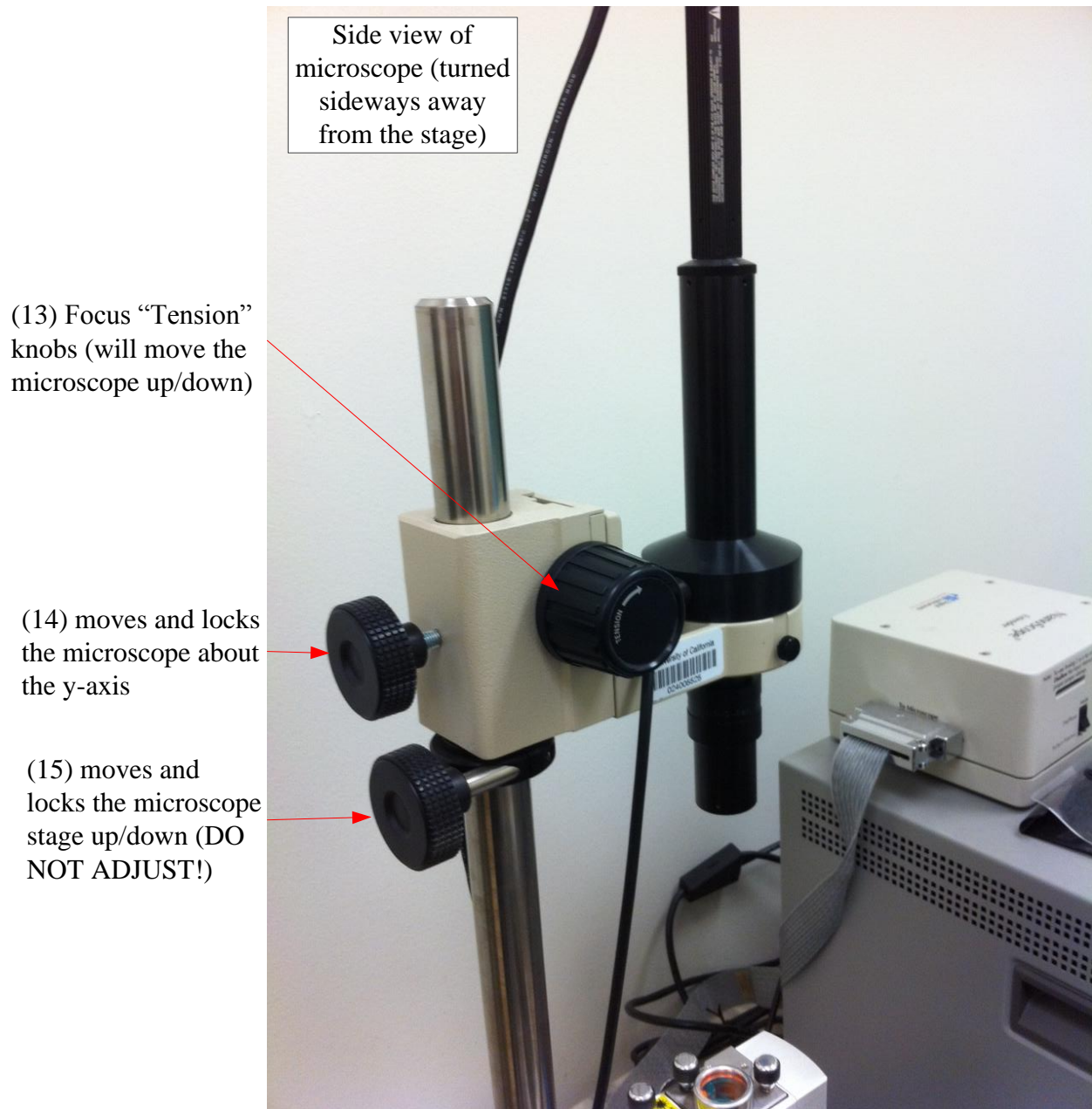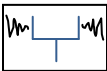
Figure D-3. Picture of AFM system microscope (side view).

The numbers referenced in following procedure refer to the numbers listed in Figure D-1, Figure D-2, and Figure D-3.

1. Dry sample in a vacuum chamber for 24 hours to get rid of moisture on the sample surface

2. Place double sided tape on the an AFM chuck (i.e., sample mounting disk) (Product # APSH-0010, Bruker AFM Probes Americas, Camarillo, CA) and put the sample in the middle of the chuck (make sure that the entire sample fits within the bounds of the chuck)

3. Place the chuck with the sample onto the magnetic stage

4. Use pointy-tip tweezers to place an AFM probe (NSC15 silicon nitride probes, Digital Instruments, Veeco Metrology Group, Santa Barbara, CA) into the probe holder (Product # MFMA, Bruker AFM Probes Americas, Camarillo, CA)

   - note: new probes are positioned vertical in the probe box, used probes are positioned horizontal in the probe box

   - put the probe holder down on the table to allow for spring clip (gold) to raise

   - slide the probe in the holder until it reaches the line (note: place slanty side of the probe in the holder first; the slanty side faces the bottom)

5. Turn on the power to the AFM system

6. Turn on the microscope (shown in Figure D-3) light and adjust the brightness

7. Turn on the microscope TV monitor / viewing screen

8. Make sure the sample (▱) is below the 2 domes on the stage, as shown:

   - if not, move the stage up/down with #11 to adjust to the proper position (note: "up" refers to the probe tip going up; it is actually moving the stage down)

9. Place the probe holder on the AFM stage

   - the spring clip faces down, the handle should be on the right side

10. Turn the clamping screw on the back side #1 to lock in the probe holder

11. Turn knob #14 and swing optical microscope 90° clockwise to lock into place; ensure that the white light of the optical microscope is shining directly onto the sample surface, surrounding the laser

12. Turn the "tension" knob #13 to focus and find the probe

- may need to adjust #11 to move the tip up/down

  o note: never focus it sharply (by adjusting #11 too far down); if it is focused too sharp, there is a chance the probe will break by jamming it into the surface

13. Find the laser by adjusting #9 and #10

14. Move the laser on the top of the probe by adjusting #2 and #3 (should be on top of the 1st half of the probe)

15. Now that the laser is aligned, turn knob #13 to focus on the sample surface

16. Move the mirror (#6) to maximize the sum (the sum must be $\geq$ 2.5 for good resolution)

17. Place a small piece of paper to block the photodiode, adjust the laser with #2 and #3 until a solid bright red laser line occurs without spreading (this concentrates the photodiode signal, which increases the sum)

18. Adjust #4 to make sure RMS and/or VERT is 0, adjust #5 if necessary

19. Open the "Nanoscope SPM" program on the AFM computer

20. Click on the microscope icon for setup

21. Click on the tuning fork icon

22. Click "auto tune"

- a plot should pop up
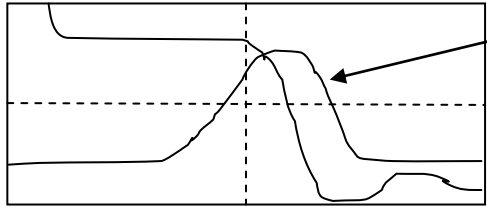
the max of this line should be
at 75% of the y-axis

23. Adjust the following on the monitor display (Figure D-4):

- amplitude setpoint: 1.1 V

- drive amplitude: start at ~175 mV (adjust this value until the white line is 75% of

  the y-axis; see step 22)

- note: never change the frequency

24. Click "back to image mode"

25. Click the approach icon
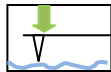
- "motor: X μm" will display on the monitor and the X will start changing as it

  approaches; the probe will become more in focus as it approaches the surface;

  when the probe has approached the surface the of the sample, the computer will

  beep; the monitor will display "tip: engaged"

- once the probe approaches, do NOT tune the RMS, VERT, or SUM anymore

26. Click the scope trace icon
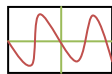
27. Adjust the following on the monitor display (Figure D-4) again:

- amplitude setpoint: 1.1 V

- drive amplitude: set to the same as was done previously in step 23, then adjust:

o such that the scope trace oscillates over ~50% of the range of the phase height (y-axis) on the scope trace plot (note: as the drive amplitude decreases, the slower and softer the cantilever taps, therefore the phase height will increase as more details are detected)
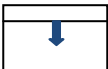
o until both the scope trace and retrace lines are visible and overlapping

o z center position of the cantilever is aligned

- scan rate: 1 Hz for quick viewing, 0.9 – 0.8 Hz for publishable image

- channel data scale: adjust value to highest feature height to view all features, e.g.,
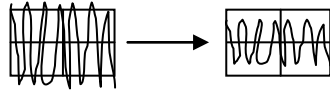
28. Click on the eye icon

29. Click on the scan from top icon (or scan from bottom icon)

- The scanning images will pop up
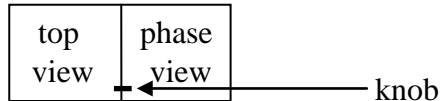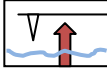
30. Select capture --> capture filename --> "name the file" --> ok

31. Click on the camera icon

- if the scan is less than 75% complete: the monitor will display "capture: on;" the computer will capture the current scanned image

- if the scan is more than 75% complete: the monitor will display "capture: next;" the computer will capture the next scanned image

- if you click on the camera icon a second time, the monitor will display "capture: force" and the computer will capture the current image, as opposed to the next scanned image

- wait until the knob reaches the top of the viewing window to ensure that the computer has captured the entire image, once this is done the monitor will display "capture: done"

32. Click on the red button to stop scanning

33. Click on the colorful mountain icon

34. Highlight the image, then select image --> select left image

35. Select modify --> flatten --> execute --> save --> okay

- note: this will overwrite the image

36. Select image --> select the right image

37. Select modify --> flatten --> execute --> save --> okay

- note: this will overwrite the image

38. Select view --> top view

39. Select view --> surface plot

- Change the data scale to 15 nm (or adjust to whatever scale that allows for full surface viewing)

40. Select analyze --> bearing

41. Select analyze --> roughness

42. To save / send images (do this before you hit "execute" for a higher quality image):

- Select utility --> TIFF export (repeat this for each image: surface, bearing, and roughness)

    o name the file

    o click ok

    o this saves the file in the "E:\afm" file

    o email images to yourself (there is no USB drive in the computer)

43. To view the roughness and skewness, select analyze --> roughness --> {left click on the image; this will create a box; move it to the area of interest} --> execute

- save and send image (see step 43)

44. Click on the microscope icon

45. Move the probe to a new area of interest (note: the laser will automatically move with the probe)

- knobs #7 and #8 move the stage left/right and up/down (fine tune)

- knobs #9 and #10 move the stage up/down and left/right (course tune)

46. Repeat steps 21 – 45

- examine at least 3 – 5 different locations on a sample surface and scan at both 0° and 90° at the same location to verify that the AFM images were free of directional errors

Troubleshooting:

- If there are large white areas in the scanned area, there may be particular or dust on the surface; move the probe to a new area of interest and re-scan.

- Skips/streaks in the scanned area can be caused by the double sided tape not being sticky enough, causing the sample to move with the tip.

- Streaking in the scanned area can be caused by a sample feature sticking to the tip; pull the tip up and re-scan. Also, changing the scan angle may help clean off the probe tip.

Scan Controls	Feedback Controls	Other Controls
Scan size: 10.0 μm (or 2.0 μm)*	Z modulation: enabled	Microscope mode: tapping
Aspect ratio: 1:1	SPM feedback:	Z limit: 3.240 μm
X offset [a]: 0.000 nm	Integral gain: 0.3000	FM igain: 40.00
Scan angle [b]: 0.00º *	Proportional gain: 3.000	FM gain: 60.00
Scan rate [c]: 1.000 Hz*	Amplitude setpoint: 1.100 V*	Amplitude limit: 2.500 V
Samples/line: 512	Drive frequency [d]: 175 Hz	Units: metric
Lines: 512	Drive amplitude: 60 mV	Color table: 12
Slow scan axis: enabled		Engage setpoint: 1.00
		Serial number: 5749 EV
Channel 1	Channel 2	Auto Gain
Data type: height	Data type: phase	Gain state: 0.200
Data scale [e]: 15.00 nm*	Data scale [f]: 30.00º *	Gain end: 0.800
Line direction: trace	Line direction: trace	Gain incr: 0.100
Scan line: main	Scan line: main	Pro. gain factor: 1.50
Real time planefit: line	Realtime planefit: line	Max shift: 0.0300
Offline planefit: full	Offline planefit: none	Gain offset: 0.900
		Lines/gain: 3

[a] this value should only be altered if there is a step change on the sample
[b] choose 0º or 90º (conduct at least 1 scan at both angles to make sure that they are free of directional errors; changing the scan angle can also help cleaning off the probe tip)
[c] this value adjusts how fast the stage/probe taps/moves; it is set at 1 Hz, however reducing this value to 0.9 Hz (which will actually display 0.898 Hz) or lower allows for higher resolution images for publications
[d] allow auto tune (Step 22) to automatically select this value and do NOT change (note: the value will be different for every tip, however)
[e] adjust value to highest feature height
[f] select 30º or 45º

Figure D-4. AFM monitor display, where * denotes that the number can be changed.

D.2   Contact Angle
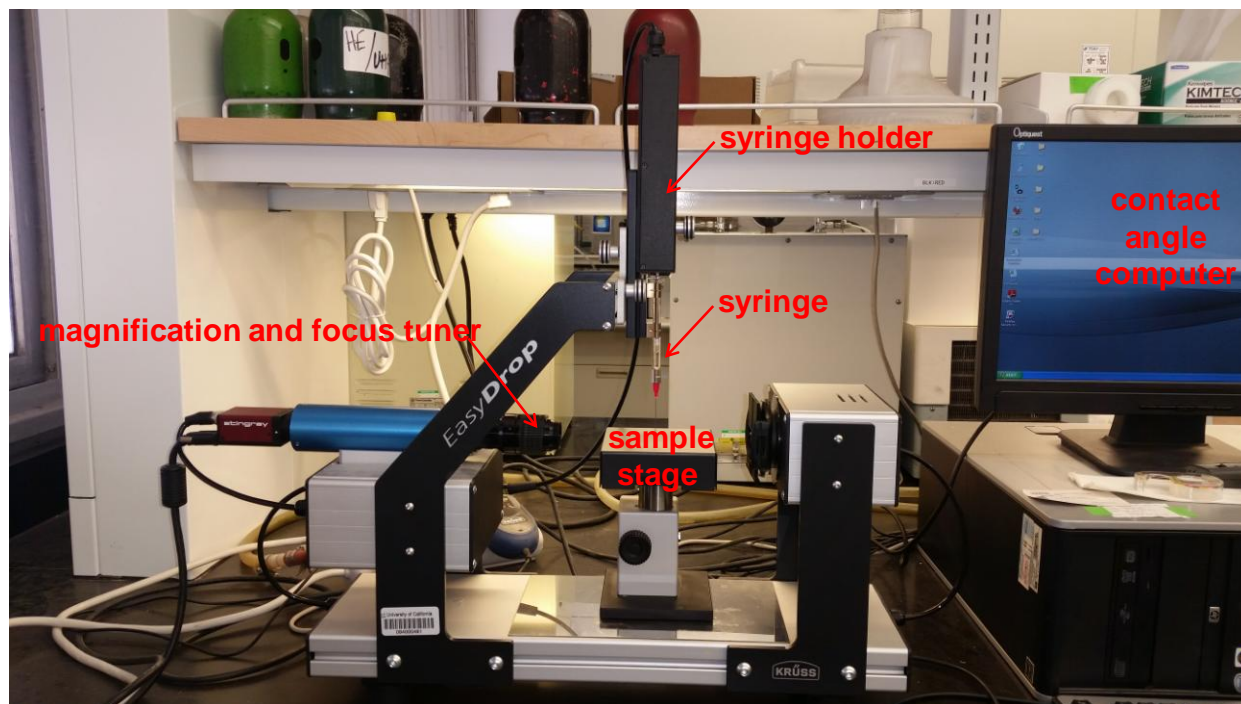
Figure D-5. Kruss Model DSA 100 contact angle measurement system.

1. Fill the 500 μL glass syringe (Model SY20, Kruss, Hamburg, Germany) using the 0.5 mm straight needle (Model NE41, Kruss, Hamburg, Germany) (for use in sessile drop method) or J-shaped needle (for use in captive bubble method) (Figure D-6) with ~100 μL of liquid (e.g. water, diiodomethane) or air, respectively
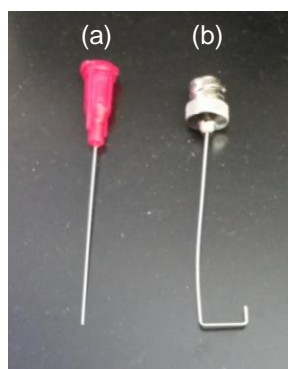
Figure D-6. Syringe needles used for contact angle analysis: (a) straight, and (b) J-shaped.

2. Place syringe with needle attached into the syringe holder of the Kruss Model DSA 100 (Hamburg, Germany) contact angle analyzer (Figure D-5)

3. Place the syringe holder in the contact angle analyzer and tighten the knob to secure

4. For the captive bubble method, place the transparent glass box (SC02, Kruss, Hamburg, Germany) on the sample stage and fill with a sufficient amount of DI water such that DI water touches the bottom of the sample clips (tan color) that are attached to the box; then, place a wet membrane sample facing down on the sample clips

5. For the sessile drop method, place the sample on the stage

6. Open the "Drop Shaper Analysis" Program on the contact angle computer, and click the "video camera" icon to acquire images

7. In the "DSA Device Control Panel," select "continuous"

8. Adjust the sample stage such that both the needle and the sample can be seen on the computer monitor

9. Adjust the magnification and focus of the camera to sharpen liquid (sessile drop method) or air (captive bubble method) bubble image

10. In the "DS Device Control Panel," select "volume" and set the air volume at 2 μL for sessile drop method or 10 μL for captive bubble method

11. Inject a liquid/air drop/bubble on the sample surface

12. Measure the contact angle ~5 seconds after the drop/bubble touches the sample surface

13. Repeat the measurement 3 – 5 times

14. Repeat the above procedure for at least 5 locations on the sample surface

D.3 X-ray Photoelectron Spectroscopy (XPS)

The following XPS (AXIS Ultra DLD, Kratos Analytical Ltd., Manchester, England) (Figure D-7) protocol was adapted from an operating procedure created by Ignacio Martini. If the software is not open or not communicating, the controller processor unit will display "E4". Re-start the software. The CPU should show "d3" when communicating normally to the computer.

Figure D-7. AXIS Ultra DLD XPS System.

D.3.1 Starting Up the System

1. Double click on the "Zones" icon on the desktop of the XPS computer.

- Zones taskbar should appear at the top of the screen.

2. Double click on the "Shortcut to Manager" icon on the desktop to open the manager software.

3. Click on the window menu and open manual window and open real time display.

4. Left click on the Zones button in the top task bar and choose "Control".

5. Drag the manual window into the manual zone.

6. Drag the real time display window into the manual zone and into the manager zone.

7. Verify that the dual anode gun located on the back of the SAC chamber is all the way out (away from the sample stage), and that nothing is sticking out from the sample stage.

8. Calibrate the stage.

   • When calibration is completed, the calibrated light will turn green.

9. In the Stage window click on "Load table" and open C:/Stage Positions/Bars_and_Stub.dset.

D.3.2 Sample Loading into the Sample Transfer Chamber (STC)

1. Mount samples onto the sample bar (Figure D-8).

   • Always wear gloves when handling samples and sample holders to limit contamination; use the conductive tape (3M Electrical Tape Ruban isolant, 1/2") to adhere samples onto bar.

load at this end   do not load samples in this area

load top side onto fork (i.e., magazine in the STC)
load bottom side onto hook (i.e., transfer arm)
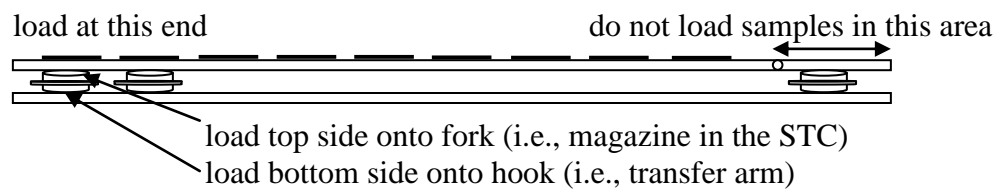
Figure D-8. XPS sample bar.

2. Turn on light to ~3000K intensity and aperture C (Figure D-9).

Figure D-9. XPS light and aperture control box.

3. Scroll down to Vacuum Control section in the Manual Control Window.
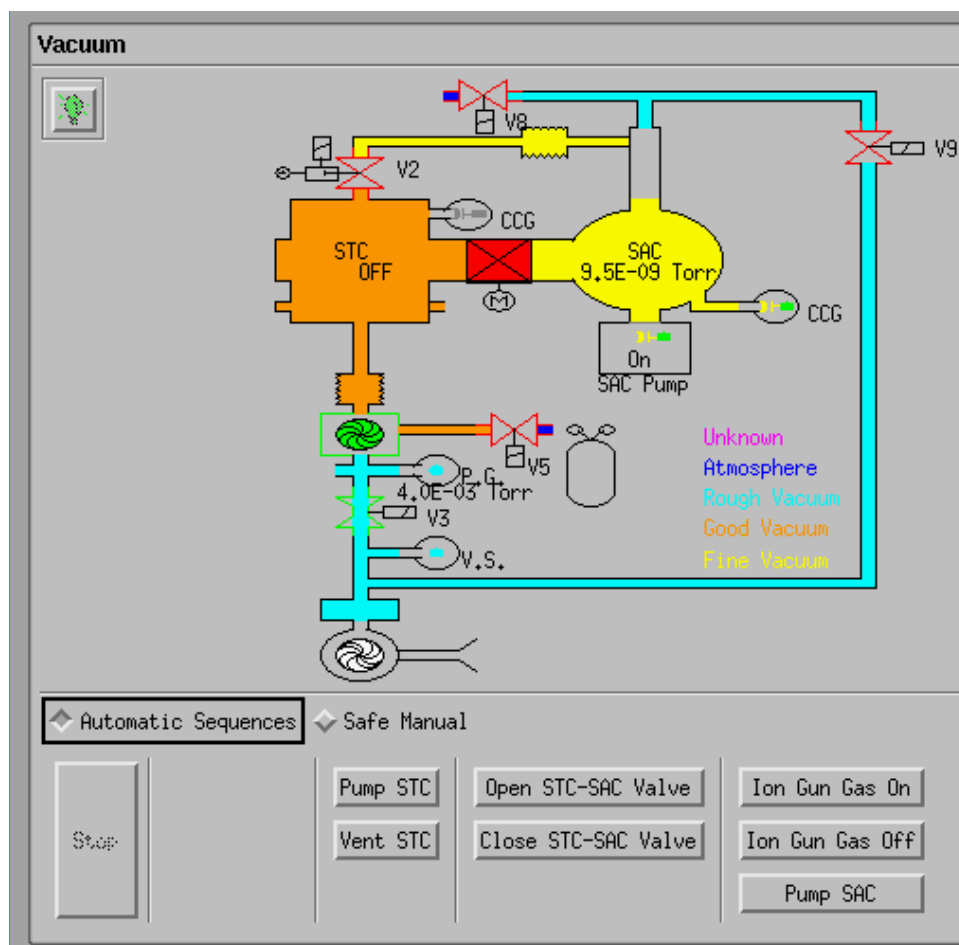
Figure D-10. Manual controls window in the XPS controls interface.

4. Confirm that the Sample Analysis Chamber (SAC) pressure is $< 1 \times 10^{-8}$ and Sample Transfer Chamber (STC) pressure is $< 5 \times 10^{-7}$ (Figure D-10).

5. Select the automatic sequence box (Figure D-10) and verify that the LED at the end of the transfer rod is green.

6. Click on "Vent STC" to allow the STC pressure to reach ambient state in order for sample loading; wait till the STC turns green in the manual controls window (Figure D-10).

7. Partially unscrew the three brass screws on the end of the STC chamber and wait for chamber to completely vent; note that the o-ring which seals the STC will open slightly due to the nitrogen gas purge.

8. Completely unscrew the three brass screws on the end of the STC chamber and rotate the chamber door open.

9. Rotate the translation knob to move the transfer arm forward for sample loading, and attach the sample bar to the end of the transfer arm (load top side onto fork) or to the magazine in the STC (load bottom side onto hook) if there is a sample currently in the SAC.

10. Rotate the translation knob to move the transfer arm back and close the chamber door.

11. Click on "Pump STC" and wait for pump down to complete (~ 15 minutes to get to 100%).

12. Wait until the STC pressure is < 5 x 10^{-7} Torr. DO NOT open the STC-SAC valve (flap valve) if the STC pressure is > 5 x 10^{-7}.

13. In "Automatic Sequence", click on "Open STC-SAC Valve" and wait to see valve open (Figure D-10).

14. Verify that the Dual Anode is backed out from the sample area, or retract it manually (all the way).

15. Scroll to Stage section in the Manual Control Window and click on "Table" in the Positions section.
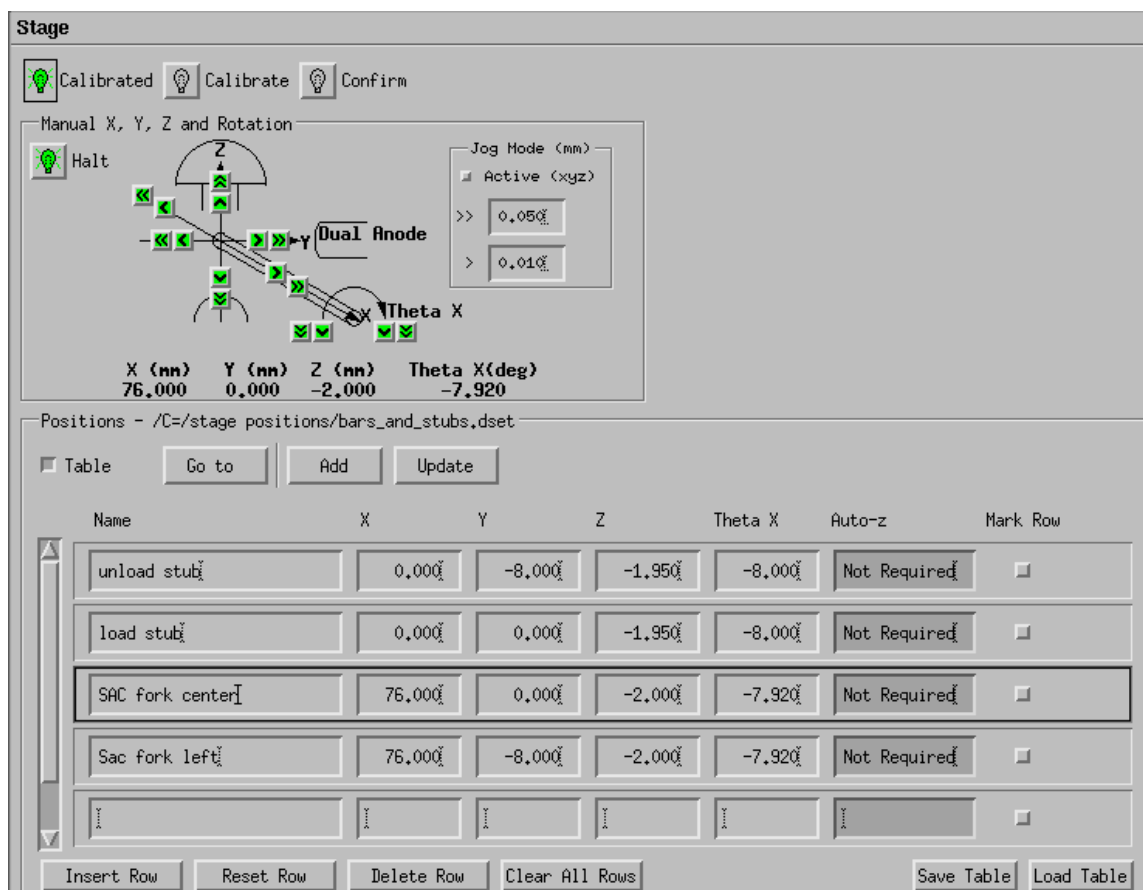
Figure D-11. Stage section in the manual controls window in the XPS controls interface.

16. If positions table is not displayed, click on "Load table" and open C:/Stage Positions/Bars_and_Stub.dset.

17. Highlight the appropriate position table row, depending on sample holder, and click on "Go to".

   - This will move the stage to the proper position for transferring the sample holder.

18. While looking through the viewing window, rotate the translation knob to move the sample into the SAC until it interlinks with the stage.

19. Again, highlight SAC fork left to release the sample holder from the transfer arm while slightly jiggling the translator knob to help with the release of the claw.

20. After the sample bar is released from the transfer arm, rotate the translator knob so that the transfer arm is all the way back and the green LED lights up at the end of the transfer arm.

21. Click "Close STC-SAC Valve" from manual controls window (Figure D-10).

22. Click "Pump STC" and wait until the SAC pressure is $< 1x10^{-8}$ (~2 hours).

23. Position sample using the stage manual controller (Figure D-12) while watching the video monitor.

   - Magnification on monitor can be varied by adjusting zoom control on video camera.

   - Your sample region of interest should be in focus in the focal area of the video monitor.

Figure D-12. XPS controller.

D.3.3 Optimizing the Z-axis

This procedure may be performed in order to optimize the z-axis height (i.e., achieve maximum counts) after achieving an approximate target z-axis height via using the controller (Figure D-12) to manually move the sample up/down.

1. Turn on neutralizer and x-ray gun, and ensure that C 1s is active.

2. In Manual, scroll to sample area of interest and open position table and clear all rows.

3. Click add (the location will pop up on the window).

4. In auto-z (Figure D-13), adjust the No. Increments to 21 (must be odd), increment size to 0.05 mm, and ensure that the "Ordinate Choice" button is set to "Area."
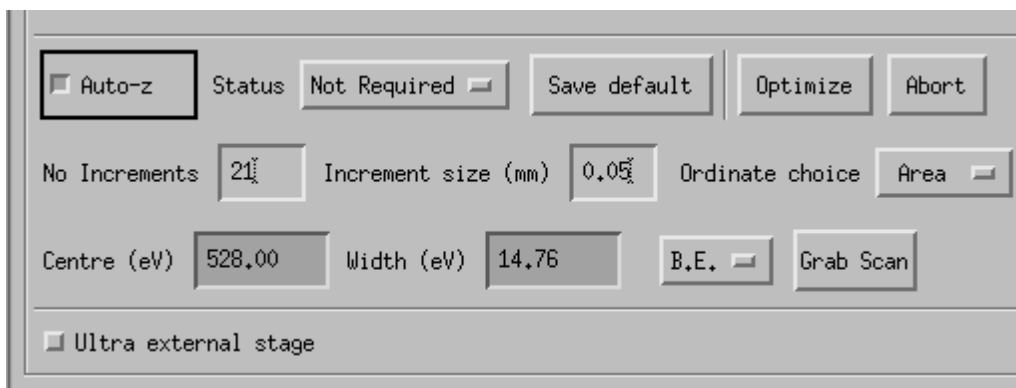
Figure D-13. Auto-z section in the manual controls window in the XPS controls interface.

5. In auto-z, click on "Grab Scan" to load the current active snapshot settings into the "Auto Z" routine.

6. Click on the "optimize" position button to begin the automatic sample height routine; upon completion, the stage will move to the optimized height.

7. A new object labeled "Auto Z Profile" will be written to the Acquiring section in the manager window.

D.3.4 Performing a Survey Scan from the Manager

1. Select the "Manager" zone and click "resume" button at the top of the window to set to Automatic mode.
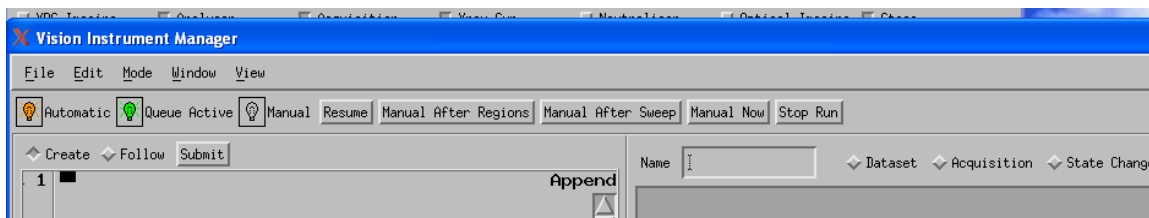
Figure D-14. Manager zone in the XPS controls interface.

2. Select instrument manager, acquiring (left bottom), open dataset.

   Choose the "Dataset" button and enter a filename for storing your data (e.g., /C=/data/Kari/*.dset   /C=/data/Kari/filename), then name the dataset, and hit apply.

3. Click the middle mouse button to paste the "Filename" sequence in the flow chart section of the manager.

4. Choose the "Acquisition" button and set up the parameters for the survey scan (Table D-1).

Table D-1. Parameters for the survey scan acquisition.

Region Name	Start (eV)	End (eV)	Step (eV)	Dwell (ms)	# sweeps
Survey	1200	-5	1	100.0	5

- X-Ray PSU: Filament: Mono(Al), Emission(mA): 10:0, Anode HT(kV): 15:0.0

- Never go above 20mA with emission current

- Standby Control: click Standby

- Analyzer: Mode: Spectrum, Lens Mode: Hybrid, Resolution: Pass Energy 160, Aperture: Slot

- Scan Control: Region, Name: type in "Survey" on an empty row, click enter then right click on header to change from Centre eV to Start eV

- Click on "Active" box

- Charge Neutralizer: ON

- X-Ray gun: click on

- Acquisition: click on, and it will start scanning; click off, and it will stop scanning once the current scan is complete

5. Choose "Acquiring" in the view window to see the scan data being collected in the real time window.

6. When completed, the scan may be viewed in the real time window by highlighting the item in the acquiring window and middle mouse button "pasting" into the right-hand section of the real-time display window.

    - Using mouse control menus you may zoom in on regions of the scan, change the scan label, etc.

    - Choose element list from manager windows pull down menu to open up an element list; clicking on peaks of interest in the real time window will cause associated element to display in the element list window.

D.3.5 Performing Spectroscopy for Elements of Interest

1. Set up and perform a survey scan as described in Section D.3.4.

2. Select the following conditions:

Analyzer

    Mode: spectrum, Lens: Hybrid, Res: pass energy 20, slot

Excitation

    x-ray gun

    source: mono(Al), emission (mA): 10, Anode HT (kV): 15.0

Neutralizer

switch ON

Scan Control

XPS, spectrum, B.E., Al(mono)

3. Choose the "Acquisition" button and set up the parameters.

4. In the energy regions table, enter region name manually in the exact way (e.g., spacing, capitalization) that it is written in the database (e.g., O 1s) and input the conditions presented in Table D-2.

Table D-2. Parameters for acquisition of peaks of interest.

Region Name	Centre (eV)	Width (eV)	Step (eV)	Dwell (ms)	# sweeps
C 1s	282	14	0.1	300.0	20-25 (16)
O 1s	528	12	0.1	200.0	20-40 (10)
N 1s	396.5	10	0.1	200.0	20 (20)
S 2p	162	16	0.1	200.0	25 (16)
Na 1s	1068	8	0.1	200.0	10 (10)

D.3.6 Manager Sequence

A manager sequence (e.g., Figure D-15) can be created in order to conduct spectroscopy automatically. A manager sequence can be helpful when taking a large number of scans at different positions on the sample. Be sure to enter the proper number for "Counter." The number of counter of cycles is equal to the number of scans minus one (e.g., if there are 8 areas of interest, the number of cycles = 7).
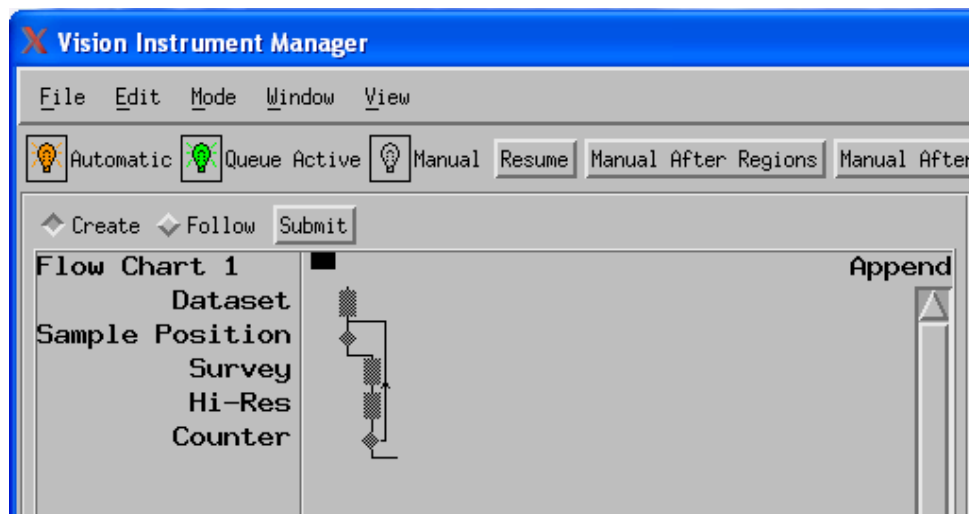
Figure D-15. A typical manager sequence used to conduct automatic spectroscopy.

Once a sequence is created, execute Load Run:

1. In Manager, select File-> Load Run.

2. In Filter, type in filename (e.g., /C=/data/KariMoses/*.dset).

3. Click enter.

4. In Files, select sequence.

5. Click "apply" and then click "okay".

Once the sequence is loaded, execute Start Run:

1. Once the sequence is created, select File->Save Run.

2. Click on "Submit" (the sequence will show in the queue). Note: selecting follow (next to submit), allows to increase or decrease number of sweeps after submission.

3. Click resume to start scanning the sequence.

4. Choose "Acquiring" in the view window to see the scan data being collected in the real time window.

D.3.7 Data Analysis

The raw spectroscopy data obtained from XPS measurements needs to be converted to ".vms" files for data analysis using the following protocol:

1. Open the "CnvtSet" Program.

2. Select convert selection to ".kal ASCII".

3. Open the "CasaXPS" Program.

4. Select file->convert, and select ".kal ASCII file".

    - The ".vms" file will automatically save.

5. Click "edit mode" button to show sample names.

D.4   Ellipsometry

The thickness of the graft polymerized polymer layer was measured in ambient air by ellipsometry (LSE Stokes 7109-C-351A, Gaertner Scientific Corporation, Skokie, IL) using a HeNe laser with a 632.8 nm wavelength and 1 mm beam diameter at an incidence angle of 70º. All thickness measurements are given in Å.

1. Turn on both lasers.

2. Turn on the ellipsometer computer and monitor.

3. Enter the password for Dunn lab computer: "Dunn".

4. Open the Gardener Ellipsometer Measurement Program (GEMP).

5. Click on the following icon:

6. Input the following values:

   (Exp) Thickness 1: 100

   Polyamide Refractive Index ((Exp) N_f 1): 1.48

   Substrate Refractive Index (N_s): 3.875

   Calibration Standard (K_s): -0.018

7. Place sample under laser.

8. Click F9 and adjust the sample table knobs in order for the "+" to move to the middle.

9. Click "ok".

10. Click "Measure F8" and calculate.

11. Record thickness and Nf1 values.

12. Replace (Exp) N_f 1 with the value calculated.

13. Move sample and take 5 – 10 measurements to achieve an accurate average thickness by repeating steps 8 – 10.

Manufacturer provided values for refractive index (Sigma-Aldrich):

- Polyacrylic acid: 1.395

- Polyvinyl sulfonic acid: 1.389

- Poly(2-hydroxyl methacrylate): 1.512

Appendix E RO Membrane Filtration System

E.1 RO Cell Design

The plate-and-frame membrane cell (Figure E-1) along with the spacer (Figure E-2) that were used for membrane filtration studies presented in Chapter 5, Figure 5-2a.
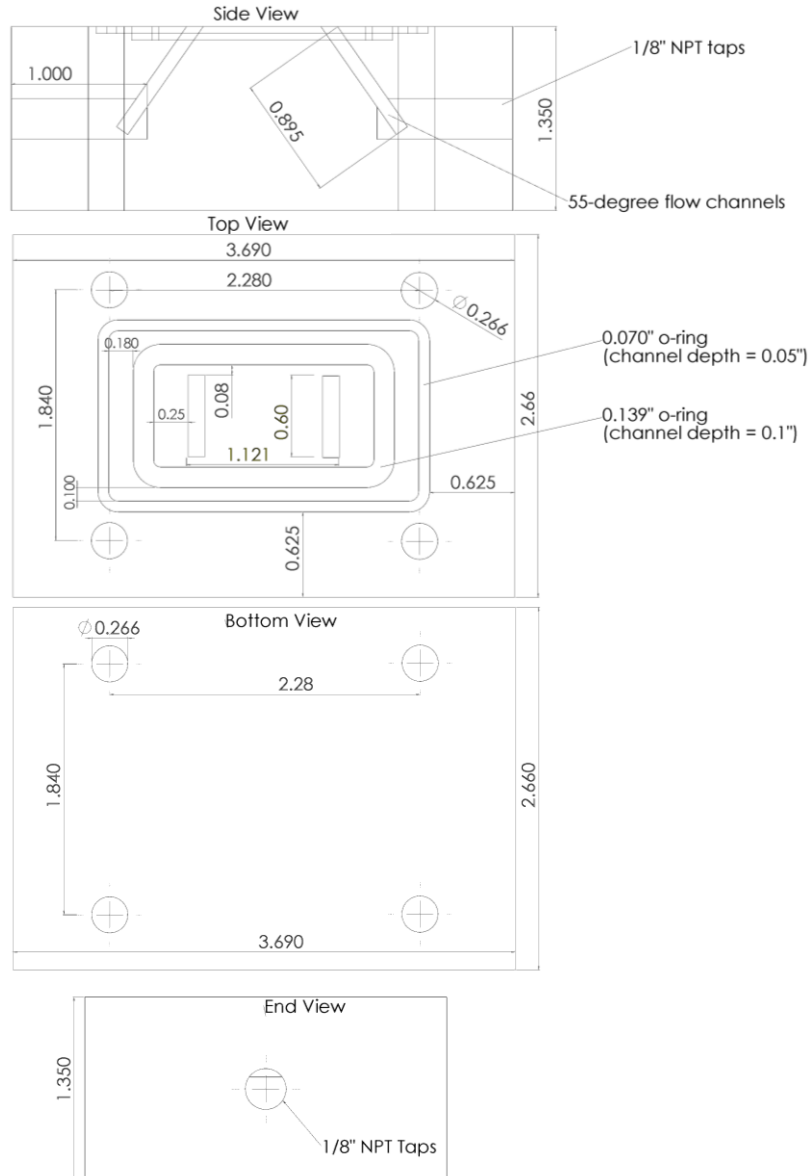
Figure E-1. Schematic of the plate-and-frame membrane cell made of white Delrin acetal resin (Note: all dimensions are in inches).

Figure E-2. Schematic of the membrane cell spacer made with white Delrin acetal resin having dimensions of 2.66" (width) x 3.69 (length) x 0.09375 (height) (Note: all dimensions are in inches).

From top to bottom, the cell is composed of: stainless steel plate (Catalog No. 9090K72), white Delrin acetal resin top (Catalog No. 8739K67) with both large (0.139", Catalog No. 9557K76) and small (0.070", Catalog No. 9557K65) o-rings in the grooves, 3/32" white Delrin acetal resin spacer (Catalog No. 8573K12), RO membrane, mesh spacer, white Delrin acetal resin bottom (Catalog No. 8739K67) with both large (0.139", Catalog No. 9557K76) and small (0.070", Catalog No. 9557K65) o-rings in the grooves, stainless steel plate (Catalog No. 9090K72). The cell is bolted together with flange hex nuts (Catalog No. 94758A028) and 1/4"-20 thread size screws (Catalog No. 93190A557). All materials (aside from membrane and mesh spacer) purchased from McMaster-Carr (Santa Fe Springs, CA).

199

E.2　　　RO Cell Operating Protocol

For the PFRO system presented in Chapter 5, Figure 5-2a, water was fed to the PFRO membrane channel using a high pressure 1/2 hp (373 W) positive displacement feed water pump (Hydra-Cell Pump Model No. M03XRSGSHEP, Wanner Engineering Inc., Minneapolis, MN). The transmembrane pressure and feed water flow rate were regulated by adjusting the pump variable frequency drive (VFD), and bypass and backpressure valves. Feed side pressure was monitored with a digital gauge pressure (PGP-25B-300, Omega, Stamford, CT). Digital flow meters were used to monitor feed (S-112, Georgetown, TX) and permeate (FlowCal 5000 digital flow meter, Tovatech, South Orange, NJ) flow rates.

E.2.1 Installing a Membrane into the Plate-and-Frame Membrane Cell

1. Cut the membrane so that it fits exactly inside the larger (0.139", Catalog No. 9557K76, McMaster-Carr, Santa Fe Springs, CA) o-ring; the curly side should face up in the cell, as shown: ⌣‿‿‿‿⌣ .

2. Align the mesh spacer to encompass the inside area of the smaller o-ring (0.070", Catalog No. 9557K65, McMaster-Carr, Santa Fe Springs, CA) completely.

3. Tighten the cell screws by tightening one flange hex nut/bolt, then the bolt diagonal from it, the next bolt, then the one diagonal from that one, and so on until they are very secure, such that there is no water leakage.

E.2.2 System Startup

1. Supply the feed tank with 20 L of fresh DI water.

2. Turn on the temperature controller (heat exchanger with coil) to 25ºC.

3. Turn on the power (make sure the power cable to the valve is plugged in properly since it tends to fall away from the power strip). Manually open the bypass valve (the black knob on the system near the pressure dial) and push the "run" button on the variable frequency drive (VFD).

4. On the PFRO system computer desktop, open the Labview program "MeMo_Standalone_Control_JT_LG_v9.vi", which is used to control the RO system backpressure valve actuator (Model VA8V-10-0-10, ETI Systems Inc., Carlsbad, CA) and high pressure 1/2 hp (373 W) positive displacement feed water pump (Hydra-Cell Pump Model No. M03XRSGSHEP, Wanner Engineering Inc., Minneapolis, MN) settings (Figure E-3 and Figure E-4). The above program was developed at the UCLA Water Technology Research Center. It is noted that adjusting the backpressure valve and feed water pump affects the solution feed water flow rate (and crossflow velocity) and transmembrane pressure.

5. Set the "Serial COM port" to "COM1".

6. Change the "Output Low (Valve)" to 0.005.

7. Set the "Valve Setting" to 3. Hit the "run" button (white arrow). Make sure you hear the valve moving.

8. Set the "VFD Setting" to 3. After ~30 s, increase the VFD to 5. After ~30 s, increase the VFD to 6.

9. Adjust the bypass valve (manually), backpressure valve setting, and VFD such that the pressure reaches 250 psi at a retentate flow of 319 mL/min. Typically this is done by

adjusting the bypass valve such that there are ~4 threads visible, at a backpressure valve setting of <0.1, and VFD setting of ~6 – 8.

- First, manually adjust the bypass valve to see a pressure increase of ~150-200 psi.

- Second, adjust the backpressure valve in the following increments, waiting ~1 min in between adjustments to allow for stabilization: from 3 to 2, then from 2 to 1, then from 1 to 0.7, then from 0.7 to 0.5, then from 0.5 to 0.4, then from 0.4 to 0.3, then from 0.3 to 0.2, then from 0.2 to 0.1.

- Finally, adjust all 3 variables (bypass valve, backpressure valve setting, and VFD) to reach the desired pressure and crossflow velocity.
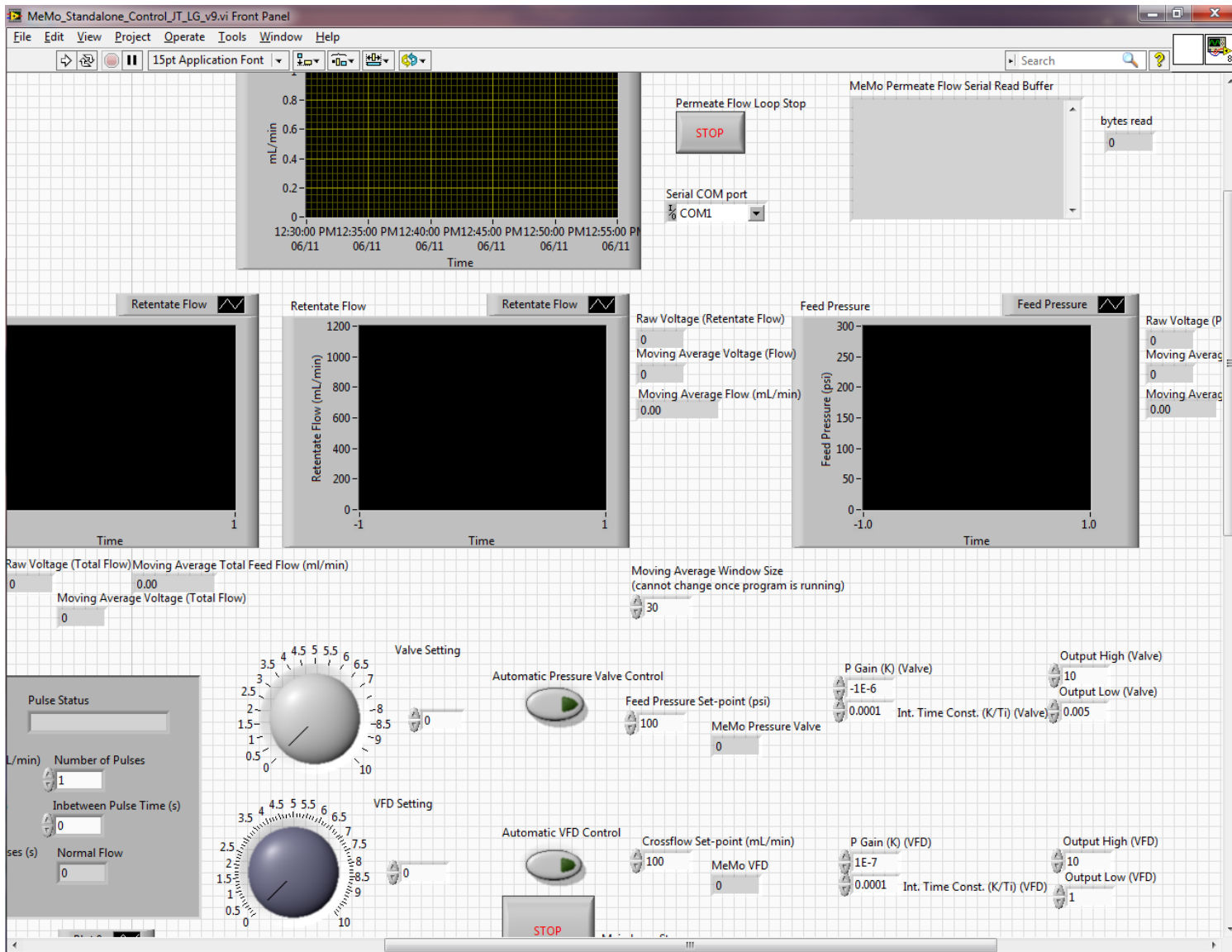
Figure E-3. Screenshot of the Labview software interface used to control membrane filtration.
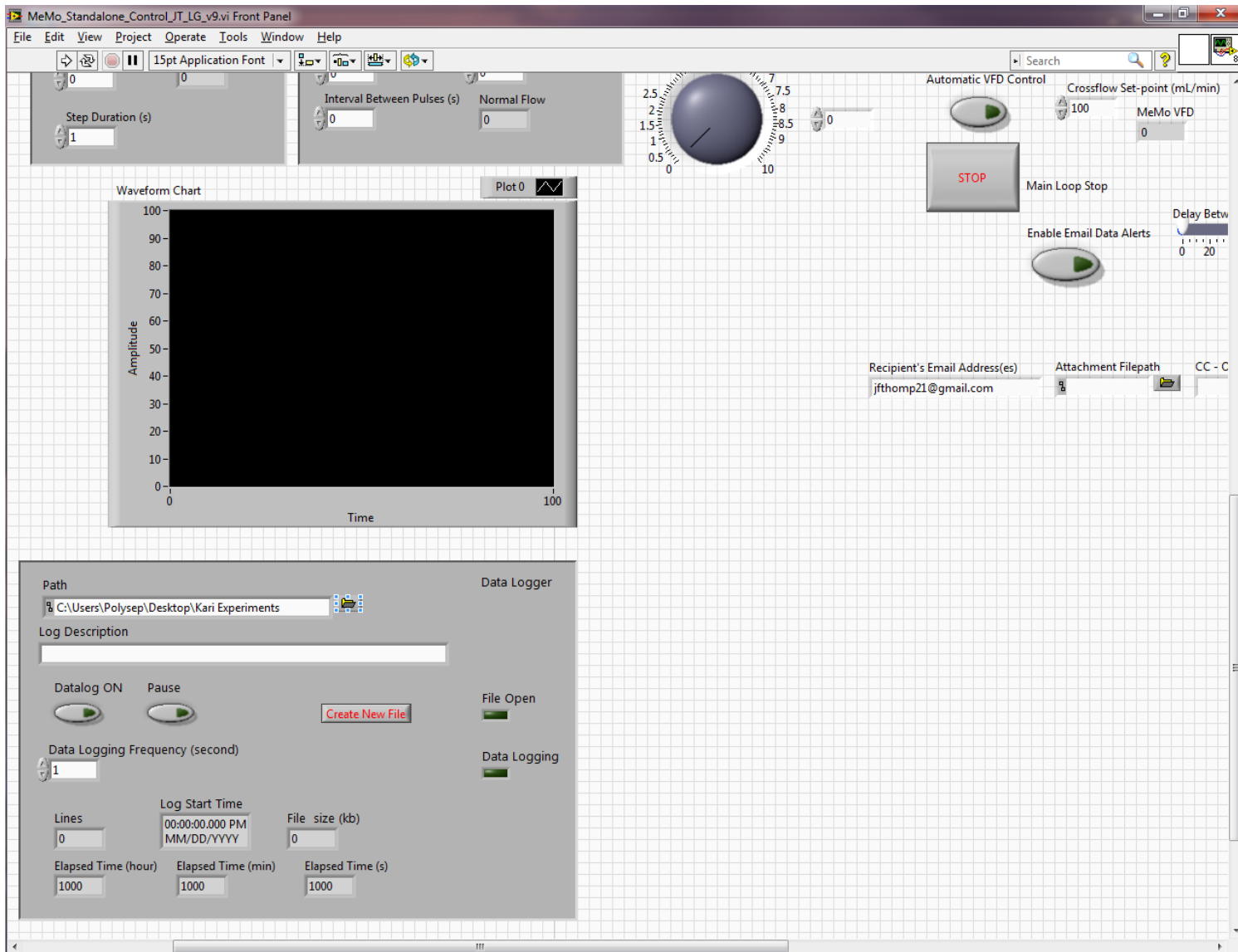
Figure E-4. Screenshot of the Labview software interface used to control membrane filtration.

E.2.3 Membrane Conditioning

The membranes are conditioned at the following conditions: pressure at 250 psi, retentate flow rate at 319 mL/min (0.15 m/s crossflow velocity for the small cell), and temperature at 25ºC.

1. Ensure the system is running on "COM1". If not, shut down the system and restarts in order to properly record permeate flux measurements measured by digital flow meter (Serial No: 4-1110, GJC Instruments Ltd., Cheshire, UK).

2. Set the "Output Low (Valve)" to 0.005. Once the pressure and crossflow velocity are set and stabilized, turn on the "automatic pressure valve control." The button/arrow should turn green.

3. Set the "Data Logger" "Path" to "C:\Users\Polysep\Desktop\Kari Experiments" by clicking on the folder and selecting "Kari Experiments" file, located on the "Desktop". Then, click on "Current Folder". This will allow "C:\Users\Polysep\Desktop\Kari Experiments" to show up in the path area. Then, click the "Datalog ON" button to start collecting data. The button/arrow should turn green.

4. Open up the file on the computer to ensure that the data logger is collecting data properly. The filename is usually in this form "6-11-2014 3_57_1 PM" as a excel document with columns with values for Time Elapsed (s), Permeate Flow Rate (mL/min), Total Feed Flow (mL/min), Retentate Flow (mL/min), and Feed Pressure (psi). Make sure it is collecting data for all 5 columns (i.e. not outputting "0").

5. Monitor the system such that the pressure and crossflow velocity are constant throughout the conditioning period.

6. Once the permeate flowrate becomes constant (i.e. the permeate flowrate fluctuates less than 5% in a 30 min period), conditioning/compaction is complete. This should take ~6 hours.

7. Turn off the data logger.

E.2.4 Membrane Permeability Measurements

1. Measure the permeate flowrate at 5 or more pressure settings between 125 – 300 psi. Wait for the flowrates to stabilize for at least 5 minutes after adjusting the pressure before recording measurements.

2. Determine the slope of pressure versus permeate flowrate (from the obtained data), and use to calculate membrane permeability, L_p, where $J_p = L_p(P\text{-}\Delta\pi)$.

   - The R^2 value for the linear pressure-flowrate correlation should be >0.98, otherwise repeat steps 1 and 2.

E.2.5 Membrane Rejection Measurements

1. Use the mass balance to measure 20 g NaCl (i.e., create 20 L of 1000 ppm NaCl).

2. Place NaCl in beaker and fill 75% of the beaker with DI water. Place a stir bar in the beaker and use a stir plate to dissolve the NaCl.

3. Dump the well mixed solution of NaCl/water in the containment vessel. Add DI water to reach 20 L, and make sure the solution is well mixed.

4. Set the pressure to 225 psi and retentate flowrate to 319 mL/min (0.15 m/s crossflow velocity for the small cell).

5. Allow the system to circulate for at least 30 min before collecting the permeate to allow for enough time for the freshwater to cycle though.

6. Measure the conductivity of the retentate stream (there is a valve on the retentate line that use can open to collect a sample). It should be ~2 mS (2000 µS).

7. Collect at least 10 mL of the permeate water in a 40 mL vial, and subsequently measure the conductivity.

8. The observed rejection is equal to one minus the permeate concentration divided by the bulk concentration.

   - RO rejection is typically ~94-98%

9. Clean the RO cell and tubing by rinsing with DI water such that the retentate line is less than 5 µS. This will rinsing the system at least 3 times: Drain the saltwater out of the collection tank, and refill the tank with DI water. Rinse out the system by circulating DI water at 150 psi and high feed flowrate (~1000 mL/min) for at least 10 min. Drain the water from the collection tank, and refill with DI water again and circulate DI water at low pressure and high crossflow velocity for at least 10 min, repeat.

10. Turn the system off by clicking the stop button (red circle)

References

1.   Greenlee, L.F., et al., *Reverse osmosis desalination: Water sources, technology, and today's challenges.* Water Research, 2009. 43(9): p. 2317-2348.
2.   Herzberg, M. and M. Elimelech, *Biofouling of reverse osmosis membranes: Role of biofilm-enhanced osmotic pressure.* Journal of Membrane Science, 2007. 295(1-2): p. 11-20.
3.   Kang, S.T., et al., *Direct observation of biofouling in cross-flow microfiltration: mechanisms of deposition and release.* Journal of Membrane Science, 2004. 244(1-2): p. 151-165.
4.   Mansouri, J., S. Harrisson, and V. Chen, *Strategies for controlling biofouling in membrane filtration systems: challenges and opportunities.* Journal of Materials Chemistry, 2010. 20(22): p. 4567-4586.
5.   Baek, Y., et al., *Effect of surface properties of reverse osmosis membranes on biofouling occurrence under filtration conditions.* Journal of Membrane Science, 2011. 382(1-2): p. 91-99.
6.   Goosen, M.F.A., et al., *Fouling of reverse osmosis and ultrafiltration membranes: A critical review.* Separation Science and Technology, 2004. 39(10): p. 2261-2297.
7.   Vrouwenvelder, J.S., et al., *Biofouling of spiral-wound nanofiltration and reverse osmosis membranes: A feed spacer problem.* Water Research, 2009. 43(3): p. 583-594.
8.   Flemming, H.C., *Biofouling in water systems - cases, causes and countermeasures.* Applied Microbiology and Biotechnology, 2002. 59(6): p. 629-640.
9.   Cohen, Y. and G.T. Lewis, *Fouling and Scaling Resistant Nano-structured Reverse Osmosis Membranes*. 2013: United States Patent 8445076.
10.   Cohen, Y., et al., *Membrane Surface Nano-Structuring with Terminally Anchored Polymers Chains*, in *Functional Nanostructured Materials and Membranes for Water Treatment*, D.Z. M. Duke, and R. Semiat, Editor. 2013, Wiley-VCH Verlag GmbH & Co. KGaA: Weinheim, Germany. p. 85-124.
11.   Kim, M.M., et al., *Surface nano-structuring of reverse osmosis membranes via atmospheric pressure plasma-induced graft polymerization for reduction of mineral scaling propensity.* Journal of Membrane Science, 2010. 354(1-2): p. 142-149.
12.   Lin, N.H., et al., *Polymer surface nano-structuring of reverse osmosis membranes for fouling resistance and improved flux performance.* Journal of Materials Chemistry, 2010. 20(22): p. 4642-4652.
13.   Bhattacharya, A. and B.N. Misra, *Grafting: a versatile means to modify polymers - Techniques, factors and applications.* Progress in Polymer Science, 2004. 29(8): p. 767-814.
14.   Khayet, M., M.N. Abu Seman, and N. Hilal, *Response surface modeling and optimization of composite nanofiltration modified membranes.* Journal of Membrane Science, 2010. 349(1-2): p. 113-122.
15.   Kilduff, J.E., et al., *Photochemical modification of poly(ether sulfone) and sulfonated poly(sulfone) nanofiltration membranes for control of fouling by natural organic matter.* Desalination, 2000. 132(1-3): p. 133-142.
16.   Susanto, H., M. Balakrishnan, and M. Ulbricht, *Via surface functionalization by photograft copolymerization to low-fouling polyethersulfone-based ultrafiltration membranes.* Journal of Membrane Science, 2007. 288(1-2): p. 157-167.

17. Yu, H.Y., et al., *Manipulating membrane permeability and protein rejection of UV-modified polypropylene macroporous membrane.* Journal of Membrane Science, 2010. 364(1-2): p. 203-210.

18. Gupta, B., et al., *Preparation of ion exchange membranes by radiation grafting of acrylic acid on FEP films.* Radiation Physics and Chemistry, 2008. 77(1): p. 42-48.

19. Mehta, I.K., et al., *Grafting onto Isotactic Polypropylene .3. Gamma-Rays Induced Graft-Copolymerization of Water-Soluble Vinyl Monomers.* Journal of Applied Polymer Science, 1990. 41(5-6): p. 1171-1180.

20. Kim, H.I. and S.S. Kim, *Fabrication of reverse osmosis membrane via low temperature plasma polymerization.* Journal of Membrane Science, 2001. 190(1): p. 21-33.

21. Wavhal, D.S., Fisher, E. R., *Membrane Surface Modification by Plasma-Induced Polymerization of Acrylamide for Improved Surface Properties and Reduced Protein Fouling.* Langmuir, 2003. 19: p. 79-85.

22. Milner, S.T., *Polymer Brushes.* Science, 1991. 251(4996): p. 905-914.

23. Altintas, E., et al., *Numerical and experimental characterization of 3-phase rectification of nanobead dielectrophoretic transport exploiting Brownian motion.* Sensors and Actuators a-Physical, 2009. 154(1): p. 123-131.

24. Rana, D. and T. Matsuura, *Surface Modifications for Antifouling Membranes.* Chemical Reviews, 2010. 110(4): p. 2448-2471.

25. Belfer, S., et al., *Surface modification of commercial composite polyamide reverse osmosis membranes.* Journal of Membrane Science, 1998. 139(2): p. 175-181.

26. Nguyen, T., F.A. ROddick, and L. Fan, *Biofouling of Water Treatment Mmebranes: A Review of the Underlying Causes, Monitoring Techniques and Control Measures.* Membranes, 2012. 2: p. 804-840.

27. Childress, A.E. and M. Elimelech, *Relating nanofiltration membrane performance to membrane charge (electrokinetic) characteristics.* Environmental Science & Technology, 2000. 34(17): p. 3710-3716.

28. Wang, Z.K., et al., *Polymer surface wettability modification using femtosecond laser irradiation.* SIMTech technical reports, 2010. 11(1): p. 23-27.

29. Wei, Q.B., et al., *Dramatically Tuning Friction Using Responsive Polyelectrolyte Brushes.* Macromolecules, 2013. 46(23): p. 9368-9379.

30. Hwang, Y.J., et al., *Effects of atmospheric pressure helium/air plasma treatment on adhesion and mechanical properties of aramid fibers.* Journal of Adhesion Science and Technology, 2003. 17(6): p. 847-860.

31. Okubo, M., et al., *Surface modification of fluorocarbon polymer films for improved adhesion using atmospheric-pressure nonthermal plasma graft-polymerization.* Thin Solid Films, 2008. 516(19): p. 6592-6597.

32. Chang, Y., et al., *Hemocompatibility of Poly(vinylidene fluoride) Membrane Grafted with Network-Like and Brush-Like Antifouling Layer Controlled via Plasma-Induced Surface PEGylation.* Langmuir, 2011. 27(9): p. 5445-5455.

33. Park, J., et al., *Antibiofouling amphiphilic polymer-coated superparamagnetic iron oxide nanoparticles: synthesis, characterization, and use in cancer imaging in vivo.* Journal of Materials Chemistry, 2009. 19(35): p. 6412-6417.

34. Telford, A.M., et al., *Thermally Cross-Linked PNVP Films As Antifouling Coatings for Biomedical Applications.* Acs Applied Materials & Interfaces, 2010. 2(8): p. 2399-2408.

35. Liu, L., et al., *Influence of moisture regain of aramid fibers on effects of atmospheric pressure plasma treatment on improving adhesion with epoxy.* Journal of Applied Polymer Science, 2006. 102(1): p. 242-247.

36. Boguslavsky, Y., et al., *Controlling the wettability properties of polyester fibers using grafted functional nanomaterials.* Journal of Materials Chemistry, 2011. 21(28): p. 10304-10310.

37. de Leon, A. and R.C. Advincula, *Reversible Superhydrophilicity and Superhydrophobicity on a Lotus-Leaf Pattern.* Acs Applied Materials & Interfaces, 2014. 6(24): p. 22666-22672.

38. Pogodin, S., et al., *Biophysical Model of Bacterial Cell Interactions with Nanopatterned Cicada Wing Surfaces.* Biophysical Journal, 2013. 104(4): p. 835-840.

39. Roach, P., N.J. Shirtcliffe, and M.I. Newton, *Progess in superhydrophobic surface development.* Soft Matter, 2008. 4(2): p. 224-240.

40. Freger, V., Gilron, J., Belfer, S., *TFC Polyamide Membrane Modified by Grafting of Hydrophilic Polymers: an FT-IR/AFM/TEM Study.* Journal of Membrane Science, 2002. 209: p. 283-292.

41. Jamaly, S., et al., *A short review on reverse osmosis pretreatment technologies.* Desalination, 2014. 354: p. 30-38.

42. Cornelissen, E.R., et al., *Periodic air/water cleaning for control of biofouling in spiral wound membrane elements* Journal of Membrane Science, 2007. 287: p. 94 - 101.

43. Lee, H., et al., *Cleaning strategies for flux recovery of an ultrafiltration membrane fouled by natural organic matter* Water Research, 2001. 35: p. 3301 - 3308.

44. Madaeni, S.S., T. Mohamamdi, and M.K. Moghadam, *Chemical Cleaning of Reverse Osmosis Membranes.* Desalination, 2001. 134: p. 77-82.

45. Muthukmaran, S., et al., *The optimisation of ultrasonic cleaning procedures for dairy fouled ultrafiltration membranes.* Ultrasonics Sonochemistry, 2005. 12: p. 29 - 35.

46. Belfer, S., et al., *Surface characterization by FTIR-ATR spectroscopy of polyethersulfone membranes-unmodified, modified and protein fouled.* Journal of Membrane Science, 2000. 172(1-2): p. 113-124.

47. Kang, G.D. and Y.M. Cao, *Development of antifouling reverse osmosis membranes for water treatment: A review.* Water Research, 2012. 46(3): p. 584-600.

48. Wilbert, M.C., J. Pellegrino, and A. Zydney, *Bench-scale testing of surfactant-modified reverse osmosis/nanofiltration membranes.* Desalination, 1998. 115(1): p. 15-32.

49. Jeong, B.-H., Hoek, E. M. V., Yan, Y., Subramni, A., Huang, X., Hurwitz, G., Ghosh, A. K., Jawor, A., *Interfacial Polymerization of Thin Film Nanocomposites: A New Concept for Reverse Osmosis Membranes.* Journal of Membrane Science, 2007. 294: p. 1-7.

50. Lee, H.S., Im, S. J., Kim, J. H., Kim, H. J., Kim, J. P., Min, B. R., *Polyamide Thin-Film Nanofiltration Membranes Containing TiO$_2$ Nanoparticles.* Desalination, 2008. 219: p. 48-56.

51. Pendergast, M.M., A.K. Ghosh, and E.M.V. Hoek, *Separation performance and interfacial properties of nanocomposite reverse osmosis membranes.* Desalination, 2013. 308: p. 180-185.

52. Dimov, A., Islam, M. A., *Hydrophilization of Polyethylene Membranes.* Journal of Membrane Science, 1990. 50: p. 97-100.

53. Kulkarni, A., D. Mukherjee, and W.N. Gill, *Flux enhancement by hydrophilization of thin film composite reverse osmosis membranes.* Journal of Membrane Science, 1996. 114(1): p. 39-50.

54. Bryjak, M., et al., *Modification of polysulfone membranes 4. Ammonia plasma treatment.* European Polymer Journal, 2002. 38(4): p. 717-726.

55. Gancarz, I., G. Pozniak, and M. Bryjak, *Modification of polysulfone membranes 1. CO2 plasma treatment.* European Polymer Journal, 1999. 35(8): p. 1419-1428.

56. Kim, K.S., et al., *Surface modification of polysulfone ultrafiltration membrane by oxygen plasma treatment.* Journal of Membrane Science, 2002. 199(1-2): p. 135-145.

57. Yu, H.Y., et al., *Surface modification of polypropylene microporous membrane to improve its antifouling property in MBR: CO2 plasma treatment.* Journal of Membrane Science, 2005. 254(1-2): p. 219-227.

58. Gonzalez, E., et al., *Remote Atmospheric-Pressure Plasma Activation of the Surfaces of Polyethylene Terephthalate and Polyethylene Naphthalate.* Langmuir, 2008. 24(21): p. 12636-12643.

59. Bernards, M.T., et al., *Nonfouling Polymer Brushes via Surface-Initiated, Two-Component Atom Transfer Radical Polymerization.* Macromolecues, 2008. 41: p. 42-16 - 4219.

60. Li, Q., Z. Xu, and I. Pinnau, *Fouling of reverse osmosis membranes by biopolymers in wastewater secondary effluent: Role of membrane surface properties and initial permeate flux.* Journal of Membrane Science, 2007. 290(1-2): p. 173-181.

61. Kang, G., et al., *Preparation and characterization of crosslinked poly(ethylene glyco) diacrylate membranes with excellent antifouling and solvent-resistant properties.* Journal of Membrane Science, 2008. 318: p. 227 - 232.

62. Kim, J.-H., et al., *Surface Modification of Nanofiltration Membranes to Improve the Removal of Organic Micro-Pollutants (EDCs and PhACs) in Drinking Water Treatment: Graft Polymeriation and Cross-Linking Followed by Functional Group Substitution.* Journal of Membrane Science, 2008. 321: p. 190-1998.

63. Belfer, S., Y. Purinson, and O. Kedem, *Surface modification of commercial polyamide reverse osmosis membranes by radical grafting: An ATR-FTIR study.* Acta Polymerica, 1998. 49(10-11): p. 574-582.

64. Deng, J., et al., *Developments and new applications of UV-induced surface graft polymerizations* Progress in Polymer Science, 2009. 34: p. 156 - 193.

65. Shim, J.K., et al., *Surface modification of polypropylene membranes by γ-ray induced graft copolymerization and their solute permeation characteristics* Journal of Membrane Science, 2001. 190: p. 215 - 226.

66. Dessouki, A.M., N.H. Taher, and M.B. El-Arnaouty, *Gamma ray induced graft copolymerization of N-vinylpyrrolidone, acrylamide and their mixtures onto polypropylene films.* Polymer International, 1998. 45: p. 67 - 76.

67. Bucio, E., Arenas, E., Burillo, G., *Radiation Grafting of N-Isopropylacrylamide onto Polypropylene Films by Preirradition Method.* Mol. Cryst. Liq. Cryst., 2006. 447: p. 203-213.

68. Ulbricht, M., et al., *Photo-induced graft polymerization surface modifications for the preparation of hydrophilic and low-proten-adsorbing ultrafiltration membranes.* Journal of Membrane Science, 1996. 115: p. 31 - 47.

69.   Taniguchi, M., et al., *UV-assisted graft polymerization of synthetic membranes: mechanistics studies.* Chem. Mater., 2003. 15: p. 3805 - 3812.

70.   Susanto, H. and M. Ulbricht, *Photografted thin polymer hydrogel layer on PES ultrafiltration membranes: characterization, stablility, and influence on separation performance.* Langmuir, 2007. 23: p. 7818 - 7830.

71.   Yasuda, H., Bumgarner, M. O., Marsh, H. C., Morosoff, N., *Plasma Polymerization of Some Organic Compounds and Properties of Polymers.* Journal of Polymer Science Part A: Polymer Chemistry, 1976. 14: p. 195-224.

72.   Chen, H., Belfort, G., *Surface Modification of Poly(ether sulfone) Ultrafiltration membranes by Low-Temperature Plasma-Induced Graft Polymerization.* Journal of Applied Polymer Science, 1999. 72: p. 1699-1711.

73.   Cohen, Y., Lewis, G. T., *Graft Polymerization Induced by Atmospheric Pressure Plasma.* 2006: United States Patent 60/857874.

74.   El Harrak, A., et al., *Atom transfer radical polymerization from silica nanoparticles using the 'grafting from' method and structural study via small-angle neutron scattering.* Polymer, 2005. 46: p. 1095 - 1104.

75.   Nguyen, V., W. Yoshida, and Y. Cohen, *Graft polymerization of vinyl acetate onto silica.* Journal of Applied Polymer Science, 2003. 87(2): p. 300-310.

76.   Lewis, G.T., et al., *Reverse Atom Transfer Radical Graft Polymerization of 4-Vinylpyridine onto Inorganic Oxide Surfaces.* Journal of Applied Polymer Science, 2009. 113(1): p. 437-449.

77.   Browne, T., M. Chaimberg, and Y. Cohen, *Graft-Polymerization of Vinyl-Acetate onto Silica.* Journal of Applied Polymer Science, 1992. 44(4): p. 671-677.

78.   Chaimberg, M. and Y. Cohen, *Free-Radical Graft-Polymerization of Vinylpyrrolidone onto Silica.* Industrial & Engineering Chemistry Research, 1991. 30(12): p. 2534-2542.

79.   Bialk, M., O. Prucker, and J. Ruhe, *Grafting of polymers to silid surfaces by using immobilized methacrylates.* Colloids and Surfaces A: Physicochemical and Engineering Aspects, 2002. 198: p. 543 - 549.

80.   Lewis, G.T., et al., *Inorganic surface nanostructuring by atmospheric pressure plasma-induced graft polymerization.* Langmuir, 2007. 23(21): p. 10756-10764.

81.   Bouhacina, T., et al., *Tribological behavior of a polymer grafted on silanized silica probed with a nanotip.* Physical Review B, 1997. 56(12): p. 7694-7703.

82.   Drummond, C., M. In, and P. Richetti, *Behavior of adhesive boundary lubricated surfaces under shear: Effect of grafted diblock copolymers.* European Physical Journal E, 2004. 15(2): p. 159-165.

83.   Orefice, R.L., E. Clark, and A.B. Brenna, *AFM study on the interactions across interfaces containing attached polymer chains.* Macromolecular Materials and Engineering, 2006. 291(4): p. 377-386.

84.   Chen, Y., et al., *Controlled grafting from poly(vinylidene fluoride) microfiltration membranes via reverse atom transfer radical polymerization and antifouling properties* Polymer, 2007. 48: p. 7604 - 7613.

85.   Liu, Z.-M., et al., *Surface modification of polypropylene microfiltration membranes by graft polymerization of N-vinyl-2-pyrrolidone* European Polymer Journal, 2004. 40: p. 2077 - 2087.

86.   Wavhal, D.S. and E.R. Fisher, *Hydrophilic modification of polyethersulfone membranes by low temperature plasma-induced graft polymerization* Journal of Membrane Science, 2002. 209: p. 255 - 269.

87.   Belfer, S., et al., *Modification of NF membrane properties by in situ redox initiated graft polymerization with hydrophilic monomers.* Journal of Membrane Science, 2004. 239(1): p. 55-64.

88.   Gu, M.H., J.E. Kilduff, and G. Belfort, *High throughput atmospheric pressure plasma-induced graft polymerization for identifying protein-resistant surfaces.* Biomaterials, 2012. 33(5): p. 1261-1270.

89.   Sun, J., et al., *Surface modification of PET films by atmospheric pressure plasma-induced acrylic acid inverse emulsion graft polymerization.* Surface & Coatings Technology, 2010. 204(24): p. 4101-4106.

90.   Sun, J., et al., *Effect of storage condition and aging on acrylic acid inverse emulsion surface-grafting polymerization of PET films initiated by atmospheric pressure plasmas.* Surface & Coatings Technology, 2011. 205(8-9): p. 2799-2805.

91.   Zhong, S.F., *Surface Modification of Polypropylene Microporous Membrane by Atmospheric-Pressure Plasma Immobilization of N,N-dimethylamino Ethyl Methacrylate.* Plasma Science & Technology, 2010. 12(5): p. 619-627.

92.   Zhong, S.F., *Surface Modification of Polypropylene Microporous Membrane by Atmospheric-pressure Plasma Induced N-vinyl-2-pyrrolidone Graft Polymerization.* Journal of Wuhan University of Technology-Materials Science Edition, 2012. 27(2): p. 301-309.

93.   Wang, J.K., X.Y. Liu, and H.S. Choi, *Graft copolymerization kinetics of acrylic acid onto the poly(ethylene terephthalate) surface by atmospheric pressure plasma inducement.* Journal of Polymer Science Part B-Polymer Physics, 2008. 46(15): p. 1594-1601.

94.   Borra, J.P., et al., *Atmospheric Pressure Deposition of Thin Functional Coatings: Polymer Surface Patterning by DBD and Post-Discharge Polymerization of Liquid Vinyl Monomer from Surface Radicals.* Plasma Processes and Polymers, 2012. 9(11-12): p. 1104-1115.

95.   Chen, S.H., et al., *Hemocompatible Control of Sulfobetaine-Grafted Polypropylene Fibrous Membranes in Human Whole Blood via Plasma-Induced Surface Zwitterionization.* Langmuir, 2012. 28(51): p. 17733-17742.

96.   Davis, R., A. El-Shafei, and P. Hauser, *Use of atmospheric pressure plasma to confer durable water repellent functionality and antimicrobial functionality on cotton/polyester blend.* Surface & Coatings Technology, 2011. 205(20): p. 4791-4797.

97.   D'Sa, R.A., et al., *Atmospheric pressure plasma induced grafting of poly(ethylene glycol) onto silicone elastomers for controlling biological response.* Journal of Colloid and Interface Science, 2012. 375: p. 193-202.

98.   Edwards, B., et al., *Towards flame retardant cotton fabrics by atmospheric pressure plasma-induced graft polymerization: Synthesis and application of novel phosphoramidate monomers.* Surface & Coatings Technology, 2012. 209: p. 73-79.

99.   Gu, M.H., et al., *Combinatorial synthesis with high throughput discovery of protein-resistant membrane surfaces.* Biomaterials, 2013. 34(26): p. 6133-6138.

100.   Ji, H., et al., *Emulsion Grafting of Glycidyl Methacrylate onto Plasma-treated Polypropylene Surface.* Polymer-Korea, 2012. 36(1): p. 65-70.

101.   Kuroki, T., et al., *Microfabrication and Metal Plating Technologies on Polytetrafluoroethylene Film Surface Treated by Atmospheric-Pressure Nonthermal-Plasma Graft Polymerization Process.* Ieee Transactions on Industry Applications, 2014. 50(1): p. 45-50.

102.   Lewis, G.T. and Y. Cohen, *Controlled Nitroxide-Mediated Styrene Surface Graft Polymerization with Atmospheric Plasma Surface Activation.* Langmuir, 2008. 24(22): p. 13102-13112.

103.   Lin, L., et al., *Modification of hydrophobic acrylic intraocular lens with poly(ethylene glycol) by atmospheric pressure glow discharge: A facile approach.* Applied Surface Science, 2010. 256(24): p. 7354-7364.

104.   Malshe, P., et al., *Functional Military Textile: Plasma-Induced Graft Polymerization of DADMAC for Antimicrobial Treatment on Nylon-Cotton Blend Fabric.* Plasma Chemistry and Plasma Processing, 2012. 32(4): p. 833-843.

105.   Malshe, P., et al., *Multi-functional military textile: Plasma-induced graft polymerization of a C6 fluorocarbon for repellent treatment on nylon-cotton blend fabric.* Surface & Coatings Technology, 2013. 217: p. 112-118.

106.   Mazloumpour, M., et al., *Conferring durable antimicrobial properties on nonwoven polypropylene via plasma-assisted graft polymerization of DADMAC.* Surface & Coatings Technology, 2013. 224: p. 1-7.

107.   Myung, S.W., et al., *Preparation of a reticulated polyurethane foam grafted with poly(acrylic acid) through atmospheric pressure plasma treatment and its lysozyme immobilization.* Journal of Materials Science-Materials in Medicine, 2005. 16(8): p. 745-751.

108.   Njatawidjaja, E., et al., *Polymerization of acrylic acid on expanded poly(tetrafluoroethylene) tube by APGD plasma treatment.* Plasma Processes and Polymers, 2006. 3(4-5): p. 338-341.

109.   Okubo, M., N. Saeki, and T. Yamamoto, *Development of functional sportswear for controlling moisture and odor prepared by atmospheric pressure nonthermal plasma graft polymerization induced by RF glow discharge.* Journal of Electrostatics, 2008. 66(7-8): p. 381-387.

110.   Okubo, M., et al., *Preparation of PTFE Film With Adhesive Surface Treated by Atmospheric-Pressure Nonthermal Plasma Graft Polymerization.* Ieee Transactions on Industry Applications, 2010. 46(5): p. 1715-1721.

111.   Okubo, M., et al., *Plating technology for fluorocarbon polymer films using atmospheric-pressure nonthermal plasma graft polymerization.* Journal of Photopolymer Science and Technology, 2008. 21(2): p. 219-224.

112.   Ramamoorthy, A., A. El-Shafei, and P. Hauser, *Plasma Induced Graft Polymerization of C6 Fluorocarbons on Cotton Fabrics for Sustainable Finishing Applications.* Plasma Processes and Polymers, 2013. 10(5): p. 430-443.

113.   Sun, F.Q., et al., *Enhancing Hydrophilicity and Protein Resistance of Silicone Hydrogels by Plasma Induced Grafting with Hydrophilic Polymers.* Chinese Journal of Polymer Science, 2010. 28(4): p. 547-554.

114.   Sun, F.Q., et al., *Improving Hydrophilicity and Protein Antifouling of Electrospun Poly(Vinylidenefluoride-Hexafluoropropylene) Nanofiber Membranes.* Chinese Journal of Polymer Science, 2010. 28(5): p. 705-713.

115. Vladkova, T., et al., *Surface modification of polymeric ultrafiltration membranes: III. Effect of plasma-chemical surface modification onto some characteristics of polyacrylonitrile ultrafiltration membranes.* High Energy Chemistry, 2013. 47(6): p. 346-352.

116. Wan, J., et al., *Plasma-Induced Direct-Grafting on Polytetrafluoroethylene Films by Quasi-Glow Discharge at Atmospheric Pressure.* Plasma Processes and Polymers, 2009. 6(12): p. 825-830.

117. Widodo, M., A. El-Shafei, and P.J. Hauser, *Surface nanostructuring of kevlar fibers by atmospheric pressure plasma-induced graft polymerization for multifunctional protective clothing.* Journal of Polymer Science Part B-Polymer Physics, 2012. 50(16): p. 1165-1172.

118. Xu, L.H., et al., *Surface-initiated graft polymerization on multiwalled carbon nanotubes pretreated by corona discharge at atmospheric pressure.* Nanoscale, 2010. 2(3): p. 389-393.

119. Painter, P.C. and M.M. Coleman, *Fundamentals of Polymer Science: An Introductory Text, Second Edition*. 1997: CRC Press.

120. Castro, R.P., H.G. Monbouquette, and Y. Cohen, *Shear-induced permeability changes in a polymer grafted silica membrane* Journal of Membrane Science, 2000. 179: p. 207 - 220.

121. Edmondson, S., V.L. Osborne, and W.T.S. Huck, *Polymer brushes via surface-initiated polymerizations.* Chemical Society Reviews, 2004. 33: p. 14 - 22.

122. Lewis, G., *Greg Lewis PhD Thesis*, in *Chemical Engineering Department*. 2008, UCLA: Los Angeles.

123. Inagaki, N., *Plasma surface modification and plasma polymerization*. 1996, Lancaster, PA: Technomic Publishing Company, Inc.

124. Tran, T.D., S. Mori, and M. Suzuki, *Plasma modification of polyacrylonitrile ultrafiltation membrane.* Thin Solid Films, 2007. 515: p. 4148 - 4152.

125. Xu, Z., et al., *Microporous polypropylene hollow fiber membrane: Part I. Surface modification by the graft polymerization of acrylic acid* Journal of Membrane Science, 2002. 196: p. 221 - 229.

126. Suzuki, M., et al., *Graft copolymerization of acrylamide onto a polyethylene surface pretreated with a glow discharge.* Macromolecules, 1986. 19: p. 1804 - 1808.

127. Nguyen, V., et al., *Kinetics of free-radical graft polymerization of 1-vinyl-2-pyrrolidone onto silica.* Journal of Polymer Science Part a-Polymer Chemistry, 2002. 40(1): p. 26-42.

128. Bowen, W.R., A. Mongruel, and P.M. Williams, *Prediction of the rate of cross-flow membrane ultrafiltration: A colloidal interaction approach.* Chemical Engineering Science, 1996. 51(18): p. 4321-4333.

129. Chaimberg, M. and Y. Cohen, *Kinetic Modeling of Free-Radical Graft-Polymerization.* Aiche Journal, 1994. 40(2): p. 294-311.

130. Wingrave, J.A., *Oxide surfaces*. Surfactant science series. 2001, New York: Marcel Dekker.

131. Yoshida, W., et al., *Multilayer alkoxysilane silylation of oxide surfaces.* Langmuir, 2001. 17(19): p. 5882-5888.

132. Chaimberg, M., R. Parnas, and Y. Cohen, *Graft-Polymerization of Polyvinylpyrrolidone onto Silica.* Journal of Applied Polymer Science, 1989. 37(10): p. 2921-2931.

133. Faibish, R.S., Cohen, Y., *Fouling and Rejection Behavior of Ceramic and Polymer-Modified Ceramic Membranes for Ultrafiltration of Oil-in-Water Emulsions and Microemulsions.* Colloids and Surfaces, 2001. 191: p. 27-40.

134. Rovira-Bru, M., F. Giralt, and Y. Cohen, *Protein adsorption onto zirconia modified with terminally grafted polyvinylpyrrolidone.* Journal of Colloid and Interface Science, 2001. 235(1): p. 70-79.

135. Lewis, G.T., V. Nguyen, and Y. Cohen, *Synthesis of poly(4-vinylpyridine) by reverse atom transfer radical polymerization.* Journal of Polymer Science Part a-Polymer Chemistry, 2007. 45(24): p. 5748-5758.

136. Sanli, O. and E. Pulat, *Solvent-Assisted Graft-Copolymerization of Acrylamide on Poly(Ethylene-Terephthalate) Films Using Benzoyl Peroxide Initiator.* Journal of Applied Polymer Science, 1993. 47(1): p. 1-6.

137. Wei, X.Y., et al., *Surface modification of commercial aromatic polyamide reverse osmosis membranes by graft polymerization of 3-allyl-5,5-dimethylhydantoin.* Journal of Membrane Science, 2010. 351(1-2): p. 222-233.

138. Shi, Q., et al., *Graft polymerization of methacrylic acid onto polyethersulfone for potential pH-responsive membrane materials.* Journal of Membrane Science, 2010. 347(1-2): p. 62-68.

139. Childs, R.F., et al., *Formation of pore-filled microfiltration membranes using a combination of modified interfacial polymerization and grafting.* Journal of Polymer Science Part a-Polymer Chemistry, 2002. 40(2): p. 242-250.

140. Wang, H., et al., *Surface Modification of Polypropylene Microporous Membrane by Grafting Acrylic Acid Using Physisorbed Initiators Method.* Journal of Applied Polymer Science, 2009. 112(6): p. 3728-3735.

141. Odian, G.G., *Principles of polymerization.* 1970, New York,: McGraw-Hill.

142. Mishra, M.K. and Y. Yagci, *Handbook of vinyl polymers : radical polymerization, process, and technology.* 2nd ed. Plastics engineering (CRC Press). 2009, Boca Raton, Fla.: CRC Press.

143. Gaylord, N.G. and M.K. Mishra, *Nondegradative Reaction of Maleic-Anhydride and Molten Polypropylene in the Presence of Peroxides.* Journal of Polymer Science Part C-Polymer Letters, 1983. 21(1): p. 23-30.

144. Dougherty, T., *Chemistry of 2,2'-Azobisisobutyramidine Hydrochloride in Aqueous Solution - a Water-Soluble Azo Initiator.* Journal of the American Chemical Society, 1961. 83(23): p. 4849-4853.

145. Gilron, J., et al., *Effects of surface modification on antifouling and performance properties of reverse osmosis membranes.* Desalination, 2001. 140(2): p. 167-179.

146. Reddy, A.V.R., et al., *Fouling resistant membranes in desalination and water recovery.* Desalination, 2005. 183(1-3): p. 301-306.

147. Wang, M., et al., *Preparation of pH-responsive phenolphthalein poly(ether sulfone) membrane by redox-graft pore-filling polymerization technique.* Journal of Membrane Science, 2007. 287(2): p. 257-263.

148. Sarac, A.S., *Redox polymerization.* Progress in Polymer Science, 1999. 24(8): p. 1149-1204.

149. Murugan, R. and K.P. Rao, *Graft polymerization of glycidylmethacrylate onto coralline hydroxyapatite.* Journal of Biomaterials Science-Polymer Edition, 2003. 14(5): p. 457-468.

150. Filho, A.A.M.F. and A.S. Gomes, *Copolymerization of styrene onto polyethersulfone films induced by gamma ray irradiation.* Polymer Bulletin, 2006. 57(4): p. 415-421.

151. Mehta, I.K., D.S. Sood, and B.N. Misra, *Grafting onto Polypropylene. 2. Solvent Effect on Graft-Copolymerization of Acrylonitrile by Preirradiation Method.* Journal of Polymer Science Part a-Polymer Chemistry, 1989. 27(1): p. 53-62.

152. Misra, B.N., D.S. Sood, and I.K. Mehta, *Grafting onto Polypropylene .1. Effect of Solvents in Gamma-Radiation-Induced Graft-Copolymerization of Poly(Acrylonitrile).* Journal of Polymer Science Part a-Polymer Chemistry, 1985. 23(6): p. 1749-1757.

153. Sportelli, L., et al., *Effect of Gamma-Irradiation on Membranes of Normal and Pathological Erythrocytes (Beta-Thalassemia).* Radiation and Environmental Biophysics, 1987. 26(1): p. 81-84.

154. Vijayavergiya, V. and A. Mookerjee, *Effect of Gamma-Radiation on Cation-Transport across an Artificial Membrane.* Journal of Radioanalytical and Nuclear Chemistry-Articles, 1989. 134(1): p. 39-44.

155. Brandrup, J., E.H. Immergut, and E.A. Grulke, *Polymer Handbook.* 4 ed. 1999, New York: John Wiley.

156. Abu Seman, M.N., M. Khayet, and N. Hilal, *Comparison of two different UV-grafted nanofiltration membranes preparede for reduction of humic acid fouling using acrylic acid and N-vinylpyrrolidone.* Desalination 2010. 287: p. 19-29.

157. Bilongo, T.G., J.C. Remigy, and M.J. Clifton, *Modification of hollow fibers by UV surface grafting.* Journal of Membrane Science, 2010. 364(1-2): p. 304-308.

158. Kaeselev, B., J. Pieracci, and G. Belfort, *Photoinduced grafting of ultrafiltration membranes: comparison of poly(ether sulfone) and poly(sulfone).* Journal of Membrane Science, 2001. 194(2): p. 245-261.

159. Rahimpour, A., *Preparation and modification of nano-porous polyimide (PI) membranes by UV photo-grafting process: Ultrafiltration and nanofiltration performance.* Korean Journal of Chemical Engineering, 2011. 28(1): p. 261-266.

160. Abu Seman, M.N., et al., *Reduction of nanofiltration membrane fouling by UV-initiated graft polymerization technique.* Journal of Membrane Science, 2010. 355: p. 133-141.

161. Crivello, J.V., G. Belfort, and H. Yamagishi, *Low Fouling Ultrafiltration and Microfiltration Aryl Polysulfone.* 1995: United States Patent 5,468,390.

162. Taniguchi, M. and G. Belfort, *Low protein fouling synthetic membranes by UV-assisted surface grafting modification: varying monomer type.* Journal of Membrane Science, 2004. 231(1-2): p. 147-157.

163. Yamagishi, H., J.V. Crivello, and G. Belfort, *Development of a Novel Photochemical Technique for Modifying Poly(Arylsulfone) Ultrafiltration Membranes.* Journal of Membrane Science, 1995. 105(3): p. 237-247.

164. Kochkodan, V.M., et al., *Effect of the surface modification of polymer membranes on their microbiological fouling.* Colloid Journal, 2006. 68(3): p. 267-273.

165. Yang, Q., et al., *Fabrication of glycosylated surface on polymer membrane by UV-induced graft polymerization for lectin recognition.* Langmuir, 2006. 22(22): p. 9345-9349.

166. Yu, H.Y., et al., *Photoinduced graft polymerization to improve antifouling characteristics of an SMBR.* Journal of Membrane Science, 2007. 302(1-2): p. 235-242.

167. Yu, H.Y., et al., *Photoinduced graft polymerization of acrylamide on polypropylene microporous membranes for the improvement of antifouling characteristics in a*

submerged membrane-bioreactor. Separation and Purification Technology, 2007. 53(1): p. 119-125.

168.   Hong, K.H., N. Liu, and G. Sun, *UV-induced graft polymerization of acrylamide on cellulose by using immobilized benzophenone as a photo-initiator.* European Polymer Journal, 2009. 45(8): p. 2443-2449.

169.   Malaisamy, R., et al., *Development of reactive thin film polymer brush membranes to prevent biofouling.* Journal of Membrane Science, 2010. 350(1-2): p. 361-370.

170.   Hilal, N., et al., *Methods Employed for Control of Fouling in MF and UF Membranes: A Comprehensive Review.* Separation Science and Technology, 2005. 40: p. 1957-2005.

171.   Van der Bruggen, B., *Chemical Modification of Polyethersulfone Nanofiltration Membranes: A Review.* Journal of Applied Polymer Science, 2009. 114(1): p. 630-642.

172.   Schutze, A., et al., *The atmospheric-pressure plasma jet: A review and comparison to other plasma sources.* Ieee Transactions on Plasma Science, 1998. 26(6): p. 1685-1694.

173.   Akashi, N. and S. Kuroda, *Preparation and characterization of Protein A-immobilized PVDF and PES membranes.* Express Polymer Letters, 2015. 9(1): p. 2-13.

174.   Inagaki, N., et al., *Surface characterization of plasma-modified poly(ethylene terephthalate) film surfaces.* Journal of Polymer Science Part B-Polymer Physics, 2004. 42(20): p. 3727-3740.

175.   Steen, M.L., A.C. Jordan, and E.R. Fisher, *Hydrophilic modification of polymeric membranes by low temperature H2O plasma treatment.* Journal of Membrane Science, 2002. 204(1-2): p. 341-357.

176.   Bryjak, M., et al., *Air plasma treatment of polyacrylonitrile porous membrane.* Angewandte Makromolekulare Chemie, 1996. 234: p. 21-29.

177.   Zhu, L.P., et al., *Corona-induced graft polymerization for surface modification of porous polyethersulfone membranes.* Applied Surface Science, 2007. 253(14): p. 6052-6059.

178.   Akamatsu, K., et al., *Plasma graft polymerization to develop low-fouling membranes grafted with poly(2-methoxyethylacrylate).* Separation and Purification Technology, 2013. 102: p. 157-162.

179.   Chen, J., et al., *Nanofiltration membrane prepared from polyacrylonitrile ultrafiltration membrane by low-temperature plasma: 5. Grafting of styrene in vapor phase and its application.* Surface & Coatings Technology, 2007. 201(15): p. 6789-6792.

180.   Kaur, S., et al., *Plasma-induced graft copolymerization of poly(methacrylic acid) on electrospun poly(vinylidene fluoride) nanofiber membrane.* Langmuir, 2007. 23(26): p. 13085-13092.

181.   Li, M.S., et al., *Controllable modification of polymer membranes by LDDLT plasma flow: Antibacterial layer onto PE hollow fiber membrane module.* Chemical Engineering Journal, 2015. 265: p. 16-26.

182.   Wang, X.L., et al., *Preparation and characterization of negatively charged hollow fiber nanofiltration membrane by plasma-induced graft polymerization.* Desalination, 2012. 286: p. 138-144.

183.   Zhao, Z.P., et al., *Nanofiltration membrane prepared from polyacrylonitrile ultrafiltration membrane by low-temperature plasma: 4. Grafting of N-vinylpyrrolidone in aqueous solution.* Desalination, 2005. 184(1-3): p. 37-44.

184.   Imbrogno, J., M.D. Williams, and G. Belfort, *A New Combinatorial Method for Synthesizing, Screening, and Discovering Antifouling Surface Chemistries.* Acs Applied Materials & Interfaces, 2015. 7(4): p. 2385-2392.

185. Tyszler, D., et al., *Reduced fouling tendencies of ultrafiltration membranes in wastewater treatment by plasma modification.* Desalination, 2006. 189(1-3): p. 119-129.

186. Zhu, A.H., P.D. Christofides, and Y. Cohen, *On RO membrane and energy costs and associated incentives for future enhancements of membrane permeability.* Journal of Membrane Science, 2009. 344(1-2): p. 1-5.

187. Cadotte, J.E., et al., *A new thin-film composite seawater reverse osmosis membrane.* Desalination, 1980. 32: p. 25 - 31.

188. Singh, P.S., et al., *Probing the structural variations of thin film composite RO membranes obtained by coating polyamide over polysulfone membranes of different pore dimensions.* Journal of Membrane Science, 2006. 278: p. 19 - 25.

189. Zhu, A.H., et al., *Reverse osmosis desalination with high permeability membranes - Cost optimization and research needs.* Desalination and Water Treatment, 2010. 15(1-3): p. 256-266.

190. Wang, J.W., et al., *A critical review of transport through osmotic membranes.* Journal of Membrane Science, 2014. 454: p. 516-537.

191. Chen, G., et al., *Novel thin-film composite membranes with improved water flux from sulfonated cardo poly(arylene ether sulfone) bearing pendant amino groups.* Journal of Membrane Science, 2008. 310(1-2): p. 102-109.

192. Fathizadeh, M., A. Aroujalian, and A. Raisi, *Effect of lag time in interfacial polymerization on polyamide composite membrane with different hydrophilic sub layers.* Desalination, 2012. 284: p. 32-41.

193. Jegal, J., S.G. Min, and K.H. Lee, *Factors affecting the interfacial polymerization of polyamide active layers for the formation of polyamide composite membranes.* Journal of Applied Polymer Science, 2002. 86(11): p. 2781-2787.

194. Rahimpour, A., et al., *Preparation and characterization of asymmetric polyethersulfone and thin-film composite polyamide nanofiltration membranes for water softening.* Applied Surface Science, 2010. 256(6): p. 1657-1663.

195. Kanani, D.A., X.H. Sun, and R. Ghosh, *Reversible and irreversible membrane fouling during in-line microfiltration of concentrated protein solutions.* Journal of Membrane Science, 2008. 315(1-2): p. 1-10.

196. Tiraferri, A., et al., *Relating performance of thin-film composite forward osmosis membranes to support layer formation and structure.* Journal of Membrane Science, 2011. 367(1-2): p. 340-352.

197. Yip, N.Y., et al., *High Performance Thin-Film Composite Forward Osmosis Membrane.* Environmental Science & Technology, 2010. 44(10): p. 3812-3818.

198. Chai, G.Y. and W.B. Krantz, *Formation and Characterization of Polyamide Membranes Via Interfacial Polymerization.* Journal of Membrane Science, 1994. 93(2): p. 175-192.

199. Huang, S.H., et al., *Effect of chemical structures of amines on physicochemical properties of active layers and dehydration of isopropanol through interfacially polymerized thin-film composite membranes.* Journal of Membrane Science, 2008. 307(1): p. 73-81.

200. Rao, A.P., et al., *Structure-performance correlation of polyamide thin film composite membranes: effect of coating conditions on film formation.* Journal of Membrane Science, 2003. 211(1): p. 13-24.

201. Koltuniewicz, A.B., R.W. Field, and T.C. Arnot, *Cross-Flow and Dead-End Microfiltration of Oily-Water Emulsion .1. Experimental-Study and Analysis of Flux Decline.* Journal of Membrane Science, 1995. 102: p. 193-207.

202. Lee, S., Y. Aurelle, and H. Roques, *Concentration Polarization, Membrane Fouling and Cleaning in Ultrafiltration of Soluble Oil.* Journal of Membrane Science, 1984. 19(1): p. 23-38.

203. Lipp, P., et al., *A Fundamental-Study of the Ultrafiltration of Oil-Water Emulsions.* Journal of Membrane Science, 1988. 36: p. 161-177.

204. Nystrom, M., *Ultrafiltration of O/W Emulsions Stabilized by Limiting Amounts of Tall Oil.* Colloids and Surfaces, 1991. 57(1-2): p. 99-114.

205. Song, L.F. and M. Elimelech, *Theory of Concentration Polarization in Cross-Flow Filtration.* Journal of the Chemical Society-Faraday Transactions, 1995. 91(19): p. 3389-3398.

206. Hasson, D., A. Drak, and R. Semiat, *Inception of CaSO4 scaling on RO membranes at various water recovery levels.* Desalination, 2001. 139(1-3): p. 73-81.

207. Le Gouellec, Y.A. and M. Elimelech, *Calcium sulfate (gypsum) scaling in nanofiltration of agricultural drainage water.* Journal of Membrane Science, 2002. 205(1-2): p. 279-291.

208. Lyster, E. and Y. Cohen, *Numerical study of concentration polarization in a rectangular reverse osmosis membrane channel: Permeate flux variation and hydrodynamic end effects.* Journal of Membrane Science, 2007. 303(1-2): p. 140-153.

209. Flemming, H.C., et al., *Biofouling - the Achilles heel of membrane processes.* Desalination, 1997. 113(2-3): p. 215-225.

210. Gonzalez, E. and R.F. Hicks, *Surface Analysis of Polymers Treated by Remote Atmospheric Pressure Plasma.* Langmuir, 2010. 26(5): p. 3710-3719.

211. Van Oss, C.J., *Interfacial forces in aqueous media*. 1994, New York: Marcel Dekker, Inc.

212. van Oss, C.J., *The properties of water and their role in colloidal and biological systems*. 1 ed. Interface Science and Technology, ed. A. Hubbard. Vol. 16. 2008, Amsterdam: Elsevier.

213. Owens, D.K. and R.C. Wendt, *Estimation of Surface Free Energy of Polymers.* Journal of Applied Polymer Science, 1969. 13(8): p. 1741-1747.

214. Cini, R., G. Loglio, and A. Ficalbi, *Temperature dependence of the surface tension of water by the equilibrium ring method.* Journal of Colloid and Interface Science, 1972. 41(2): p. 287-297.

215. Zhao, Q., Y. Liu, and E.W. Abel, *Effect of temperature on the surface free energy of amorphous carbon films.* Journal of Colloid and Interface Science, 2004. 280(1): p. 174-183.

216. Matyjaszewsk, K. and T.P. Davis, *Handbook of Radical Polymerization*. 2002, Hoboken: John Wiley and Sons, Inc.

217. Lin, N.H. and Y. Cohen, *QCM study of mineral surface crystallization on aromatic polyamide membrane surfaces.* Journal of Membrane Science, 2011. 379(1-2): p. 426-433.

218. Faibish, R.S., W. Yoshida, and Y. Cohen, *Contact angle study on polymer-grafted silicon wafers.* Journal of Colloid and Interface Science, 2002. 256(2): p. 341-350.

219. Uchida, E., Y. Uyama, and Y. Ikada, *A Novel Method for Graft-Polymerization onto Poly(Ethylene-Terephthalate) Film Surface by Uv Irradiation without Degassing.* Journal of Applied Polymer Science, 1990. 41(3-4): p. 677-687.

220. Li, Q., et al., *Exploring the dependence of bulk properties on surface chemistries and microstructures of commercially composite RO membranes by novel characterization approaches.* Desalination, 2012. 292: p. 9-18.

221. Wenzel, R.N., *Resistance of solid surfaces to wetting by water.* Industrial and Engineering Chemistry, 1936. 28: p. 988-994.

222. Hansen, C.M., *Hansen Solubility Parameters: A User's Handbook.* 2000, Boca Raton, FL: CRC Press.

223. Barton, A.F.M., *CRC handbook of polymer-liquid interaction parameters and solubility parameters.* 1990, Boca Raton, FL: CRC Press.

224. Thakur, A., R.K. Wanchoo, and P. Singh, *Structural Parameters and Swelling Behavior of pH Sensitive Poly(acrylamide-co-acrylic acid) Hydrogels.* Chemical and Biochemical Engineering Quarterly, 2011. 25(2): p. 181-194.

225. Farahani, B.V., et al., *Qualitative Investigation on some H-bonded Interpolymer Complexes by Determination of Thermodynamic Parameters.* Journal of the Mexican Chemical Society, 2011. 56(2): p. 212-216.

226. Ito, Y., et al., *Synthesis and Nonthrombogenicity of Polyetherurethaneurea Film Grafted with Poly(Sodium Vinyl Sulfonate).* Journal of Biomedical Materials Research, 1991. 25(11): p. 1347-1361.

227. Yu, H.Y., et al., *Improvement of the antifouling characteristics for polypropylene microporous membranes by the sequential photoinduced graft polymerization of acrylic acid.* Journal of Membrane Science, 2006. 281(1-2): p. 658-665.

228. Zhu, L.J., et al., *Hydrophilic and anti-fouling polyethersulfone ultrafiltration membranes with poly(2-hydroxyethyl methacrylate) grafted silica nanoparticles as additive.* Journal of Membrane Science, 2014. 451: p. 157-168.

229. Chen, C., et al., *XPS investigation of Nafion (R) membrane degradation.* Journal of Power Sources, 2007. 169(2): p. 288-295.

230. Carson, C., et al., *Blobworld: Image segmentation using expectation-maximization and its application to image querying.* Ieee Transactions on Pattern Analysis and Machine Intelligence, 2002. 24(8): p. 1026-1038.

231. Dempster, A.P., N.M. Laird, and D.B. Rubin, *Maximum Likelihood from Incomplete Data Via Em Algorithm.* Journal of the Royal Statistical Society Series B-Methodological, 1977. 39(1): p. 1-38.

232. Ng, S.K. and G.J. McLachlan, *Speeding up the EM algorithm for mixture model-based segmentation of magnetic resonance images.* Pattern Recognition, 2004. 37(8): p. 1573-1589.

233. van Krevelen, D.W., *Properties of Polymers: Their Correlation with Chemical Structure; their Numerical Estimation and Prediction from Additive Group Contributions.* 3rd ed. 1990, New York: Elsevier.

234. Barton, A.F.M., *CRC Handbook of solubility parameters and other Cohesion parameters.* 2nd ed. 1991, Boca Raton, FL: CRC Press LLC.

235. Kang, G.D., et al., *Surface modification of a commercial thin film composite polyamide reverse osmosis membrane by carbodiimide-induced grafting with poly(ethylene glycol) derivatives.* Desalination, 2011. 275(1-3): p. 252-259.

236. Tiwari, A. and L. Uzun, *Advanced Functional Materials.* 2015, Hoboken, NJ: John Wiley & Sons, Inc.

237.	Barabanova, A.I., et al., *Radical Polymerization of Vinylsulfonic Acid and Its Copolymerization with Acrylamide in Aqueous-Solution.* Vysokomolekulyarnye Soedineniya Seriya a & Seriya B, 1994. 36(6): p. A901-A907.

238.	Barth, J., W. Meiser, and M. Buback, *SP-PLP-EPR Study into Termination and Transfer Kinetics of Non-Ionized Acrylic Acid Polymerized in Aqueous Solution.* Macromolecules, 2012. 45(3): p. 1339-1345.

239.	Alvarez, J., M. Encinas, and E.A. Lissi, *Solvent effects on the rate of polymerization of 2-hydroxyethyl methacrylate photoinitiated with aliphatic azo compounds.* Macromolecular Chemistry and Physics, 1999. 200(10): p. 2411-2415.

240.	Fahrner, R.L., et al., *Polyelectrolyte precipitation and purification of antibodies*. 2011, Genentech, Inc: Germany.

241.	Ferreira, L., M.M. Vidal, and M.H. Gil, *Evaluation of poly(2-hydroxyethyl methacrylate) gels as drug delivery systems at different pH values.* International Journal of Pharmaceutics, 2000. 194(2): p. 169-180.

242.	Hu, M.X., Q. Yang, and Z.K. Xu, *Enhancing the hydrophilicity of polypropylene microporous membranes by the grafting of 2-hydroxyethyl methacrylate via a synergistic effect of photoinitiators.* Journal of Membrane Science, 2006. 285(1-2): p. 196-205.

243.	Thompson, J., et al., *RO membrane mineral scaling in the presence of a biofilm.* Journal of Membrane Science, 2012. 415-416: p. 181-191.

244.	Cadotte, J.E., et al., *Interfacial Synthesis in the Preparation of Reverse Osmosis Membranes.* Journal of Macromolecular Science-Chemistry, 1981. A15: p. 727-755.

245.	Burns, D.B. and A.L. Zydney, *Buffer effects on the zeta potential of ultrafiltration membranes.* Journal of Membrane Science, 2000. 172(1-2): p. 39-48.

246.	Elimelech, M., W.H. Chen, and J.J. Waypa, *Measuring the Zeta (Electrokinetic) Potential of Reverse-Osmosis Membranes by a Streaming Potential Analyzer.* Desalination, 1994. 95(3): p. 269-286.

247.	Meiron, T.S., Marmur, A., Saguy, I.S., *Contact Angle Measurment on Rough Surfaces.* Colloid and Interface Science, 2004. 274: p. 637 - 644.

248.	Rahardianto, A., B.C. McCool, and Y. Cohen, *Reverse osmosis desalting of inland brackish water of high gypsum scaling propensity: kinetics and mitigation of membrane mineral scaling.* Environ. Sci. Technol., 2008. 42: p. 4292 - 4297.

249.	Baker, J.S. and L.Y. Dudley, *Biofouling in membrane systems- a review.* Desalination, 1998. 118: p. 81 - 90.

250.	Lawrence, J.R. and T.R. Neu, *Confocal laser scanning microscopy for analysis of microbial biofilms.* Biofilms, 1999. 310: p. 131-144.

251.	Bradford, M., *A Rapid and Sensitive Method for the Quantitation of Microgram Quantities of Protein Utilizing the Principle of Protein-Dye Binding.* Analytical Biochemistry, 1976. 72(1-2): p. 248-254.

252.	Dubois, M., et al., *Colorimetric method for determination of sugars and related substances.* Analytical Chemistry, 1956. 28(3): p. 350-356.

253.	Li, T.G., R.B. Bai, and J.X. Liu, *Distribution and composition of extracellular polymeric substances in membrane-aerated biofilm.* Journal of Biotechnology, 2008. 135(1): p. 52-57.

254.	Ye, F.X., Y.F. Ye, and Y. Li, *Effect of C/N ratio on extracellular polymeric substances (EPS) and physicochemical properties of activated sludge flocs.* Journal of Hazardous Materials, 2011. 188(1-3): p. 37-43.

255.   Krafft, R., *Developing and characterizing biofilms from secondary wastewater on reverse osmosis membranes using a flat sheet flow cell*. 2008, University of Duiberg: Essen.

256.   Shih, W.-Y., et al., *Morphometric characterization of calcium sulfate dihydrate (gypsum) scale on reverse osmosis membranes. Journal of Membrane Science*, 2005. 252: p. 253-263.

257.   Sim, S.T.V., et al., *Monitoring membrane biofouling via ultrasonic time-domain reflectometry enhanced by silica dosing.* Journal of Membrane Science, 2013. 428: p. 24-37.

258.   Katebian, L. and S.C. Jiang, *Marine bacterial biofilm formation and its responses to periodic hyperosmotic stress on a flat sheet membrane for seawater desalination pretreatment.* Journal of Membrane Science, 2013. 425-426: p. 182-189.

259.   Northcott, K., et al., *Development of membrane testing protocols for characterisation of RO and NF membranes.* Desalination, 2009. 236: p. 194 - 201.

260.   Park, C., et al., *Effect of cake layer structure on colloidal fouling in reverse osmosis membranes.* Desalination, 2008. 220: p. 335 - 344.

261.   McCool, B.C., et al., *Feasibilty of reverse osmosis desalination of brackish agricultural drainage water in the San Joaquin Valley.* Desalination, 2010. 261: p. 240 - 250.

262.   Lyster, E., et al., *A method for evaluating antiscalant retardation of crystal nucleation and growth on RO membranes.* Journal of Membrane Science, 2010. 364: p. 122 - 131.

263.   Shah, H.N., et al., *Approaches to the study of the systematics of anaerobic, Gram-negative, non-sporeforming rods: Current status and perspectives.* Anaerobe, 2009. 15(5): p. 179-194.

264.   Flemming, H.C., Schaule, G., *Biofouling on Membranes: A Microbiological Approach.* Desalination, 1988. 70: p. 95-119.

265.   Flemming, H.C., *Reverse osmosis membrane biofouling.* Experimental Thermal and Fluid Science, 1997. 14(4): p. 382-391.

266.   Belfort, G., R.H. Davis, and A.L. Zydney, *The behavior of suspensions and macromolecular solutions in crossflow microfiltration.* Journal of Membrane Science, 1994. 96: p. 1-58.

267.   Ye, Y.S., J. Huang, and X.L. Wang, *Fabrication of a Self-Cleaning Surface via the Thermosensitive Copolymer Brush of P(NIPAAm-PEGMA).* Acs Applied Materials & Interfaces, 2015. 7(40): p. 22128-22136.

268.   Faibish, R.S., M. Elimelech, and Y. Cohen, *Effect of interparticle electrostatic double layer interactions on permeate flux decline in crossflow membrane filtration of colloidal suspensions: An experimental investigation.* Journal of Colloid and Interface Science, 1998. 204(1): p. 77-86.

269.   Ang, W.S., et al., *Fouling and cleaning of RO membranes fouled by mixtures of organic foulants simulating wastewater effluent.* Journal of Membrane Science, 2011. 376: p. 196-206.

270.   Ang, W.S., et al., *Chemical cleaning of RO membranes fouled by wastewater effluent: achieving higher efficiency with dual-step cleaing.* Journal of Membrane Science, 2011. 382: p. 100 - 106.

271.   Li, Q. and M. Elimelech, *Organic fouling and chemical cleaning of nanofiltration membranes: measurements and mechanisms.* Environ. Sci. Technol., 2004. 38: p. 4683 - 4693.